



Durham E-Theses

Rydberg dark states in external fields

TANASITTIKOSOL, MONSIT

How to cite:

TANASITTIKOSOL, MONSIT (2011) *Rydberg dark states in external fields*, Durham theses, Durham University. Available at Durham E-Theses Online: <http://etheses.dur.ac.uk/3287/>

Use policy

The full-text may be used and/or reproduced, and given to third parties in any format or medium, without prior permission or charge, for personal research or study, educational, or not-for-profit purposes provided that:

- a full bibliographic reference is made to the original source
- a [link](#) is made to the metadata record in Durham E-Theses
- the full-text is not changed in any way

The full-text must not be sold in any format or medium without the formal permission of the copyright holders.

Please consult the [full Durham E-Theses policy](#) for further details.

Rydberg dark states in external fields

Monsit Tanasittikosol

Abstract

We initially discuss the theory of three-level systems using the dressed state formalism. One of the dressed states, containing a ground state and a Rydberg state, does not couple with the probe laser; thus, the medium becomes transparent to the latter. This phenomenon is known as electromagnetically induced transparency (EIT) and this dressed state is known as a Rydberg dark state. We show that EIT can be used to extract the reduced dipole matrix element for transitions to a Rydberg state. However, a problem with three-level Rydberg EIT in a vapour cell is the occurrence of space charges caused by photoelectric ionisation of Rb metal deposited inside the cell. To avoid this problem, we consider adding a third laser resonant with a fourth level. This is to avoid using the laser whose wavelength is less than the threshold wavelength. In cold atoms, the effect of the third laser is to split the usual EIT resonance into a doublet. In thermal atoms, we observe narrow features due to electromagnetically induced absorption and electromagnetically induced transparency in the Doppler-free configuration. Next we consider the action of a far off-resonance radio frequency (rf) field in the three-level system. We demonstrate the formation of rf-dressed EIT resonances in a thermal Rb vapour and show that such states exhibit enhanced sensitivity to dc electric fields compared to their bare counterparts. Fitting the corresponding EIT profile enables precise measurements of the dc field independent of laser frequency fluctuations. We further investigate the theory of rf-dressed Rydberg EIT using the Floquet approach in order to understand the formation of the sideband structure of the Rydberg state. We find that if the time scale of the rf interaction is much shorter than that of the system evolution and decoherence, the sideband structure is well resolved. We also show that the intermediate state exhibits a sideband structure, induced by the Rydberg state, when the Rabi frequency of coupling laser is larger than twice the modulation frequency. Finally we consider resonant microwave coupling between the Rydberg states which leads to an Autler-Townes splitting of the EIT resonance in cold atoms. This splitting can be employed to vary the group index by $\pm 10^5$ allowing independent control of the absorptive and dispersive properties of the medium, i.e., one can switch the transparency of the medium or control the group velocity of a pulse propagation by tuning on and off the microwave field.

Rydberg dark states in external fields

Monsit Tanasittikosol

A thesis submitted in partial fulfilment
of the requirements for the degree of
Doctor of Philosophy



Department of Physics
Durham University

October 12, 2011

Declaration

I confirm that no part of the material offered has previously been submitted by myself for a degree in this or any other University. Where material has been generated through joint work, the work of others has been indicated.

Monsit Tanasittikosol
Durham, October 12, 2011

The copyright of this thesis rests with the author. No quotation from it should be published without their prior written consent and information derived from it should be acknowledged.

*To my father, who now lives peacefully in heaven,
I will never forget the wonderful memories of you.*

*To my mother,
for her endless love and encouragement.*

Acknowledgements

It comes to my realisation while I am writing this thesis that PhD study is truly a journey. Without the great help from my supervisors, Dr Potvliege and Prof Adams, I would not have been able to complete such a journey. Not only did they give me invaluable advices, but they have also been my excellent consultants for every problem I have encountered during the period of my study. I am really grateful to both of them.

Special thanks must go to Ashok, Jon and, especially, Mark for their great work on the experiments and for stimulating discussions. I also want to thank Paul for his invaluable discussion not only in physics, but also in English culture. Another person whom I must recognise is Dr Hughes. He is an amazing man who can make hard physics easy to understand. Dr Gardiner is also a great pastoral interviewer whom I feel relaxed when talking to him. I also want to thank my friends, especially Nim, Tung, Bid, P'Kay and P'Lec, who made my 8 years in Durham a wonderful experience. I am also indebted to Carrie who always take me out to Newcastle to have fun. Her invaluable friendship makes me feel like UK is my second home.

Finally, I would like to thank all of my family, especially my mum and dad who are always by my side no matter what happens. Thanks for their encouragement and care they have been giving me for 27 years.

Contents

	Page
Abstract	i
Title Page	ii
Declaration	iii
Acknowledgements	v
Contents	vi
List of Figures	ix
List of Tables	xi
1 Introduction	1
1.1 Electromagnetically induced transparency and dark states . . .	1
1.2 Rydberg EIT	2
1.3 Dressing atoms with rf fields	4
1.4 Thesis layout	6
2 Interaction of three-level atoms with EM fields	8
2.1 Hamiltonian of the atom-fields system	8
2.2 Dressed state formalism for three-level system	12
2.2.1 Dynamical evolution of three-level system	13
2.2.2 Eigenvalue spectrum of three-level system	14
2.3 Adiabatic elimination of intermediate state	21
2.4 Relaxation and optical Bloch equations	26
2.5 Weak probe limit	28
2.6 Susceptibility of the system	31
2.7 Doppler broadening	32
2.8 Summary	34
3 Measuring a dipole matrix element using Rydberg EIT	35
3.1 Experimental set up	36
3.2 Theoretical modelling of EIT	37

3.2.1	Y systems	38
3.2.2	Modelling the EIT transmission of ^{85}Rb	43
3.3	Observation of EIT resonances and wavevector mismatch	46
3.4	Extracting reduced matrix element	47
3.5	Summary and conclusions	52
4	Rydberg EIT with three-photon transition	54
4.1	Theory of three-photon transition for cold atoms	57
4.2	Theory of three-photon transition with Doppler broadening	61
4.3	EIT lineshape for the parallel configuration	66
4.4	EIT lineshape for Doppler free configuration	67
4.4.1	Effect of residual wavevectors in two-photon transition	69
4.4.2	EIT and EIA with Doppler free configuration	71
4.5	Summary and conclusions	73
5	Enhanced electric field sensitivity of rf-dressed Rydberg dark states	76
5.1	Theoretical framework	77
5.1.1	Phase modulation by a weak field	77
5.1.2	EIT modelling	82
5.2	Comparison between theory and experiment	88
5.3	Observation of Floquet dark states	94
5.4	Enhanced electric field sensitivity of Floquet dark states	95
5.5	Summary and conclusions	98
6	Sidebands shifts and induced sidebands in rf-dressed Rydberg systems	101
6.1	Equations of motion	102
6.2	Floquet formalism of rf-dressed two-level subsystems	108
6.2.1	Floquet Hamiltonian	108
6.2.2	Quasienergy spectrum	114
6.2.3	N -level approximation	121
6.3	Dressed state dynamics of rf-dressed two-level subsystems	123
6.3.1	Dynamics of Floquet Hamiltonian	123
6.3.2	Dynamics in the N -level approximation	130
6.4	RF-dressed three-level systems	131
6.4.1	Floquet formalism	131
6.4.2	N -level approximation	137
6.4.3	Strong coupling field	140
6.4.4	Electromagnetically induced transparency	144
6.5	Conclusions	150
7	Microwave dressing of Rydberg dark states	152
7.1	Experimental set up	153
7.2	Theoretical modelling of EIT lineshapes	154

7.3	Destructive interference of the microwave couplings	162
7.4	Group index, dispersion and pulse propagation	169
7.4.1	Switching signs of group index	169
7.4.2	Gaussian pulse propagation	171
7.5	Conclusions and Outlook	176
8	Conclusions	177
A	Factorising the dipole matrix element	182
B	Diagonalising the matrix H_c	184
	Bibliography	187

List of Figures

Figure	Page
2.1 Schematic of three-level cascade system	9
2.2 Population dynamics of three-level system: $\Delta_c = 0$	14
2.3 Population dynamics of three-level system: $\Delta_c \neq 0$	15
2.4 Eigenvalue spectrum of three-level system: $\Delta_c = 0$	18
2.5 Eigenvalue spectrum of three-level system: $\Delta_c \neq 0$	19
2.6 Demonstration of adiabatic elimination	22
2.7 Population dynamics of effective two-level system	25
2.8 Demonstration of violation of weak probe condition	29
2.9 Demonstration of validity of weak probe condition	30
3.1 Schematic of experimental set up and energy level of ^{85}Rb	36
3.2 EIT transmission and its residual plot	38
3.3 Schematic of the level scheme of a Y (four-level) system	39
3.4 Image plot of the absorption coefficient before velocity average	48
3.5 Plot of $(\Omega_c^{\text{eff}}/2\pi)^2$ against coupling power	51
4.1 Schematic of four-level cascade system	56
4.2 The evolution of the absorption lineshapes of cold atoms	59
4.3 The absorption lineshape for thermal atoms in parallel configuration	65
4.4 Image plot of the absorption coefficient before velocity average for parallel configuration	66
4.5 The effect of residual wavevector on the transmission lineshape for thermal atoms	68
4.6 The effect of a finite Δ_{c_1} on the transmission lineshape for thermal atoms	69
4.7 Image plot of the absorption coefficient before velocity average: positive residual wavevector	71
4.8 Image plot of the absorption coefficient before velocity average: negative residual wavevector	72
4.9 EIA absorption lineshape in Doppler-free configuration	74
4.10 EIT transmission lineshape in Doppler-free configuration	75
5.1 Schematic of the energy levels scheme of ^{87}Rb with the manifold of Rydberg state	83

5.2	Schematic of the experimental set up of rf-dressed system . . .	89
5.3	Demonstration of the validity of the Taylor approximation . . .	90
5.4	Demonstration of the violation of the Taylor approximation . . .	91
5.5	Comparison between the observed EIT spectra and the theoretical model	92
5.6	The effect of ac and dc electric fields on the Rydberg EIT spectrum	95
5.7	The difference signal obtained by turning the dc field on and off	96
5.8	The increase in the amplitude of the dc electrometry signal as a function of \mathcal{E}_{ac}	99
5.9	The theoretical prediction of the enhancement as a function of \mathcal{E}_{dc}	100
6.1	Schematic of the rf-dressed three-level (Rydberg) system . . .	104
6.2	Schematic of the manifolds of the rf-dressed two-level subsystem and N -level approximation	110
6.3	The quasienergy spectrum and $\langle \rho_{bb}(\infty) \rangle$ of \mathbf{H}'_{2F}	117
6.4	The quasienergy calculated using the iteration method vs. perturbation theory	118
6.5	The plots of the instantaneous lineshape: difference ω_{rf}	126
6.6	The plots of the instantaneous lineshape: difference Γ_c	127
6.7	The plots of the instantaneous lineshape: difference Ω_c	128
6.8	The plots of quasienergy spectrum and imaginary part of $\langle \rho_{ab}(\infty) \rangle$ calculated from \mathbf{H}'_{3F}	135
6.9	Demonstration of the effect of induced sideband	142
6.10	EIT of rf dressing in cold atoms	145
6.11	EIT of rf dressing in thermal atoms	148
7.1	Schematic of the experimental setup and energy level	153
7.2	Schematic of ten-level system	155
7.3	EIT spectra with increasing microwave coupling	160
7.4	Schematic of the five-level toy-model	161
7.5	Demonstration of symmetry on the ρ_{ba}^s lineshape	166
7.6	Transmission and calculated group index	171
7.7	Propagation of $0.5 \mu s$ pulse in the medium	174
7.8	Propagation of $0.05 \mu s$ pulse in the medium	175

List of Tables

3.1	The values of the parameters producing the best fit	46
5.1	The values of the parameters producing the best fit	93
7.1	Dressed states in the case of symmetry $\Omega_2^* \Omega_3 = \Omega_1^* \Omega_4$	163
7.2	Dressed states in the case of hidden symmetry	165

Chapter 1

Introduction

1.1 Electromagnetically induced transparency and dark states

The work presented in this thesis is concerned with electromagnetically induced transparency (EIT) [1] involving highly-excited Rydberg states. Its main focus is on the modification of Rydberg EIT induced by an external radio frequency (rf) or microwave fields, for example, the generation of EIT sidebands and the splitting of the EIT feature due to radio frequency (rf) fields and microwave, respectively.

Electromagnetically induced transparency is the phenomenon in which an opaque medium, e.g., an atomic vapour, becomes transparent due to the application of electromagnetic fields [1]. This phenomenon arises due to destructive interference between two excitation pathways driven by two laser fields within a three-level atomic system. This results in the cancellation of the probability amplitudes for the transition from the ground state to the intermediate state [1–3]. In the dressed state picture, a dark state, i.e., the dressed state containing a ground state and an excited state, is responsible for this phenomenon since it does not interact with the intermediate state via

the probe laser [2, 3]. EIT-like effects are also observed in classical systems, e.g., a system of driven coupled oscillators [4, 5] and in RLC circuits [5]. In a system of three oscillators connected by two springs, the forces driving the middle oscillator cancel each other since they are out-of-phase. This leads to the reduction of the power absorbed by the middle oscillator, and thus creates an EIT-like profile.

One important application of EIT is to optically control the transmission [6–8] and the dispersion [8–10] of a probe laser in an atomic ensemble, and hence, the group velocity of light [11, 12]. The abrupt change in the refractive index and transmission has been proposed for use as a magnetometer by Scully et al. [13]. The propagation of light through an EIT medium can be described in terms of dark state polaritons [14]. By varying the control field one can reversibly convert between the light and atomic excitations and thereby implement photon storage [15–19].

Moreover, the three-level EIT system can be modified by adding an on-resonance electromagnetic field into the system. This results in a modification of dispersion; and hence, the dynamics of the dark state. For example, dressing the system by microwave field switches the group index from positive to negative, giving rise to “superluminal” propagation [20–22].

1.2 Rydberg EIT

Rydberg atoms with highly excited principal quantum number ($n > 10$) [23, 24] present novel applications in precision electrometry [25] and quantum information [24, 26, 27] due to their extreme polarisability (scaling as n^7 for low orbital angular momentum) and long range interactions. Rydberg atoms can be created using the technique of charge exchange in which positive ions collide with ground state atoms, or by electron impact in which the ground state atoms are excited by a beam of electrons [23]. Optical excitation in

which one or more lasers are used to excite the atom to a Rydberg state is also employed by atomic physicists [23, 28, 29]. Recently, adiabatic rapid passage has been proposed as an efficient way to create a single Rydberg atom [30].

The application of Rydberg states as electric field sensors has been explored using a supersonic beam of krypton atoms with principal quantum number $n = 91$. By measuring the Stark shifts of highly excited Rydberg states, the value of the electric field was obtained with a $20 \mu\text{V cm}^{-1}$ accuracy [31]. However, a disadvantage of using Rydberg atoms is that the standard detection technique of pulsed field ionization means that the measurement cannot be performed continuously, the electrodes required for ionization may perturb the field under investigation, and typically the detection system is relatively large. Recently, the coherent optical detection of Rydberg states using EIT has been demonstrated in a thermal vapour cell [32], in an atomic beam [33] and in ultra-cold atoms [34]. This detection technique has the advantage that it is continuous and can be performed in confined geometries down to the micron scale [35]. Consequently one can envisage a compact electrometry device analogous to a chip scale atomic magnetometer [36].

Ladder EIT [3] involving a Rydberg state arises due to the formation of Rydberg dark states, which are coherent superpositions of the ground state and a Rydberg state. Rydberg dark resonances result in a narrow feature in the susceptibility, and thereby an enhanced electro-optic effect compared to bare Rydberg states [37]. Rydberg EIT has been used to study interactions in cold Rydberg gases [34, 38, 39]. Possible applications of Rydberg dark states include single-photon entanglement [40], the generation of exotic entangled states [29] and mesoscopic quantum gates [41]. In addition they are of interest to applications in electrometry [21, 35], owing to their giant dc Kerr coefficient [37]. However, the sensitivity of a Rydberg dark state electrometer is limited by laser frequency fluctuations. Since reducing those to a suitable

level entails a considerable experimental overhead, a technique to measure electric fields that is insensitive to the absolute laser frequency is desirable. One of the results from the work presented in this thesis suggests a possible way to achieve the goal.

Another interesting application of Rydberg EIT is the microwave coupling of Rydberg states. In such system the probe and coupling lasers perform the usual two-photon transition to a Rydberg state, and then this Rydberg state couples to another Rydberg state by a microwave field. The effect of the microwave coupling is to split the EIT peak of three-level Rydberg EIT into a doublet EIT. This results in independent control of the absorptive and dispersive properties of the medium [21]. Moreover, the microwave dressing leads to the enhanced interactions due to an effective increase in the blockade radius. In particular, the evidence for the energy shift due to the long range dipole-dipole interaction between Rydberg states resonantly coupled by the microwave field has recently been presented [21]. By exploiting this enhanced long-range interaction by microwave dressing, Bariani et al. [42] proposed a scheme for the fast entanglement generation in Rydberg ensembles.

1.3 Dressing atoms with rf fields

Historically, the dressing of atomic systems by an rf field has been one of the most important developments in atomic physics. It was Autler and Townes [43] who first studied such systems and predicted both the Stark shift and the formation of a sideband structure in the low-frequency perturbation regime. These sideband resonances are at even multiples of the rf frequency away from the central resonance, shifted by the Stark effect, and their heights fall off as given by Bessel functions [43, 44]. It was later explained by Shirley [45], using Floquet theory, that the sideband resonances are due to the rf-photon transition between Floquet states. This feature was first experimentally con-

firmed by Townes and Merritt [46].

The presence of the sideband structure has been used to investigate atomic properties, e.g., Floquet spectroscopy of atoms and Rydberg atoms [47–50] or the dipole-dipole resonances between two Rydberg ensembles due to rf-photon multitransitions [51, 52]. In addition, the oscillatory behaviour of the Bessel function has been interpreted as Stückelberg oscillations [51]. Thus the rf field could be a good candidate for probing the long-range interaction between Rydberg atoms. Not only does the rf field result in a Stark shift and sideband resonances, but the characteristic properties of the sidebands, e.g., the width and height of the sidebands, are also sensitive to the amplitude and the frequency of the applied rf field. This sensitivity of the sideband structure allows one to precisely control the system with high accuracy. The sensitivity of the rf-dressed system has been utilized in many applications, for example, in polarisability measurements [53], the control of atomic photoabsorption [54] and, recently, electrometry using Rydberg atoms [25].

In addition to the atomic systems, the fundamental theory of rf dressing is applicable to systems found in condensed matter physics such as Cooper-pair boxes¹ and Josephson flux qubits². For example, Chu et al. theoretically investigated the combined Josephson junction rf SQUID [66]. They found a similar manifold structure of the resonances as previously described. However, the system exhibits no Stark shift in energy and the resonances occur at multiples of the rf frequency or thereabout, not at even multiples of the rf frequency as in the atomic system [25]. They also reported a slight shift in frequency of the resonance position, which was not yet reported by Autler and Townes [43]. In our work, we report a similar resonance shift in Rydberg EIT.

¹A Cooper-pair box is a man-made two-level system, made from superconducting materials. Its qubit state is determined by the number of Cooper pairs. [55–62].

²Another example of a man-made two-level system. Its qubit states are determined by the directions of the current flux. [63–67].

1.4 Thesis layout

The structure of this thesis is as follows.

- Chapter 2: Using the semi-classical theory, the description of a three-level atom interacting with two electromagnetic fields is presented. The resonance structure of the system is discussed in terms of dressed states, which allows us to gain much physical insight. Some of the phenomena associated with laser-dressed three-level systems, e.g., EIT, are also illustrated in this chapter.
- Chapter 3: A theoretical model for Rydberg EIT in ^{85}Rb is developed. The model takes into account Doppler broadening and the hyperfine structure of the atoms. We show that by fitting this model to experimental data, we can obtain the reduced dipole matrix element for the transition between the $5\text{P}_{3/2}$ state and a Rydberg state.
- Chapter 4: In this chapter, we present a theoretical model of four-level, three-colour Rydberg EIT. Two configurations for the laser set up are considered here: The first one is when the propagation directions of all the three lasers are parallel. The other is when the three lasers form a Doppler-free configuration, i.e., the three wavevectors cancel each other.
- Chapter 5: We present the theory of three-level Rydberg EIT dressed by an rf field. This results in the formation of Floquet states of the Rydberg states and these are detected as EIT sideband resonances in the absorption lineshape. By fitting the EIT transmission lineshape model to experimental data, we can extract the value of a dc field applied across the vapour cell.
- Chapter 6: We extend the theory of rf-dressed Rydberg state to the regime where the Floquet formalism breaks down. In this chapter, the

Floquet formalism is used to explore two- and three-level systems. The aim of this chapter is to find the conditions for which well-defined EIT sidebands do no longer exist, and those for which they do exist.

- Chapter 7: We study the effect of a resonant microwave field on three-level Rydberg EIT. A theoretical modelling of a ten-level system is developed in order to understand the absorption and dispersion property of the cold ^{87}Rb ensemble. A theoretical demonstration of the possibility of fast light in the system is also presented in this chapter.
- Chapter 8: The conclusions of the thesis and possible future work are discussed in this chapter.

Chapter 2

Interaction of three-level atoms with EM fields

In this chapter, we study the interaction between the three-level atom with two electromagnetic (EM) fields, using semi-classical theory [68, 69], in which the atomic system is treated quantum mechanically, whereas the EM fields are treated classically. In particular, we discuss the occurrence of electromagnetically induced transparency (EIT) [1] in three-level system and the adiabatic elimination of the intermediate state [70–72].

2.1 Hamiltonian of the atom-fields system

Consider the cascade (ladder) system shown in Figure 2.1(a), consisting of three eigenstates of the field-free Hamiltonian — a ground state, $|1\rangle$, an intermediate state, $|2\rangle$, and an excited state, $|3\rangle$, whose eigenenergies are $\hbar\omega_1$, $\hbar\omega_2$ and $\hbar\omega_3$, respectively. The ground state is metastable, i.e., its lifetime is so long that this state hardly decays. The other two states possess finite lifetimes due to spontaneous emission. In this model, the intermediate state decays with the natural decay rate Γ_2 and the excited state decays with the natural decay rate Γ_3 . The time-independent Hamiltonian of the bare

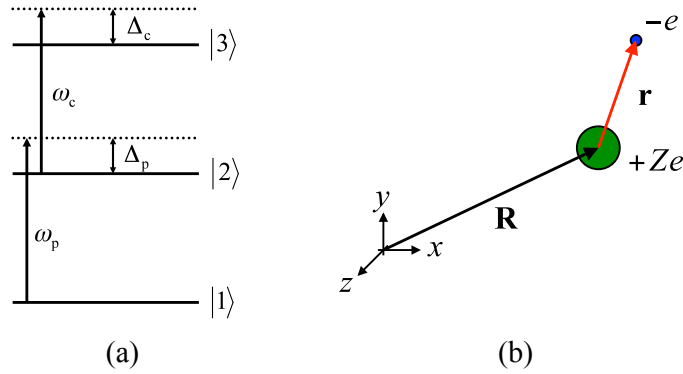


Figure 2.1: (a) Schematic of a three-level system which consists of a ground state, $|1\rangle$, an intermediate state, $|2\rangle$, and an excited state, $|3\rangle$. A weak probe laser whose angular frequency is ω_p couples $|1\rangle$ with $|2\rangle$ and a coupling laser whose angular frequency is ω_c couples $|2\rangle$ with $|3\rangle$. Δ_p and Δ_c are the laser detunings of the probe and coupling lasers, respectively. (b) Schematic showing how the electron and the atom are placed with respect to the co-ordinate system. The external degree of freedom parameter \mathbf{R} is the position vector of the atom while the internal parameter \mathbf{r} is the position of the electron. The strength of the dipole moment is related to the internal parameter \mathbf{r} .

atomic system is thus given by

$$\mathcal{H}_0 = \hbar\omega_1 |1\rangle \langle 1| + \hbar\omega_2 |2\rangle \langle 2| + \hbar\omega_3 |3\rangle \langle 3|. \quad (2.1)$$

The system interacts with two classical, monochromatic EM fields, where the first field is the probe field of frequency $\omega_p/2\pi$ (driving the transition $|1\rangle \leftrightarrow |2\rangle$) and the second field is the coupling field of frequency $\omega_c/2\pi$ (driving the transition $|2\rangle \leftrightarrow |3\rangle$). The electric field at the position of the electron is given by,

$$\mathbf{E}(\mathbf{R}, \mathbf{r}, t) = \frac{1}{2} E_p \hat{\mathbf{e}}_p e^{i[\mathbf{k}_p(\mathbf{R}+\mathbf{r})-\omega_p t]} + \frac{1}{2} E_c \hat{\mathbf{e}}_c e^{i[\mathbf{k}_c(\mathbf{R}+\mathbf{r})-\omega_c t]} + \text{c.c.}, \quad (2.2)$$

where $\hat{\mathbf{e}}_{p(c)}$, $\mathbf{k}_{p(c)}$, and $E_{p(c)}$ are the polarisation unit vectors, the wavevectors, the effective field strength [73] of the probe (coupling) electric field and c.c. denotes the complex conjugate of the first two terms. The position of

the centre-of-mass (CM) of the atomic system is measured with respect to the origin of the co-ordinate system (given by position vector \mathbf{R}), while the position of the electron is measured with respect to CM of the system (given by position vector \mathbf{r}), as shown in Figure 2.1(b). Note that we assume an infinite mass for the nucleus; hence, the CM of the system coincides with the nucleus of the atom. At this point, a first approximation is made by considering the scale of the field wavelength and the atomic size. It turns out that the typical atomic size is much smaller than the wavelengths of the fields; and thus, the spatial variation of the fields across the atom is negligible, i.e., $\exp(i\mathbf{k}_{p(c)} \cdot \mathbf{r}) \approx 1$. This approximation is known as the dipole approximation or long-wavelength approximation [69, 74–77]. Furthermore, since the atom is (instantaneously) stationary, without loss of generality, one can consider the atom to be located at the origin, i.e., $\mathbf{R} = 0$ [78]. With these assumptions, the electric field in Equation (2.2) depends on the time variable only.

The EM fields perturb the atomic system via the dipole interaction. Thus the interaction Hamiltonian for a one-electron atom due to the EM fields is given by,

$$\mathcal{H}_I = e\mathbf{r} \cdot \mathbf{E}(t), \quad (2.3)$$

where e is the magnitude of the electron charge. Rewriting Equation (2.3) in terms of $|1\rangle$, $|2\rangle$, and $|3\rangle$, the interaction Hamiltonian becomes,

$$\begin{aligned} \mathcal{H}_I = & \frac{\hbar\Omega_p^{(1,2)}}{2} |1\rangle\langle 2| e^{-i\omega_p t} + \frac{\hbar\Omega_p^{(2,1)}}{2} |2\rangle\langle 1| e^{-i\omega_p t} \\ & + \frac{\hbar\Omega_c^{(2,3)}}{2} |2\rangle\langle 3| e^{-i\omega_c t} + \frac{\hbar\Omega_c^{(3,2)}}{2} |3\rangle\langle 2| e^{-i\omega_c t} + \text{h.c.}, \quad (2.4) \end{aligned}$$

where h.c. denotes the hermitian conjugate of the first four terms, and $\Omega_p^{(m,n)}$ and $\Omega_c^{(m,n)}$ are given by

$$\hbar\Omega_p^{(m,n)} = eE_p \langle m | \mathbf{r} \cdot \hat{\boldsymbol{\epsilon}}_p | n \rangle, \quad (2.5a)$$

$$\hbar\Omega_c^{(m,n)} = eE_c \langle m | \mathbf{r} \cdot \hat{\boldsymbol{\epsilon}}_c | n \rangle. \quad (2.5b)$$

The time-dependent dynamics of the system governed by the total Hamiltonian $\mathcal{H}_0 + \mathcal{H}_1$ contains fast oscillation at the angular frequencies ω_1 , ω_2 and ω_3 , as well as at the angular frequencies ω_p and ω_c . To remove the rapidly-oscillating contributions, we transform into a representation in which the phases of the probability amplitudes of $|1\rangle$, $|2\rangle$ and $|3\rangle$ are approximately stationary [68]. The transformation from the rapidly-oscillating variables to slowly-oscillating variables is given by \mathcal{U} , where,

$$\mathcal{U} = e^{i\omega_1 t} |1\rangle \langle 1| + e^{i(\omega_1 + \omega_p)t} |2\rangle \langle 2| + e^{i(\omega_1 + \omega_p + \omega_c)t} |3\rangle \langle 3|. \quad (2.6)$$

Then the total Hamiltonian of the system and the state vector are transformed as [79],

$$|\Psi\rangle \rightarrow |\Psi'\rangle = \mathcal{U} |\Psi\rangle, \quad (2.7a)$$

$$\mathcal{H} \rightarrow \mathcal{H}' = \mathcal{U}\mathcal{H}\mathcal{U}^\dagger - i\hbar\dot{\mathcal{U}}\mathcal{U}^\dagger, \quad (2.7b)$$

where $\mathcal{H} = \mathcal{H}_0 + \mathcal{H}_1$, prime denotes the state vector and Hamiltonian in the new representation, dagger denotes hermitian conjugate and the dot on \mathcal{U} means the derivative of \mathcal{U} with respect to time. Note here that the transformation preserves the norm of the wavevector $|\Psi\rangle$ since \mathcal{U} is a unitary operator. Applying the transformation and making the rotating wave approximation [76], the total Hamiltonian becomes,

$$\begin{aligned} \mathcal{H}' = & -\hbar\Delta_p |2\rangle \langle 2| - \hbar\Delta_R |3\rangle \langle 3| \\ & + \frac{\hbar\Omega_p}{2} |2\rangle \langle 1| + \frac{\hbar\Omega_c}{2} |3\rangle \langle 2| + \text{h.c.} . \end{aligned} \quad (2.8)$$

The rotating wave approximation is to neglect the rapidly-oscillating terms, i.e., terms with the angular frequencies of $2\omega_p$ and $2\omega_c$, are neglected and h.c. represents the hermitian conjugate of the second row. Here we drop the superscript (2,1) and (3,2) from $\Omega_p^{(2,1)}$ and $\Omega_c^{(3,2)}$, i.e., $\Omega_p \equiv \Omega_p^{(2,1)}$ and $\Omega_c \equiv \Omega_c^{(3,2)}$. The probe and coupling detunings in Equation (2.8) are defined

as

$$\Delta_p = \omega_p - (\omega_2 - \omega_1), \quad (2.9a)$$

$$\Delta_c = \omega_c - (\omega_3 - \omega_2), \quad (2.9b)$$

and $\Delta_R = \Delta_p + \Delta_c$ is known as two-photon Raman detuning. The first line of Equation (2.8) represents the Hamiltonian of the bare atomic states in the rotating frame (\mathcal{H}'_0), whereas the second line represents the atom-field interactions (\mathcal{H}'_1). It is worth noting that, in the absence of the interactions, the Hamiltonian given by Equation (2.8), is diagonal and the (new) eigenenergies of $|1\rangle$, $|2\rangle$ and $|3\rangle$ are 0, $-\Delta_p$ and $-\Delta_R$, respectively. Thus the effect of the transformation is to shift the energy of the excited state and the intermediate state such that the excited state and the intermediate state lie lower than the ground state by the amounts of Δ_R and Δ_p , respectively. Using Equation (2.8), the Schrödinger equation of the three-level system then reads

$$i\hbar \frac{d}{dt} \begin{pmatrix} u_1 \\ u_2 \\ u_3 \end{pmatrix} = \frac{\hbar}{2} \begin{pmatrix} 0 & \Omega_p^* & 0 \\ \Omega_p & -2\Delta_p & \Omega_c^* \\ 0 & \Omega_c & -2\Delta_R \end{pmatrix} \begin{pmatrix} u_1 \\ u_2 \\ u_3 \end{pmatrix}, \quad (2.10)$$

where $|u_n|^2$ is the probability of finding the atom in the state $|n\rangle$.

2.2 Dressed state formalism for three-level system

In this section, we discuss the characteristic properties of the solutions of Equation (2.10) using two approaches. The first approach is to solve this equation for the evolution of the system. However, this approach does not give much physical insight in such issues as the occurrence of resonances. A better way to look at the system is to study the eigenvalues and eigenvectors of the atom-field system. This allows us to understand the formation process of the resonances.

2.2.1 Dynamical evolution of three-level system

Mathematically, the Schrödinger equation, given by Equation (2.10), is an homogeneous first order coupled differential equation (CDE). Owing to the time-independence of the Hamiltonian, one can turn the CDE into the eigenvalue problem [80]

$$\mathcal{H}' |\psi_n\rangle = E_n |\psi_n\rangle, \quad (2.11)$$

where E_n is an eigenvalue of \mathcal{H}' and $|\psi_n\rangle$ is the corresponding eigenvector of \mathcal{H}' . Having determined the eigenvalues and eigenvectors, the solution of the Schrödinger equation is given by

$$\begin{aligned} |\Psi'(t)\rangle &= \exp\left(-\frac{i\mathcal{H}'t}{\hbar}\right) |\Psi'(0)\rangle, \\ &= \sum_{n=1}^3 \exp\left(-\frac{iE_n t}{\hbar}\right) \alpha_n |\psi_n\rangle, \end{aligned} \quad (2.12)$$

where $|\Psi'(t)\rangle \equiv (u_1(t), u_2(t), u_3(t))^T$ is the solution of the Schrödinger equation, $|\Psi'(0)\rangle$ is the initial state of the system and $\alpha_n \equiv \langle \psi_n | \Psi'(0) \rangle$ is the coefficient of expansion. It is obvious from Equation (2.12) that if the population is prepared in one of the bare states, $|1\rangle$, $|2\rangle$ and $|3\rangle$, the population would transfer back and forth between the bare states since these bare states are no longer the eigenstates of the atom-field system. Thus, one may refer to the bare states as the coupled basis as they are not independent from one another and the population oscillates among them. In contrast to these coupled states, the eigenvectors of \mathcal{H}' are stationary and independent of the atom-field interaction, i.e., if the initial state is prepared to be one of these eigenstates $|\psi_n\rangle$, there will be no population transfer within the eigenstates. Thus one may refer to these states ($|\psi_n\rangle$) as the uncoupled basis.

The typical behaviour of Equation (2.12) is oscillatory as shown in Figure 2.2 and Figure 2.3. However, due to the complexity of Equation (2.12), one cannot predict when the system would exhibit the resonance, i.e., oscillate with large amplitude. This is when the study of the dressed states becomes useful, as discussed in the next subsection.

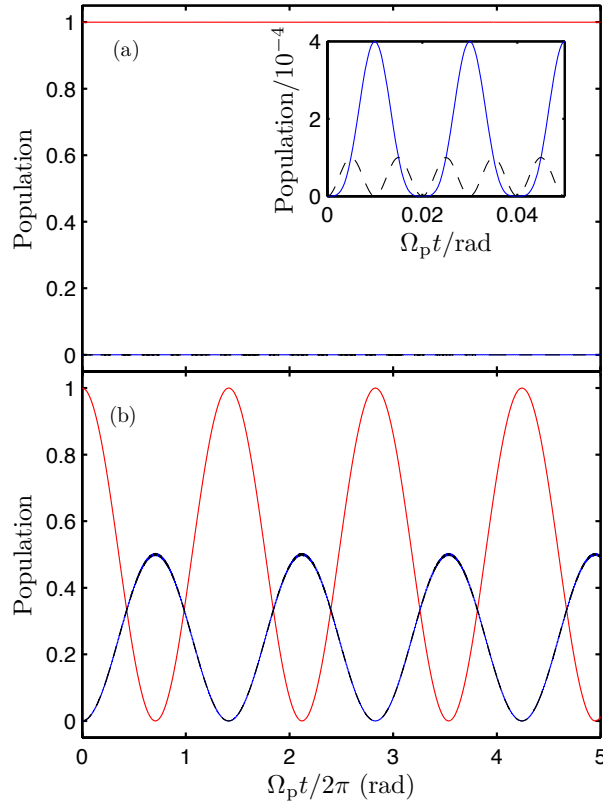


Figure 2.2: Population dynamics of $|1\rangle$ (red solid line), $|2\rangle$ (black dashed line) and $|3\rangle$ (blue solid line) for the parameters $\Omega_p/2\pi = 0.1$ MHz, $\Omega_c/2\pi = 10$ MHz and $\Delta_c/2\pi = 0$ MHz. (a) $\Delta_p/2\pi = 0$ MHz, the interaction due to the probe laser hardly affects the system since $|1\rangle$ is non-degenerate with $|+\rangle$ and $|-\rangle$ (see Figure 2.4(a)). Thus there is hardly population transferred to $|2\rangle$ and $|3\rangle$. The inset shows the population dynamics of $|2\rangle$ and $|3\rangle$. (b) $\Delta_p/2\pi = 5$ MHz, $|1\rangle$ is on resonance with $|+\rangle$, the populations vigorously oscillate. Since the dressed state $|+\rangle$ contains an equal amount of $|2\rangle$ and $|3\rangle$, the population dynamics of $|2\rangle$ is exactly the same as that of $|3\rangle$. It is assumed in the calculation that the population of the system is initially in $|1\rangle$ in (a) and (b).

2.2.2 Eigenvalue spectrum of three-level system

The eigenvalues of the system can be obtained by diagonalising the Hamiltonian, \mathcal{H}' , and the associated eigenvectors are referred to as the dressed states.

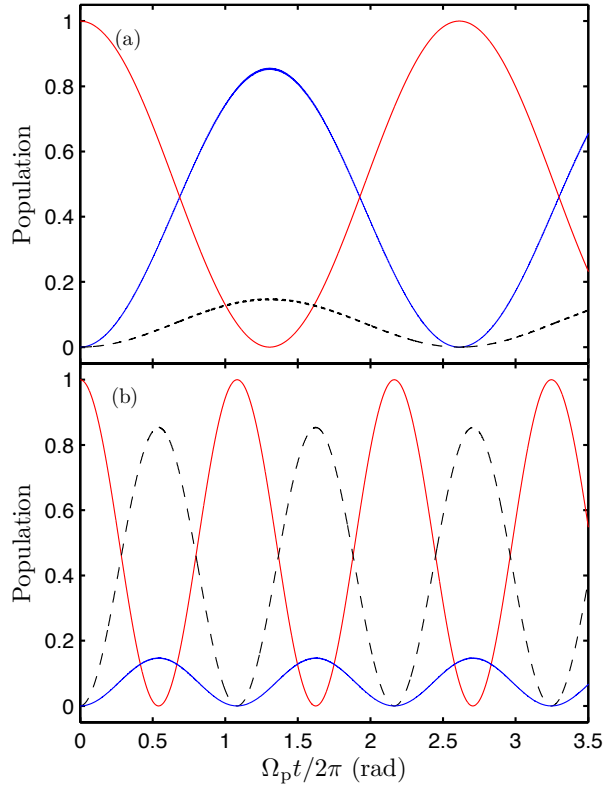


Figure 2.3: The same as Figure 2.2, except that $\Delta_c/2\pi = -10$ MHz. The initial population is prepared in the ground state, $|1\rangle$. When $\Delta_p/2\pi \approx 12$ MHz, shown in (a), $|1\rangle$ is on resonance with $|+\rangle$ (see Figure 2.5(a)). Since $|+\rangle$ contains a larger proportion of $|3\rangle$ than of $|2\rangle$, the population is significantly transferred to $|3\rangle$, resulting in a large amplitude of the oscillation of $|3\rangle$. In (b), $|1\rangle$ is on resonance with $|-\rangle$, i.e., $\Delta_p/2\pi \approx -2$ MHz. We observe a large population transferred from $|1\rangle$ to $|2\rangle$, i.e., a large amplitude of the population dynamics of $|2\rangle$. This is because $|-\rangle$ contains a larger proportion of $|2\rangle$ than of $|3\rangle$.

In the most general case, the set of eigenvalues are given by [71, 81, 82]

$$E_1 = -\frac{1}{6}A + \frac{1}{3}\sqrt{A^2 - 3B} \cos\left(\frac{\theta}{3}\right), \quad (2.13a)$$

$$E_2 = -\frac{1}{6}A - \frac{1}{3}\sqrt{A^2 - 3B} \cos\left(\frac{\theta}{3} + \frac{\pi}{3}\right), \quad (2.13b)$$

$$E_3 = -\frac{1}{6}A - \frac{1}{3}\sqrt{A^2 - 3B} \cos\left(\frac{\theta}{3} - \frac{\pi}{3}\right), \quad (2.13c)$$

with

$$A = 2(2\Delta_p + \Delta_c), \quad (2.14a)$$

$$B = 4\Delta_p(\Delta_p + \Delta_c) - (|\Omega_c|^2 + |\Omega_p|^2), \quad (2.14b)$$

$$C = -2|\Omega_p|^2(\Delta_p + \Delta_c), \quad (2.14c)$$

$$\cos \theta = -\frac{27C + 2A^3 - 9AB}{2(A^2 - 3B)^{3/2}}. \quad (2.14d)$$

The corresponding (non-normalised) eigenvector is

$$|\psi_n\rangle = \Omega_p^*(2\Delta_R + E_n) |1\rangle + (2\Delta_R + E_n)E_n |2\rangle + \Omega_c E_n |3\rangle, \quad (2.15)$$

where $n = 1, 2$ or 3 .

Clearly, the expressions for the eigenvalues and eigenvectors, given by Equation (2.13) and Equation (2.15), are complicated. Rather than studying the general case, we investigate two particular cases in order to gain some insight on the time-evolution of the three-level system.

Case 1: $|\Omega_p| \ll |\Omega_c|$.

In this regime where the Rabi frequency of the coupling laser is much stronger than that of the probe laser, one can treat the weak probe coupling as a perturbation to the system. This can be done by first neglecting the weak probe interaction between $|1\rangle$ and $|2\rangle$ and only considering the strong coupling between $|2\rangle$ and $|3\rangle$ via Ω_c . In this picture, a pair of dressed states, $|\pm\rangle$, are formed from $|2\rangle$ and $|3\rangle$. Diagonalising the Hamiltonian \mathcal{H}' with $\Omega_p = 0$, the (non-normalised) dressed states are given by

$$|\pm\rangle = (\Delta_c \pm \sqrt{\Delta_c^2 + |\Omega_c|^2}) |2\rangle + \Omega_c |3\rangle, \quad (2.16)$$

and the associated eigenenergies are

$$E_{\pm} = -\Delta_p - \frac{\Delta_c}{2} \pm \frac{1}{2}\sqrt{\Delta_c^2 + |\Omega_c|^2}. \quad (2.17)$$

In view of Equation (2.17), the energy separation between two dressed states is $\sqrt{\Delta_c^2 + |\Omega_c|^2}$, where the centre of the energy gap of the two dressed states

with respect to the eigenenergy of $|1\rangle$ is at $-\Delta_p - \Delta_c/2$. After determining a pair of dressed states, $|\pm\rangle$, we then consider the interaction due to Ω_p . We can distinguish two cases, namely, one in which $|1\rangle$ is off-resonance with any of $|+\rangle$ and $|-\rangle$, and one in which $|1\rangle$ is on-resonance with any of $|+\rangle$ and $|-\rangle$. When $|1\rangle$ is not in the vicinity of any dressed states $|\pm\rangle$, i.e., the probe laser is off-resonance, the dressed states $|\pm\rangle$, together with $|1\rangle$, are approximately the eigenvectors of the system since the weak probe hardly perturbs the system [45, 71, 83]. However, when the energy of $|1\rangle$ is close to $|+\rangle$ or $|-\rangle$, i.e., on resonance, the perturbation Ω_p creates avoided crossings at the locations where E_+ or E_- is equal to zero [45, 71, 83]. The eigenenergy of $|1\rangle$, and the energy gap at the avoided crossing is then proportional to $\langle 1 | \mathbf{e} \mathbf{r} \cdot \hat{\mathbf{e}}_p | \pm \rangle / \langle \pm | \pm \rangle^{1/2}$. At the locations of the avoided crossings, the system is most active, i.e., the population oscillates among $|1\rangle$, $|2\rangle$ and $|3\rangle$, as shown in Figure 2.2(b) and Figure 2.3.

Figure 2.4(a) shows the eigenenergies as a function of probe detuning, for $\Omega_p/2\pi = 0.1$ MHz, $\Omega_c/2\pi = 10$ MHz and $\Delta_c/2\pi = 0$ MHz. The eigenvalue spectrum of the system is symmetric around zero probe detuning since $\Delta_c/2\pi = 0$ MHz. The avoided crossings occur at the locations where $|1\rangle$ is degenerate with $|+\rangle$ or $|-\rangle$. In this case, the resonances are at $\Delta_p = \pm 5$ MHz and these locations corresponds to the peak of the resonances for the line-shape of $\text{Im}[\rho_{12}^s]$ as shown in (b).¹ The heights of the resonances are identical since $|+\rangle$ and $|-\rangle$ contain an identical amount of $|2\rangle$. However when we detune the coupling laser to $\Delta_c/2\pi = -10$ MHz, the symmetry of the eigenvalue spectrum is destroyed as shown in Figure 2.5(a). Now $|+\rangle$ contain a smaller amount of $|2\rangle$ than $|-\rangle$ does. This results in a smaller avoided crossing (see Figure 2.5(a)), and a weaker resonance (see Figure 2.5(b)), located

¹ ρ_{12}^s is the steady state solution of the coherence element between $|1\rangle$ and $|2\rangle$ of the density matrix ρ and its imaginary part is proportional to the absorption coefficient of the system. More details of density matrix and absorption coefficient are given in Section 2.4, 2.5 and 2.6.

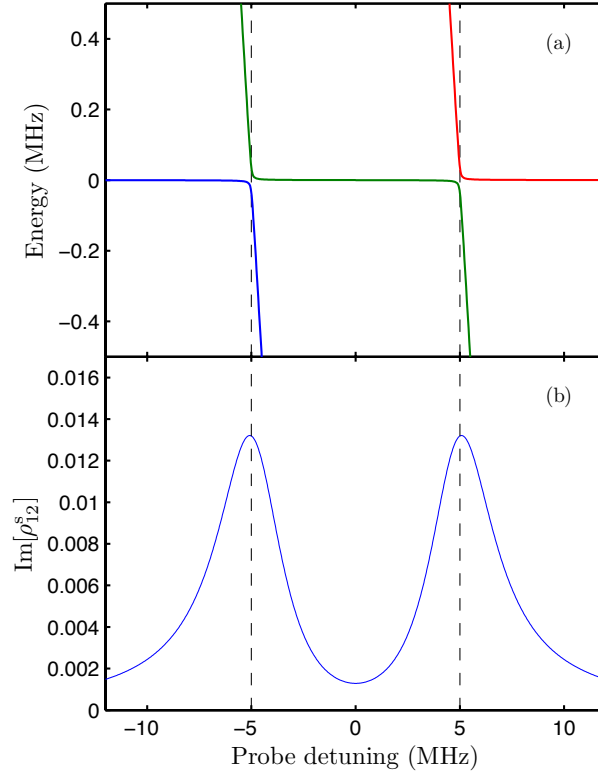


Figure 2.4: The eigenvalue spectrum of \mathcal{H}' and the lineshape of $\text{Im}[\rho_{12}^s]$ as a function of $\Delta_p/2\pi$ are shown in (a) and (b), respectively. The parameters Ω_p , Ω_c and Δ_c are the same as those used in Figure 2.2. For a typical EIT experiment involving Rb atom, the values of the decay rates used in (b) are $\Gamma_2/2\pi = 6$ MHz, $\Gamma_3/2\pi = 1$ MHz and $\gamma_p/2\pi = \gamma_c/2\pi = 0.1$ MHz [84]. The avoided crossings occur when $|1\rangle$ is degenerate with $|+\rangle$ and $|-\rangle$, i.e., at $\Delta_p/2\pi = 5$ and -5 MHz, respectively. The locations of the avoided crossings, indicated by the vertical dashed lines, correspond to the resonance locations of the $\text{Im}[\rho_{12}^s]$ lineshape in (b). Note that the strengths of both resonances are identical since $|+\rangle$ and $|-\rangle$ contain an identical amount of $|2\rangle$.

at $\Delta_p/2\pi \approx 12$ MHz.

Case 2: Two-photon Raman resonance, i.e., $\Delta_p + \Delta_c = 0$

This condition happens when, viewed in the coupled basis, the total excitation is exactly on resonance with the transition from $|1\rangle$ to $|3\rangle$, regardless

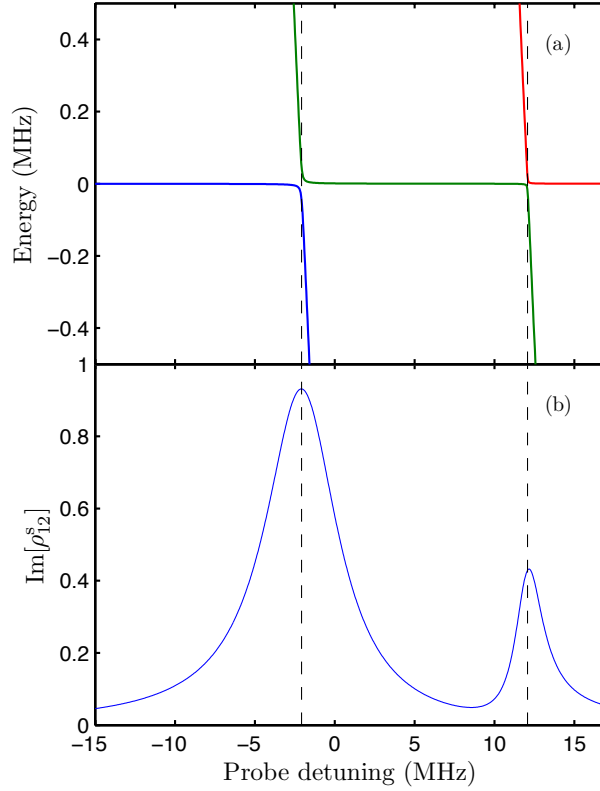


Figure 2.5: The same as Figure 2.4, except that $\Delta_c/2\pi = -10$ MHz. The avoided crossings occur when $|1\rangle$ is degenerate with $|+\rangle$ and $|-\rangle$, i.e., at $\Delta_p \approx 12$ MHz and -2 MHz, respectively. The locations of the avoided crossings, indicated by the vertical dashed lines, correspond to the resonance locations of the $\text{Im}[\rho_{12}^s]$ lineshape in (b). Since $|+\rangle$ contains a smaller amount of $|2\rangle$ than $|-\rangle$ does. The resonance is weaker at $\Delta_p/2\pi \approx 12$ MHz.

of the position of the eigenenergy of $|2\rangle$, i.e., Δ_p could have a finite value. Substituting $\Delta_p + \Delta_c = 0$ into Equation (2.13), the eigenvalues of the dressed states in this case are

$$E_+ = \frac{\hbar}{2}(-\Delta_p + \sqrt{\Delta_p^2 + |\Omega_p|^2 + |\Omega_c|^2}), \quad (2.18a)$$

$$E_0 = 0, \quad (2.18b)$$

$$E_- = \frac{\hbar}{2}(-\Delta_p - \sqrt{\Delta_p^2 + |\Omega_p|^2 + |\Omega_c|^2}), \quad (2.18c)$$

and the associated (non-normalised) eigenvectors are

$$|+\rangle = \Omega_p^* |1\rangle - (\Delta_p - \sqrt{\Delta_p^2 + |\Omega_p|^2 + |\Omega_c|^2}) |2\rangle + \Omega_c |3\rangle, \quad (2.19a)$$

$$|0\rangle = -\Omega_c^* |1\rangle + \Omega_p |3\rangle, \quad (2.19b)$$

$$|-\rangle = \Omega_p^* |1\rangle - (\Delta_p + \sqrt{\Delta_p^2 + |\Omega_p|^2 + |\Omega_c|^2}) |2\rangle + \Omega_c |3\rangle. \quad (2.19c)$$

The interesting physics in this case is that $|0\rangle$ contains no contribution from $|2\rangle$ in the dressed state picture and its eigenenergy is always zero. Furthermore, the amounts of $|1\rangle$ and $|3\rangle$ contained in $|0\rangle$ can be controlled by adjusting the ratio $|\Omega_c^*/\Omega_p|$. This can be experimentally implemented by controlling the intensities of both lasers.

Suppose that state $|2\rangle$ has a natural linewidth of Γ_2 (for $5P_{3/2}$ of Rb atom, this is $2\pi \times 6$ MHz) and we would like to transfer the population from $|1\rangle$ to $|3\rangle$ without losing any population from the lossy state $|2\rangle$. One way to achieve this is to exploit the property of the state $|0\rangle$. Initially, one gradually increases the intensity of the coupling laser while the probe laser is turned off. This causes the initial state $|1\rangle$ to coincide with the instantaneous $|0\rangle$. Then, the intensity of the probe laser gradually increases while that of the coupling laser gradually decreases until it is turned off. During this step, $|0\rangle$ gradually changes from $|1\rangle$ to $|3\rangle$ without interacting with $|2\rangle$. If the process occurs slowly enough², the population is adiabatically transferred from $|1\rangle$ to $|3\rangle$. This process in which the population is transferred from the ground state to the excited state is known as stimulated Raman rapid passage (STIRAP) [82, 85, 86]. Adiabatic rapid passage has been recently reported to be an effective way to create a single-atom excitation in a Rydberg ensemble [30].

Moreover, it turns out that $|0\rangle$ does not interact with $|2\rangle$, i.e., $\langle 2 | \mathcal{H}'_1 | 0 \rangle$ vanishes, since $|0\rangle$ is one of the eigenvectors of the system. This means that no interaction can drive the transition between $|0\rangle$ and $|2\rangle$, and the medium physically becomes transparent to the probe beam when its initial

²Mathematical criterion for the adiabatic population transfer is $\sqrt{|\Omega_p|^2 + |\Omega_c|^2} \Delta\tau > 10$, where $\Delta\tau$ is the period during which the pulses overlap [82].

state is prepared to be $|0\rangle$. This phenomenon is known as electromagnetically induced transparency (EIT) and $|0\rangle$ is referred to as a dark state [1]. There is a similarity between EIT and ATS (Autler-Townes splitting) [43] phenomena. However, the main criterion to distinguish EIT from AT is the interference due to the dark state [87, 88], whereas no such interference is observed in ATS. Figure 2.4(b) shows the reduction in the absorption of the medium when $\Delta_p + \Delta_c = 0$ and $\Delta_p = 0$ as expected from the dressed states analysis. One way to prepare such a dark state is to make the Rabi frequency of the coupling laser larger than that of the probe laser. Under this condition, the dark state is approximately $|1\rangle$ which is the ground state of the system; thus, we automatically prepare the dark state [3].

2.3 Adiabatic elimination of intermediate state

Suppose that, in the dressed state picture, both lasers are tuned close to the two-photon Raman transition, i.e., $\Delta_R \approx 0$, while $|2\rangle$ is far off-resonance from both $|1\rangle$ and $|3\rangle$. One would expect $|1\rangle$ and $|3\rangle$ effectively to become a two-level system. This phenomenon is clearly shown in Figure 2.6. If this is the case, one would be able to excite the atoms from the ground state to the excited state using two-photon transition. It is said that the intermediate state is eliminated in this situation and this is known as adiabatic elimination of the intermediate state [70–72]. The difference between this method and STIRAP is that, for this method, the atom is excited using the Rabi oscillation, while for STIRAP, the population is adiabatically transferred to the excited state by the change in the components of the dark state in which the Rabi oscillation does not play a role.

For simplicity, it is assumed that Ω_p and Ω_c are real quantities. Writing

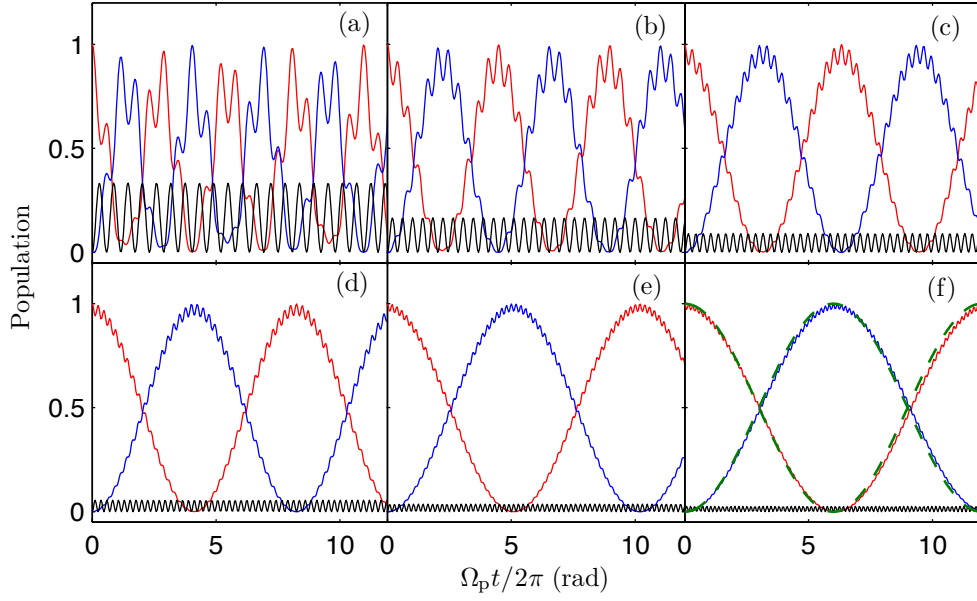


Figure 2.6: Population dynamics of $|1\rangle$ (red solid line), $|2\rangle$ (black solid line) and $|3\rangle$ (blue solid line) for various values of $\Delta_p/2\pi$, i.e., $\Delta_p/2\pi$ is (a) 10 MHz, (b) 20 MHz, (c) 30 MHz, (d) 40 MHz, (e) 50 MHz and (f) 60 MHz. In all plots, $\Omega_p/2\pi = \Omega_c/2\pi = 10$ MHz and the system is subject to the two-photon Raman resonance condition, i.e., $\Delta_p + \Delta_c = 0$. The population of $|1\rangle$ and $|3\rangle$ oscillate with angular frequency given by the generalised Rabi frequency $(\Omega_p^2 + \Omega_c^2)/4\Delta_p$ which decreases as Δ_p increases. It is clear that the larger the value of Δ_p is, the closer the three-level system is to an ideal effective two-level system. In (f), the green dashed lines represent the predictions of Equation (2.27).

Equation (2.10) explicitly, we have

$$\frac{du_1}{dt} = -\frac{i}{2}\Omega_p u_2, \quad (2.20a)$$

$$\frac{du_2}{dt} = -\frac{i}{2}\Omega_p u_1 + i\Delta_p u_2 - \frac{i}{2}\Omega_c u_3, \quad (2.20b)$$

$$\frac{du_3}{dt} = -\frac{i}{2}\Omega_c u_2 + i\Delta_R u_3. \quad (2.20c)$$

One could write a second order differential equation for u_2 by, first, differenti-

ating Equation (2.20b), and then substituting \dot{u}_1 and \dot{u}_3 into \ddot{u}_2 . The result is

$$\ddot{u}_2 = -\frac{1}{4}(\Omega_p^2 + \Omega_c^2)u_2 + \frac{1}{2}\Omega_c\Delta_R u_3 + i\Delta_p\dot{u}_2. \quad (2.21)$$

Equation (2.21) still couples with u_3 ; thus, it could not be solved analytically. However, if the system is subject to two-photon resonance, the differential equation no longer couples to u_3 and the solution, subject to the initial condition $|\Psi(0)\rangle = (1, 0, 0)^T$, is given by

$$u_2(t) = -\frac{i\Omega_p}{\sqrt{\Delta_p^2 + \Omega_p^2 + \Omega_c^2}}e^{i\Delta_p t/2} \sin\left(\frac{1}{2}t\sqrt{\Delta_p^2 + \Omega_p^2 + \Omega_c^2}\right). \quad (2.22)$$

The population of the intermediate state, $|2\rangle$, evolves sinusoidally with an angular frequency of $(\Delta_p^2 + \Omega_p^2 + \Omega_c^2)^{1/2}/2$ and the amplitude of the oscillation is $\Omega_p^2/(\Delta_p^2 + \Omega_p^2 + \Omega_c^2)$. Now suppose that $|2\rangle$ is far from resonance with $|1\rangle$ and $|3\rangle$, i.e., $\Delta_p \gg \Omega_p, \Omega_c$, then the amplitude of the oscillation approaches zero. This implies that $|2\rangle$ is hardly populated and one could approximate $u_2(t)$ and $\dot{u}_2(t)$ to zero. Note that this approximation is also valid when Δ_R is close to zero and Δ_p is large (see Figure 2.7). Setting $\dot{u}_2 = 0$ in Equation (2.20b) and re-arranging for u_2 , one obtains

$$u_2 = \frac{\Omega_p}{2\Delta_p}u_1 + \frac{\Omega_c}{2\Delta_p}u_3. \quad (2.23)$$

Then substituting Equation (2.23) into Equation (2.20a) and Equation (2.20c), the set of CDE becomes,

$$i\hbar\frac{d}{dt}\begin{pmatrix} u_1 \\ u_3 \end{pmatrix} = \frac{\hbar}{2}\begin{pmatrix} \Omega_p^2/2\Delta_p & \Omega_p\Omega_c/2\Delta_p \\ \Omega_p\Omega_c/2\Delta_p & \Omega_c^2/2\Delta_p - 2\Delta_R \end{pmatrix}\begin{pmatrix} u_1 \\ u_3 \end{pmatrix}. \quad (2.24)$$

The reduced CDE is similar to the Schrödinger equation for two-level system where the Rabi coupling is $\Omega_p\Omega_c/2\Delta_p$ and the eigenenergies of $|1\rangle$ and $|3\rangle$ are shifted by the amounts of $\Omega_p^2/2\Delta_p$ and $\Omega_c^2/2\Delta_p$, respectively. In the picture of an effective two-level system, the effective detuning, namely, the separation between $|1\rangle$ and $|3\rangle$, is given by

$$\Delta_{\text{eff}} = -\left(\Delta_R + \frac{\Omega_p^2}{2\Delta_p} - \frac{\Omega_c^2}{2\Delta_p}\right). \quad (2.25)$$

For the special case where Δ_R is exactly zero, the expressions for u_1 and u_3 are given by³

$$u_1(t) = \frac{\Omega_c^2}{\Omega_c^2 + \Omega_p^2} + \frac{\Omega_p^2}{\Omega_c^2 + \Omega_p^2} \exp\left(-\frac{i(\Omega_p^2 + \Omega_c^2)t}{4\Delta_p}\right), \quad (2.26a)$$

$$u_3(t) = -\frac{\Omega_p\Omega_c}{\Omega_c^2 + \Omega_p^2} + \frac{\Omega_p\Omega_c}{\Omega_c^2 + \Omega_p^2} \exp\left(-\frac{i(\Omega_p^2 + \Omega_c^2)t}{4\Delta_p}\right), \quad (2.26b)$$

and the corresponding populations are

$$P_1(t) = \frac{\Omega_c^4 + \Omega_p^4}{(\Omega_p^2 + \Omega_c^2)^2} + 2\left(\frac{\Omega_c\Omega_p}{\Omega_c^2 + \Omega_p^2}\right)^2 \cos\left(\frac{\Omega_c^2 + \Omega_p^2}{4\Delta_p}t\right), \quad (2.27a)$$

$$P_3(t) = \frac{4\Omega_p^2\Omega_c^2}{(\Omega_p^2 + \Omega_c^2)^2} \sin^2\left(\frac{\Omega_c^2 + \Omega_p^2}{8\Delta_p}t\right). \quad (2.27b)$$

The generalised Rabi frequency, for this special case, is $(\Omega_p^2 + \Omega_c^2)/4\Delta_p$. Note that our derivation for adiabatic elimination is similar to that given in [89].

Figure 2.6 shows the population dynamics of the three-level system obtained using Equation (2.12). Both Rabi frequencies, $\Omega_p/2\pi$ and $\Omega_c/2\pi$, are 10 MHz and the system is subject to two-photon Raman resonance. From (a) to (f), $\Delta_p/2\pi$ increases from 10 MHz to 60 MHz at the step of 10 MHz. As we increase Δ_p , $|2\rangle$ is further away from both $|1\rangle$ and $|3\rangle$; and hence, the system effectively behaves like a two-level system. This results in a decrease in amplitude of the population of $|2\rangle$. Increasing Δ_p also decreases the frequency of the oscillation since the angular frequency of the oscillation is given by $(\Omega_p^2 + \Omega_c^2)/4\Delta_p$. The green dashed lines in (f) are the population dynamics calculated from Equation (2.27).

Figure 2.7 shows the population dynamics of the three-level system, for $\Omega_p/2\pi = 1$ MHz, $\Omega_c/2\pi = 10$ MHz and $\Delta_p/2\pi = 100$ MHz. In (a) where $\Delta_p/2\pi = 0$ MHz, the system is subject to two-photon Raman resonance. However, little amount of the population transfer is observed, as shown in (a). This is because, in the dressed state picture, the effective detuning between $|1\rangle$ and $|3\rangle$ does not vanish since $\Omega_p \neq \Omega_c$. In (b), Δ_p is set up such that

³The solutions are subject to the initial condition $|\Psi'(0)\rangle = (1, 0, 0)^T$.

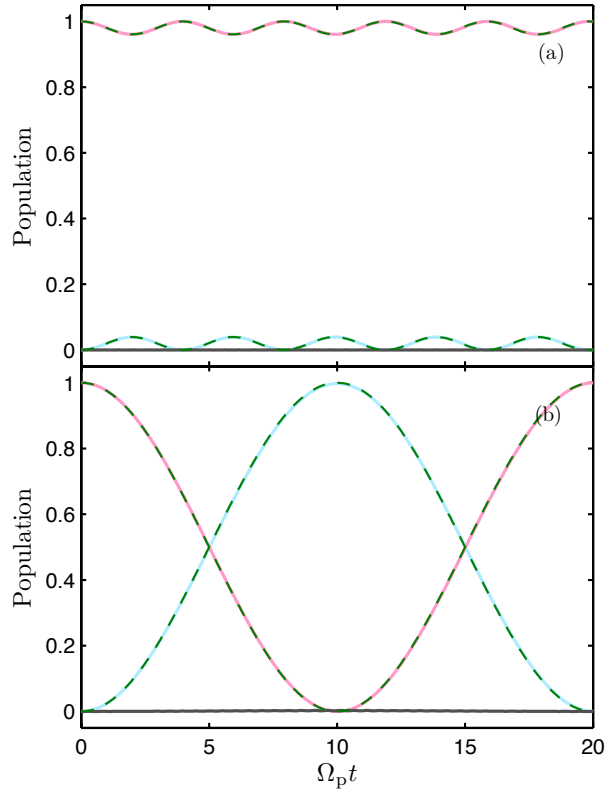


Figure 2.7: Population dynamics of $|1\rangle$ (red solid line), $|2\rangle$ (black solid line) and $|3\rangle$ (blue solid line) for $\Omega_p/2\pi = 1$ MHz, $\Omega_c/2\pi = 10$ MHz and $\Delta_p/2\pi = 100$ MHz. Since Ω_p is not equal to Ω_c , $|1\rangle$ is now not degenerate with $|3\rangle$ even though the system is subject to two-photon Raman resonance, i.e., the effective detuning does not vanish. The system then shows an off-resonance behaviour, i.e., the amplitude of the oscillation is small as shown in (a). To recover the resonance condition, we set Δ_p such that the effective detuning vanishes. For this case, the effective detuning vanishes when $\Delta_p/2\pi = -99.7525$ MHz. The amplitude of the oscillation, in this case, is large, as shown in (b). This is because $|1\rangle$ and $|3\rangle$ are effectively on resonance. Note that the green dashed lines in both (a) and (b) are the solutions obtained by solving Equation (2.24).

the effective detuning vanishes, e.g., in this case $\Delta_p/2\pi = -99.7525$ MHz. The population dynamics show a large oscillation amplitude, namely, there is a significant population transferred to $|3\rangle$. Note that the green dashed lines in both (a) and (b) are the solutions obtained by solving Equation (2.24).

2.4 Relaxation in three-level system and optical Bloch equations

The description of the three-level system, up to now, has not taken into account the effect of the relaxation, which would destroy the coherent property of the system. Thus the Rabi oscillations of the actual system are dampened and the populations eventually reach a steady state. In order to include relaxation into the macroscopic description of the system, the density matrix formalism is needed. The optical Bloch equations, namely, the equation describing the evolution of the system in terms of density matrix, can be obtained using Linblad master equation

$$\frac{\partial \rho'}{\partial t} = -\frac{i}{\hbar}[\mathcal{H}', \rho'] + \sum_i \mathcal{L}(\rho', \sigma_i) + \mathcal{L}_d(\rho'), \quad (2.28)$$

where $\mathcal{L}(\rho', \sigma_i) = \sum_i \sigma_i \rho' \sigma_i^\dagger - (\sigma_i^\dagger \sigma \rho' + \rho' \sigma_i^\dagger \sigma)/2$ is the Linblad superoperator [90] describing the spontaneous decay, $\mathcal{L}_d(\rho')$ is a dephasing matrix which accounts for the linewidth of the EM field and ρ' is the transformed density matrix, i.e.,

$$\rho \rightarrow \rho' = \mathcal{U} \rho \mathcal{U}^\dagger, \quad (2.29)$$

where \mathcal{U} is the unitary transformation given by Equation (2.6). For the three-level system considered here, in which the excited state $|3\rangle$ decays with the rate of Γ_3 to the intermediate state $|2\rangle$ and the intermediate state $|2\rangle$ decays with the rate of Γ_2 to the ground state $|1\rangle$; the natural decays from $|2\rangle$ and $|3\rangle$ can be included into the optical Bloch equation using the operators $\sigma_1 = \sqrt{\Gamma_2}|2\rangle\langle 1|$ and $\sigma_2 = \sqrt{\Gamma_3}|3\rangle\langle 2|$, respectively. Following the argument

given in [84], the dephasing matrix accounting for the linewidths of the EM fields is given by

$$\mathcal{L}_d(\rho') = \begin{pmatrix} 0 & -\gamma_p \rho'_{12} & -(\gamma_p + \gamma_c) \rho'_{13} \\ -\gamma_p \rho'_{21} & 0 & -\gamma_c \rho'_{23} \\ -(\gamma_p + \gamma_c) \rho'_{31} & -\gamma_c \rho'_{32} & 0 \end{pmatrix}, \quad (2.30)$$

where $\gamma_{p(c)}$ is the laser linewidth of the probe (coupling) laser.

Using Equation (2.28) and Equation (2.30), the optical Bloch equations for the three-level system are

$$\dot{\rho}'_{11} = \Gamma_2 \rho'_{22} + \frac{i}{2} (\Omega_p \rho'_{12} - \Omega_p^* \rho'_{21}), \quad (2.31a)$$

$$\dot{\rho}'_{22} = -\Gamma_2 \rho'_{22} + \Gamma_3 \rho'_{33} - \frac{i}{2} (\Omega_p \rho'_{12} - \Omega_p^* \rho'_{21}) + \frac{i}{2} (\Omega_c \rho'_{23} - \Omega_c^* \rho'_{32}), \quad (2.31b)$$

$$\dot{\rho}'_{33} = -\Gamma_3 \rho'_{33} - \frac{i}{2} (\Omega_c \rho'_{23} - \Omega_c^* \rho'_{32}), \quad (2.31c)$$

$$\dot{\rho}'_{12} = -\left(i\Delta_p + \frac{\Gamma_2}{2} + \gamma_p\right) \rho'_{12} - \frac{i\Omega_p^*}{2} (\rho'_{22} - \rho'_{11}) + \frac{i\Omega_c}{2} \rho'_{13}, \quad (2.31d)$$

$$\dot{\rho}'_{23} = -\left(i\Delta_c + \frac{\Gamma_2 + \Gamma_3}{2} + \gamma_c\right) \rho'_{23} - \frac{i\Omega_c^*}{2} (\rho'_{33} - \rho'_{22}) - \frac{i\Omega_p}{2} \rho'_{13}, \quad (2.31e)$$

$$\dot{\rho}'_{13} = -\left(i\Delta_R + \frac{\Gamma_3}{2} + \gamma_p + \gamma_c\right) \rho'_{13} + \frac{i\Omega_c^*}{2} \rho'_{12} - \frac{i\Omega_p^*}{2} \rho'_{23}. \quad (2.31f)$$

To obtain the density matrix, Equation (2.31) together with the constraint $\rho'_{11} + \rho'_{22} + \rho'_{33} = 1$ are numerically solved. The solutions of this set of coupled differential equations contain two different parts. The first part describes the damped oscillation of the populations of the system. The second represents the final state the system eventually reaches after being damped. One often refers to this final state of the system as the steady state solution. To solve for the steady state solution⁴, ρ_{ij}^s , one sets the derivative of the density matrix to zero since there is no oscillation after the system reaches the steady state. The system of coupled differential equations now becomes a system of algebraic equations and can be solved numerically. However, solving these algebraic equations analytically for the steady states is still impossible. Figure 2.4(b)

⁴To avoid double superscript notation the steady state of the transformed density matrix is denoted as ρ_{ij}^s .

shows the lineshape of $\text{Im}[\rho_{12}^s]$ when $\Delta_c/2\pi = 0$ MHz and Figure 2.5(b) shows the same lineshape but $\Delta_c/2\pi \neq 0$, where ρ_{12}^s is obtained numerically.

Although the steady state can be solved numerically, one normally uses the weak probe condition to obtain an approximate steady state solution. The weak probe limit makes it possible to reduce the number of coupled algebraic equations so that one can obtain an expression of ρ_{12}^s analytically.

2.5 Weak probe limit

The weak probe limit is when the intensity of the probe laser is so small that it hardly drives the transition to the intermediate and excited states. Mathematically, this approximation means that $\rho_{11}^s \approx 1$ while ρ_{22}^s and ρ_{33}^s are zero. Under this approximation, the equations for ρ_{12}^s , ρ_{13}^s and ρ_{23}^s read

$$\rho_{12}^s = \frac{i\Omega_p^*/2}{i\Delta_p + \Gamma_2/2 + \gamma_p} + \frac{i\Omega_c\rho_{13}^s/2}{i\Delta_p + \Gamma_2/2 + \gamma_p}, \quad (2.32a)$$

$$\rho_{13}^s = -\frac{i\Omega_p^*\rho_{23}^s/2}{i\Delta_R + \Gamma_3/2 + \gamma_p + \gamma_c} + \frac{i\Omega_c^*\rho_{12}^s/2}{i\Delta_R + \Gamma_3/2 + \gamma_p + \gamma_c}, \quad (2.32b)$$

$$\rho_{23}^s = -\frac{i\Omega_p\rho_{13}^s/2}{i\Delta_c + (\Gamma_2 + \Gamma_3)/2 + \gamma_c}. \quad (2.32c)$$

Substituting Equation (2.32c) into Equation (2.32b), we have

$$\rho_{13}^s = -\frac{|\Omega_p|^2/4}{(i\Delta_R + \Gamma_3/2 + \gamma_p + \gamma_c)(i\Delta_c + (\Gamma_2 + \Gamma_3)/2 + \gamma_c)} + \frac{i\Omega_c^*\rho_{12}^s/2}{i\Delta_R + \Gamma_3/2 + \gamma_p + \gamma_c}. \quad (2.33)$$

Suppose that $|\Omega_p|^2/4 \ll (\Gamma_3/2 + \gamma_p + \gamma_c)(\Gamma_3/2 + \Gamma_2/2 + \gamma_c)$. The first term of Equation (2.33) can then be neglected as it is of second order in $|\Omega_p|^2$. In the three-level system which we will deal with later, γ_p and γ_c are much smaller than Γ_2 and Γ_3 . Thus the condition $|\Omega_p|^2/4 \ll (\Gamma_3/2 + \gamma_p + \gamma_c)(\Gamma_3/2 + \Gamma_2/2 + \gamma_c)$ reduces to $|\Omega_p|^2 \ll \Gamma_3(\Gamma_3 + \Gamma_2)$ and we refer to the condition $|\Omega_p|^2 \ll \Gamma_3(\Gamma_3 + \Gamma_2)$ as the weak probe condition. Substituting ρ_{13}^s (without

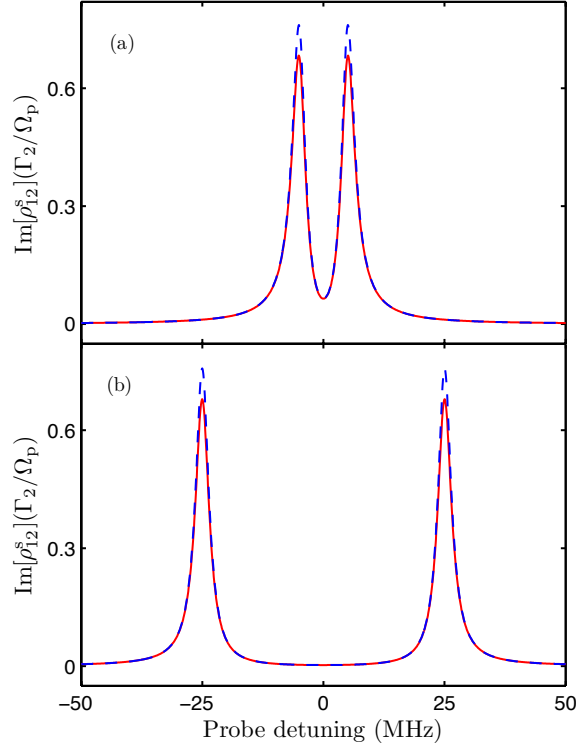


Figure 2.8: Comparison between the lineshape of $\text{Im}[\rho_{12}^s](\Gamma_2/\Omega_p)$ numerically calculated from Equation (2.31) (solid red line) and that calculated from Equation (2.34) (blue dashed line) as a function of $\Delta_p/2\pi$. The parameters used in the plot are $\Omega_p/2\pi = 1$ MHz, $\Gamma_2/2\pi = 5$, $\Gamma_3/2\pi = 1$ MHz and $\gamma_p/2\pi = \gamma_c/2\pi = 0.1$ MHz, which gives $\Omega_p^2/[\Gamma_3(\Gamma_3 + \Gamma_2)] = 1/6$. Thus the weak probe condition holds loosely for these parameters. This results in a small differences at the peaks of the resonances, regardless of the value of $\Omega_c/2\pi$, i.e., $\Omega_c/2\pi = 10$ MHz and 50 MHz in (a) and (b), respectively. Note that increasing Ω_c only results in an increase in the separation between two resonances, whereas the difference between two lineshapes does not reduce.

the first term) into Equation (2.32a) and re-arranging for ρ_{12}^s , we then have

$$\rho_{12}^s = \frac{i\Omega_p^*}{2} \left[i\Delta_p + \frac{\Gamma_2}{2} + \gamma_p + \frac{|\Omega_c|^2/4}{i\Delta_R + \Gamma_3/2 + \gamma_p + \gamma_c} \right]^{-1}. \quad (2.34)$$

Figure 2.8 compares the lineshape of $\text{Im}[\rho_{12}^s](\Gamma_2/\Omega_p)$ numerically calculated from Equation (2.31) (solid red line) to that calculated from Equation (2.34)

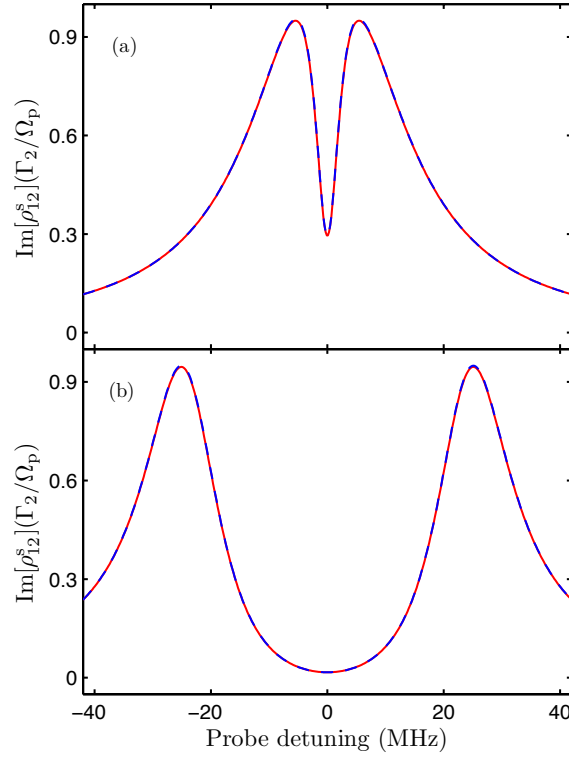


Figure 2.9: The same as Figure 2.8, except that $\Gamma_2/2\pi = 30$ MHz. The weak probe condition holds strongly as $\Omega_p^2/[\Gamma_3(\Gamma_3 + \Gamma_2)] = 1/31$. In this situation, the results calculated from both methods are in good agreement with each other as seen in (a) and (b), regardless of the value of Ω_c .

(blue dashed line) as a function of $\Delta_p/2\pi$. The parameters used in (a) and (b) are $\Omega_p/2\pi = 1$ MHz, $\Gamma_2/2\pi = 5$ MHz, $\Gamma_3/2\pi = 1$ MHz and $\gamma_p/2\pi = \gamma_c/2\pi = 0.1$ MHz. For the set of parameters, the weak probe condition holds loosely since $\Omega_p^2/[\Gamma_3(\Gamma_3 + \Gamma_2)] = 1/6$. This results in a small differences at the peaks of the resonances, regardless of the value of $\Omega_c/2\pi$, i.e., $\Omega_c/2\pi = 10$ MHz and 50 MHz in (a) and (b), respectively. Note that increasing Ω_c only results in an increase in the separation between the two resonances, whereas the difference between two lineshapes does not reduce.

Figure 2.9 shows a similar case as those of Figure 2.8, except that $\Gamma_2/2\pi = 30$ MHz. For these parameters, the weak probe condition holds

strongly since $\Omega_p^2/[\Gamma_3(\Gamma_3 + \Gamma_2)] = 1/31$. In this situation, the results calculated from both methods are in good agreement with each other as seen in (a) and (b), regardless of the value of Ω_c .

2.6 Susceptibility of the system

For an isotropic, linear medium the polarisation density of the system as a function of probe frequency (or probe detuning) is defined as $\mathbf{P}(t) = \epsilon_0 \chi(\Delta_p) \mathbf{E}_p(t)$, where ϵ_0 is the permittivity of free space. After substituting $\mathbf{E}_p(t) = (1/2)E_p \boldsymbol{\epsilon}_p e^{-i\omega_p t} + \text{c.c.}$, the polarisation density of the system is given by

$$\mathbf{P}(t) = \frac{1}{2} \epsilon_0 \chi(\Delta_p) E_p \boldsymbol{\epsilon}_p e^{-i\omega_p t} + \text{c.c.} \quad (2.35)$$

When an ensemble of the atoms is considered, $\mathbf{P}(t)$ represents the average over the ensemble [91]. One can also write the average of the polarisation density using the density matrix, i.e.,

$$\mathbf{P}(t) = -e\mathcal{N} \text{Tr}[\boldsymbol{\rho} \mathbf{r}], \quad (2.36)$$

where \mathcal{N} is the number density of the ensemble and $e\mathbf{r}$ is the dipole operator. Since we are interested in the transmission of the probe beam, it is sufficient to include only $|1\rangle$ and $|2\rangle$ in the expansion of $\mathbf{P}(t)$, i.e.,

$$\mathbf{P}(t) = -e\mathcal{N} (\rho_{12} \mathbf{r}_{21} + \rho_{21} \mathbf{r}_{12}). \quad (2.37)$$

Note that Equation (2.35) contains a fast oscillation at the frequency ω_p from the probe laser, whereas in Equation (2.37) this fast oscillation is hidden in ρ_{12} and ρ_{21} . To demonstrate this fast oscillating terms, we use Equation (2.29) to transform the density matrix into the new representation [68, 92].

This gives

$$\rho_{12} \rightarrow \rho'_{12} = \rho_{12} e^{-i\omega_p t}, \quad (2.38)$$

and Equation (2.37) becomes,

$$\mathbf{P}(t) = -e\mathcal{N} (\rho'_{12} \mathbf{r}_{21} e^{i\omega_p t} + \rho'_{21} \mathbf{r}_{12} e^{-i\omega_p t}). \quad (2.39)$$

Comparing Equation (2.35) with Equation (2.39), we have

$$\epsilon_0 E_p \epsilon_p \chi(\Delta_p) = -2e\mathcal{N}\rho'_{21} \mathbf{r}_{12}. \quad (2.40)$$

Taking the inner product of Equation (2.40) with $e\mathbf{r}_{12}$ on both sides and re-arranging for $\chi(\Delta_p)$, we have, using Equation (2.5a)

$$\chi(\Delta_p) = -\frac{2\mathcal{N}|\mathbf{d}_{12}|^2}{\hbar\epsilon_0\Omega_p}\rho'_{21}, \quad (2.41)$$

with $\mathbf{d}_{12} \equiv e\mathbf{r}_{12}$ and in the steady state ρ'_{21} is ρ_{21}^s .

The susceptibility is a complex number whose imaginary part is proportional to the absorption coefficient (α) and whose real part is related to the refractive index of the medium (n_R) [93]:

$$\alpha = k_p \text{Im}[\chi], \quad (2.42a)$$

$$n_R = 1 + \text{Re}[\chi]/2. \quad (2.42b)$$

2.7 Doppler broadening

The description of the atom-field interaction, up to now, is valid for cold atoms whose motion is negligible, i.e., when the Doppler width of the atoms is much smaller than the width of the absorption resonance⁵. For an ensemble of thermal atoms, the movement of the atoms results in a broadening of the lineshape, known as Doppler broadening. To add the effect of atomic motion, let us consider an atom moving with velocity v towards the laser beam with angular frequency ω . In the frame in which the atom is at rest, the atom would “see” the laser beam with angular frequency ω' , where, using Lorentz transformation [96], the relationship between ω and ω' is given by

$$\omega' = \sqrt{\frac{1+v/c}{1-v/c}}\omega, \quad (2.43)$$

⁵Mathematically, the Doppler effect can be neglected when $k_p u \ll \Gamma_2 + \Gamma_3$, where u is the most probable speed of the atoms at a temperature, T (see Equation (2.45)) [94, 95].

where c is the speed of light in vacuum. Typically the atomic velocity at room temperature is much smaller than the speed of light; thus,

$$\omega' \approx \omega \left(1 + \frac{v}{c}\right). \quad (2.44)$$

To include the Doppler effect into the model, we consider the system in which the probe and coupling beams are counter-propagating. Within this set up, the frequency of the atom moving towards the probe beam is upshifted by an amount $k_p v$, while that of the coupling beam is downshifted by an amount $k_c v$. This modifies the susceptibility of the system to

$$\begin{aligned} \chi(v)dv &= \frac{i|\mathbf{d}_{12}|^2}{\hbar\epsilon_0} \left[\gamma_{21} - i\Delta_p - ik_p v + \frac{|\Omega_c|^2/4}{\gamma_{31} - i\Delta_R - i(k_p - k_c)v} \right]^{-1} \\ &\times \frac{\mathcal{N}_0}{u\sqrt{\pi}} \exp\left(-\frac{v^2}{u^2}\right) dv, \end{aligned} \quad (2.45)$$

with $\gamma_{21} = \Gamma_2/2 + \gamma_p$, $\gamma_{31} = \Gamma_3/2 + \gamma_p + \gamma_c$ and $u \equiv \sqrt{2k_B T/m}$, where m is the mass of the atom. The term in the second line is the Maxwell-Boltzman velocity distribution [97] of the atoms. The total susceptibility can be obtained by performing the integration over the atomic velocities, i.e.,

$$\chi(\Delta_p, \Delta_c) = \int_{-\infty}^{\infty} \chi(v)dv. \quad (2.46)$$

Though the integrand is complicated, it is still integrable. To integrate $\chi(v)dv$, we rewrite the integrand, using the method of partial fraction, as

$$\chi(v)dv = \frac{|\mathbf{d}_{12}|^2 \mathcal{N}_0}{2\hbar\epsilon_0 u \sqrt{\pi} k_p} \left[\frac{d-1}{z-z_1} - \frac{d+1}{z-z_2} \right] e^{-z^2} dz, \quad (2.47)$$

where

$$d = \frac{i}{z_1 - z_2} \left[\frac{\gamma_{21} - i\Delta_p}{k_p u} - \frac{\gamma_{31} - i\Delta_R}{(k_p - k_c)u} \right], \quad (2.48a)$$

$$\begin{aligned} z_{1,2} &= -\frac{i}{2} \left[\frac{\gamma_{21} - i\Delta_p}{k_p u} + \frac{\gamma_{31} - i\Delta_R}{(k_p - k_c)u} \right] \\ &\pm \frac{i}{2} \left[\left(\frac{\gamma_{21} - i\Delta_p}{k_p u} - \frac{\gamma_{31} - i\Delta_R}{(k_p - k_c)u} \right)^2 - \frac{|\Omega_c|^2}{k_p(k_p - k_c)u^2} \right]^{1/2}. \end{aligned} \quad (2.48b)$$

Using the standard integral

$$\int_{-\infty}^{\infty} \frac{e^{-z^2}}{z - z_0} dz = -i\pi s e^{-z_0^2} [1 - s \operatorname{erf}(iz_0)], \quad (2.49)$$

where⁶ $s = -\operatorname{sgn}[\operatorname{Im}(z_0)]$ and $\operatorname{erf}(z_0)$ is the error function of z_0 [98, 99], then the total susceptibility is given by

$$\begin{aligned} \chi(\Delta_p, \Delta_c) = \frac{i|\mathbf{d}_{12}|^2 \mathcal{N}_0 \sqrt{\pi}}{2\hbar\epsilon_0 u k_p} \{ & (1 - d) s_1 e^{-z_1^2} [1 - s_1 \operatorname{erf}(iz_1)] \\ & + (1 + d) s_2 e^{-z_2^2} [1 - s_2 \operatorname{erf}(iz_2)] \}. \end{aligned} \quad (2.50)$$

Here $s_{1(2)} = -\operatorname{sgn}[\operatorname{Im}(z_{1(2)})]$. Equation (2.50) coincides with a result obtained by Gea-Banacloche et al. [84].

2.8 Summary

In this chapter, we discussed the theory of three-level system interacting with two EM fields. Using the dressed state formalism, we can determine the positions of the resonances of the absorption lineshape. Furthermore, the dressed state analysis gives us physical insight into various interesting phenomena, e.g., electromagnetically induced transparency, coherent population trapping and stimulated Raman adiabatic passage. We also discussed the weak probe condition which allowed us to find the steady state solution of the density matrix analytically. This condition is that $|\Omega_p|^2$ is much less than $\Gamma_3(\Gamma_3 + \Gamma_2)$. Finally the effect of the Doppler broadening was taken into account in order to obtain the total susceptibility of the system.

⁶ $\operatorname{sgn}(x)$ is the sign function. Its value is 1 when $x > 0$, -1 when $x < 0$ and 0 otherwise.

Chapter 3

Measuring a dipole matrix element using Rydberg EIT

In this chapter, we present a theoretical model for the electromagnetically induced transparency (EIT) absorption feature of ^{85}Rb , in which the dark state is a superposition between the $5S_{1/2}$ and $46S_{1/2}$ states. We also take into account the effect of Doppler broadening on the absorption lineshape. The model is then tested against experimental data (obtained by Bason et al. [92]) and a good agreement between the data and the model is demonstrated. By fitting the theoretical model with the experimental data, the reduced dipole matrix element between the $5P_{3/2}$ and $46S_{1/2}$ states can be extracted.

The measurement of the reduced matrix element has also been reported by other groups [24, 100]. For example, in the experiment of Deiglmayr et al. [100], the value of the reduced matrix element for the transition $5P_{3/2} \rightarrow 45S_{1/2}$ was measured using Autler-Townes splitting in cold Rb atoms. The measured value is in good agreement with the value they calculated. Recently, Piotrowicz et al. [101] used a relatively similar method to obtain the reduced matrix element for the transition $5P_{3/2} \rightarrow nD_{3/2}$ ($n = 22$ and 44). As a consequence, Rydberg EIT can be used as a tool to obtain the transition dipole matrix in Rydberg atoms.

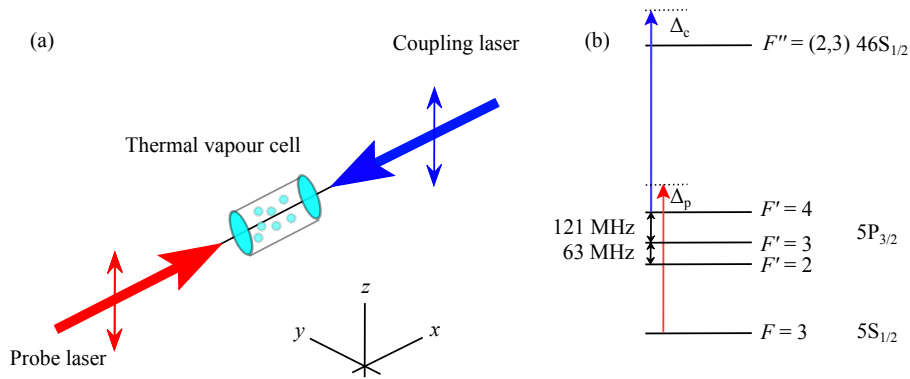


Figure 3.1: (a) Schematic of the experimental set up. The probe beam and coupling beam counter-propagate through a 75 mm-long Rb vapour cell. The quantisation axis is in the positive z direction. The polarisations of both fields are also parallel to the quantisation axis; hence, they drive π transitions within ^{85}Rb . The probe transmission is fixed while the frequency of the coupling field is scanned through the resonance transition $5\text{P}_{3/2}$, $F' = 4 \rightarrow 46\text{S}_{1/2}$, $F'' = (2, 3)$. (b) Simplified level scheme of ^{85}Rb showing the transitions driven by the probe and coupling fields.

3.1 Experimental set up

Figure 3.1 shows the schematics of the experimental set up with the coordinate axes and the energy levels of ^{85}Rb [102]. The details of the experiment have been discussed by Bason et al. [92]. In a few words, the experiments are performed on a thermal vapour cell containing a mixture of ^{85}Rb and ^{87}Rb . The length of the cell is 75 mm. The weak probe beam with wavelength of 780 nm and the co-axial counter-propagating beam (coupling beam) with wavelength of 480 nm¹ are directed along the positive and negative x axes, respectively. The polarisations of both beams are parallel to one another such that both beams drive the linear (π) transition in the ladder EIT system. The probe beam is stabilised on the resonance transition between $5\text{S}_{1/2}$, $F = 3$ and $5\text{P}_{3/2}$, $F' = 4$ of ^{85}Rb , while the coupling

¹The transition wavelength is obtained from [103].

beam is scanned through the resonance transition between $5P_{3/2}$, $F' = 4$ and $4S_{1/2}$, $F'' = (2, 3)$ of ^{85}Rb using a commercial frequency doubled diode laser system (Toptica TA-SHG). The focused probe and coupling beams are assumed to have a constant $1/e^2$ radius throughout the length of the vapour cell respectively of 0.49 ± 0.01 mm and 1.01 ± 0.10 mm. Note that the radius of the coupling beam is twice of that of the probed beam as this is to ensure that all atoms within the probe beam are involved in the EIT mechanism. The transmission of the probe beam at room temperature (approximately 18°C) is recorded using a photodiode. The experiment is then repeated for various values of coupling powers and a typical EIT transmission lineshape is shown in Figure 3.2(a). To understand the EIT spectrum we fit the data with the model presented in the next section.

3.2 Theoretical modelling of EIT

As seen in Figure 3.2(a), the transmission lineshape shows three EIT resonances, corresponding to the three sets of EIT transitions in ^{85}Rb . The main EIT resonance (on the right) corresponds to the transition $F = 3 \rightarrow F' = 4 \rightarrow F'' = 3$, the middle resonance corresponds to the transition $F = 3 \rightarrow F' = 3 \rightarrow F'' = (2, 3)$, and the resonance on the left is from the transition $F = 3 \rightarrow F' = 2 \rightarrow F'' = (2, 3)$. Obviously, the first transition can be understood in the framework of a three-level system, whereas the latter two transitions have the structure of a Y (four-level) system in which the two Rydberg states are approximately degenerate in energy.

In this section we begin with the discussion of the theory of the Y system, including the effect of Doppler broadening. Then the susceptibility obtained from the Y system is used to calculate the total susceptibility of the ^{85}Rb system.

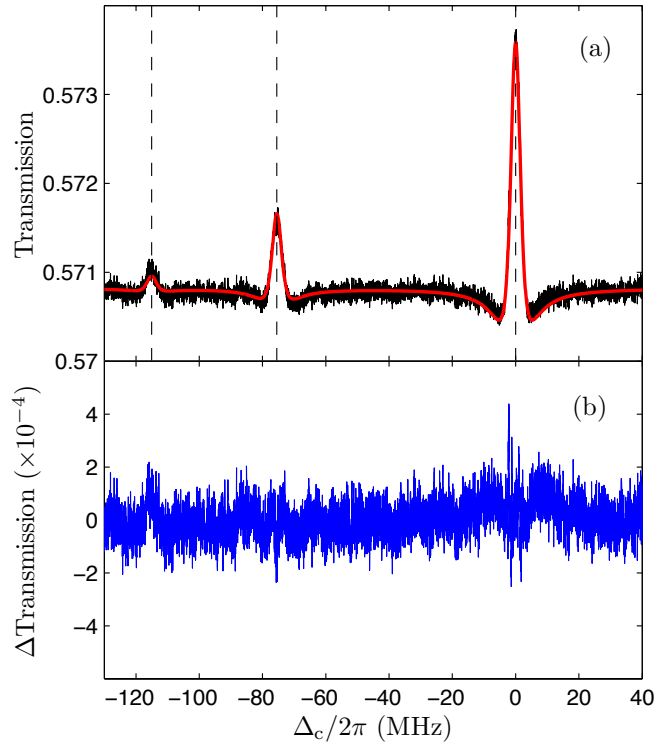


Figure 3.2: (a) EIT transmission for a coupling power of 170 mW, corresponding to $\Omega_c^{\text{eff}}/2\pi$ of 1.56 MHz, plotted against the coupling detuning. The vertical dashed lines represent the positions of the EIT resonances calculated from Equation (3.18), taking into account the effect of the wavevector mismatch in which the resonance position is shifted due to the residue of the wavevectors. This topic will be discussed in Section 3.3. The red solid line is the theoretical fit given by the model discussed in Section 3.2. The experimental data and the fitted curve are in good agreement as reflected in small difference between the calculated transmission and experimental data in (b). The data were collected by Bason et al. [92].

3.2.1 Y systems

Consider a four-level, Y system as shown in Figure 3.3, consisting of one ground state ($|1\rangle$), one intermediate state ($|2\rangle$), and two degenerate Rydberg states ($|3\rangle$ and $|4\rangle$). An example of the degenerate Rydberg states is in ^{85}Rb ,

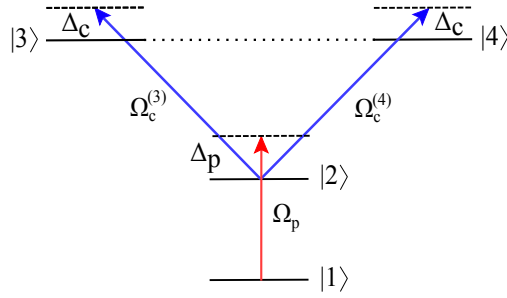


Figure 3.3: Schematic of the level scheme of Y (four-level) system. The ground state, $|1\rangle$, couples to the intermediate state, $|2\rangle$, via the weak coupling Ω_p . Then the intermediate state, $|2\rangle$, couples to the degenerate Rydberg states, $|3\rangle$ and $|4\rangle$, via the couplings $\Omega_c^{(3)}$ and $\Omega_c^{(4)}$, respectively. The detunings Δ_p and Δ_c are defined as shown in the diagram. The natural linewidth of $|2\rangle$ is Γ_2 , while the linewidths of the probe and coupling lasers are γ_p and γ_c , respectively.

where the hyperfine splitting between the $F'' = 2$ and 3 levels of $46\text{S}_{1/2}$ is approximately $0.2 \times 2\pi$ MHz [104], which can be neglected. The system interacts with an EM field given by

$$\mathbf{E}(t) = \frac{1}{2}E_p\hat{z}e^{-i\omega_p t} + \frac{1}{2}E_c\hat{z}e^{-i\omega_c t} + \text{c.c.}, \quad (3.1)$$

where the first (second) term represents the probe (coupling) field whose amplitude and angular frequency are E_p and ω_p (E_c and ω_c), respectively. These two fields drive π transitions, where $\Delta m_F = 0$, as their polarisations are parallel to z direction. The notation c.c. means the complex conjugate of the first two terms. The Hamiltonian of the atom-light interaction for this system, after applying the rotating-wave approximation and the slowly-varying variables, is given by $\mathcal{H} = \mathcal{H}_0 + \mathcal{H}_{\text{EIT}}$, where

$$\mathcal{H}_0 = -\hbar\Delta_p |2\rangle \langle 2| - \hbar(\Delta_p + \Delta_c)(|3\rangle \langle 3| + |4\rangle \langle 4|), \quad (3.2a)$$

$$\mathcal{H}_{\text{EIT}} = \frac{\hbar\Omega_p}{2} |1\rangle \langle 2| + \frac{\hbar\Omega_c^{(3)}}{2} |2\rangle \langle 3| + \frac{\hbar\Omega_c^{(4)}}{2} |2\rangle \langle 4| + \text{h.c.} \quad (3.2b)$$

Here $\Delta_{p(c)}$ is the probe (coupling) detuning and h.c. represents the hermitian conjugate of the first three terms. The Rabi frequencies associated with the probe and coupling fields (Ω_p , $\Omega_c^{(3)}$ and $\Omega_c^{(4)}$, respectively) are given by

$$\Omega_p = \frac{E_p}{\hbar} \langle 2 | \mathbf{e} \mathbf{r} \cdot \hat{\mathbf{z}} | 1 \rangle, \quad (3.3a)$$

$$\Omega_c^{(3)} = \frac{E_c}{\hbar} \langle 3 | \mathbf{e} \mathbf{r} \cdot \hat{\mathbf{z}} | 2 \rangle, \quad (3.3b)$$

$$\Omega_c^{(4)} = \frac{E_c}{\hbar} \langle 4 | \mathbf{e} \mathbf{r} \cdot \hat{\mathbf{z}} | 2 \rangle, \quad (3.3c)$$

where $-\mathbf{e} \mathbf{r}$ is the dipole operator. Having determined the Hamiltonian, the equations of motion for the density matrix, ρ , are

$$\dot{\rho}_{11} = \Gamma_2 \rho_{22} + \frac{i\Omega_p}{2} (\rho_{12} - \rho_{21}), \quad (3.4a)$$

$$\dot{\rho}_{22} = -\Gamma_2 \rho_{22} - \frac{i\Omega_p}{2} (\rho_{12} - \rho_{21}) + \frac{i}{2} \sum_{k=3}^4 \Omega_c^{(k)} (\rho_{2k} - \rho_{k2}), \quad (3.4b)$$

$$\dot{\rho}_{12} = -\left(\frac{\Gamma_2}{2} + \gamma_p + i\Delta_p\right) \rho_{12} + \frac{i\Omega_p}{2} (\rho_{11} - \rho_{22}) + \frac{i}{2} \sum_{k=3}^4 \Omega_c^{(k)} \rho_{1k}, \quad (3.4c)$$

$$\dot{\rho}_{1k} = -[\gamma_p + \gamma_c + i(\Delta_p + \Delta_c)] \rho_{1k} - \frac{i\Omega_p}{2} \rho_{2k} + \frac{i\Omega_c^{(k)}}{2} \rho_{12}, \quad (3.4d)$$

$$\begin{aligned} \dot{\rho}_{2k} = & -\left(\frac{\Gamma_2}{2} + \gamma_c + i\Delta_c\right) \rho_{2k} - \frac{i\Omega_p}{2} \rho_{1k} \\ & + \frac{i\Omega_c^{(k)}}{2} (\rho_{22} - \rho_{kk}) - \frac{i\Omega_c^{(j)}}{2} \rho_{jk}, \end{aligned} \quad (3.4e)$$

$$\dot{\rho}_{ik} = -\frac{i\Omega_c^{(i)}}{2} \rho_{2k} + \frac{i\Omega_c^{(k)}}{2} \rho_{i2}, \quad (3.4f)$$

where the index j is $j = 7 - k$, Γ_2 is the linewidth of $|2\rangle$ and $\gamma_{p(c)}$ is the linewidth of the probe (coupling) laser. The linewidths of the Rydberg states are relatively small; and hence, can be neglected. The steady state solution of the density matrix, ρ^s , is obtained by setting $\dot{\rho} = 0$ and Equation (3.4) becomes a set of algebraic equations, which can be solved numerically. However, the weak probe condition allows us to solve the set of algebraic equations analytically [84]. This can be done by assuming that $\rho_{11}^s \approx 1$, and $\rho_{nm}^s \approx 0$ when $n \neq 1$ and $m \neq 1$. Under the weak probe condition, a simple

calculation shows that ρ_{21}^s is given by

$$\rho_{21}^s = \frac{i\Omega_p}{2} \left[i\Delta_p - \frac{\Gamma_2}{2} - \gamma_p + \frac{(\Omega_c^{(3)}/2)^2}{i(\Delta_p + \Delta_c) - \gamma_c - \gamma_p} + \frac{(\Omega_c^{(4)}/2)^2}{i(\Delta_p + \Delta_c) - \gamma_c - \gamma_p} \right]^{-1}, \quad (3.5)$$

where the second and third terms in the squared bracket represent the EIT effect caused by the couplings $\Omega_c^{(3)}$ and $\Omega_c^{(4)}$, respectively. In the general case where $|3\rangle$ and $|4\rangle$ are not degenerate in energy, the denominators of the second and third terms in the bracket would be different, namely, the coupling detuning in the denominators, Δ_c , now changes to $\Delta_c^{(3)}$ and $\Delta_c^{(4)}$, corresponding to the coupling detunings of the transition between $|2\rangle$ and $|3\rangle$, and, $|2\rangle$ and $|4\rangle$, respectively. Note that Equation (3.5) has the same form as that obtained for an inverted Y system [105]. This is not surprised as both Y system and inverted Y system have the same topological geometry. In [105], it has been shown that the inverted Y system produces three absorption resonances, corresponding to EIT doublet.

In our case, the denominators of the second and third terms in the bracket are the same; and hence, Equation (3.5) can be written as,

$$\rho_{21}^s = \frac{i\Omega_p}{2} \left[i\Delta_p - \frac{\Gamma_2}{2} - \gamma_p + \frac{(\Omega_{\text{eff}}/2)^2}{i(\Delta_p + \Delta_c) - \gamma_c - \gamma_p} \right]^{-1}, \quad (3.6)$$

where Ω_{eff} is the effective Rabi frequency and is given by $(\Omega_{\text{eff}})^2 = (\Omega_c^{(3)})^2 + (\Omega_c^{(4)})^2$. Comparing ρ_{21}^s obtained from a Y system and a three-level system, the two degenerate Rydberg states act as if they were a single state which couples to $|2\rangle$ with the coupling strength equal to the effective Rabi frequency and the absorption lineshape contains only two absorption resonances. Thus the symmetry of the Rydberg states reduces one absorption resonance from the system of non-degenerate Rydberg states [105]. Having determined ρ_{21}^s , the susceptibility of the Y system is given by

$$\chi = -\frac{i\mathcal{N}d_{21}^2}{\hbar\epsilon_0} \left[i\Delta_p - \frac{\Gamma_2}{2} - \gamma_p + \frac{(\Omega_{\text{eff}}/2)^2}{i(\Delta_p + \Delta_c) - \gamma_c - \gamma_p} \right]^{-1}, \quad (3.7)$$

where \mathcal{N} is the total number of ^{85}Rb per unit volume and $d_{21} = \langle 2 | \mathbf{e} \mathbf{r} \cdot \hat{\mathbf{z}} | 1 \rangle$ is the dipole matrix element between $|2\rangle$ and $|1\rangle$.

Note that Equation (3.7) is only valid for non-moving atoms; however, in a thermal system where the atoms move in all directions with a velocity distribution given by the Maxwell-Boltzmann distribution, the effect of Doppler broadening must be taken into account. To include this effect we make changes to Δ_p , Δ_c and \mathcal{N} with the following substitutions:

$$\Delta_p \rightarrow \Delta_p + k_p v, \quad (3.8a)$$

$$\Delta_c \rightarrow \Delta_c - k_c v, \quad (3.8b)$$

$$\mathcal{N} \rightarrow \frac{\mathcal{N}_0}{u\sqrt{\pi}} \exp\left(-\frac{v^2}{u^2}\right), \quad (3.8c)$$

where $k_{p(c)}$ is the wavevector of the probe (coupling) field, v is the atomic velocity parallel to the propagation axis, $u \equiv \sqrt{2k_B T/m}$ is the most probable speed of the atoms at a given temperature T and m is the atomic mass of a ^{85}Rb atom. Using the ideal gas equation [106], the total number density of the system, \mathcal{N}_0 , as a function of temperature is [102]

$$\mathcal{N}_0 = 0.7217 \times \frac{p \times 133.3223684}{k_B T}, \quad (3.9)$$

where the factor 0.7217 is the atomic abundance of ^{85}Rb [102], the factor 133.3223684 is the conversion factor converting the pressure in Torr to Pa and p is the pressure measured in Torr. It turns out that the pressure is also a function of temperature [107]:

$$\log_{10} p = 2.881 + 4.857 - \frac{4215}{T}. \quad (3.10)$$

Thus one can control the number density by changing only the temperature of the vapour cell in the experiment. To obtain the susceptibility of the system, one averages $\chi(v)$ over the entire velocity distribution [84], i.e.,

$$\begin{aligned} \chi_D(\Delta_p, \Delta_c) &= \int_{-\infty}^{\infty} \chi(v) dv \\ &= \left(\frac{id_{21}^2 \sqrt{\pi} \mathcal{N}_0}{2\hbar \epsilon_0 u k_p} \right) \left\{ (1-d) s_1 e^{-z_1^2} [1 - s_1 \text{erf}(iz_1)] \right. \\ &\quad \left. + (1+d) s_2 e^{-z_2^2} [1 - s_2 \text{erf}(iz_2)] \right\}, \quad (3.11) \end{aligned}$$

where $s_{1(2)} = -\text{sgn} [\text{Im}(z_{1(2)})]$, and, d and $z_{1,2}$ are

$$d = \frac{i}{z_1 - z_2} \left[\frac{\Gamma_2 + \gamma_p - i\Delta_p}{k_p u} + \frac{\gamma_p + \gamma_c - i(\Delta_p + \Delta_c)}{(k_p - k_c)u} \right], \quad (3.12a)$$

$$z_{1,2} = -\frac{i}{2} \left[\frac{\Gamma_2 + \gamma_p - i\Delta_p}{k_p u} + \frac{\gamma_p + \gamma_c - i(\Delta_p + \Delta_c)}{(k_p - k_c)u} \right] \pm \frac{i}{2} \left[\left(\frac{\Gamma_2 + \gamma_p - i\Delta_p}{k_p u} - \frac{\gamma_p + \gamma_c - i(\Delta_p + \Delta_c)}{(k_p - k_c)u} \right)^2 - \frac{\Omega_{\text{eff}}^2}{k_p(k_p - k_c)u^2} \right]^{1/2}. \quad (3.12b)$$

Note that to reduce the result to that of three-level system, we simply replace either $\Omega_c^{(3)}$ or $\Omega_c^{(4)}$ by zero. Thus Equation (3.11) holds for both a three-level and a Y system and it is the starting point in our calculation of the total susceptibility of ^{85}Rb .

3.2.2 Modelling the EIT transmission of ^{85}Rb

As mentioned at the beginning of this section, the total susceptibility of ^{85}Rb is the sum of the susceptibilities of three different transitions. The expression of the total susceptibility of ^{85}Rb is given by

$$\chi_{\text{TOT}}(\Delta_p, \Delta_c) = \frac{1}{12} \left\{ \sum_{m_F=-3}^3 \chi_D(\delta_p^1, \delta_c^1) + \sum_{m_F=-3}^3 \chi_D(\delta_p^2, \delta_c^2) + \sum_{m_F=-2}^2 \chi_D(\delta_p^3, \delta_c^3) \right\}, \quad (3.13)$$

where the factor of 1/12 accounts for the fact that the initial population is evenly populated among the magnetic sublevels of $5S_{1/2}$, $F = (2, 3)$. The first term in Equation (3.13) represents the susceptibility of the transition $F = 3 \rightarrow F' = 4 \rightarrow F'' = 3$, which is composed of seven individual sub-transitions, corresponding to the magnetic sublevels $m_F = -3 \rightarrow 3$. Since Δ_p and Δ_c are measured with respect to $F' = 4$ and $F'' = 3$, δ_p^1 and δ_c^1 are simply Δ_p and Δ_c , respectively. The susceptibility of the transition $F = 3 \rightarrow F' = 3 \rightarrow F'' = (2, 3)$, shown as the second term in Equation (3.13), is also

the sum of seven susceptibilities, accounting for seven magnetic sublevels. The frequency separation between the reference level $F' = 4$ and $F' = 3$ is $120.94 \times 2\pi$ MHz. This difference in frequency introduces a shift in both probe and coupling detunings, i.e., $\delta_p^2 = \Delta_p + (2\pi \times 120.94)$ MHz and $\delta_c^2 = \Delta_c - (2\pi \times 120.94)$ MHz. And finally, the susceptibility of the transition $F = 3 \rightarrow F' = 2 \rightarrow F'' = (2, 3)$ is shown as the third term in Equation (3.13). In contrast to the previous two transitions, there are no transitions starting from $m_F = \pm 3$ as the intermediate state has no $m_F = \pm 3$ magnetic sublevels. Thus the index of the summation only runs from -2 to 2 . The frequency difference between $F' = 4$ and $F' = 2$ is $184.36 \times 2\pi$ MHz; thus, $\delta_p^3 = \Delta_p + (2\pi \times 184.36)$ MHz and $\delta_c^3 = \Delta_c - (2\pi \times 184.36)$ MHz.

Using the Wigner-Eckart theorem, the dipole matrix element, d_{21} , for the transition $5S_{1/2}(F, m_F)$ to $5P_{3/2}(F', m'_F)$ is given by

$$\begin{aligned} d_{21}^2 &= |\langle 5P_{3/2}(F', m'_F) | ez | 5S_{1/2}(F, m_F) \rangle|^2 \\ &= 4e^2(2F+1)(2F'+1) \begin{pmatrix} F & 1 & F' \\ m_F & 0 & -m'_F \end{pmatrix}^2 \begin{Bmatrix} 3/2 & 1/2 & 1 \\ F & F' & 5/2 \end{Bmatrix}^2 \\ &\quad \times |\langle 5P_{3/2} || r || 5S_{1/2} \rangle|^2, \end{aligned} \quad (3.14)$$

where $\langle 5P_{3/2} || r || 5S_{1/2} \rangle$ is known as a reduced matrix element [108, 109]. For the transition between $5S_{1/2}$ and $5P_{3/2}$, $\langle 5P_{3/2} || r || 5S_{1/2} \rangle$ is $2.989a_0$ [110]. And the effective Rabi frequency between $5P_{3/2}(F', m'_F)$ and $46S_{1/2}(F'', m''_F)$ is given by

$$\begin{aligned} (\Omega_{\text{eff}})^2 &= \left(\frac{E_c}{\hbar} \right)^2 \sum_{F''=2,3} |\langle 46S_{1/2}(F'', m''_F) | ez | 5P_{3/2}(F', m'_F) \rangle|^2 \\ &= \sum_{F''=2,3} (2F''+1)(2F'+1) \begin{pmatrix} F' & 1 & F'' \\ m'_F & 0 & -m''_F \end{pmatrix}^2 \begin{Bmatrix} 1/2 & 3/2 & 1 \\ F' & F'' & 5/2 \end{Bmatrix}^2 \\ &\quad \times \frac{4}{3} \Omega_c^2, \end{aligned} \quad (3.15)$$

where the reduced dipole matrix element of the system is absorbed into Ω_c^2 , i.e., $\Omega_c^2 \equiv (eE_c \langle 46S_{1/2} || r || 5P_{3/2} \rangle / \hbar)^2$. Note that it just happens in this

case that the reduced matrix element is equal to the radial integral, where the radial integral between the $46S_{1/2}$ and $5P_{3/2}$ states, $\langle 46S_{1/2}|r|5P_{3/2}\rangle$, is defined as

$$\langle 46S_{1/2}|r|5P_{3/2}\rangle = \int_0^\infty r^3 R_{46}^0(r) R_5^1(r) dr, \quad (3.16)$$

with $R_n^L(r)$ is the radial wavefunction of state n with the orbital angular momentum L [74].

Putting everything together, the EIT transmission of ^{85}Rb , T , is

$$T = \exp(-\mathcal{L}k_p \text{Im}[\chi_{\text{TOT}}]), \quad (3.17)$$

where \mathcal{L} is the length of the cell. It is found in the experiment that the linewidth of the probe laser, $\gamma_p/2\pi$, is less than 300 kHz, which is much smaller than the natural linewidth of $5P_{3/2}$ ($\Gamma_2/2\pi = 6$ MHz); thus, γ_p can be neglected in the expression for χ_{TOT} . Moreover $\Delta_p = 0$ since the probe laser is on resonance with the transition $F = 3 \rightarrow F' = 4$. The transmission is then a function of three parameters, i.e., Ω_c , γ_c and T . We fit the experimental data against the theoretical calculation predicted using Equation (3.17) for five values of coupling powers, P_c . The best fit is obtained when the set of Ω_c , γ_c and T produces minimum chi-squared (χ^2). The values of Ω_c , γ_c and T which produce the best fit for five coupling powers are shown in Table 3.1. Note that the intensity of the coupling beam is assumed to be constant across the cross-section of the beam while fitting the data. Thus the value of Ω_c obtained from the fit is the effective value, i.e., the average value of the intensity as if the system were illuminated with a constant intensity². We will deal with the problem of a Gaussian beam later when the radial matrix element is extracted.

²The fact that the probe intensity is not constant is not important in the calculation since the weak probe limit is assumed throughout the calculation.

Table 3.1: The values of the three parameters which produce the minimum χ^2 . Ω_c^{eff} and γ_c are expressed in unit of 2π MHz. Note that the uncertainties of the fitted parameters calculated from $\chi^2 + 1$ method are so tiny that they do not affect the fitted parameters quoted with 3 significant figures.

P_c (mW)	Ω_c^{eff}	γ_c	T ($^{\circ}\text{C}$)
170	1.56	0.19	17.5
140	1.45	0.19	17.5
110	1.29	0.20	17.5
80	1.08	0.21	17.5
50	0.79	0.20	17.5

3.3 Observation of EIT resonances and wavevector mismatch

The EIT transmission of ^{85}Rb for the coupling power of 170 mW is shown in Figure 3.2(a) where the red solid line is the theoretical fit. The transmission encompasses three EIT resonances corresponding to the transitions via $5\text{P}_{3/2}$, $F' = 2, 3$ and 4. It is clear that the result calculated from the theoretical model is in good agreement with the experimental data. The fitting procedure also yields reasonable values of γ_c and T , i.e., they are approximately constant for all coupling powers. The main EIT resonance (right peak) is at $\Delta_c/2\pi = 0$ MHz. However, the middle and the left EIT resonances are not located at $\Delta_c/2\pi = -120.94$ and -184.36 MHz, respectively. This is because the wavevectors of both lasers do not totally cancel each other. Thus the EIT resonances are displaced by the effect of the Doppler broadening. This wavevector mismatch can be understood by looking at the plot of the absorption coefficient of ^{85}Rb before average over the velocity distribution, shown in Figure 3.4(Top). The values of $\gamma_c/2\pi$ and T used in the figure are 0.2 MHz and 17.5 $^{\circ}\text{C}$, respectively. For the purpose of a clear splitting where the EIT

resonances are located, we assume $\Omega_c/2\pi = 21$ MHz. The total absorption can be calculated by integrating the absorption coefficient per unit velocity over velocity. The EIT resonances occur when the horizontal bright lines are disconnected since the integral over velocity at these locations are minimum, shown in Figure 3.4(Bottom). These locations are also where the dark states exist. From the figure, the horizontal bright lines are at the velocity classes such that the probe frequency is shifted onto resonance with $F' = 2, 3$ and 4 , i.e., $\Delta_p + \Delta_{\text{hfs}} + k_p v_{\text{EIT}} = 0$, where Δ_{hfs} is the hyperfine splitting between $F' = 4$ and $F' = 2$ or 3 . The predicted velocity classes from this equation are $v_{\text{EIT}} = 0, -94.36$ and -143.85 m/s. For each of the velocity classes, the EIT resonance occurs when the coupling frequency is exactly on resonance between $F' = (2, 3, 4)$ and the Rydberg states, i.e., $\Delta_c^{\text{EIT}} - \Delta_{\text{hfs}} - k_c v_{\text{EIT}} = 0$. This equation is the thin oblique line which cuts through the three horizontal lines in Figure 3.4(Top). Solving these two equations with $\Delta_p = 0$, the location of the EIT resonance is given by

$$\Delta_c^{\text{EIT}} = \left(\frac{k_p - k_c}{k_p} \right) \Delta_{\text{hfs}}. \quad (3.18)$$

Using Equation (3.18), the positions of the middle and the left EIT resonances, $\Delta_c^{\text{EIT}}/2\pi$, are -75.47 and -115.05 MHz, respectively, and they are clearly in agreement with the experimental data as observed in Figure 3.2(a).

3.4 Extracting reduced matrix element

We demonstrate, in this section, that Rydberg EIT can be used to find the reduced matrix element (or radial integral) for the transition between $5P_{3/2}$ and the Rydberg state. A complication arises due to the non-homogeneity of the coupling intensity. However, we overcome the problem of non-homogeneity by using a Taylor expansion of the absorption coefficient. Thus a linear relation between coupling power and the fitted parameter $(\Omega_c^{\text{eff}})^2$ is achieved.

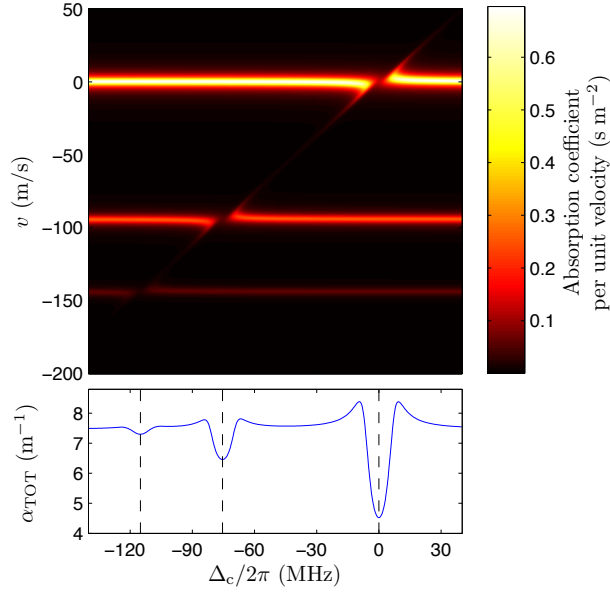


Figure 3.4: (Top) Image plot of the absorption coefficient of ^{85}Rb before average over the velocity for different values of atomic velocities and coupling detunings. The values of $\gamma_c/2\pi$ and T used in the figure are 0.2 MHz and 17.5 °C, respectively, and $\Omega_c/2\pi$ is assumed to be 21 MHz in order to produce a clear splittings of the EIT resonances. (Bottom) The total absorption calculated by summing the absorption coefficient across the velocity axis against coupling detuning. The location where the bright horizontal line is disconnected corresponds to the EIT resonance. These resonances are located by the vertical dashed lines. Note that the positions of the bright horizontal lines correspond to the velocity classes such that $\Delta_p + \Delta_{\text{hfs}} + k_p v_{\text{EIT}} = 0$. And the positions of the EIT resonances, Δ_c^{EIT} , correspond to the intercept points of $\Delta_p + \Delta_{\text{hfs}} + k_p v_{\text{EIT}} = 0$ and $\Delta_c^{\text{EIT}} - \Delta_{\text{hfs}} - k_c v_{\text{EIT}} = 0$.

It is clear from Equation (3.11) that the absorption coefficient³ is also a function of the intensity of the coupling laser through Ω_c . Thus it is, in turn, a function of the spatial coordinates y and z , i.e., the radial direction along the cross-section of the beam. Let us consider the output power and the

³The absorption coefficient is $\alpha_{\text{TOT}} = k_p \text{Im}[\chi_{\text{TOT}}]$.

input intensity of the probe beam in which their relationship is given by⁴

$$P_p^f = 2\pi \int_0^\infty I_p(x_i, r) e^{-\alpha(r)\mathcal{L}} r dr. \quad (3.19)$$

Here P_p^f is the output probe power, I_p is the probe intensity, x_i is the x position at the entrance of the vapour cell, r is the radius of in the cross-section plane and it is related to y and z via $r^2 = y^2 + z^2$. The simplest case is when α is constant and the integral becomes $P_p^f = P_p^i \exp(-\alpha\mathcal{L})$, where P_p^i is the input probe power and is defined as

$$P_p^i = 2\pi \int_0^\infty I_p(x_i, r) r dr. \quad (3.20)$$

Generally, the integration in Equation (3.19) cannot be performed analytically due to the complicated form of the absorption coefficient. Alternatively, we expand the absorption coefficient in terms of Ω_c^2 as⁵

$$\alpha(\Omega_c^2) = \alpha_0 + \alpha_1 \Omega_c^2 + \mathcal{O}(\Omega_c^4), \quad (3.21)$$

where α_0 and α_1 are the coefficients of the expansion and, generally, $\alpha_1 \ll \alpha_0$. Substituting the first order expansion of α into Equation (3.19) and assuming⁶ $\alpha_1 \Omega_c^2 \ll 1$, we have

$$\begin{aligned} P_p^f &= e^{-\alpha_0 \mathcal{L}} \times 2\pi \int_0^\infty I_p(x_i, r) e^{-\alpha_1 \Omega_c^2(r)\mathcal{L}} r dr \\ &\approx e^{-\alpha_0 \mathcal{L}} \left[P_p^i - 2\pi \alpha_1 \mathcal{L} \int_0^\infty I_p(x_i, r) \Omega_c^2(r) r dr \right] \end{aligned} \quad (3.22)$$

Assuming both probe and coupling beams have a Gaussian intensity profile, the expressions of Ω_c^2 and I_p change to

$$\Omega_c^2 \rightarrow \Omega_c^2 \left(\frac{w_c^0}{w_c(x)} \right)^2 e^{-2(r/w_c(x))^2}, \quad (3.23a)$$

$$I_p \rightarrow I_p \left(\frac{w_p^0}{w_p(x)} \right)^2 e^{-2(r/w_p(x))^2}, \quad (3.23b)$$

⁴For simplicity, we drop the subscript TOT from α_{TOT} .

⁵We want to expand the absorption coefficient in terms of the coupling intensity which is, in turn, proportional to Ω_c^2 .

⁶The geometry component of the Rabi frequency is contained in α_1 .

where $w_{p(c)}^0$ is the probe (coupling) beam waist at the centre of the vapour cell, $w_{p(c)}(x)$ is the probe (coupling) beam waist at the position x , and, Ω_c^2 and I_p are constant. Substituting Equation (3.23) into Equation (3.22) and evaluating the integral, we have

$$P_p^f = e^{-\alpha_0 \mathcal{L}} P_p^i \left[1 - \alpha_1 \mathcal{L} \frac{4e^2 \langle 46S_{1/2} || r || 5P_{3/2} \rangle^2}{\hbar^2 c \epsilon_0 \pi [w_c^2(x_i) + w_p^2(x_i)]} P_c \right]. \quad (3.24)$$

Here we have used, for the profile given by Equation (3.23), $P_p^i = \pi(w_p^0)^2 I_p / 2$ and $P_c = c \epsilon_0 (w_c^0)^2 \pi E_c^2 / 4$. It is assumed that the beam waists of both probe and coupling beams are constant throughout the length of the vapour cell in order to evaluate the integral and the medium is lossless for the coupling power. Without loss of generality, we apply Equation (3.21) and Equation (3.22) for the case in which the Rabi coupling is constant, i.e., the Rabi coupling is the effective Rabi frequency, Ω_c^{eff} , which has been obtained from the fitting. Thus we have

$$P_p^f = e^{-\alpha_0 \mathcal{L}} P_p^i [1 - \alpha_1 \mathcal{L} (\Omega_c^{\text{eff}})^2]. \quad (3.25)$$

Comparing Equation (3.24) to Equation (3.25), the relationship between $(\Omega_c^{\text{eff}})^2$ and P_c is given by

$$(\Omega_c^{\text{eff}})^2 = \frac{4e^2 \langle 46S_{1/2} || r || 5P_{3/2} \rangle^2}{\hbar^2 c \epsilon_0 \pi [w_c^2(x_i) + w_p^2(x_i)]} P_c. \quad (3.26)$$

According to Equation (3.26), the reduced matrix element $\langle 46S_{1/2} || \mathbf{r} || 5P_{3/2} \rangle$, or the radial integral in this particular case, is proportional to the ratio between $(\Omega_c^{\text{eff}})^2$ and P_c . In other words, the reduced matrix element can be extracted from the gradient of a plot of $(\Omega_c^{\text{eff}})^2$ against P_c . The linear relationship between $(\Omega_c^{\text{eff}})^2$ and P_c is demonstrated in Figure 3.5(a) assuming a 5% error for the coupling powers, whereas the error for Ω_c^{eff} is too small to be noticed in the figure⁷. The data points form a straight line as expected from Equation (3.26). Using the least-squares method, the regression line is plotted against the data points. It is clear that the regression line lies within

⁷The error for Ω_c^{eff} is calculated using $\chi^2 + 1$ method, see [111] for more detail.

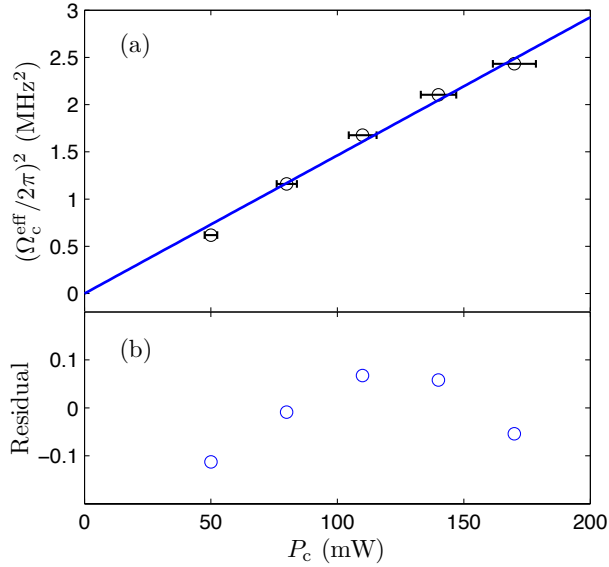


Figure 3.5: (a) Plot between $(\Omega_c^{\text{eff}}/2\pi)^2$ against coupling power, P_c . According to Equation (3.26), the gradient of the straight line is proportional to the reduced matrix element. The linear relationship between $(\Omega_c^{\text{eff}})^2$ and P_c is demonstrated with a 5% error for the coupling powers. The error bars for Ω_c^{eff} are too small to be noticeable. The blue solid line is the regression line calculated from the least-squares method. The reduced matrix element $\langle 46\text{S}_{1/2} || r || 5\text{P}_{3/2} \rangle$ extracted from the gradient of the straight line is $(1.5 \pm 0.1) \times 10^{-2} a_0$, which is in good agreement with the values quoted in [24, 100]. (b) The residuals between the fitted line and the experimental data are relatively small, suggesting that a linear straight line could be a good fit. However, the residual plot shows that the residuals form a curve which does not suggest the random distribution. This implies that there could be a contribution from the higher order terms which have not been taken into account.

the error bars of the data points. However, the residual plot, shown in Figure 3.5(b), reflects the fact that the higher order corrections should be taken into account in order to improve the fitting since the residuals are not randomly distributed. They instead form a curve which is approximately parabola.

Using Equation (3.26) and taking into account the uncertainty on the waists of the beams, the reduced matrix element $\langle 46S_{1/2} || r || 5P_{3/2} \rangle$ is $(1.5 \pm 0.1) \times 10^{-2} a_0$, where a_0 is the Bohr radius. The error of the radial matrix element are due to the error of the slope obtained from the least-squares method and the errors from the beam waists of probe and coupling lasers. The percentage errors of the slope, the coupling beam waist and the probe beam waist are 1%, 8% and 0.4%, respectively. Thus the total error for the reduced matrix element is given by the quadrature sum of the individual error components. Thus the error of the reduced matrix element is 8%, which is $0.1 \times 10^{-2} a_0$ (quoted with 2 significant figures). The most significant source of error is from the measurement of the coupling beam waists which could be reduced by optimising the set up to decrease the error of the coupling beam waist. Another way round this problem is to use a shorter vapour cell [112, 113] in which the variation of the beam across the cell due to the divergence can be minimised. The value of the reduced matrix element extracted from the experiment is in agreement with the value of $(1.59 \pm 0.16) \times 10^{-2} a_0$ quoted in the literature, e.g., [24, 100].

3.5 Summary and conclusions

In this chapter, we presented a theoretical model for a Rydberg EIT system with the effect of Doppler broadening. A good agreement between the model and the experimental data was demonstrated. We also showed the well-known effect of the wavevector mismatch which scales with the distance, in frequency, between the EIT resonances by a factor of $(k_p - k_c)/k_p$. This effect arises from the fact that the vector sum of the wavevectors is not totally cancelled with each other.

We also demonstrated that, by fitting the theoretical model with the experimental data, the reduced matrix element between the $5P_{3/2}$ and the $nS_{1/2}$

Rydberg state can be extracted. By expanding the absorption coefficient up to first order, it was found that $(\Omega_c^{\text{eff}})^2$ has a linear relationship with P_c , and the reduced matrix element can be extracted from the gradient of the plot $(\Omega_c^{\text{eff}})^2$ against P_c . Piotrowicz et al. used a relatively similar method to exploit the reduced matrix element between the $5P_{3/2}$ and the nD_J Rydberg state [101]. In contrast to our method, Piotrowicz et al. tackled the problem of inhomogeneous coupling field intensity by numerically calculating the spatial variation of the absorption image and fitting the calculated results to the experimental absorption image to obtain the fitting parameters and the reduced dipole matrix element [101].

It was assumed in our calculation that the cross-section of both beams were approximately constant throughout the length of the cell. However, there was a small variation of the cross-section across the length of the cell. To get around this problem one could do the experiment with a thin cell [112, 113], where the variation of the beam across the cell is easier to control.

Chapter 4

Rydberg EIT with three-photon transition

In the previous chapter, Rydberg electromagnetically induced transparency (EIT) in a thermal vapour cell has been demonstrated with good agreement between experiment and theory. However, it was found by Bason et al. [25, 32] that the results were affected by the occurrence of screening charges, presumably due to the photoelectric ionisation of Rb atoms deposited on the inside of the vapour cell [114]. This effect produces ions and electrons inside the vapour cell when the coupling field has a wavelength (~ 480 nm) less than the threshold wavelength of Rb metal, i.e., ~ 550 nm [115]. One way to get around this problem is to use only lasers whose wavelengths are longer than 550 nm. This is where the three-photon scheme becomes useful. Rather than using a 480 nm laser to couple $5P_{3/2}$ to Rydberg states, we can break the transition into two in which the individual transition wavelength is larger than 550 nm. A possible transition is $5S_{1/2} \rightarrow 5P_{3/2} \rightarrow 5D_{5/2} \rightarrow nP$ or nF Rydberg states. With this configuration the transition from $5P_{3/2}$ to Rydberg states can be, for example, achieved by two lasers whose wavelengths are 776 nm and 1290 nm [103, 116]. An advantage of this scheme is that one can configure the set up of the lasers such that all lasers' wavevectors cancel

each other and the system is in a Doppler-free configuration.

There have been several theoretical [117–119] and experimental [120–122] works on the three-photon transitions, most of which are with the N system¹ as this system provides many interesting results, e.g., electromagnetically induced absorption (EIA). It has been experimentally demonstrated by many groups of people that a narrow absorptive resonance can be observed in a thermal vapour cell of rubidium atoms where all lasers beams are parallel [117, 121, 122, 128]. The narrow linewidth in N system is the result of two (out of three) lasers being in a Doppler-free configuration. Contrasting with our cascade system, we do not observe a narrow absorption resonance when all lasers are in parallel as the wavevectors do not cancel each other. However, when we set up the system such that three wavevectors cancel each other, we theoretically observe a narrow EIT/EIA feature. To our knowledge, EIT with Doppler-free set up in a cascade system has not yet been seen elsewhere.

In this chapter, we present the theoretical model of three-photon transition with the effect of Doppler broadening in a cascade system. There are two laser configurations considered in this chapter — the first one is when the probe laser counter-propagates with the two coupling lasers (parallel configuration) and the latter is the Doppler-free configuration. It turns out that, for the parallel configuration with Doppler broadening, we can have three EIT resonances, although these three EIT resonances cannot be achieved in cold atoms. We also study the transmission and absorption lineshapes for the Doppler-free configuration.

¹There are three types of 4-level systems which have been discussed by various groups of people, namely, N system [117, 118, 120–122], inverted Y system [105, 123, 124], and tripod system [125–127].

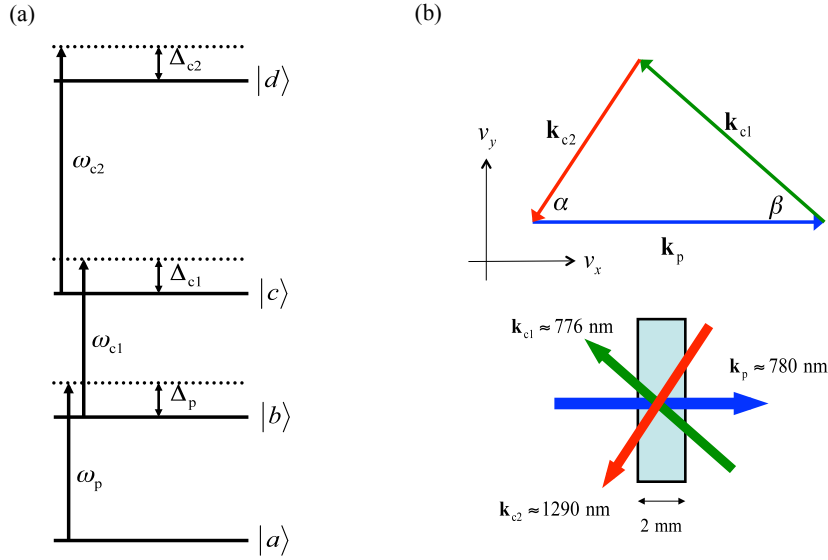


Figure 4.1: (a) A four-level system consisting of four states, $|a\rangle$, $|b\rangle$, $|c\rangle$ and $|d\rangle$ whose eigenfrequencies are $\omega_a/2\pi$, $\omega_b/2\pi$, $\omega_c/2\pi$ and $\omega_d/2\pi$ respectively. A weak probe laser whose Rabi frequency is Ω_p probes the transition between the ground and first intermediate states. The coupling lasers whose Rabi frequencies are Ω_{c_1} and Ω_{c_2} couple $|b\rangle$ and $|c\rangle$, and, $|c\rangle$ and $|d\rangle$, respectively. (b) The configuration of the three lasers is such that the first coupling laser makes an angle of β to the probe laser and the second coupling laser makes an angle of α to the probe laser. Note that the colour of the arrows do not correspond to their frequencies. The parallel configuration is when α and β are zero and the Doppler-free configuration is when the sum of the three wavevectors vanishes. The length of the cell is assumed to be 2 mm.

4.1 Theory of three-photon transition for cold atoms

We consider the ladder EIT system, composed of a ground state $|a\rangle$, a first intermediate state $|b\rangle$, a second intermediate state $|c\rangle$, and a Rydberg state $|d\rangle$, whose eigenfrequencies are $\omega_a/2\pi$, $\omega_b/2\pi$, $\omega_c/2\pi$, and $\omega_d/2\pi$, respectively. The energy level of the system is schematically shown in Figure 4.1(a). The first coupling laser whose frequency is $\omega_{c_1}/2\pi$ couples $|b\rangle$ and $|c\rangle$, and the second coupling laser whose frequency is $\omega_{c_2}/2\pi$ couples $|c\rangle$ and $|d\rangle$. The absorption property of the system is detected by scanning the probe laser, of frequency $\omega_p/2\pi$, around the resonance transition between $|a\rangle$ and $|b\rangle$. The laser detunings are defined as

$$\Delta_p = \omega_p - \omega_{ba}, \quad (4.1a)$$

$$\Delta_{c_1} = \omega_{c_1} - \omega_{cb}, \quad (4.1b)$$

$$\Delta_{c_2} = \omega_{c_2} - \omega_{dc}, \quad (4.1c)$$

where $\omega_{ij} \equiv \omega_i - \omega_j$. The Hamiltonian of the system, \mathcal{H} , after applying the rotating-wave approximation and slow-varying variables transformations, is composed of two components: the bare atom Hamiltonian (\mathcal{H}_0) and the atom-field interaction Hamiltonian (\mathcal{H}_L), namely,

$$\mathcal{H}_0 = -\hbar\Delta_p - \hbar(\Delta_p + \Delta_{c_1}) - \hbar(\Delta_p + \Delta_{c_1} + \Delta_{c_2}), \quad (4.2a)$$

$$\mathcal{H}_L = \frac{\hbar\Omega_p}{2} |a\rangle \langle b| + \frac{\hbar\Omega_{c_1}}{2} |c\rangle \langle b| + \frac{\hbar\Omega_{c_2}}{2} |d\rangle \langle c| + \text{h.c.}, \quad (4.2b)$$

where h.c. denotes the hermitian conjugate of the first three terms and $\mathcal{H} = \mathcal{H}_0 + \mathcal{H}_L$. The strengths of the couplings of the probe, first coupling and second coupling lasers are proportional to the Rabi frequencies, Ω_p , Ω_{c_1} , and Ω_{c_2} , respectively.

Using the Liouville equation [129], the equations of motion for the density

matrix ρ of the system are given by

$$\dot{\rho}_{aa} = \Gamma_b \rho_{bb} + \frac{i\Omega_p}{2} (\rho_{ab} - \rho_{ba}), \quad (4.3a)$$

$$\dot{\rho}_{bb} = -\Gamma_b \rho_{bb} + \Gamma_c \rho_{cc} + \frac{i\Omega_{c1}}{2} (\rho_{bc} - \rho_{cb}) - \frac{i\Omega_p}{2} (\rho_{ab} - \rho_{ba}), \quad (4.3b)$$

$$\dot{\rho}_{cc} = -\Gamma_c \rho_{cc} + \frac{i\Omega_{c2}}{2} (\rho_{cd} - \rho_{dc}) - \frac{i\Omega_{c1}}{2} (\rho_{bc} - \rho_{cb}), \quad (4.3c)$$

$$\dot{\rho}_{ba} = \left(i\Delta_p - \frac{\Gamma_b}{2} - \gamma_p \right) \rho_{ba} + \frac{i\Omega_p}{2} (\rho_{bb} - \rho_{aa}) - \frac{i\Omega_{c1}}{2} \rho_{ca}, \quad (4.3d)$$

$$\begin{aligned} \dot{\rho}_{ca} = & \left[i(\Delta_p + \Delta_{c1}) - \frac{\Gamma_c}{2} - \gamma_p - \gamma_{c1} \right] \rho_{ca} + \frac{i\Omega_p}{2} \rho_{cb} \\ & - \frac{i\Omega_{c1}}{2} \rho_{ba} - \frac{i\Omega_{c2}}{2} \rho_{da}, \end{aligned} \quad (4.3e)$$

$$\dot{\rho}_{da} = [i(\Delta_p + \Delta_{c1} + \Delta_{c2}) - \gamma_p - \gamma_{c1} - \gamma_{c2}] \rho_{da} + \frac{i\Omega_p}{2} \rho_{db} - \frac{i\Omega_{c2}}{2} \rho_{ca}, \quad (4.3f)$$

$$\begin{aligned} \dot{\rho}_{cb} = & \left(i\Delta_{c1} - \frac{\Gamma_b + \Gamma_c}{2} - \gamma_{c1} \right) \rho_{cb} + \frac{i\Omega_{c1}}{2} (\rho_{cc} - \rho_{bb}) \\ & + \frac{i\Omega_p}{2} \rho_{ca} - \frac{i\Omega_{c2}}{2} \rho_{db}, \end{aligned} \quad (4.3g)$$

$$\begin{aligned} \dot{\rho}_{db} = & \left[i(\Delta_{c1} + \Delta_{c2}) - \frac{\Gamma_b}{2} - \gamma_{c1} - \gamma_{c2} \right] \rho_{db} + \frac{i\Omega_p}{2} \rho_{da} \\ & + \frac{i\Omega_{c1}}{2} \rho_{dc} - \frac{i\Omega_{c2}}{2} \rho_{cb}, \end{aligned} \quad (4.3h)$$

$$\dot{\rho}_{dc} = \left(i\Delta_{c2} - \frac{\Gamma_c}{2} - \gamma_{c2} \right) \rho_{dc} + \frac{i\Omega_{c2}}{2} (\rho_{dd} - \rho_{cc}) + \frac{i\Omega_{c1}}{2} \rho_{db}, \quad (4.3i)$$

where $\rho_{aa} + \rho_{bb} + \rho_{cc} + \rho_{dd} = 1$. It is assumed, in the system, that $|b\rangle$ and $|c\rangle$ have the decay linewidths of Γ_b and Γ_c , respectively, and, γ_p , γ_{c1} and γ_{c2} are the linewidths of the probe, first coupling and second coupling lasers, respectively. The natural linewidth of the Rydberg state $|d\rangle$ is so small that it can be neglected. In the weak probe limit, where it is assumed that the population always stays in the ground state, the steady state solution ρ^s is obtained by setting $\dot{\rho} = 0$. Simple calculation shows that the coherence ρ_{ba}^s is given by

$$\begin{aligned} \rho_{ba}^s = & \frac{i\Omega_p}{2} \left[i\Delta_p - \frac{\Gamma_b}{2} - \gamma_p + \frac{\Omega_{c1}^2}{4} \left[i(\Delta_p + \Delta_{c1}) - \frac{\Gamma_c}{2} - \gamma_p - \gamma_{c1} \right. \right. \\ & \left. \left. + \frac{\Omega_{c2}^2}{4} \left[i(\Delta_p + \Delta_{c1} + \Delta_{c2}) - \gamma_p - \gamma_{c1} - \gamma_{c2} \right]^{-1} \right]^{-1}. \end{aligned} \quad (4.4)$$

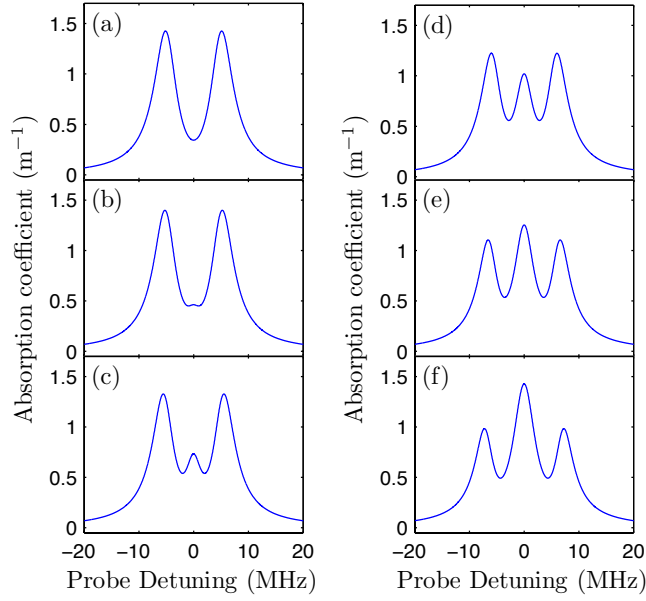


Figure 4.2: The evolution of the absorption lineshapes of cold atoms for various values of $\Omega_{c_2}/2\pi$, namely, (a) 0 MHz, (b) 2 MHz, (c) 4 MHz, (d) 6 MHz, (e) 8 MHz, (f) 10 MHz. The Rabi frequency of the first coupling laser is $\Omega_{c_1}/2\pi = 10$ MHz, all laser linewidths are 0.5 MHz, and the atomic density is $N = 1.7 \times 10^{13} \text{ m}^{-3}$. The natural linewidths $\Gamma_b/2\pi$ and $\Gamma_c/2\pi$ are 6 MHz and 1 MHz, respectively. The absorption property of the medium at zero probe detuning is enhanced when the ratio $\Omega_{c_2}/\Omega_{c_1}$ is large since $|0\rangle$ contains a large amount of $|b\rangle$ according to Equation (4.7b). (b) to (f) show that there exists only two EIT resonances or three absorption resonances in the spectrum obtained from cold atoms.

The complex susceptibility is related to ρ_{ba}^s via

$$\chi = -\frac{2Nd_{ba}^2}{\hbar\epsilon_0\Omega_p}\rho_{ba}^s, \quad (4.5)$$

where N is the atomic density and d_{ba} is the dipole matrix element between $|b\rangle$ and $|a\rangle$. Note that Equation (4.4) is independent of the wavevectors; and hence, the lineshape of the complex susceptibility is independent of the lasers' configuration.

Figure 4.2 shows the evolution of the absorption lineshape in cold atoms

with increasing in Ω_{c_2} . In the figure, it is assumed that $\Omega_{c_1}/2\pi = 10$ MHz and $\gamma_p/2\pi = \gamma_{c_1}/2\pi = \gamma_{c_2}/2\pi = 0.5$ MHz. The atomic density is $N = 1.7 \times 10^{13} \text{ m}^{-3}$. The natural linewidths of $|b\rangle$ and $|c\rangle$ are assumed to be those for $5P_{3/2}$ and $5D_{5/2}$, respectively, i.e., $\Gamma_b/2\pi = 6$ MHz and $\Gamma_c/2\pi = 1$ MHz [130, 131]. The first and second coupling lasers are tuned such that they both are on-resonance with $|b\rangle$ and $|c\rangle$, and, $|c\rangle$ and $|d\rangle$, respectively. It is obvious from the figure that the effect of the second coupling laser is to split a single EIT resonance (obtained from two-photon transition) into two EIT resonances or to add an absorption resonance at the zero probe detuning. Increasing the value of Ω_{c_2} results in a large absorption resonance at zero probe detuning. To understand the evolution of the lineshapes, we look into the dressed states formed from $|b\rangle$, $|c\rangle$ and $|d\rangle$. When both coupling lasers are on resonance, the eigenenergies are

$$E_+ = \frac{\hbar}{2} \sqrt{\Omega_{c_1}^2 + \Omega_{c_2}^2}, \quad (4.6a)$$

$$E_0 = 0, \quad (4.6b)$$

$$E_- = -\frac{\hbar}{2} \sqrt{\Omega_{c_1}^2 + \Omega_{c_2}^2}, \quad (4.6c)$$

with their associated eigenvectors,

$$|+\rangle = \frac{1}{\sqrt{2}} \frac{\Omega_{c_1}}{\sqrt{\Omega_{c_1}^2 + \Omega_{c_2}^2}} |b\rangle + \frac{1}{\sqrt{2}} |c\rangle + \frac{1}{\sqrt{2}} \frac{\Omega_{c_2}}{\sqrt{\Omega_{c_1}^2 + \Omega_{c_2}^2}} |d\rangle, \quad (4.7a)$$

$$|0\rangle = \frac{\Omega_{c_2}}{\sqrt{\Omega_{c_1}^2 + \Omega_{c_2}^2}} |b\rangle - \frac{\Omega_{c_1}}{\sqrt{\Omega_{c_1}^2 + \Omega_{c_2}^2}} |d\rangle, \quad (4.7b)$$

$$|-\rangle = \frac{1}{\sqrt{2}} \frac{\Omega_{c_1}}{\sqrt{\Omega_{c_1}^2 + \Omega_{c_2}^2}} |b\rangle - \frac{1}{\sqrt{2}} |c\rangle + \frac{1}{\sqrt{2}} \frac{\Omega_{c_2}}{\sqrt{\Omega_{c_1}^2 + \Omega_{c_2}^2}} |d\rangle. \quad (4.7c)$$

The resonances in absorption correspond to the interactions between $|a\rangle$ with one of the three dressed states; hence, it predicts three absorption resonances (and two EIT resonances). The absorption resonance in the middle gradually increases when the ratio $\Omega_{c_2}/\Omega_{c_1}$ increases. This is because the dipole matrix element $\langle a | \mathbf{e} \mathbf{r} | 0 \rangle$ is proportional to $\Omega_{c_2}/\sqrt{\Omega_{c_1}^2 + \Omega_{c_2}^2}$ according to Equation (4.7b). The splitting in energy between the left and the right absorption

resonances is given by $E_+ - E_- = \hbar\sqrt{\Omega_{c_1}^2 + \Omega_{c_2}^2}$, which is consistent with the results shown in Figure 4.2.

4.2 Theory of three-photon transition with Doppler broadening

In contrast to the case of cold atoms, Equation (4.4) must be corrected for the Doppler effect in the case of thermal atoms. This can be done by the transformations:

$$\Delta_p \rightarrow \Delta_p - \mathbf{k}_p \cdot \mathbf{v}, \quad (4.8a)$$

$$\Delta_{c_1} \rightarrow \Delta_{c_1} - \mathbf{k}_{c_1} \cdot \mathbf{v}, \quad (4.8b)$$

$$\Delta_{c_2} \rightarrow \Delta_{c_2} - \mathbf{k}_{c_2} \cdot \mathbf{v}, \quad (4.8c)$$

where \mathbf{k}_p , \mathbf{k}_{c_1} and \mathbf{k}_{c_2} are the wavevectors of the probe, first coupling and second coupling lasers, respectively, and \mathbf{v} is the atomic velocity. The distribution of the atoms is given by the three-dimensional Maxwell-Boltzmann distribution,

$$N \rightarrow \frac{N_0}{u^3 \pi^{3/2}} \exp\left(-\frac{v_x^2}{u^2}\right) \exp\left(-\frac{v_y^2}{u^2}\right) \exp\left(-\frac{v_z^2}{u^2}\right), \quad (4.9)$$

where $u = \sqrt{2k_B T/m}$ is the most probable speed of the atom and N_0 is the total atomic density of the system. Since the Doppler effect is independent of v_z , we can integrate over Equation (4.9) with respect to v_z and we have,

$$N \rightarrow \frac{N_0}{u^2 \pi} \exp\left(-\frac{v_x^2}{u^2}\right) \exp\left(-\frac{v_y^2}{u^2}\right). \quad (4.10)$$

With the transformations given by Equation (4.8) and Equation (4.10), the susceptibility of the system becomes,

$$\chi(v_x, v_y) dv_x dv_y = \frac{id_{ba}^2 N_0}{\epsilon_0 \hbar \pi u^2} \times \exp\left(-\frac{v_x^2}{u^2}\right) \exp\left(-\frac{v_y^2}{u^2}\right) dv_x dv_y \times \left[A + ik_p v_x + \frac{\Omega_{c_1}^2}{4} \left[B + i(\Delta k_1) v_x + \frac{\Omega_{c_2}^2}{4} [C + i(\Delta k_2) v_x]^{-1} \right]^{-1} \right]^{-1}, \quad (4.11)$$

with

$$A = \frac{\Gamma_b}{2} + \gamma_p - i\Delta_p, \quad (4.12a)$$

$$B = \frac{\Gamma_c}{2} + \gamma_p + \gamma_{c_1} - i(\Delta_p + \Delta_{c_1}) + ik_{c_1}v_y \sin \beta, \quad (4.12b)$$

$$C = \gamma_p + \gamma_{c_1} + \gamma_{c_2} - i(\Delta_p + \Delta_{c_1} + \Delta_{c_2}) \\ + i(k_{c_1} \sin \beta - k_{c_2} \sin \alpha)v_y, \quad (4.12c)$$

$$\Delta k_1 = k_p - k_{c_1} \cos \beta, \quad (4.12d)$$

$$\Delta k_2 = k_p - k_{c_1} \cos \beta - k_{c_2} \cos \alpha. \quad (4.12e)$$

The angles β and α are defined as shown in Figure 4.1(a). It is possible to analytically integrate Equation (4.11) over v_x ; however, the subsequent analytical integration over v_y is not possible and numerical integration must be used to this end.

To evaluate the integral over v_x , first, we use the substitution $z = v_x/u$ and rearrange Equation (4.11) as

$$\chi(v_x, v_y)dv_x dv_y = \frac{d_{ba}^2 N_0}{\epsilon_0 \hbar \pi u^2 k_p} \left(\frac{z^2 + pz + q}{z^3 + \lambda z^2 + \mu z + \theta} \right) e^{-z^2} e^{-v_y^2/u^2} dz dv_y, \quad (4.13)$$

with

$$p = -\frac{i}{u} \left(\frac{B}{\Delta k_1} + \frac{C}{\Delta k_2} \right), \quad (4.14a)$$

$$q = -\frac{1}{u^2} \left(\frac{4BC + \Omega_{c_2}^2}{4\Delta k_1 \Delta k_2} \right), \quad (4.14b)$$

$$\lambda = -\frac{i}{u} \left(\frac{A}{k_p} + \frac{B}{\Delta k_1} + \frac{C}{\Delta k_2} \right), \quad (4.14c)$$

$$\mu = -\frac{1}{u^2} \left(\frac{AB}{k_p \Delta k_1} + \frac{AC}{k_p \Delta k_2} + \frac{BC}{\Delta k_1 \Delta k_2} + \frac{\Omega_{c_2}^2}{4\Delta k_1 \Delta k_2} + \frac{\Omega_{c_1}^2}{4k_p \Delta k_1} \right), \quad (4.14d)$$

$$\theta = \frac{i}{u^3} \left(\frac{4ABC + A\Omega_{c_2}^2 + C\Omega_{c_1}^2}{4k_p \Delta k_1 \Delta k_2} \right). \quad (4.14e)$$

The denominator of Equation (4.13) has three roots [132], i.e., z_1 , z_2 and z_3 ,

where

$$z_1 = \frac{1}{6}(-2\lambda + U + V), \quad (4.15a)$$

$$z_2 = \frac{1}{12}[-4\lambda - (1 + \sqrt{3}i)U - (1 - \sqrt{3}i)V], \quad (4.15b)$$

$$z_3 = \frac{1}{12}[-4\lambda - (1 - \sqrt{3}i)U - (1 + \sqrt{3}i)V], \quad (4.15c)$$

$$U = \sqrt[3]{4}(-27\theta - 2\lambda^3 + 9\lambda\mu + 3\sqrt{81\theta^2 + 120\lambda^3 - 540\lambda\mu - 3\lambda^2\mu^2 + 12\mu^3})^{1/3}, \quad (4.15d)$$

$$V = \frac{4(\lambda^2 - 3\mu)}{U}. \quad (4.15e)$$

Thus the integrand $(z^2 + pz + q)/(z^3 + \lambda z^2 + \mu z + \theta)$ can be re-written, using the partial fraction method, as

$$\begin{aligned} \frac{z^2 + pz + q}{z^3 + \lambda z^2 + \mu z + \theta} &= \frac{q + pz_1 + z_1^2}{(z_1 - z_2)(z_1 - z_3)} \frac{1}{z - z_1} \\ &+ \frac{q + pz_2 + z_2^2}{(z_2 - z_1)(z_2 - z_3)} \frac{1}{z - z_2} + \frac{q + pz_3 + z_3^2}{(z_3 - z_1)(z_3 - z_2)} \frac{1}{z - z_3}. \end{aligned} \quad (4.16)$$

Substituting Equation (4.16) back into Equation (4.11) and evaluating the integration over z [84], we have

$$\begin{aligned} \chi(v_y)dv_y &= - \left(\frac{id_{ba}^2 N_0}{\epsilon_0 \hbar k_p u^2} \right) \left[\frac{q + pz_1 + z_1^2}{(z_1 - z_2)(z_1 - z_3)} s_1 e^{-z_1^2} \operatorname{erfc}(is_1 z_1) \right. \\ &+ \frac{q + pz_2 + z_2^2}{(z_2 - z_1)(z_2 - z_3)} s_2 e^{-z_2^2} \operatorname{erfc}(is_2 z_2) \\ &\left. + \frac{q + pz_3 + z_3^2}{(z_3 - z_1)(z_3 - z_2)} s_3 e^{-z_3^2} \operatorname{erfc}(is_3 z_3) \right] e^{-v_y^2/u^2} dv_y, \end{aligned} \quad (4.17)$$

where $s_{1(2,3)} = -\operatorname{sgn}[\operatorname{Im}(z_{1(2,3)})]$ and $\operatorname{erfc}(z)$ is the complementary error function [133]. The susceptibility of the system is obtained by numerically integrating Equation (4.17) over v_y .

The results simplify into two special cases, which we now consider, namely, the case where all lasers are parallel to one another and the Doppler-free configuration.

Case 1. All three lasers are parallel to one another, i.e., $\alpha, \beta = \{0, \pm\pi\}$.

In this case the system effectively reduces to one dimension and the analytical

integration of Equation (4.17) over v_y is now possible. Using the standard Gaussian integral, namely,

$$\int_{-\infty}^{\infty} \exp\left(-\frac{v_y^2}{u^2}\right) dv_y = u\sqrt{\pi}, \quad (4.18)$$

the total susceptibility of the system is given by

$$\begin{aligned} \chi = - \left(\frac{id_{ba}^2 N_0 \sqrt{\pi}}{\epsilon_0 \hbar k_p u} \right) & \left[\frac{q + pz_1 + z_1^2}{(z_1 - z_2)(z_1 - z_3)} s_1 e^{-z_1^2} \operatorname{erfc}(is_1 z_1) + \right. \\ & \left. \frac{q + pz_2 + z_2^2}{(z_2 - z_1)(z_2 - z_3)} s_2 e^{-z_2^2} \operatorname{erfc}(is_2 z_2) + \frac{q + pz_3 + z_3^2}{(z_3 - z_1)(z_3 - z_2)} s_3 e^{-z_3^2} \operatorname{erfc}(is_3 z_3) \right]. \end{aligned} \quad (4.19)$$

When both α and β are zero, we refer to this configuration as the parallel configuration.

Case 2. Doppler-free configuration, i.e., $\mathbf{k}_p + \mathbf{k}_{c_1} + \mathbf{k}_{c_2} = 0$.

When the sum of the wavevectors vanishes, one of the poles of the integrand in Equation (4.11) disappears. Equation (4.17) reduces to,

$$\begin{aligned} \chi(v_y) dv_y = - \left(\frac{iN_0 d_{ba}^2}{2\hbar\epsilon_0 u^2 k_p} \right) & \left\{ (1+d)e^{-z_1^2} s_1 [1 - s_1 \operatorname{erf}(iz_1)] \right. \\ & \left. + (1-d)e^{-z_2^2} s_2 [1 - s_2 \operatorname{erf}(iz_2)] \right\} e^{-v^2/u^2} dv_y, \end{aligned} \quad (4.20)$$

with

$$z_{1,2} = \frac{i}{2} \left(\frac{A}{uk_p} + \frac{B}{u\Delta k} \right) \pm \frac{i}{2} \sqrt{\left(\frac{A}{uk_p} - \frac{B}{u\Delta k} \right)^2 - \frac{\Omega_{c_1}^2}{u^2 k_p \Delta k}}, \quad (4.21a)$$

$$\Delta k = k_p - k_{c_1} \cos \beta, \quad (4.21b)$$

$$A = \frac{\Gamma_b}{2} + \gamma_p - i\Delta_p, \quad (4.21c)$$

$$\begin{aligned} B = \frac{\Gamma_c}{2} + \gamma_p + \gamma_{c_1} - i(\Delta_p + \Delta_{c_1}) + ik_{c_1} v_y \sin \beta \\ + \frac{\Omega_{c_2}^2/4}{\gamma_p + \gamma_{c_1} + \gamma_{c_2} - i(\Delta_p + \Delta_{c_1} + \Delta_{c_2})}, \end{aligned} \quad (4.21d)$$

$$d = \frac{i}{z_1 - z_2} \left(\frac{A}{uk_p} - \frac{B}{u\Delta k} \right), \quad (4.21e)$$

and $s_{1,2}$ are as previously defined.

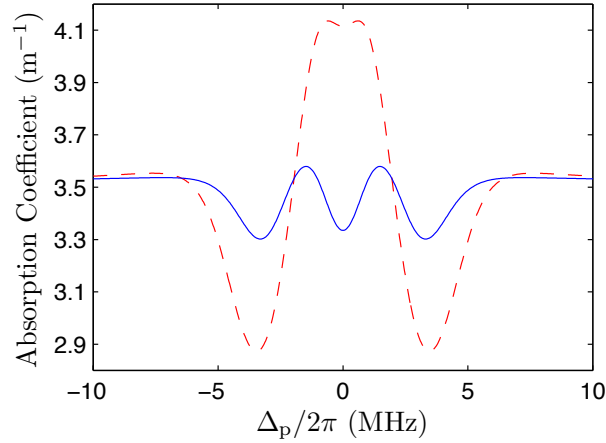


Figure 4.3: The absorption lineshape for thermal atoms with two different values of $\Omega_{c_2}/2\pi$, namely, 2 MHz (solid blue line) and 4 MHz (red dashed line). The probe laser is counter-propagating with the other two coupling lasers and the other parameters are the same as those used in Figure 4.2. The temperature of the cell is 17 °C. In contrast to the lineshape obtained for cold atoms, for a small value of $\Omega_{c_2}/\Omega_{c_1}$, the lineshape for thermal atoms exhibits three EIT resonances. However, for a large value of $\Omega_{c_2}/\Omega_{c_1}$, we recover the absorption lineshape with two EIT resonances as the middle EIT resonance (at zero probe detuning) switches to an absorption resonance in which the medium becomes significantly more absorptive with respect to the background absorption.

In the subsequent sections, the absorption (and transmission) properties of the system will be investigated using Equation (4.19) and Equation (4.20) as our main equations.

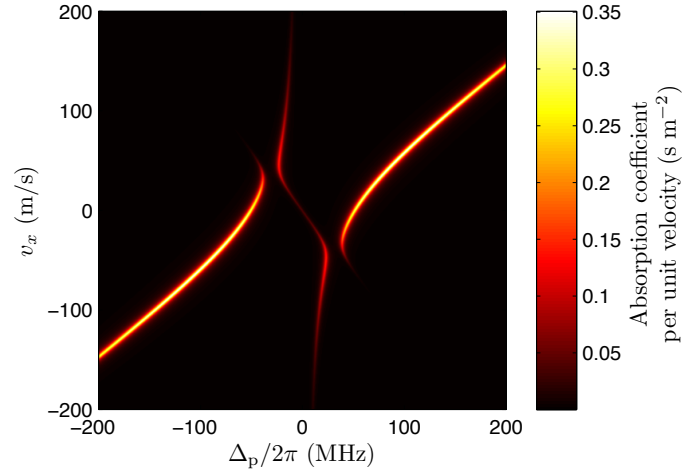


Figure 4.4: Image plot of the absorption coefficient before velocity average, $k_p \text{Im}[\chi(v_x, \Delta_p)]$, against v_x and Δ_p . For reasons of clarity, the values of $\Omega_{c_1}/2\pi$ and $\Omega_{c_2}/2\pi$ are 100 MHz and 20 MHz, respectively, in which the ratio $\Omega_{c_2}/\Omega_{c_1}$ is maintained at 0.2 as used for the solid blue line in Figure 4.3. All the other parameters are kept the same as those used in Figure 4.3. The small absorption resonance at zero probe detuning before the velocity average (corresponding to the dark line in the middle of the plot) results in a small total absorption coefficient after integrating over velocity. This leads to transparency in the middle of the absorption profile.

4.3 EIT lineshape for the parallel configuration

In contrast to the presence of two EIT resonances in cold atoms, the EIT lineshape observed in thermal atoms can have either two or three EIT resonances for the parallel configuration, depending on the strength of the second coupling laser compared to the first coupling lasers as illustrated in Figure 4.3. The middle EIT resonance is sensitive to the ratio $\Omega_{c_2}/\Omega_{c_1}$. Namely, this resonance switches to an absorption resonance when $\Omega_{c_2}/\Omega_{c_1}$ increases, and the medium becomes significantly more absorptive with respect to the back-

ground absorption. The presence of the middle EIT feature can be understood by studying the image plot of the absorption coefficient before average over velocity, $k_p \text{Im}[\chi(v_x, \Delta_p)]$ (Figure 4.4). Let us consider the overlap integral $\langle a | e \mathbf{r} | 0 \rangle$, which is proportional to $\Omega_{c_2} / \sqrt{\Omega_{c_2}^2 + \Omega_{c_1}^2}$ as $|a\rangle$ only couples to $|b\rangle$. For the case where $\Omega_{c_2} / \Omega_{c_1}$ is small, the overlap integral is negligible. This results in a small absorption resonance at zero probe detuning. This is seen in the figure as a dark line with negative gradient in the middle of the plot. Thus when integrating the absorption coefficient over all velocities, the total absorption coefficient becomes small, which leads to the transparency window at $\Delta_p / 2\pi = 0$ MHz. However, when the ratio $\Omega_{c_2} / \Omega_{c_1}$ increases, the overlap integral $\langle a | e \mathbf{r} | 0 \rangle$, as well as the middle absorption resonance, becomes large. Thus after averaging over all velocities, the value of the total absorption is now significant. Note that the transparency in the middle is not due to the formation of a dark state; it is due to the relatively small absorption resonance at the middle before the velocity average.

It should be emphasised here that the absorption lineshape for cold atoms always exhibits two EIT resonances since there are three dressed states in which $|a\rangle$ can be interact with. However, the lineshape for thermal atoms shows more interesting physics, namely, it can contain either two or three EIT resonances, depending on the ratio $\Omega_{c_2} / \Omega_{c_1}$. Note that the extra EIT resonance does not corresponding to a dark state formation, but it is due to the weak interaction of Ω_{c_2} at zero probe detuning.

4.4 EIT lineshape for Doppler free configuration

In contrast to the parallel configuration in which the absorption lineshape does not exhibit a narrow resonance, this (narrow resonance) feature is observed in the Doppler-free configuration in thermal atoms.

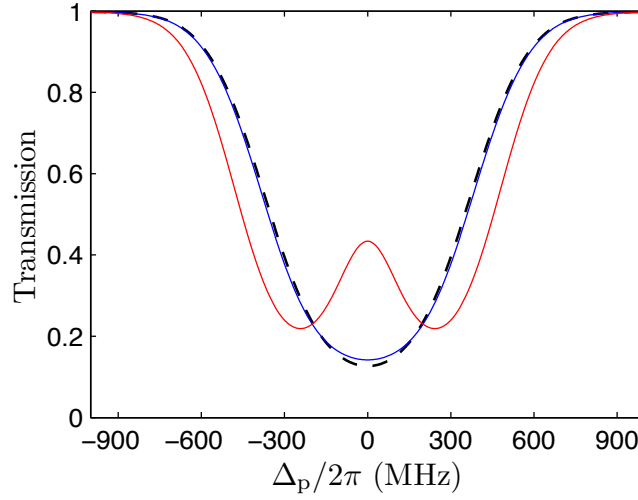


Figure 4.5: The effect of Doppler broadening of the transmission lineshape for thermal atoms when there is no second coupling laser. The temperature is now 80 °C as we would like to increase the optical depth of the transmission profile and the angle β is $\sim 35^\circ$. All linewidths are kept the same as those used in Figure 4.2. The reference profile (black dashed line) is for $\Omega_{c_1}/2\pi = 0$ MHz. Even at $\Omega_{c_1}/2\pi = 100$ MHz (blue solid line), the transmission profile does not show an EIT resonance as this feature is suppressed by the positive residual wavevector. For a very large value of Ω_{c_1} , for example, $\Omega_{c_1}/2\pi = 400$ MHz (red solid line), a broadened EIT resonance is observed at zero probe detuning.

To understand the absorption (and transmission) for the Doppler-free configuration, we first study the lineshape for the case in which the second coupling is turned off. This is a two-photon transition where the first coupling laser makes an angle of β with respect to the probe laser. Then we move on to the Doppler free configuration where all wavevectors cancel each other.

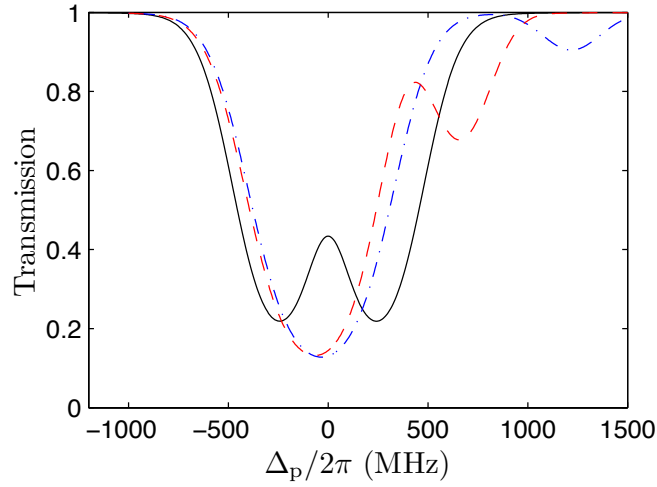


Figure 4.6: The effect of a finite Δ_{c_1} on the transmission lineshape of the thermal atoms. The value of $\Omega_{c_1}/2\pi$ is 400 MHz and the other parameters are those used in Figure 4.5. One of the absorption resonance can be moved towards the either positive or negative value of Δ_p by changing Δ_{c_1} . The black solid line, red dashed line and blue dot-dashed line correspond to $\Delta_{c_1}/2\pi$ of 0 MHz, -600 MHz and -1200 MHz, respectively.

4.4.1 Effect of residual wavevectors in two-photon transition

In this situation, the EIT resonance due to the two-photon transition ($|a\rangle \rightarrow |b\rangle \rightarrow |c\rangle$) is suppressed by the effect of Doppler broadening since the residual wavevector $k_p - k_{c_1} \cos\beta$ is now positive and in the direction of probe laser. To recover the transparency to the system we need to work with a large coupling Ω_{c_1} ; however, the EIT resonance is broadened due to power broadening as illustrated in Figure 4.5. In the figure, the temperature is raised to 80°C in order to increase the optical depth of the transmission profiles. All linewidths are kept the same as those used in the previous section and $\Delta_{c_1}/2\pi = 0$ MHz. Even at $\Omega_{c_1}/2\pi = 100$ MHz (blue solid line), there is no evidence for an EIT resonance as the feature is destroyed by the positive residual wavevector. The effect of the Doppler broadening, in this

case, is to cause a small distortion of the transmission profile as compared with the reference profile where $\Omega_{c1}/2\pi = 0$ MHz (black dashed line). When $\Omega_{c1}/2\pi = 400$ MHz (red solid line), an EIT resonance is observed at zero probe frequency; however, this resonance is broadened with a full-width at half maximum of ~ 250 MHz as shown in Figure 4.6. We can also detune Δ_{c1} such that one of the absorption resonance moves to an either side of the transmission dip, depending on the sign of Δ_{c1} , as shown in Figure 4.6. The black solid line, red dashed line and blue dot-dashed line correspond to $\Delta_{c1}/2\pi$ of 0 MHz, -600 MHz and -1200 MHz, respectively.

To understand why a positive residual wavevector leads to the suppression of the EIT resonance, we consider the three-level system with counter-propagating lasers configuration. Assuming that the probe laser has the wavelength of 780 nm and the coupling laser has the wavelength of 900 nm, the image plot of the absorption coefficient before velocity average, $k_p \text{Im}[\chi(v_x, \Delta_p)]$, against v_x and Δ_p is shown in Figure 4.7. Following the argument given in Chapter 3, the bright line across the diagonal of the plot corresponds to the values of v_x and Δ_p for which the probe laser is on resonance with the transition $|a\rangle \rightarrow |b\rangle$, namely, $\Delta_p - 2\pi v_x/(780 \text{ nm}) = 0$. The asymptotic line which cuts through the bright line corresponds to the two-photon resonance, namely, $\Delta_p - 2\pi v_x/(780 \text{ nm}) + 2\pi v_x/(900 \text{ nm}) = 0$. Note that the bright lines shown in the figure are the loci of the resonances between the ground state and the dressed states $|+\rangle$ and $|-\rangle$ (see Chapter 2), i.e.,

$$\Delta_p = k_p v_x - \frac{1}{2} k_c v_x \pm \frac{1}{2} \sqrt{k_c^2 v_x^2 + \Omega_{c1}^2}. \quad (4.22)$$

The asymptotic forms equations of Equation (4.22) for large value of v_x are $\Delta_p = k_p v_x$ and $\Delta_p = (k_p - k_c) v_x$ as expected. For the wavelengths used in the plot, the asymptotic line has a positive gradient (resulting in a positive residual wavevector) as shown in the figure. This causes two maxima of absorption as a function of v_x . After integrating the integrand over velocity, the two resonances lead to the suppression of the EIT resonance in the to-

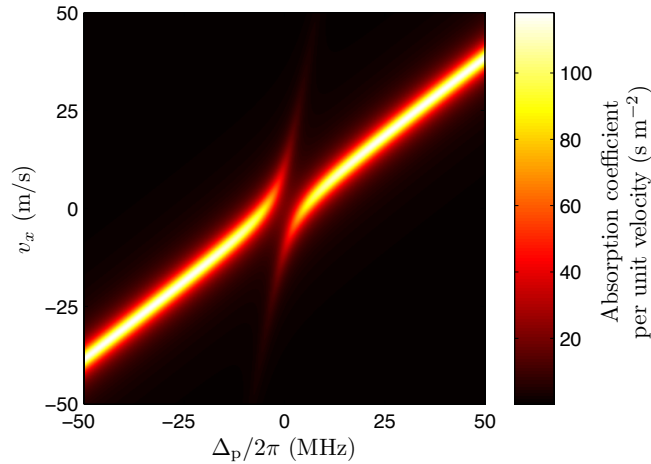


Figure 4.7: Image plot of the absorption coefficient before velocity average, $k_p \text{Im}[\chi(v_x, \Delta_p)]$, as a function of v_x and Δ_p for a coupling wavelength of 900 nm. All parameters are the same as those used in Figure 4.5, except that $\Omega_{c_1}/2\pi = 10$ MHz. For this coupling wavelength, the residual wavevector is positive. This results in the positive gradient of the asymptotic line which cuts through the thick bright line. At zero probe detuning, there exists absorption resonances for two different velocity classes, which, after integrating the integrand over velocity, it leads to the suppression of the EIT resonance.

tal transmission lineshape. However, when the wavelength of the coupling laser is 480 nm, the residual wavevector becomes negative. The asymptotic line then has a negative gradient and $k_p \text{Im}[\chi(v_x, \Delta_p)]$ has no peak as a function of v_x , as shown in Figure 4.8. Thus after summing the integrand for all velocities, the total transmission lineshape shows an EIT resonance at $\Delta_p/2\pi = 0$ MHz.

4.4.2 EIT and EIA with Doppler free configuration

We now turn on the second coupling laser, which leads to a Doppler-free configuration. The effect of the second coupling laser is to create a sharp and

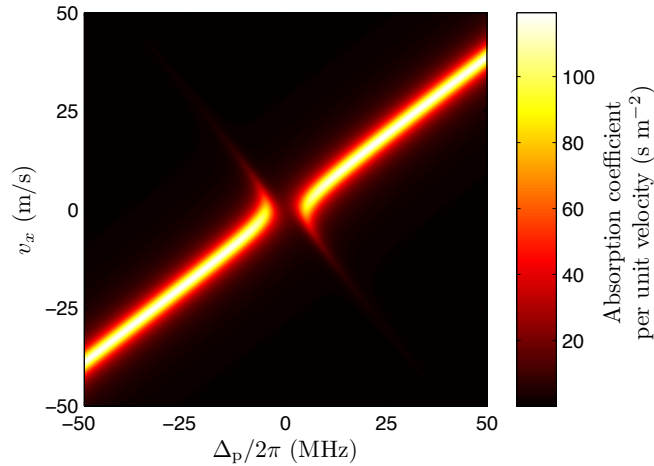


Figure 4.8: Image plot of the absorption coefficient before velocity average, $k_p \text{Im}[\chi(v_x, \Delta_p)]$, as a function of v_x and Δ_p for a coupling wavelength of 480 nm. All parameters are the same as those used in Figure 4.5, except that $\Omega_{c_1}/2\pi = 10$ MHz. For this coupling wavelength, the residual wavevector is negative. This results in the negative gradient of the asymptotic line which cuts through the thick bright line. At zero probe detuning, there exists no absorption resonances, which, after integrating the integrand over velocity, it leads to an EIT resonance.

narrow EIT or EIA (Electromagnetically induced absorption²) resonances, depending on where we tune Δ_{c_1} . To obtain a sharp EIA feature, we set $\Delta_{c_1} = \Delta_{c_2} = 0$ MHz. The EIA feature is observed at the zero probe detuning (where the peak of the EIT resonance is) with a linewidth less than the natural linewidth of $|b\rangle$, i.e., $\gamma_{\text{EIA}} < \Gamma_b$. The strength of the EIA resonance and its FWHM increases with Ω_{c_2} as illustrated in Figure 4.9. In the figure, the black solid line, red dot-dashed line and blue dashed line represent Ω_{c_2} of 10 MHz, 30 MHz and 50 MHz, respectively. It is worth noting the similarity of the sharp EIA resonance obtained in our calculation with the previous work done by many groups with N system [117, 121, 122, 128]. In their set up, three wavevectors do not cancel with one another as in our set up. Only

²The details of EIA can be found in the literature, for example, [118, 128, 134–136].

the probe and the first coupling laser in their set up leads to the Doppler free. The physical origin of this EIA resonance is from the fact that the transition is enhanced as the three lasers are simultaneously on resonance, i.e., $\Delta_p = \Delta_{c_1} = \Delta_{c_2} = 0$ MHz [117].

When we detune Δ_{c_1} to a finite value and $\Delta_{c_2} = 0$ MHz, the system can now be viewed as a two-photon transition in which the first transition is a combination between the probe photon and the first coupling photon. Thus the system is effectively a three-level system, consisting of $|a\rangle$, $|c\rangle$ and $|d\rangle$. For such system, an EIT resonance is created at the centre of the small transmission dip where $\Delta_p = -\Delta_{c_1}$ (see Figure 4.6), as shown in Figure 4.10, and the strength of the EIT resonance and the linewidth, again, increases with Ω_{c_2} [117]. Note that even though all three transitions are not simultaneously on resonance, the sum of all detunings is still zero. In Figure 4.10, an EIT resonance occurs at around $\Delta_p/2\pi = 1200$ MHz as $\Delta_{c_1}/2\pi = -1200$ MHz, and the sum of the three detunings are zero. The black solid line, red dot-dashed line and blue dashed line represent $\Omega_{c_2} = 10$ MHz, 30 MHz and 50 MHz, respectively.

In both cases the width of EIA/EIT is less than the natural linewidth of $|b\rangle$, i.e., $\gamma_{\text{EIA/EIT}} < \Gamma_b$ for small Ω_{c_2} . This is because, at the three-photon Raman resonance ($\Delta_p + \Delta_{c_1} + \Delta_{c_2} = 0$), the system is free from Doppler effect [128].

4.5 Summary and conclusions

In conclusion, we have studied the system of three-photon transition with the effect of Doppler broadening. The advantage of the three-photon scheme is to prevent the creation of electric charges inside the vapour cell due to the photoelectric effect. To this end, the 480 nm laser considered in Chapter 3 was replaced by two lasers whose wavelengths are 776 nm and 1290 nm.

It was demonstrated that for the case of parallel configuration in which the

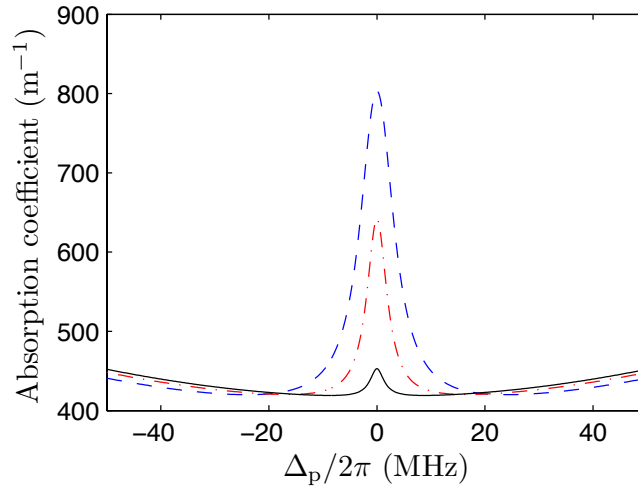


Figure 4.9: The absorption coefficient against probe detuning for various Ω_{c_2} . The second coupling detuning, $\Delta_{c_1}/2\pi$, is zero and all the other parameters are the same as those used in Figure 4.6. The black solid line, red dot-dashed line and blue dashed line represent $\Omega_{c_2} = 10$ MHz, 30 MHz and 50 MHz, respectively. The strength of the EIA resonance and its FWHM increase with Ω_{c_2} . The EIA resonance is the result of the enhanced transition of the simultaneous resonance.

probe laser counter-propagates with respect to the two coupling lasers, the transmission lineshape of the thermal atom could exhibit an extra EIT resonance at zero probe detuning when $\Omega_{c_2}/\Omega_{c_1}$ is small. This extra EIT resonance is not observed in the transmission lineshape for cold atoms. For a large value of $\Omega_{c_2}/\Omega_{c_1}$, the EIT resonance at zero probe detuning disappears and the absorption coefficient of the system significantly increases. It turns out that the existence of the middle EIT resonance is due to the incomplete destruction of the EIT resonance, which manifests when averaging the absorption coefficient over all velocity classes.

In the Doppler-free configuration, one needs to work at a very high Ω_{c_1} as, in the step of the first two-photon transition, a positive residual wavevector suppresses the EIT resonance. An EIA resonance can be created when both

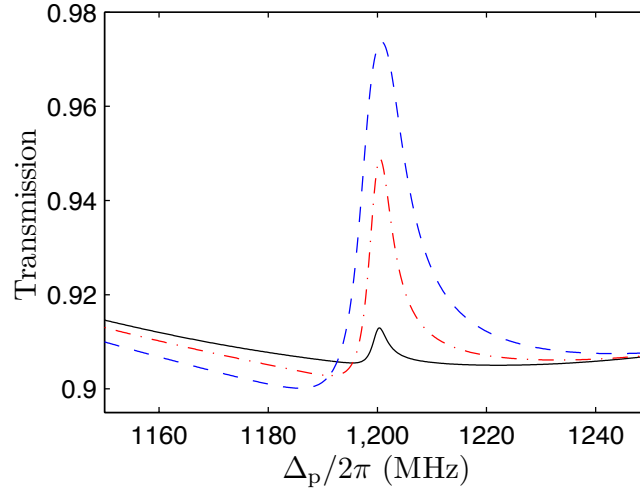


Figure 4.10: The transmission lineshape as a function of probe detuning for various Ω_{c_2} . The first coupling detuning, $\Delta_{c_1}/2\pi$, is -1200 MHz and all the other parameters are the same as those used in Figure 4.6. The black solid line, red dot-dashed line and blue dashed line represent $\Omega_{c_2} = 10$ MHz, 30 MHz and 50 MHz, respectively. The strength of the EIT resonance and its FWHM increases with Ω_{c_2} .

Δ_{c_1} and Δ_{c_2} are zero. This physically corresponds to the enhanced three-photon transition as the three lasers are simultaneously on resonance. If one detunes the first coupling laser by a finite amount, the system is now effectively a three-level system, consisting of $|a\rangle$, $|c\rangle$ and $|d\rangle$. This results in a displacement of one of the transmission dip to either side of the lineshape, depending on the sign of Δ_{c_1} , and a creation of an EIT feature at the centre of the dip.

Chapter 5

Enhanced electric field sensitivity of rf-dressed Rydberg dark states

In this chapter, we demonstrate the formation of Rydberg dark states dressed by a radio frequency (rf) field. Microwave or rf dressing of Rydberg states has previously been observed using laser excitation and field ionisation of an atomic beam [47, 50, 53] or of cold atoms [51]. Here, however, the resulting Floquet states are observed as EIT resonances in the absorption spectrum of the probe laser beam in a vapour cell. We show that these rf-dressed dark states have an enhanced sensitivity to dc electric fields. We also show that the strength of the dc electric field is encoded not only in the overall shift of the corresponding EIT feature but also in the shape of the transparency window. As a consequence, and as has been illustrated by an actual measurement [92], rf dressing may help determine the dc field without absolute knowledge of the laser frequency. In addition, we show how the lineshape of the dark state resonance provides information about the electric field inhomogeneity within the interaction region.

5.1 Theoretical framework

We focus on EIT in the ladder system in which a weak probe laser (wavelength 780 nm) is scanned through resonance with the transitions from the ground $5S_{1/2}, F = 2$ state to the $5P_{3/2}, F' = (2, 3)$ states of ^{87}Rb , and a coupling laser (wavelength 480 nm) resonant with the $5P_{3/2}, F' = 3$ to the $32S_{1/2}, F'' = 2$ transition. Such a ladder system is ideal as the two components of the dark state have a large differential shift in an external field and there is no additional splitting of the $J = 1/2$ Rydberg state.

In addition to the laser fields, the system is exposed to both dc and ac electric fields which mainly perturb the Rydberg state, $32S_{1/2}$, due to the large polarisability [137]. The experiment shows that not only does the effect of the dc and ac electric fields shift the energy level of $32S_{1/2}$ state, but also creates sideband resonances in the EIT transmission spectrum. The existence of the sidebands can be understood in the context of phase modulation of Rydberg state by the weak field, which is the main discussion of this section. We also describe the model of EIT with Doppler effect for such rf-dressed Rydberg system.

5.1.1 Phase modulation by a weak field

Consider the atoms which are exposed to the joint action of a static field of strength \mathcal{E}_{dc} and of a parallel oscillating electric field of amplitude \mathcal{E}_{ac} . At any point in the cell, the local applied electric field can be written as

$$\mathcal{E}(t) = \mathcal{E}_{\text{dc}} + \mathcal{E}_{\text{ac}} \sin \omega_{\text{m}} t . \quad (5.1)$$

In the experiment, $\omega_{\text{m}}/2\pi$ ranges from 10 to 30 MHz, which is much less than the relevant optical transition frequencies. Ignoring the laser fields and decoherence for the time being, we can work within the adiabatic approximation and describe each of the hyperfine components of the $32S_{1/2}$ state by

a time-dependent state vector of the form [43, 138]

$$|\Psi(t)\rangle = \exp\left(-\frac{i}{\hbar} \int^t E[\mathcal{E}(t')] dt'\right) |\psi[\mathcal{E}(t)]\rangle . \quad (5.2)$$

In this expression, $|\psi(\mathcal{E})\rangle$ is the Stark state that develops from the field-free state when a static field is adiabatically turned on from 0 to \mathcal{E} , and $E(\mathcal{E})$ is the corresponding eigenenergy of the Stark Hamiltonian. The dc and ac fields are sufficiently weak that one can take

$$E(\mathcal{E}) = E^{(0)} - \frac{1}{2}\alpha\mathcal{E}^2 , \quad (5.3)$$

and

$$|\psi(\mathcal{E})\rangle = |\psi^{(0)}\rangle + \mathcal{E}|\psi^{(1)}\rangle , \quad (5.4)$$

where α denotes the static dipole polarisability of the Rydberg state [137], $E^{(0)}$ and $|\psi^{(0)}\rangle$ are the energy and state vector in the absence of the field, and $|\psi^{(1)}\rangle$ is the first-order coefficient of the perturbative expansion of the Stark state $|\psi(\mathcal{E})\rangle$ in powers of \mathcal{E} . In view of Equation (5.1), we have

$$\mathcal{E}^2(t) = \mathcal{E}_{\text{dc}}^2 + \frac{1}{2}\mathcal{E}_{\text{ac}}^2 + 2\mathcal{E}_{\text{dc}}\mathcal{E}_{\text{ac}} \sin \omega_{\text{m}}t - \frac{1}{2}\mathcal{E}_{\text{ac}}^2 \cos 2\omega_{\text{m}}t . \quad (5.5)$$

Hence,

$$\begin{aligned} \exp\left(-\frac{i}{\hbar} \int^t E[\mathcal{E}(t')] dt'\right) = \\ \exp\left[-\frac{i}{\hbar} \left(E^{(0)} - \frac{\alpha^2}{2}\mathcal{E}_{\text{dc}}^2 - \frac{\alpha^2}{4}\mathcal{E}_{\text{ac}}^2\right) t\right] B(x, y, \omega_{\text{m}}t) , \end{aligned} \quad (5.6)$$

where

$$B(x, y, \omega_{\text{m}}t) = \exp\{-i[x \cos \omega_{\text{m}}t + y \sin 2\omega_{\text{m}}t]\} , \quad (5.7)$$

with

$$x = \alpha\mathcal{E}_{\text{dc}}\mathcal{E}_{\text{ac}}/(\hbar\omega_{\text{m}}) , \quad (5.8a)$$

$$y = \alpha\mathcal{E}_{\text{ac}}^2/(8\hbar\omega_{\text{m}}) . \quad (5.8b)$$

Since the product $B(x, y, \omega_{\text{m}}t)[|\psi^{(0)}\rangle + \mathcal{E}(t)|\psi^{(1)}\rangle]$ oscillates in time with angular frequency ω_{m} , the state vector of the rf-dressed Rydberg state, $|\Psi(t)\rangle$,

can be written in the Floquet-Fourier form

$$|\Psi(t)\rangle = \exp(-i\varepsilon_0 t/\hbar) \sum_{N=-\infty}^{\infty} \exp(-iN\omega_m t) |\psi_N\rangle, \quad (5.9)$$

where ε_0 is known as quasienergy and ψ_N is the harmonic components of the Fourier expansion (see Chapter 6 for more details). To obtain the explicit forms of ε_0 and $|\psi_N\rangle$, we expand the function $B(x, y, \omega_m t)$ in a Fourier series, as

$$B(x, y, \omega_m t) = \sum_{N=-\infty}^{\infty} B_N(x, y) \exp(-iN\omega_m t), \quad (5.10)$$

where the expansion coefficients $B_N(x, y)$ are so-called “modified generalised Bessel functions” [139]. For the problem we are considering, they are best evaluated in terms of ordinary Bessel functions. Using the Jacobi-Anger expansion [139],

$$\exp[-ix \cos \omega_m t] = \sum_{n=-\infty}^{\infty} i^n J_{-n}(x) \exp[-in\omega_m t], \quad (5.11a)$$

$$\exp[-iy \sin 2\omega_m t] = \sum_{n=-\infty}^{\infty} J_n(y) \exp[-2in\omega_m t], \quad (5.11b)$$

we obtain

$$B_N(x, y) = \sum_{M=-\infty}^{\infty} i^{N-2M} J_{2M-N}(x) J_M(y). \quad (5.12)$$

Thus the expressions for the quasienergy ε_0 and for the harmonic components $|\psi_N\rangle$ can be written down by recasting $|\Psi(t)\rangle$, as given by Equation (5.2) and Equation (5.6), in the form of Equation (5.9):

$$\varepsilon_0 = E^{(0)} - \frac{\alpha^2}{2} \mathcal{E}_{\text{dc}}^2 - \frac{\alpha^2}{4} \mathcal{E}_{\text{ac}}^2, \quad (5.13a)$$

$$|\psi_N\rangle = B_N |\psi^{(0)}\rangle + C_N |\psi^{(1)}\rangle, \quad (5.13b)$$

with $B_N \equiv B_N(x, y)$ and

$$C_N = B_N \mathcal{E}_{\text{dc}} + (B_{N+1} - B_{N-1}) \frac{\mathcal{E}_{\text{ac}}}{2i}. \quad (5.14)$$

Hence, when decoherence is ignored, the ac field creates multiple sidebands: everything happens as if in the presence of the field each of the two hyperfine

components of the $32S_{1/2}$ state becomes a manifold of infinitely many states of energies $\varepsilon_N = \varepsilon_0 + N\hbar\omega_m$ ($N = 0, \pm 1, \pm 2, \dots$), whose state vectors are the respective harmonic components $|\psi_N\rangle$ [47, 50, 51, 53]. The energies ε_N are equally spaced and are shifted by $\varepsilon_N - E^{(0)}$ with respect to the zero-field position of the $32S_{1/2}$ state. Seen in a different way, the $5P_{3/2}$ state, which is not significantly perturbed by the field, can couple to the $32S_{1/2}$ state by absorption of one laser photon and of N rf photons ($N = 0, \pm 1, \pm 2, \dots$). Because the vectors $|\psi^{(0)}\rangle$ and $|\psi^{(1)}\rangle$ have opposite parity, $|\psi^{(1)}\rangle$ does not couple to the $5P_{3/2}$ state. Therefore, the Rabi frequency for the transition from a particular hyperfine component of this state to a particular component of the dressed Rydberg state differs from the corresponding zero-field Rabi frequency only by a factor $|B_N|$ (for the transition to the component with energy ε_N). The $5S_{1/2}$ and $5P_{3/2}$ states are also dressed by the applied field, but their polarisability is too small for any of their Floquet sideband states to be significantly populated at the ac field amplitudes considered here.

To further examine the effect of the weak-field modulation, we divide the discussion into three cases.

Case 1 No dc field, i.e., $\mathcal{E}_{dc} = 0$

If the ac field acts alone, then $x = 0$ and the coefficients $B_N(x, y)$ vanish for odd values of N . Consequently

$$\varepsilon_0 = E^{(0)} - \frac{\alpha^2}{4} \mathcal{E}_{ac}^2, \quad (5.15)$$

and, with $r = 0, \pm 1, \pm 2, \dots$,

$$|\psi_N\rangle = \begin{cases} J_r(y) |\psi^{(0)}\rangle & \text{for } N = 2r, \\ [J_{r+1}(y) - J_r(y)] \mathcal{E}_{ac} |\psi^{(1)}\rangle / (2i) & \text{for } N = 2r + 1. \end{cases} \quad (5.16)$$

Although the harmonic components $|\psi_N\rangle$ do not vanish for N odd, there are no odd-order sidebands when $\mathcal{E}_{dc} = 0$. Indeed, these harmonic components are all proportional to $|\psi^{(1)}\rangle$, which under inversion of space has the parity opposite to that of $|\psi^{(0)}\rangle$; the coupling between the $5P_{3/2}$ state and these

harmonic components are thus forbidden by the dipole selection rules. Even-order sidebands are not forbidden, however; Equation (5.16) predicts that $|\Omega_N| = |J_N(y)\Omega^{(0)}|$, where $\Omega^{(0)}$ is the Rabi frequency in the absence of the ac-field. Note that $|\Omega_N|$ does not depend on the sign of N ; the sidebands predicted are therefore symmetric¹.

Case 2 Both dc- and ac-fields are present, i.e., $\mathcal{E}_{\text{dc}} \neq 0$ and $\mathcal{E}_{\text{ac}} \neq 0$

The case where the dc and ac fields are both present is of particular interest in the context of this work. We have, from Equation (5.10) and Equation (5.13a),

$$|\Omega_N|^2 = |\Omega^{(0)}|^2 \times \left| \sum_{M=-\infty}^{\infty} i^{N-2M} J_{2M-N}(x) J_M(y) \right|^2. \quad (5.17)$$

In particular, when $|x| \ll 1$ and $|y| \ll 1$,

$$|\Omega_0|^2 \approx |\Omega^{(0)}|^2 [J_0(x)J_0(y)]^2, \quad (5.18a)$$

$$|\Omega_1|^2 \approx |\Omega^{(0)}|^2 [J_1(x)J_0(y) + J_1(x)J_1(y)]^2, \quad (5.18b)$$

$$|\Omega_{-1}|^2 \approx |\Omega^{(0)}|^2 [J_1(x)J_0(y) - J_1(x)J_1(y)]^2, \quad (5.18c)$$

$$|\Omega_2|^2 \approx |\Omega^{(0)}|^2 [J_0(x)J_1(y) - J_2(x)J_0(y)]^2, \quad (5.18d)$$

$$|\Omega_{-2}|^2 \approx |\Omega^{(0)}|^2 [J_0(x)J_1(y) + J_2(x)J_0(y)]^2. \quad (5.18e)$$

In this limit, the blue-detuned first-order sideband ($N = +1$) can thus be expected to be more intense than the red-detuned one ($N = -1$) because of the plus sign, and the other way round for the second-order sidebands, the asymmetry growing when \mathcal{E}_{ac} increases or ω_m decreases².

Case 3 No ac field, i.e., $\mathcal{E}_{\text{ac}} = 0$

¹This symmetry is expected to be broken by terms quadratic in $\mathcal{E}(t)$ omitted in the state vector appearing in the right-hand side of Equation (5.2).

²Whereas the EIT profile depends on the matrix elements of the dipole operator through the squared moduli of the corresponding Rabi frequencies, this dependence is not linear and therefore the heights of the EIT sidebands and central peak relative to the zero-field peak may differ from $|B_N(x, y)|^2$.

In the absence of ac field, we simply have

$$\varepsilon_0 = E^{(0)} - \frac{\alpha^2}{2} \mathcal{E}_{\text{dc}}^2, \quad (5.19\text{a})$$

$$|\psi_N\rangle = [|\psi^{(0)}\rangle + \mathcal{E}_{\text{dc}} |\psi^{(1)}\rangle] \delta_{N,0}, \quad (5.19\text{b})$$

and there are no sidebands.

It follows that under the action of the ac field, and provided the relevant relaxation times are much longer than $2\pi/\omega_m$, one should expect that the Rydberg dark states turn into Floquet manifolds of dark states and that each EIT dip in the absorption spectrum acquires multiple sidebands. That such Floquet dark states can be obtained in conditions easily accessible to experiment is one of the results of this work. (In the opposite limit where the decoherence time is much shorter than the period of modulation, EIT happens as if the applied electric field is static and the experimental signal is the time-average of the instantaneous absorption spectrum over the distribution of values of $\mathcal{E}(t)$. The timescale involved will be investigated in Chapter 6.)

5.1.2 EIT modelling

Figure 5.1 schematically shows the structure of the hyperfine magnetic sub-levels of $5S_{1/2}$, $F = 2$ state, $5P_{3/2}$, $F' = (2, 3)$ states, and the manifolds of $32S_{1/2}$, $F'' = (1, 2)$ states. The rf-dressed system interacts with π -polarised laser fields such that the transitions conserve the magnetic quantum number m_F , i.e., $\Delta m_F = 0$. In this set up, we have two distinct sub-systems for the transition, namely, $[1, 1, 2N + 1]$ and $[1, 1, 2(2N + 1)]$, where the notation $[p, q, r]$ denotes that the system contains p ground states, q intermediate states, and r excited states. The roles of the probe and coupling lasers of the first sub-system are to couple $5S_{1/2}$, $F = 2$ state to $5P_{3/2}$, $F' = 3$ state and $5P_{3/2}$, $F' = 3$ state to $2N + 1$ manifold of $32S_{1/2}$, $F'' = 2$ state, respectively, while in the latter sub-system the probe laser couples $5S_{1/2}$, $F = 2$ state to $5P_{3/2}$, $F' = 2$ state and the coupling laser couples $5P_{3/2}$, $F' = 2$ state to two

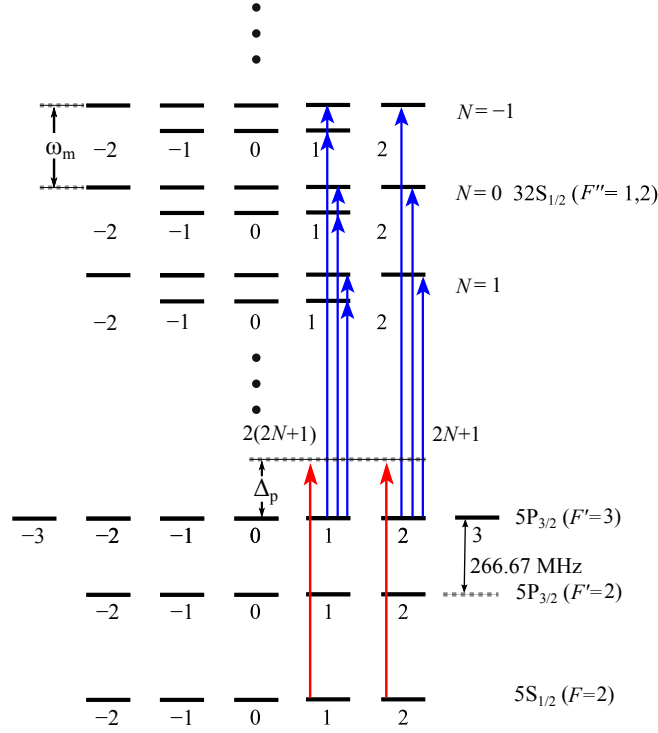


Figure 5.1: Schematic of the energy levels scheme. The probe detuning Δ_p of the probe beam is scanned between $5S_{1/2}$, $F = 2$ and $5P_{3/2}$, $F' = 3$. The coupling beam is resonant with the transition between the intermediate $5P_{3/2}$, $F' = 3$ state and the Rydberg $nS_{1/2}$, $F'' = (1, 2)$ state ($n = 32$). The hyperfine splitting of $F'' = 1$ and $F'' = 2$ of $32S_{1/2}$ is so small that these two states are effectively degenerate (the splitting shown in the figure is for the sake of clarity). The transitions due to sub-systems $[1,1,2N + 1]$ and $[1,1,2(2N + 1)]$ are labelled as $2N + 1$ and $2(2N + 1)$, respectively. An applied electric field with angular frequency ω_m generates a ladder Floquet state separated by integer multiples of ω_m . The first order Floquet dark states ($N = \pm 1$) are particularly sensitive to any dc field.

of $2N + 1$ manifolds of $32S_{1/2}$, $F'' = (1, 2)$ states.

Following the theory of the ladder EIT described in Chapter 3, the complex susceptibility of the $[1,1,2N + 1]$ system for a particular m_F state of $5S_{1/2}$,

assuming weak probe condition and atoms being at rest, is given by

$$\chi_{m_F}^{2N+1} = \frac{1}{8} \left(\frac{i|d_{m_F}|^2 \mathcal{N}}{\hbar \epsilon_0} \right) \times \left[\frac{\Gamma}{2} + \gamma_1 - i\Delta_p + \sum_{j=-N}^N \frac{|\Omega_j|^2/4}{\gamma_1 + \gamma_2 - i(\Delta_p + \Delta_c + E^{(0)} - \epsilon_j)} \right]^{-1}, \quad (5.20)$$

where \mathcal{N} is the number density of atoms, Γ is the lifetime of $5P_{3/2}$ state ($\sim 2\pi \times 6$ MHz), $\gamma_{1(2)}$ is the dephasing decay of $5P_{3/2}-5S_{1/2}$ ($32S_{1/2}-5P_{3/2}$), $\Delta_{p(c)}$ is the detuning of probe (coupling) laser when the rf-field is not applied to the system, $E^{(0)} - \epsilon_j$ is the Stark shift given by Equation (5.13a), and finally the factor of $1/8$ comes from the assumption that all magnetic sublevels of $5S_{1/2}$, $F = (1, 2)$ are evenly populated. The dipole matrix element d_{m_F} , for the transition $5S_{1/2}$ to $5P_{3/2}$ is given by,

$$\begin{aligned} |d_{m_F}|^2 &= |\langle 5P_{3/2}(F', m'_F) | ez | 5S_{1/2}(F, m_F) \rangle|^2 \\ &= 4e^2(2F+1)(2F'+1) \begin{pmatrix} F & 1 & F' \\ m_F & 0 & -m'_F \end{pmatrix}^2 \begin{Bmatrix} 3/2 & 1/2 & 1 \\ F & F' & 3/2 \end{Bmatrix}^2 \\ &\quad \times |\langle 5P_{3/2} || r || 5S_{1/2} \rangle|^2, \end{aligned} \quad (5.21)$$

where $\langle 5P_{3/2} || r || 5S_{1/2} \rangle$ is known as a reduced matrix element. For the transition between $5S_{1/2}$ and $5P_{3/2}$, $\langle 5P_{3/2} || r || 5S_{1/2} \rangle$ is $2.989a_0$ [110]. This quantity describes the physical property of the operator and system, and is independent of the orientation of quantisation axis [108, 109]. The coupling Rabi frequencies Ω_j , between the $5P_{3/2}$ state and the N -th sideband of $32S_{1/2}$ $F = 2$ state, is given by Equation (5.17), where $\Omega^{(0)}$ is defined as

$$\begin{aligned} |\Omega^{(0)}|^2 &= \left(\frac{E_c}{\hbar} \right)^2 |\langle 32S_{1/2}(F'', m''_F) | ez | 5P_{3/2}(F', m'_F) \rangle|^2 \\ &= (2F''+1)(2F'+1) \begin{pmatrix} F' & 1 & F'' \\ m'_F & 0 & -m''_F \end{pmatrix}^2 \begin{Bmatrix} 1/2 & 3/2 & 1 \\ F' & F'' & 3/2 \end{Bmatrix}^2 \\ &\quad \times \frac{4}{3} |\Omega_c^{(0)}|^2. \end{aligned} \quad (5.22)$$

The dipole matrix element of the system is absorbed into $|\Omega_c^{(0)}|^2$, i.e., $|\Omega_c^{(0)}|^2 \equiv eE_c |\langle 32S_{1/2} || r || 5P_{3/2} \rangle|^2 / \hbar$. This parameter is one of the free pa-

parameters determined from the experimental data. Theoretically, the summations in Equation (5.17) and Equation (5.20) run from $-\infty$ to ∞ ; however, in the numerical calculation, the summation of index M in Equation (5.17) runs from -30 to 30 for a fixed value of N , and the summation of j runs from -10 to 10 , i.e., ten sidebands are included in the calculation. This approximation is valid since the Bessel functions vanish for large order.

Since the hyperfine splitting between $F'' = 1$ and $F'' = 2$ is so small that the hyperfine states $F'' = 1$ and $F'' = 2$ are approximately degenerate, the complex susceptibility of $[1,1,2(2N+1)]$ sub-system also has the same form as that of $[1,1,2N+1]$, given by Equation (5.20), except that the expression for $\Omega^{(0)}$, in Equation (5.22), is now given by

$$\begin{aligned}
 |\Omega^{(0)}|^2 &= \left(\frac{E_c}{\hbar}\right)^2 \{ |\langle 32S_{1/2}(F''=2, m''_F) | ez | 5P_{3/2}(F'=2, m'_F) \rangle|^2 \\
 &\quad + |\langle 32S_{1/2}(F''=1, m''_F) | ez | 5P_{3/2}(F'=2, m'_F) \rangle|^2 \} \\
 &= \sum_{F''=1,2} (2F''+1) \begin{pmatrix} 2 & 1 & F'' \\ m'_F & 0 & -m''_F \end{pmatrix}^2 \begin{Bmatrix} 1/2 & 3/2 & 1 \\ 2 & F'' & 3/2 \end{Bmatrix}^2 \times \\
 &\quad \frac{20}{3} |\Omega_c^{(0)}|^2, \tag{5.23}
 \end{aligned}$$

where $\Omega_c^{(0)}$ is as defined above, and the probe and coupling detunings are replaced by the following substitutions:

$$\Delta_p \rightarrow \Delta_p + (2\pi \times 266.67) \text{ MHz}, \tag{5.24a}$$

$$\Delta_c \rightarrow \Delta_c - (2\pi \times 266.67) \text{ MHz}. \tag{5.24b}$$

It turns out that the susceptibility $\chi_{m_F}^{2N+1}$ is not in an appropriate form when dealing with Doppler averaging, as $\chi_{m_F}^{2N+1}$ cannot be integrated analytically. Thus numerical integration must be used; however, this has the disadvantage that the time taken by the calculation is excessively long for the needs of an optimisation scheme. Remember that the susceptibility derived from the three-level ladder system ($[1,1,1]$) can be analytically integrated when one takes into account the effect of Doppler broadening; hence, if we could rewrite $\chi_{m_F}^{2N+1}$ in terms of the sum of many three-level systems, an analytic

expression for $\chi_{m_F}^{2N+1}$ with Doppler broadening effect can be obtained. To do this, we consider the Taylor expansion:

$$\begin{aligned}
 \left(A + \sum_j \frac{B_j}{C} \right)^{-1} &= \frac{1}{A} \left[1 - \left(\sum_j \frac{B_j}{AC} \right) + \left(\sum_j \frac{B_j}{AC} \right)^2 - + \dots \right] \\
 &= \frac{1}{A} \left[1 + \sum_j \left(1 - \frac{B_j}{AC} + \left(\frac{B_j}{AC} \right)^2 - + \dots \right) - \sum_j (1) \right] \\
 &\quad + \frac{1}{A} \left[\frac{B_0 B_1}{A^2 C^2} + \frac{B_0 B_{-1}}{A^2 C^2} + \dots \right] \\
 &\approx \frac{1}{A} + \sum_j \left(A + \frac{B_j}{C} \right)^{-1} - \sum_j \frac{1}{A} + \frac{1}{A} \times \mathcal{O} \left(\frac{B_n B_m}{A^2 C^2} \right),
 \end{aligned} \tag{5.25}$$

where $n \neq m$. This expansion is valid when the sum of $B_n B_m / (AC)^2$ is small and converges, which is the case here as Ω_j approaches zero when j increases. Applying Equation (5.25) to Equation (5.20), we have

$$\chi_{m_F}^{2N+1} \approx \chi^{(0)} + \sum_{j=-N}^N (\chi^j - \chi^{(0)}), \tag{5.26}$$

with

$$\begin{aligned}
 \chi^j &= \frac{1}{8} \left(\frac{i |d_{m_F}|^2 \mathcal{N}}{\hbar \epsilon_0} \right) \times \\
 &\quad \left[\frac{\Gamma}{2} + \gamma_1 - i \Delta_p + \frac{|\Omega_j|^2 / 4}{\gamma_1 + \gamma_2 - i(\Delta_p + \Delta_c + E^{(0)} - \epsilon_j)} \right]^{-1},
 \end{aligned} \tag{5.27}$$

and $\chi^{(0)}$ is χ^j evaluated when $\Omega_j = 0$. We refer to this approximation as the incoherent sum approximation and it is valid when the condition

$$\Omega_n \Omega_m < 4 \left(\frac{\Gamma}{2} + \gamma_1 \right) \gamma_2, \quad n \neq m, \tag{5.28}$$

is fulfilled.

Up to this point we have not yet considered the effect of Doppler broadening. To include the Doppler effect, we replace Δ_p , Δ_c and \mathcal{N} by the following:

$$\Delta_p \rightarrow \Delta_p + k_p v, \tag{5.29a}$$

$$\Delta_c \rightarrow \Delta_c - k_c v, \tag{5.29b}$$

$$\mathcal{N} \rightarrow \frac{\mathcal{N}_0}{u \sqrt{\pi}} \exp \left(-\frac{v^2}{u^2} \right), \tag{5.29c}$$

where $k_{p(c)}$ is the wavevector of probe (coupling) field, \mathcal{N}_0 is the number density at zero velocity, v is the atomic velocity and $u \equiv \sqrt{2k_B T/m}$ is the most probable speed of atom at a given temperature T . Thus Equation (5.27) becomes

$$\chi^j(v) = \frac{1}{8} \left(\frac{|d_{m_F}|^2 \mathcal{N}}{\hbar \epsilon_0 u \sqrt{\pi}} \right) \times \exp\left(-\frac{v^2}{u^2}\right) \times \left[\frac{\Gamma}{2} + \gamma_1 - i\Delta_p - ik_p v + \frac{|\Omega_j|^2/4}{\gamma_1 + \gamma_2 - i(\Delta_p + \Delta_c + E^{(0)} - \varepsilon_j) - i(k_p - k_c)v} \right]^{-1}, \quad (5.30)$$

and the susceptibility with Doppler broadening effect is [84]

$$\begin{aligned} \chi_{D,m_F}^{2N+1} &= \int_{-\infty}^{\infty} \chi_{m_F}^{2N+1}(v) dv, \\ &= \chi_D^{(0)} + \sum_{j=-N}^N \left(\chi_D^j - \chi_D^{(0)} \right), \end{aligned} \quad (5.31)$$

where $\chi_D^j = \int_{-\infty}^{\infty} \chi^j(v) dv$ and $\chi_D^{(0)}$ is χ_D^j when $\Omega_j = 0$. The analytical form of χ_D^j is

$$\chi_D^j = \left(\frac{|d_{m_F}|^2 \sqrt{\pi} \mathcal{N}_0}{16 \hbar \epsilon_0 u k_p} \right) \left\{ (1-d) s_1 e^{-z_1^2} [1 - s_1 \operatorname{erf}(iz_1)] + (1+d) s_2 e^{-z_2^2} [1 - s_2 \operatorname{erf}(iz_2)] \right\}, \quad (5.32)$$

where $s_{1(2)} = -\operatorname{sgn}[\operatorname{Im}(z_{1(2)})]$ and the quantities d , z_1 , and z_2 are

$$d = \frac{i}{z_1 - z_2} \left[\frac{\Gamma/2 + \gamma_1 - i\Delta_p}{k_p u} + \frac{\gamma_1 + \gamma_2 - i(\Delta_p + \Delta_c)}{(k_p - k_c)u} \right], \quad (5.33a)$$

$$\begin{aligned} z_{1,2} &= -\frac{i}{2} \left[\frac{\Gamma/2 + \gamma_1 - i\Delta_p}{k_p u} + \frac{\gamma_1 + \gamma_2 - i(\Delta_p + \Delta_c)}{(k_p - k_c)u} \right] \\ &\pm \frac{i}{2} \left[\left(\frac{\Gamma/2 + \gamma_1 - i\Delta_p}{k_p u} - \frac{\gamma_1 + \gamma_2 - i(\Delta_p + \Delta_c)}{(k_p - k_c)u} \right)^2 - \frac{\Omega_j^2}{k_p (k_p - k_c) u^2} \right]^{1/2}. \end{aligned} \quad (5.33b)$$

Thus the total susceptibility of ^{87}Rb is

$$\chi_{\text{TOT}} = \sum_{m_F=-2}^2 \left(\chi_{D,m_F}^{2N+1} + \chi_{D,m_F}^{2(2N+1)} \right), \quad (5.34)$$

and the absorption coefficient α is $k_p \text{Im}[\chi_{\text{TOT}}]$. The transmission through the medium is then given by the Beer-Lambert law

$$T = \exp(k_p \mathcal{L} \text{Im}[\chi_{\text{TOT}}]), \quad (5.35)$$

where \mathcal{L} is the length of the cell.

5.2 Comparison between theory and experiment

A schematic of the experimental set up is shown in Figure 5.2³. It is based on a specially fabricated 11 mm-long Rb vapour cell containing two parallel plane electrodes running along its whole length and separated by a 5 mm gap. The probe beam and the co-axial, counter-propagating coupling beam are directed along the electrode cell axis and are both polarised parallel to the electrodes. Each beam is focused using 10 cm lenses. The probe beam has an input power of 300 nW and a $1/e^2$ radius of 1.7 mm. The corresponding values for the coupling beam are 40 mW and 1.0 mm. The latter is stabilized against slow drift using EIT in a reference cell [140]. The transmission through the electrode cell is monitored as a function of the probe detuning. To increase the number density of Rb atoms the electrode cell is heated to about 40 °C. The probe beam is split into two with one component propagating through the electrode cell and the other passing through a longer room temperature cell (of length 75 mm). By subtracting these two signals, the Doppler background is removed. Measuring the off-resonant probe beam power after the electrode cell allows the change in transmission, ΔT , to be calibrated. The detuning axis is calibrated using saturation/hyperfine pumping spectroscopy, i.e. the frequency separation between $F' = 2$ and 3.

A comparison between the absorption lineshape calculated using Equa-

³The experiment was performed by Bason et al. [92]

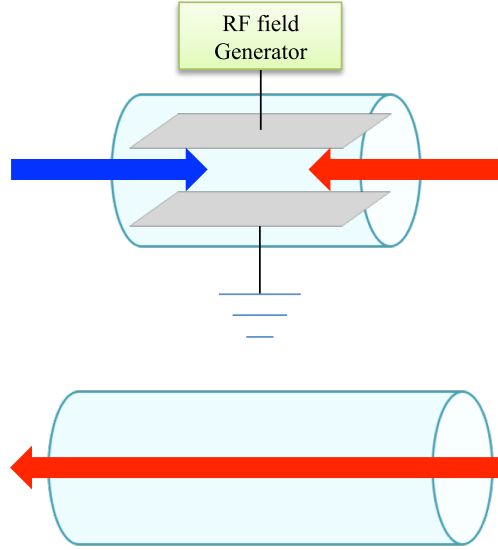


Figure 5.2: Schematic of the experimental set up. The 780 nm probe beam (red) and 480 nm coupling beam (blue) counterpropagate through a 11-mm long Rb cell containing parallel plane electrodes. The dc and the ac fields are applied by imposing a potential difference across the electrodes. The probe is also split and fed to a 75-mm long Rb cell and its two-level transmission is registered. Then the two transmission signals, obtained from both cells, are subtracted from one another, yielding the change in transmission ΔT . The advantages of this technique is to get rid of the common mode noise in the transmission signals and to partly cancel the Doppler background [92].

tion (5.20) with Doppler averaging (red solid line) and the incoherent sum approximation calculated using Equation (5.31) (black dashed line) is shown in Figure 5.3(a). The applied ac and dc electric fields are 7.7 and 0.8 V cm⁻¹, respectively, and the modulation frequency is 26 MHz. For the typical parameters used in the experiment, given in Table 5.1, the condition given by Equation (5.28) is satisfied, i.e., $\text{Max}[\Omega_n \Omega_m / (4(\Gamma/2 + \gamma_1)\gamma_2)] \approx 0.2$. This results in good agreement between both absorption lineshapes. The differ-

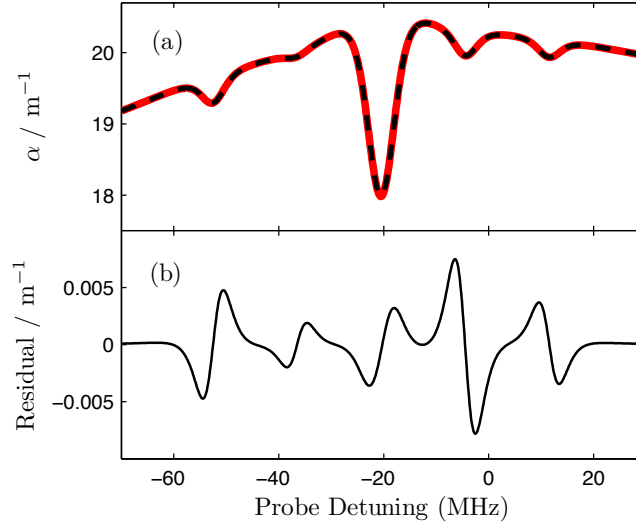


Figure 5.3: The top panel compares the absorption coefficient calculated using the coherent sum model given by Equation (5.20) (red solid line) to the incoherent sum model given by Equation (5.27) (black dashed line) for $\Omega_c^{(0)}/2\pi = 13.3$ MHz. The parameters used in the calculation are as given in Table 5.1 and the ac and dc fields are 7.7 V cm^{-1} and 0.8 V cm^{-1} , respectively. The modulation frequency is 26 MHz. For these parameters, the approximation yields a good agreement with the actual absorption lineshape, reflecting in small residuals as seen in the bottom panel. Note that, though the residual is small, it exhibits the differential lineshape structure due to a small displacement of the resonances calculated from both methods. This shift in frequency space of the resonances are similar to those discussed in Chapter 6.

ence between two lineshapes is shown in the residual plot (Figure 5.3(b)). Figure 5.4(a) and Figure 5.4(b) shows plots similar to those of Figure 5.3, but with $\Omega_c^{(0)} = 133$ MHz, i.e., ten times larger than the previous value. The condition given by (5.28) is invalid as $\text{Max}[\Omega_n\Omega_m/(4(\Gamma/2 + \gamma_1)\gamma_2)] \approx 24$, which is much larger than unity. The incoherent sum approximation is no longer a good approximation for the coherent sum model as shown in Fig-

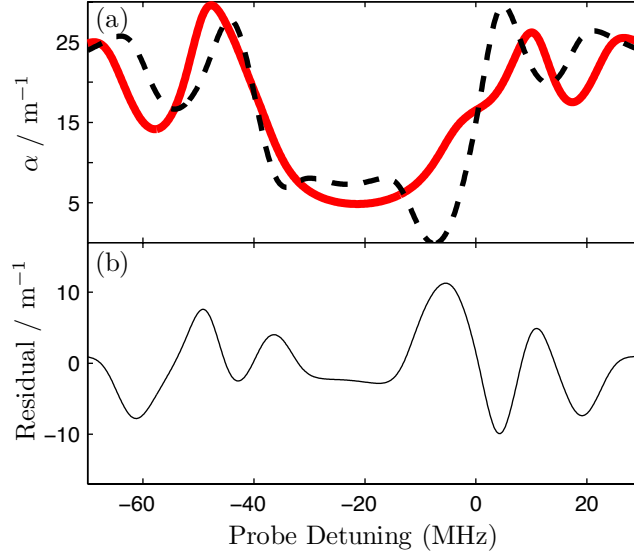


Figure 5.4: The same as Figure 5.3, except that $\Omega_c^{(0)} = 133$ MHz. For the given parameters, the approximation clearly breaks down. This results in the large residuals as shown in the bottom panel.

Figure 5.4(a) and the range variation of the residuals increases by a factor of two thousand.

A typical EIT spectrum with an applied ac field is shown in Figure 5.5 together with theoretical fits, calculated using the incoherent sum model with Doppler averaging, for different spatial profiles of the electric field. The transmission is a function of four parameters that must be derived from the data, namely, the Rabi frequency $\Omega_c^{(0)}$, the dephasing rates of the $5P_{3/2}$ – $5S_{1/2}$ and $32S_{1/2}$ – $5P_{3/2}$ coherences, and the temperature of the vapour. The values of these experimental parameters are obtained by a least-square fit of the theoretical change in transmission, ΔT , to the data and their values are given in Table 5.1. The fit covers a range of probe detunings encompassing both the $5P_{3/2}$, $F' = 2$ and $F' = 3$ states whereas only latter is shown in Figure 5.5. The mean separation between the plates is not known with sufficient precision, and therefore is derived from the data by fitting the Stark shift of the EIT resonances to Equation (5.13a) for a number of different

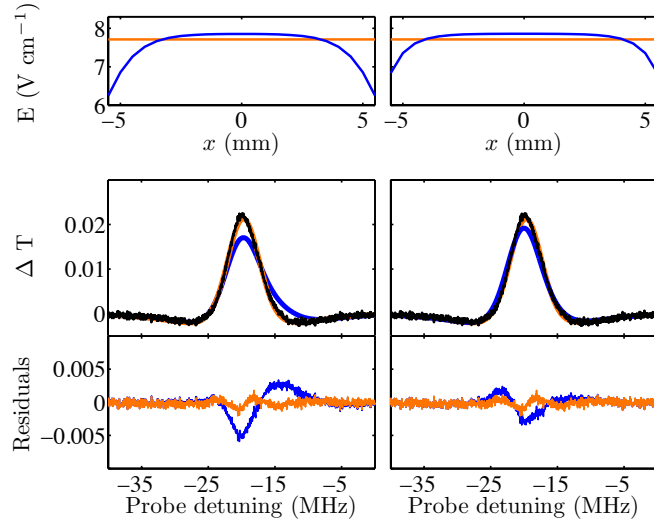


Figure 5.5: Comparison between the observed EIT spectra (black) for an applied ac electric field, $\mathcal{E}_{\text{ac}} = 7.7 \text{ V cm}^{-1}$, and the theoretical model for the field calculated for the actual electrode geometry (blue) and for a uniform field (red). In the theoretical model, it is assumed either that the laser beams are aligned exactly on the longitudinal axis of the two Stark plates (left-hand column) or that they are parallel to this axis but are offset by 1 mm towards one of the plates (right-hand column). The corresponding electric field distributions are shown at the top. In this example, the electric field frequency is 26 MHz. The theoretical model is calculated using the incoherent sum model with Doppler averaging. The theoretical results are in good agreement when the field is assumed to be uniform, resulting in a smaller residue in the residual plots. Note that the residue signals (for the uniform field case) show a small differential lineshape structure since the theoretical model does not include the resonance shift due to the finite coupling Rabi frequency (see Chapter 6).

values of the applied voltage⁴ [92].

The spatial profile of the applied electric field along the laser beam axis is unknown due to the possibility of free charges inside the cell. The evidence of

⁴The value of the dipole polarisability used here is taken from [137].

Table 5.1: The values of the four parameters which produce the minimum residual for the least-square fit. $\Omega_c^{(0)}$, γ_1 and γ_2 are expressed in unit of 2π MHz. Note that the uncertainties of the fitted parameters calculated from $\chi^2 + 1$ method are so tiny that they do not affect the fitted parameters quoted upto 1 decimal place.

$\Omega_c^{(0)}$	γ_1	γ_2	T ($^{\circ}\text{C}$)
13.3	2.4	1.6	39

the free charges were observed by Mohapatra et al. [32]. In their experiment, an electric field was applied across a whole vapour cell in order to perturb the EIT signal in ladder system. However, the presence of the space charges produced by photoelectric effect shields the Rb vapour inside the cell from the applied electric field; hence, they observed no changes to EIT signal [32].

The field produced by the Stark plates, calculated using difference method [141], drops significantly at their edges (see the top panels of Figure 5.5). If we assume that the field experienced by the atoms exposed to the laser beams varies accordingly, the resulting theoretical EIT profile is asymmetric and inconsistent with the data (see the middle and bottom panels of Figure 5.5). The theoretical results are found to be in good agreement with the data if the field is assumed to be uniform. This would occur if the free charges inside the cell equalise the electric field in the interaction region. We note in this respect that charges can be created by the photoelectric effect where the coupling laser intersects the thin layer of the Rb metal on the inner surface of the cell, the photoelectrons being ejected from the surface. The thin layer of Rb metal adhered on the inner surface of the cell are produced from the Rb vapour which condenses into the metal phase. A net positive charge of $10^6 e$ on each window distributed over the waist of the coupling laser is sufficient to produce a total field with a spatial profile consistent with the experimentally observed lineshape. We cannot exclude a misalignment of the laser beams

with respect to the centre of the plates, but the resulting offset would be less than 1 mm and even at 1 mm from the axis the field produced by the plates is more inhomogeneous than is compatible with the data (see the right-hand column of Figure 5.5).

5.3 Observation of Floquet dark states

Following the analysis in the previous section we assume that the electric field experienced by the atoms is homogeneous, and measure spectra for different combinations of ac and dc applied fields (\mathcal{E}_{dc} and \mathcal{E}_{ac}). The results are presented in Figure 5.6. The theoretical spectra are calculated assuming that the Rydberg state is described by the Floquet state vector (Equation (5.9)) and that the four experimental parameters (Ω_c^0 , γ_1 , γ_2 , and T) mentioned in Section 5.2 have the same values as in the zero-field case.

In Figure 5.6(b), we consider a case where only a pure ac field is applied. As compared to Figure 5.6(a) where no electric field is applied, the main EIT peak is shifted by the ac Stark effect and the EIT profile acquires sidebands at the second harmonics of the modulation frequency. The spacing between the sidebands and the carrier in the transmission spectrum is smaller than $2\omega_m/(2\pi)$ by a factor 480/780 due to the Doppler mismatch. In view of the good agreement between theory and the measured data, we attribute the observed sidebands to the formation of Floquet dark states. Note that the sidebands are symmetric as predicted in Section 5.1

There are no odd-order sidebands in the absence of a dc field since $B_N = 0$ for odd values of N when $\mathcal{E}_{\text{dc}} = 0$. Their absence is consistent with the dipole selection rules, which forbid transitions from a P state to an S state by exchange of one laser photon and an odd number of rf photons. The effect of adding a weak dc offset is shown in Figure 5.6(c). The spectrum acquires first order sidebands, since $|\psi^{(0)}\rangle$ contributes to every $|\psi_N\rangle$ when $\mathcal{E}_{\text{dc}} \neq 0$. As

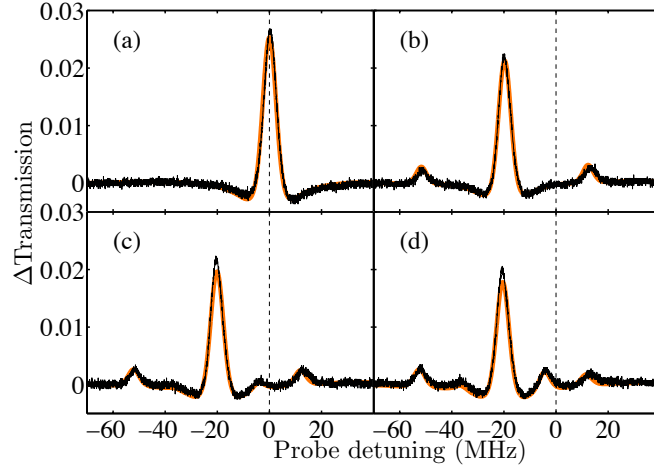


Figure 5.6: The effect of ac and dc electric fields on the Rydberg EIT spectrum. The thick curves are theoretical predictions based on the solution of the steady state optical Bloch equations. (a) Spectrum with no applied field. (b) Spectrum with an rf field with a frequency of 26 MHz ($\mathcal{E}_{\text{ac}} = 7.7 \text{ V cm}^{-1}$). (c) and (d) Spectrum with the rf field plus a dc field; $\mathcal{E}_{\text{dc}} = 0.4 \text{ V cm}^{-1}$ in (c) and 0.8 V cm^{-1} in (d).

can be seen by comparing Figure 5.6(c) and Figure 5.6(d), increasing the dc field modifies the EIT spectrum in several ways. The largest change occurs on the +1 sideband as predicted in Section 5.1. In contrast, the additional Stark shift in the position of the central peak, which would be the only effect of the increase in the dc field in the absence of the modulation, is almost invisible on the scale of the figure. The comparison demonstrates the enhanced dc field sensitivity of rf-dressed Rydberg dark states.

5.4 Enhanced electric field sensitivity of Floquet dark states

To further illustrate this enhancement effect, we now show that adding an ac modulation helps deduce the dc component of the electric field from the

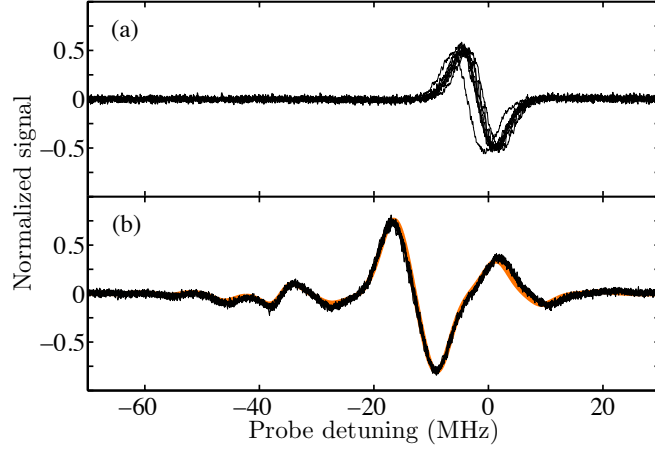


Figure 5.7: The dc field signal obtained by turning the dc field on and off at 50 kHz and using lock-in detection. The same vertical scale is used in (a) and in (b). (a) The difference signal measured for $\mathcal{E}_{ac} = 0$ and $\mathcal{E}_{dc} = 1.37 \text{ V cm}^{-1}$. Ten data sets are presented; the results shown are not corrected for the frequency fluctuations of the probe laser. (b) The difference signal measured for $\mathcal{E}_{ac} = 7.14 \text{ V cm}^{-1}$ and $\mathcal{E}_{dc} = 1.37 \text{ V cm}^{-1}$. The modulation frequency is 15 MHz. As in (a), ten data sets are presented, but here they are corrected for the frequency fluctuations of the probe laser using the Floquet model. The thick curve shows the Floquet EIT result calculated for a value of \mathcal{E}_{dc} ensuring an optimal fit between the model and one of the data sets.

EIT resonance. The difference between transmission spectra measured with and without applying a dc field are shown in Figure 5.7. Here a double modulation technique, where the dc field is switched on and off at a frequency of 50 kHz, i.e., much less than the modulation frequency, was employed [92]. The effect of the dc field was then extracted using lock-in detection resulting in a derivative lineshape. To generate the theoretical difference signal lineshape, we first calculate the theoretical transmission lineshapes, when the ac field is turned on and off, using Equation (5.34) and neglecting the transition via $5P_{3/2}$, $F' = 2$. The theoretical difference signal is then obtained by subtracting the two transmission lineshapes with each other.

Each thin black line represented in Figure 5.7 gives the difference signal averaged over four consecutive scans. Figure 5.7(a) shows the difference spectrum in the absence of ac field for 10 individual data sets. The spread in the data reflects the instability of the probe laser. Deriving \mathcal{E}_{dc} from these results is hindered by the fact that only the position of the EIT feature on the frequency axis, and not its shape, varies significantly with the strength of the dc field. Due to the experimental uncertainty in the probe frequency, a value of \mathcal{E}_{dc} cannot be obtained by fitting the model to the data from Figure 5.7(a). However, the fit is possible when these data are augmented by the difference EIT signal arising from the $5\text{P}_{3/2}, F' = 2$ state and by frequency calibration data obtained by saturation spectroscopy of $F' = 2$ and 3. The theoretical difference signal is calculated using the same procedure described above, but this time we include the theoretical signal from $5\text{P}_{3/2}, F' = 2$. The values of the Rabi frequency, dephasing rates and temperature are fixed as given in Table 5.1. We treat \mathcal{E}_{dc} as an unknown parameter. For comparison with the theory, we correct the experimental results for random variations in the calibration of the probe frequency and of the signal by rescaling and shifting the origins of the respective axes. The corresponding offsets and scaling factors are found for each individual data set, together with \mathcal{E}_{dc} , by fitting the rescaled experimental difference signal to the model. From the 10 values of \mathcal{E}_{dc} obtained in this way, we find that $\mathcal{E}_{\text{dc}} = 1.6 \pm 0.4 \text{ V cm}^{-1}$. This value is in agreement with that derived from the dc voltage applied to the electrodes, $1.37 \pm 0.02 \text{ V cm}^{-1}$, but it has a larger uncertainty.

A constant ac field is then added and the lineshape extracted once more, Figure 5.7(b). The lock-in detection still only detects changes in signal due to the dc field. In this case, for the same dc field, the difference signal is larger and contains more features. As the details of these features depend on \mathcal{E}_{dc} , the change in the spectrum due to the dc field is readily separated from the frequency fluctuations of the probe laser. Measuring \mathcal{E}_{dc} is thus easier. The theoretical difference signal is calculated in the same way as in the absence

of the rf field. We assume for \mathcal{E}_{ac} the value derived from the voltage applied to the electrodes. From the 10 values of \mathcal{E}_{dc} obtained by fitting the data from Figure 5.7(b) to the model, we find that $\mathcal{E}_{dc} = 1.36 \pm 0.04 \text{ V cm}^{-1}$ (or $1.40 \pm 0.03 \text{ V cm}^{-1}$ when the saturation spectroscopy data and the signal from $5P_{3/2}, F' = 2$ state are also taken into account). For these parameters, introducing an ac modulation thus reduces the uncertainty in the dc field measurement by one order of magnitude.

In the case considered in Figure 5.7, the application of the ac field also increases the amplitude of the difference signal by about 50%. As shown in Figure 5.8, larger enhancements⁵ (of up to about 3) can be obtained for other combinations of dc fields and modulation frequencies, e.g., $\omega_m = 10 \text{ MHz}$ and $\mathcal{E}_{dc} = 1.37 \text{ V cm}^{-1}$ (black solid line). The sudden changes in the theoretical curves occur at zeroes of the Bessel functions appearing in Equation (5.12). Figure 5.9 shows the theoretical prediction for the enhancement as a function of the dc electric field for various combination of the ac electric fields. It is clear that the enhancement decreases when the dc electric field increases. Furthermore the smaller the modulation frequency is, the larger the enhancement. Thus to achieve the maximum enhancement, one needs to work in the regime where the dc electric field and the modulation frequency are small. Note that increasing the ac electric field does not always increase the enhancement, as can be seen from Figures 5.8 and Figure 5.9(a).

5.5 Summary and conclusions

In summary, we have demonstrated the formation of Floquet dark states induced by the application of an ac field to a ladder system involving a highly-polarised Rydberg state. Bason et al. [25] have shown that these states display enhanced sensitivity to dc electric fields and provide infor-

⁵We define the enhancement as $\text{Enhancement} = (\text{Maximum range of the difference signal when } \mathcal{E}_{ac} \neq 0) / (\text{Maximum range of the difference signal when } \mathcal{E}_{ac} = 0)$.

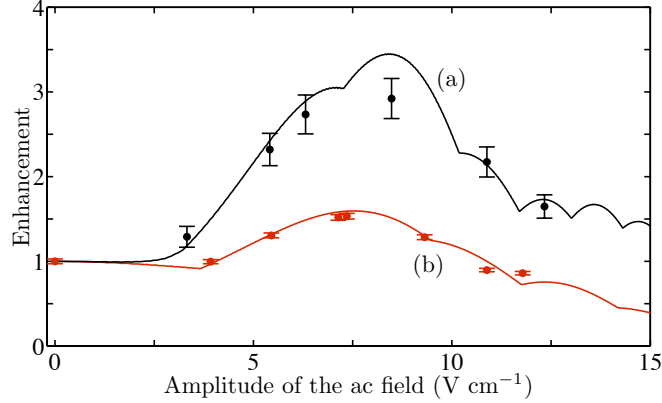


Figure 5.8: The increase in the amplitude of the dc electrometry signal as a function of \mathcal{E}_{ac} , (a) for a modulation frequency of 10 MHz and $\mathcal{E}_{dc} = 0.78 \text{ V cm}^{-1}$, (b) for a modulation frequency of 15 MHz and $\mathcal{E}_{dc} = 1.37 \text{ V cm}^{-1}$. The points are experimental data and the lines are the theoretical predictions of the model presented in the text. The sudden changes in the theoretical curves occur at zeroes of the Bessel functions appearing in Equation (5.12).

mation on the strength of the dc field independent of the laser frequency. Potentially, an ac modulation may thus facilitate the measurement of the local electric field inside a vapour cell, which is a relevant issue in the control of Rydberg-Rydberg interactions. The simple theory outlined above can be generalised to the case where the field splits the Rydberg state into several Stark components, thereby opening the possibility of using ac modulation to enhance the sensitivity of measurements based on the D states or on states of higher angular momentum. We have shown that charge imbalances in an enclosed vapour cell could probably cancel the spatial inhomogeneities of the field. Therefore for local field measurements the interaction region may need to be limited to a small volume. This would be the case, for instance, in the 3-photon Doppler-free excitation scheme considered in Chapter 4.

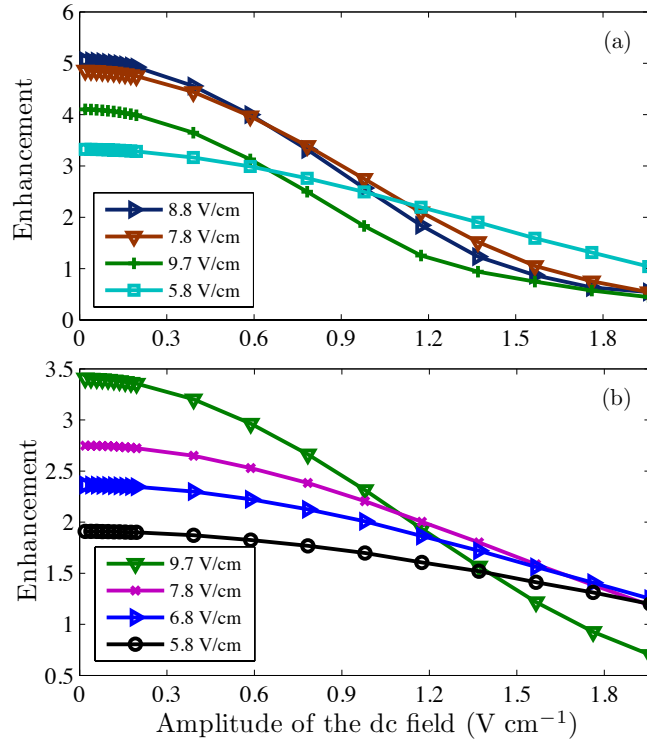


Figure 5.9: The theoretical prediction of the enhancement as a function of \mathcal{E}_{dc} for various combinations of the electric fields: (a) the modulation frequency is 10 MHz; (b) the modulation frequency is 15 MHz. It is clear that the enhancement decreases when both dc electric field and modulation frequency increase. Note that increasing the ac electric field does not always increase the enhancement because once the enhancement reaches its maximum value, increasing the ac electric field further will decrease the enhancement, as shown in (a). The insets of (a) and (b) are the values of the ac fields.

Chapter 6

Sidebands shifts and induced sidebands in rf-dressed Rydberg systems

The theory presented in Chapter 5, in which the transmission lineshape of Rydberg atoms dressed by a radio frequency (rf) field was investigated, predicts that Rydberg states may exhibit a manifold structure of independent quasienergy (or Floquet) states due to the rf field. The presence of these Floquet states can be observed as EIT caused by the dark states, in the cascade systems. This feature has been experimentally confirmed and shown to be in good agreement with the theory [25]. However, the model breaks down for large Stark shift caused by a large rf field compared to the modulation frequency.

In this chapter, we theoretically investigate the formation of the sideband structure in two- and three-level systems using the Floquet formalism. This method allows us to view the rf-dressed system as an N -level system in which the excited state manifold, composed of independent, stationary Floquet states, interacts with the ground and intermediate states via the external oscillating fields [25, 47, 51, 53, 142]. Using an N -level approximation, the

dynamics of the rf-dressed atomic system, e.g., the formation of the dark states, can be easily understood [25]. The aim of this chapter is to find, if it exists, the regime where the well-defined sideband structure due to the rf field disappears and the approximation of representing the dressed atom as a N -level system breaks down. For the case in which the sideband structure is well-defined, we will also study how well the N -level approximation represents the rf-dressed system. To our knowledge, these questions have not been investigated previously.

This chapter is organised as follows. We begin with the set up of the systems and the relevant set of equations of motion in Section 6.1. Then in Section 6.2 we discuss two-level rf-dressed subsystems. In this section, we solve the equations of motion in the framework of Floquet formalism where the effect of the rf field turns the excited state into the manifold. The properties of the quasienergy and the N -level approximation are given in Subsections 6.2.2 and 6.2.3. The dressed state dynamics is described in Section 6.3. Then we move on to the description of rf-dressed three-level systems in Section 6.4. The first two subsections describe the Floquet formalism of the system, as well as the N -level approximation. This includes the resonance structure of the absorption lineshape. The new effect, i.e., the induced sidebands of the intermediate state for large Rabi frequency of the coupling field, is investigated in Subsection 6.4.3. Then we use the N -level approximation to explain the formation of the dark states EIT for both cold atomic ensembles and thermal vapour in Subsection 6.4.4. Finally we end the chapter with conclusions, in Section 6.5.

6.1 Equations of motion

We consider the isolated three-level system composed of the ground state $|a\rangle$, the intermediate state $|b\rangle$, and the excited state $|c\rangle$, whose eigenfrequencies

cies are $\omega_a/2\pi$, $\omega_b/2\pi$, and $\omega_c/2\pi$, respectively. This system is a ladder (or cascade)-typed system and it is schematically shown in Figure 6.1(a). Two laser fields, whose angular frequencies are ω_p and ω_c , interact with the system: the first field, whose Rabi frequency is Ω_p , couples $|a\rangle$ to $|b\rangle$, whereas the second field couples $|b\rangle$ to $|c\rangle$ with the Rabi frequency of Ω_c . The letters p and c are short for probe and coupling as the first laser is used to probe the properties of the system, e.g., absorption lineshape, while the second laser couples the eigenstates of the atom. In typical experiments, one works in the weak probe regime where Ω_p is much weaker than Ω_c [3, 25, 92, 143]. The detunings of both lasers are $\Delta_p \equiv \omega_p - \omega_{ba}$ and $\Delta_c \equiv \omega_c - \omega_{cb}$, where ω_{ij} is the transition frequency from $|i\rangle$ to $|j\rangle$. (The letters i and j always denote the states a, b and c throughout the chapter, if not stated otherwise.) This system is dressed by an rf field, whose frequency is ω_{rf} , which has a significant effect on $|c\rangle$ as it is assumed that this state has a large polarisability, while its effect on $|a\rangle$ and $|b\rangle$ is negligible. An example of this system is Rydberg atoms, where the polarisability is proportional to the seventh power of the principal quantum number [23]. Since Rydberg atoms will be discussed throughout the context of three-level system, the word Rydberg state interchangeably refers to the excited state.

The Hamiltonian of the system is built from three components: the bare atom (\hat{H}_0), two laser fields interaction (\hat{H}_L), and the rf-field interaction (\hat{H}_{rf}). Since the effect of rf field is mainly on the Rydberg state and $\omega_{\text{rf}} \ll \omega_{ba}, \omega_{cb}$, then the eigenvalue equations for the bare atomic Hamiltonian and the rf-field Hamiltonian are given by [144],

$$(\hat{H}_0 + \hat{H}_{\text{rf}}) |a\rangle = \hbar\omega_a |a\rangle, \quad (6.1a)$$

$$(\hat{H}_0 + \hat{H}_{\text{rf}}) |b\rangle = \hbar\omega_b |b\rangle, \quad (6.1b)$$

$$(\hat{H}_0 + \hat{H}_{\text{rf}}) |c\rangle = \hbar(\omega_c + \frac{1}{2}\alpha\mathcal{E}_{\text{rf}}^2 \sin^2 \omega_{\text{rf}}t) |c\rangle, \quad (6.1c)$$

where α is the polarisability of $|c\rangle$, and \mathcal{E}_{rf} is the amplitude of the rf field whose form is $\mathcal{E}_{\text{rf}} \sin \omega_{\text{rf}}t$. The Hamiltonian of the interaction with the laser

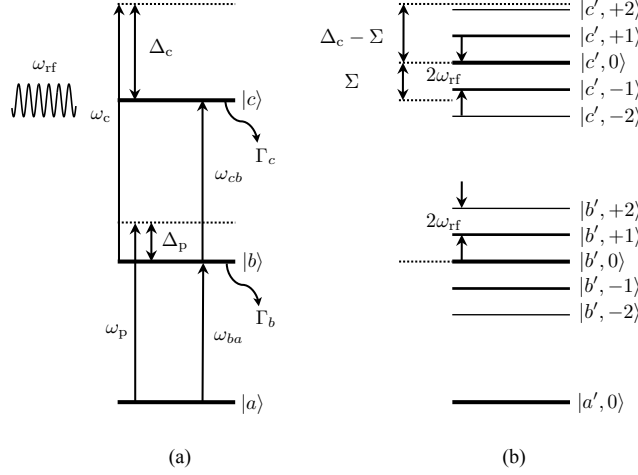


Figure 6.1: A schematic of the rf-dressed three-level (Rydberg) system is shown in (a). The probe laser, whose angular frequency is ω_p , couples $|a\rangle$ with $|b\rangle$, while the coupling laser, whose angular frequency is ω_c , couples $|b\rangle$ to $|c\rangle$. The detunings of the probe and coupling lasers from the atomic transition are Δ_p and Δ_c , respectively, and the transition (angular) frequency is $\omega_{ij} = \omega_i - \omega_j$, where i and j represent the states a, b and c . This system also interacts with the rf field, whose angular frequency is ω_{rf} . The manifolds of the intermediate and excited (or Rydberg) states are shown in (b). The separation in frequency between any adjacent Floquet states is $2\omega_{\text{rf}}$. The effect of the rf field also shifts the energy of $|c\rangle$ by Σ ; thus the coupling detuning, Δ_c , changes to $\Delta_c - \Sigma$. The N -level approximation is composed of $|a', 0\rangle$, $|b', 0\rangle$ and the manifold of the Rydberg state. The prime notation denotes that we are working in the basis where the excited state manifold is diagonalised. However, this picture breaks down for large value of Ω_c . In this limit, the intermediate state also shows the manifold structure and this manifold, as well as the Rydberg state manifold, must be taken into account in the calculation.

fields, neglecting the counter-rotating terms, is

$$\hat{H}_L = \frac{\hbar\Omega_p}{2} |b\rangle \langle a| \exp(-i\omega_p t) + \frac{\hbar\Omega_c}{2} |c\rangle \langle b| \exp(-i\omega_c t) + \text{h.c.}, \quad (6.2)$$

where h.c. means the hermitian conjugate of the first two terms. Using Equation (6.1) and (6.2), and following the method given in Chapter 2, the time-dependent Schrödinger equation is

$$\frac{d}{dt} \begin{pmatrix} u_a \\ u_b \\ u_c \end{pmatrix} = \begin{pmatrix} 0 & -i\Omega_p/2 & 0 \\ -i\Omega_p/2 & i\Delta_p & -i\Omega_c/2 \\ 0 & -i\Omega_c/2 & i[\Delta_R - 2\Sigma \sin^2 \omega_{\text{rf}}t] \end{pmatrix} \begin{pmatrix} u_a \\ u_b \\ u_c \end{pmatrix}, \quad (6.3)$$

where $\Sigma \equiv \alpha \mathcal{E}_{\text{rf}}^2 / 4\hbar$ denotes the Stark shift, $|u_i|^2$ is the population of $|i\rangle$, and $\Delta_R \equiv \Delta_p + \Delta_c$ is known as the two-photon Raman detuning. Thus the effect of the rf-field is to introduce a temporal modulation of the coupling detuning, Δ_c , with a frequency of $2\omega_{\text{rf}}$. Note that for a very large value of modulation frequency, i.e., when the time scale of the rf modulation is much smaller than the coherence time of the system, the rf field oscillates so fast that the system cannot respond to the rf field in a short period of time. Hence, the system responds to the average effect of the rf field, rather than its instantaneous value. In this limit, the change in Δ_c due to the rf field can be replaced by the time-averaged value of $2\Sigma \sin^2 \omega_{\text{rf}}t$, i.e., Σ , which is effectively equivalent to a dc Stark shift [74, 144, 145].

The general solution of Equation (6.3) has an oscillatory form whose frequency components are characterised by the so called characteristic frequency (the frequency at which the population oscillates as if there were no rf interaction) and the harmonic of $2\omega_{\text{rf}}$, i.e., the frequency of the driving rf field (more details of this can be found in Subsection 6.3.1). In the actual system, however, the oscillatory solution is dampened by relaxation (or decay) processes. To include the latter into the model, we assume that the intermediate and Rydberg states have the decay linewidths of Γ_b and Γ_c , respectively, and the laser linewidths of probe and coupling lasers are γ_p and γ_c , respectively [84].

The equations of motion then are

$$\dot{\rho}_{aa} = \Gamma_b \rho_{bb} + \frac{i\Omega_p}{2}(\rho_{ab} - \rho_{ba}), \quad (6.4a)$$

$$\dot{\rho}_{bb} = -\Gamma_b \rho_{bb} + \Gamma_c \rho_{cc} - \frac{i\Omega_p}{2}(\rho_{ab} - \rho_{ba}) + \frac{i\Omega_c}{2}(\rho_{bc} - \rho_{cb}), \quad (6.4b)$$

$$\dot{\rho}_{cc} = -\Gamma_c \rho_{cc} - \frac{i\Omega_c}{2}(\rho_{bc} - \rho_{cb}), \quad (6.4c)$$

$$\dot{\rho}_{ab} = -\left(i\Delta_p + \frac{\Gamma_b}{2} + \gamma_p\right)\rho_{ab} - \frac{i\Omega_p}{2}(\rho_{bb} - \rho_{aa}) + \frac{i\Omega_c}{2}\rho_{ac}, \quad (6.4d)$$

$$\begin{aligned} \dot{\rho}_{bc} = & -\left(i\Delta_c - 2i\Sigma \sin^2 \omega_{\text{rf}}t + \frac{\Gamma_b + \Gamma_c}{2} + \gamma_c\right)\rho_{bc} \\ & - \frac{i\Omega_c}{2}(\rho_{cc} - \rho_{bb}) - \frac{i\Omega_p}{2}\rho_{ac}, \end{aligned} \quad (6.4e)$$

$$\dot{\rho}_{ac} = -\left(i\Delta_R - 2i\Sigma \sin^2 \omega_{\text{rf}}t + \frac{\Gamma_c}{2} + \gamma_p + \gamma_c\right)\rho_{ac} + \frac{i\Omega_c}{2}\rho_{ab} - \frac{i\Omega_p}{2}\rho_{bc}, \quad (6.4f)$$

where ρ_{ij} is the element of the density operator. The decay mechanism dampens the dynamical evolution of the system until the oscillation is purely driven by the rf field, in which the oscillation contains purely the frequency of the harmonic of $2\omega_{\text{rf}}$. The physical quantities observed in the experiment, e.g., the absorption coefficient or population transferred, are the averages of the harmonic solutions over one period of the oscillation. This is mathematically defined as,

$$\langle \rho_{ij}(\infty) \rangle = \frac{1}{T} \lim_{t \rightarrow \infty} \int_t^{t+T} \rho_{ij}(t') dt', \quad (6.5)$$

where T is the period of the oscillation. For example, the absorption coefficient of the system is proportional to $\text{Im}[\langle \rho_{ab}(\infty) \rangle]$.

In the zero rf field limit ($\Sigma = 0$), Equation (6.3) and (6.4) are the equations of motion for the usual three-level system, in which, for the weak probe regime, the coupling field dresses the bare states $|b\rangle$ and $|c\rangle$ to form dressed states and the resonances occur when the ground state $|a\rangle$ and one of these dressed states are degenerate [132]. The transmission lineshape of the resonances is known as an Autler-Townes doublet [43].

Since the dressed states formation is important to the way the resonance lineshapes of the system are constructed, it is useful to study the dressed state formation between states $|b\rangle$ and $|c\rangle$. Later in Section 6.4, the description of

these dressed states is used to study the case in which the rf field is turned on for the three-level system. To understand the formation of dressed states, we investigate the equations of motion for the subsystem containing only $|b\rangle$ and $|c\rangle$. It is assumed that the ground state, $|a\rangle$, is excluded from the system and the intermediate state, $|b\rangle$, is treated as a metastable state with a long life time, i.e., we assume no decay from this state. Setting Δ_p and Ω_p to zero, the time-dependent Schrödinger equation is

$$\frac{d}{dt} \begin{pmatrix} u_b \\ u_c \end{pmatrix} = \begin{pmatrix} 0 & -i\Omega_c/2 \\ -i\Omega_c/2 & i[\Delta_c - 2\Sigma \sin^2 \omega_{\text{rf}} t] \end{pmatrix} \begin{pmatrix} u_b \\ u_c \end{pmatrix}. \quad (6.6)$$

In the zero rf field limit, Equation (6.6) is the equation of motion for a two-level system, whose solution is the Rabi oscillation, and the system is on resonance when $\Delta_c = 0$. Similarly, for large ω_{rf} , the system feels the average rf field and the excited state is shifted by Σ [74, 144, 145].

The equations of motion, describing the dynamical evolution with the relaxation process, are

$$\dot{\rho}_{bb} = \Gamma_c \rho_{cc} + \frac{i\Omega_c}{2} (\rho_{bc} - \rho_{cb}), \quad (6.7a)$$

$$\dot{\rho}_{cc} = -\Gamma_c \rho_{cc} + \frac{i\Omega_c}{2} (\rho_{cb} - \rho_{bc}), \quad (6.7b)$$

$$\dot{\rho}_{bc} = -\left\{ \frac{\Gamma_c}{2} + \gamma_c + i[\Delta_c - 2\Sigma \sin^2 \omega_{\text{rf}} t] \right\} \rho_{bc} + \frac{i\Omega_c}{2} (\rho_{bb} - \rho_{cc}). \quad (6.7c)$$

The physical quantities extracted from these equations are obtained in a similar way as given by Equation (6.5), for example, the population lineshape is $\langle \rho_{cc}(\infty) \rangle$.

We could numerically solve Equation (6.3) and (6.4) for a three-level system, as well as Equation (6.6) and (6.7) for the two-level subsystem, for the dynamical evolution. However, the disadvantage of this method is that the physics of the resonance formation, as well as the sideband structure, cannot be understood and explained in this framework. The better way to view such systems is to look at their eigenenergy spectrum and solutions in the framework of Floquet formalism, which is described in the next section.

6.2 Floquet formalism of rf-dressed two-level subsystems

In this section we investigate the formation of resonance structures using the Floquet-Fourier formalism. Exploiting the symmetry of the Hamiltonian, we introduce a new approximation, a so called iteration method, to estimate the positions of the resonances to a good accuracy, compared to the perturbation method. Furthermore the differences between the Floquet-Fourier method and the N -level approximation are discussed.

6.2.1 Floquet Hamiltonian

Equation (6.6) is a linear ordinary differential equation (ODE) with periodic Hamiltonian matrix. Such ODEs can be solved by the Floquet-Fourier method [45, 66, 146, 147]. The benefit of this method is to turn the time-dependent ODE problem into a time-independent eigenvalue problem. As the Hamiltonian is periodic in time, the solution can be written as the product between the phase factor $\exp(i\epsilon_k t)$ and a time-periodic function, which can be expanded in a Fourier series¹. Thus the form of the solution is,

$$|u(t)\rangle = e^{-i\epsilon_k t} \sum_{n=-\infty}^{\infty} e^{-2in\omega_{\text{rf}} t} |F_n(\epsilon_k)\rangle, \quad (6.8)$$

where $|u(t)\rangle$ represent the column vector of $u_{b(c)}$, $|F_n(\epsilon_k)\rangle = (b_n, c_n)^T$ is the n -th harmonic component of the Fourier expansion associated with $|b\rangle$ and $|c\rangle$, and $(\hbar)\epsilon_k$ is quasienergy². Substituting Equation (6.8) into equation (6.6) and using the Trigonometric identity

$$\sin^2 \theta = \frac{1}{4} [2 - \exp(2i\theta) - \exp(-2i\theta)], \quad (6.9)$$

¹c.f. Bloch's theorem for the periodic Hamiltonian in space [148].

²We will set $\hbar = 1$ throughout the chapter from this point.

the ODE turns into the coupled difference equations,

$$\frac{\Omega_c}{2}c_n - 2n\omega_{\text{rf}}b_n = \epsilon_k b_n, \quad (6.10a)$$

$$(\Sigma - \Delta_c - 2n\omega_{\text{rf}})c_n + \frac{\Omega_c}{2}b_n - \frac{\Sigma}{2}(c_{n-1} + c_{n+1}) = \epsilon_k c_n, \quad (6.10b)$$

which can be written in the matrix form as

$$\hat{H}_{2F} |\Psi\rangle_k = \epsilon_k |\Psi\rangle_k, \quad (6.11)$$

where $|\Psi\rangle_k$ is the infinite column vector whose components are the harmonic components b_n and c_n , i.e., $|\Psi\rangle_k = (\dots, b_{-1}, b_0, b_{+1}, \dots, c_{-1}, c_0, c_{+1}, \dots)^T$. \hat{H}_{2F} , known as Floquet Hamiltonian, is an infinite Hermitian matrix. If we define the Floquet state, $|\phi, n\rangle$, where ϕ represents the atomic states and n is the harmonic component of Fourier expansion, then the state vector $|\Psi\rangle_k$ is

$$|\Psi\rangle_k = \sum_{m=-\infty}^{\infty} (a_m |a, m\rangle + b_m |b, m\rangle), \quad (6.12)$$

where ϕ_m is the coefficient of $|\phi, m\rangle$.

In this basis the matrix representation of \hat{H}_{2F} is

$$\mathbf{H}_{2F} = \begin{pmatrix} \ddots & \vdots & \vdots & \vdots & \vdots & \vdots & \vdots & \vdots & \vdots \\ \cdots & 2\omega_{\text{rf}} & 0 & 0 & \cdots & \Omega_c/2 & 0 & 0 & \cdots \\ \cdots & 0 & 0 & 0 & \cdots & 0 & \Omega_c/2 & 0 & \cdots \\ \cdots & 0 & 0 & -2\omega_{\text{rf}} & \cdots & 0 & 0 & \Omega_c/2 & \cdots \\ \cdots & \vdots & \vdots & \vdots & \cdots & \vdots & \vdots & \vdots & \cdots \\ \cdots & \Omega_c/2 & 0 & 0 & \cdots & \Sigma - \Delta_c + 2\omega_{\text{rf}} & -\Sigma/2 & 0 & \cdots \\ \cdots & 0 & \Omega_c/2 & 0 & \cdots & -\Sigma/2 & \Sigma - \Delta_c & -\Sigma/2 & \cdots \\ \cdots & 0 & 0 & \Omega_c/2 & \cdots & 0 & -\Sigma/2 & \Sigma - \Delta_c - 2\omega_{\text{rf}} & \cdots \\ \vdots & \vdots & \vdots & \vdots & \vdots & \vdots & \vdots & \vdots & \ddots \end{pmatrix}. \quad (6.13)$$

\mathbf{H}_{2F} can be partitioned into four block matrices: the two different block matrices along the diagonal of and the two similar block (and diagonal)

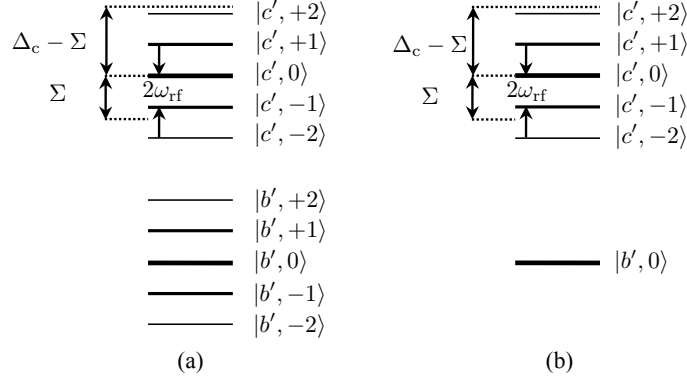


Figure 6.2: A schematic of the manifolds of the rf-dressed two-level subsystem is shown in (a). Only the manifolds of the intermediate and excited states are taken into account. It is also assumed that the intermediate state is metastable, i.e., $\Gamma_b = 0$. The N -level approximation, containing only the excited state manifold and the zeroth harmonic Floquet state from the intermediate state manifold, is shown in (b).

matrices on the off-diagonal of \mathbf{H}_{2F} . The block matrix on the top left of the diagonal, \mathbf{H}_b , is diagonal and represents the manifold of the ground state, while that of the lower right, \mathbf{H}_c , represents the manifold of the excited state. The off diagonal block matrix couples the manifold of $|b\rangle$ to that of $|c\rangle$. Note that the whole excited manifold is shifted by Σ in the frequency space with respect to the zero rf field. The energy interval between any adjacent Floquet states within the same manifold is $2\omega_{\text{rf}}$, which is consistent with the frequency of the driving term in Equation (6.6). While \mathbf{H}_b is already diagonalised, \mathbf{H}_c is not; the rf field couples $|c, n\rangle$ to $|c, n \pm 1\rangle$ with the interaction strength Σ . Mathematically, this means that the basis vector $|c, n\rangle$ is not an eigenvector of the operator \hat{H}_c as

$$\hat{H}_c |c, n\rangle = -\frac{\Sigma}{2} |c, n-1\rangle + (\Sigma - \Delta_c - 2n\omega_{\text{rf}}) |c, n\rangle - \frac{\Sigma}{2} |c, n+1\rangle. \quad (6.14)$$

Due to the rf field, each Floquet state in the ground state manifold is effectively connected to all Floquet states in the excited state manifold.

Without the rf field, i.e., $\Sigma = 0$, the system would reduce to an infinite number of independent (non-interacting) two-level systems, whose quasienergies are

$$\epsilon_{\pm,n} = -\frac{\Delta_c}{2} \pm \frac{1}{2} \sqrt{\Delta_c^2 + \Omega_c^2} \pm 2n\omega_{\text{rf}}, \quad (6.15)$$

and the eigenvectors of the system are

$$|\Psi\rangle_{+,n} = \sin\theta |b, n\rangle + \cos\theta |c, n\rangle, \quad (6.16a)$$

$$|\Psi\rangle_{-,n} = \cos\theta |b, n\rangle - \sin\theta |c, n\rangle, \quad (6.16b)$$

where \pm represents the two dressed states formed by the laser interaction and $\tan 2\theta = -\Omega_c/\Delta_c$ [68]. Substituting Equation (6.15) and (6.16) into Equation (6.8), the result is identical to the usual Rabi oscillation for two-level system. It is possible to work in the basis such that \hat{H}_c is diagonalised by using the basis transformation

$$|c', n\rangle = \sum_{k=-\infty}^{\infty} J_{n-k} \left(\frac{\Sigma}{2\omega_{\text{rf}}} \right) |c, k\rangle, \quad (6.17)$$

where $J_\mu(x)$ is the μ -th order Bessel function of the first kind (see Appendix B for further details). The eigenvalues of the system are obtained by acting \hat{H}_c on $|c', n\rangle$:

$$\begin{aligned} \hat{H}_c |c', n\rangle &= \sum_{k=-\infty}^{\infty} J_{n-k} \left[-\frac{\Sigma}{2} |c, k-1\rangle - \frac{\Sigma}{2} |c, k+1\rangle + (\Sigma - \Delta_c - 2k\omega_{\text{rf}}) |c, k\rangle \right] \\ &= \sum_{k=-\infty}^{\infty} \left[-\frac{\Sigma}{2} J_{n-k} |c, k-1\rangle - \frac{\Sigma}{2} J_{n-k} |c, k+1\rangle + (\Sigma - \Delta_c - 2k\omega_{\text{rf}}) J_{n-k} |c, k\rangle \right] \\ &= \sum_{k=-\infty}^{\infty} \left[-\frac{\Sigma}{2} J_{n-k-1} |c, k\rangle - \frac{\Sigma}{2} J_{n-k+1} |c, k\rangle + (\Sigma - \Delta_c - 2k\omega_{\text{rf}}) J_{n-k} |c, k\rangle \right] \\ &= \sum_{k=-\infty}^{\infty} \left[-\frac{\Sigma}{2} (J_{n-k-1} + J_{n-k+1}) + (\Sigma - \Delta_c - 2k\omega_{\text{rf}}) J_{n-k} \right] |c, k\rangle \\ &= \sum_{k=-\infty}^{\infty} \left[2k\omega_{\text{rf}} - 2n\omega_{\text{rf}} + \Sigma - \Delta_c - 2k\omega_{\text{rf}} \right] J_{n-k} |c, k\rangle \\ &= (\Sigma - \Delta_c - 2n\omega_{\text{rf}}) \sum_{k=-\infty}^{\infty} J_{n-k} |c, k\rangle \\ &= (\Sigma - \Delta_c - 2n\omega_{\text{rf}}) |c', n\rangle, \end{aligned} \quad (6.18)$$

where we have used the recurrence relation [133]

$$J_{n-k-1} + J_{n-k+1} = \frac{4\omega_{\text{rf}}(n-k)}{\Sigma} J_{n-k}, \quad (6.19)$$

and $J_n \equiv J_n(\Sigma/2\omega_{\text{rf}})$. Thus $|c', n\rangle$ is indeed an eigenvector of \hat{H}_c and the corresponding quasienergy (eigenvalue) is

$$\epsilon'_n = \Sigma - \Delta_c - 2n\omega_{\text{rf}}. \quad (6.20)$$

According to Equation (6.17), the effect of the rf field is to mix the old Floquet states, $|c, n\rangle$, to form the new Floquet states, $|c', n\rangle$, where the coefficients are given by Bessel functions. The energy spacing between the adjacent Floquet states remains unchanged, i.e., $2\omega_{\text{rf}}$ as shown by Equation (6.20). This manifold structure is schematically shown in Figure 6.2(a). This result is the same as in Chapter 5 and in previous work, in which the rf field turns the excited state into the manifold and the probability of each element to be found is given by the squared Bessel function [25, 43, 47, 50, 51, 53, 138].

Under this transformation the element of \hat{H}_c in the matrix representation is

$$\begin{aligned} \langle c', n | \hat{H}_c | c', m \rangle &= (\Sigma - \Delta_c - 2m\omega_{\text{rf}}) \langle c', n | c', m \rangle \\ &= (\Sigma - \Delta_c - 2m\omega_{\text{rf}}) \sum_{p,q} J_{n-p} J_{m-q} \langle c, p | c, q \rangle \\ &= (\Sigma - \Delta_c - 2m\omega_{\text{rf}}) \sum_{p,q} J_{n-p} J_{m-q} \delta_{p,q} \\ &= (\Sigma - \Delta_c - 2m\omega_{\text{rf}}) \sum_{p,q} J_{n-p} J_{m-p} \\ &= (\Sigma - \Delta_c - 2m\omega_{\text{rf}}) J_{n-m}(0) \\ &= (\Sigma - \Delta_c - 2m\omega_{\text{rf}}) \delta_{n,m}, \end{aligned} \quad (6.21)$$

where we have used the addition theorem [133]

$$J_n(u \pm v) = \sum_{k=-\infty}^{\infty} J_{n \mp k}(u) J_k(v). \quad (6.22)$$

The coupling terms of \hat{H}_{2F} also transform to

$$\begin{aligned}
 \langle b', n | \hat{H}_{2F} | c', m \rangle &= \sum_k J_{m-k} \langle b, n | \hat{H}_{2F} | c, k \rangle \\
 &= \sum_k J_{m-k} \left(\frac{\Omega_c}{2} \delta_{n,k} \right) \\
 &= \frac{\Omega_c}{2} J_{m-n},
 \end{aligned} \tag{6.23}$$

and

$$\begin{aligned}
 \langle c', n | \hat{H}_{2F} | b', m \rangle &= \sum_k J_{n-k} \langle c, k | \hat{H}_{2F} | b, m \rangle \\
 &= \sum_k J_{n-k} \left(\frac{\Omega_c}{2} \delta_{m,k} \right) \\
 &= \frac{\Omega_c}{2} J_{n-m}.
 \end{aligned} \tag{6.24}$$

Thus, the Floquet Hamiltonian, in the new basis set, is

$$\mathbf{H}'_{2F} = \begin{pmatrix} \ddots & \vdots & \vdots & \vdots & \vdots & \vdots & \vdots & \vdots & \\ \cdots & 2\omega_{\text{rf}} & 0 & 0 & \cdots & \Omega_c J_0/2 & \Omega_c J_{+1}/2 & \Omega_c J_{+2}/2 & \cdots \\ \cdots & 0 & 0 & 0 & \cdots & \Omega_c J_{-1}/2 & \Omega_c J_0/2 & \Omega_c J_{+1}/2 & \cdots \\ \cdots & 0 & 0 & -2\omega_{\text{rf}} & \cdots & \Omega_c J_{-2}/2 & \Omega_c J_{-1}/2 & \Omega_c J_0/2 & \cdots \\ \cdots & \vdots & \vdots & \vdots & \cdots & \vdots & \vdots & \vdots & \cdots \\ \cdots & \Omega_c J_0/2 & \Omega_c J_{-1}/2 & \Omega_c J_{-2}/2 & \cdots & \Sigma - \Delta_c + 2\omega_{\text{rf}} & 0 & 0 & \cdots \\ \cdots & \Omega_c J_{+1}/2 & \Omega_c J_0/2 & \Omega_c J_{-1}/2 & \cdots & 0 & \Sigma - \Delta_c & 0 & \cdots \\ \cdots & \Omega_c J_{+2}/2 & \Omega_c J_{+1}/2 & \Omega_c J_0/2 & \cdots & 0 & 0 & \Sigma - \Delta_c - 2\omega_{\text{rf}} & \cdots \\ & \vdots & \vdots & \vdots & \vdots & \vdots & \vdots & \vdots & \ddots \end{pmatrix}. \tag{6.25}$$

Now the whole interaction block matrices are filled by Rabi frequencies scaled by J_n ; and hence, any two Floquet states between the two manifolds couple to each other, i.e., $|b', n\rangle$ couples to $|c', m\rangle$, via $\Omega_c J_{m-n}$. This picture turns the n -photon interaction into a one-photon interaction whose coupling strength

is scaled by the Bessel function. For example, $|b', 0\rangle$ couples to $|c', 3\rangle$ via one-photon transition, whose strength is $\Omega_c J_{+3}$.

The structure of Floquet Hamiltonian and the vanishing of the Bessel functions for large order suggests that the rf-dressed system could be viewed as an isolated system of a ground state $|b', 0\rangle$ interacting with the Floquet states of the excited state manifold, $|c', n\rangle$, via one-photon interaction. We refer to this picture as the N -level approximation. This N -level picture is very useful in practical calculations and it has been used in Chapter 5 and in previous work to explain the physics of rf-dressed systems [25, 47, 51, 53, 142]. However, we have found that this picture is only applicable in certain conditions. In order to obtain the conditions in which it is valid, we further examine the eigenspectrum of the Floquet Hamiltonian.

6.2.2 Quasienergy spectrum

Because of the infinite dimension of the Floquet Hamiltonian, one would expect \mathbf{H}'_{2F} (or \mathbf{H}_{2F}) to have an infinite number of quasienergies. However, as the Hamiltonian is periodic and the system contains two levels, the quasienergy has a structure of double combs, where the set of quasienergies in each comb is associated with each atomic state. Diagonalising \mathbf{H}'_{2F} (or \mathbf{H}_{2F}) and letting $\epsilon''_{b,n}$ and $\epsilon''_{c,n}$ be the new quasienergies of the n -th harmonic of the new Floquet state (the dressed Floquet state), $|b'', n\rangle$ and $|c'', n\rangle$, then the quasienergies of \mathbf{H}'_{2F} are

$$\epsilon''_{b,n} = \epsilon''_{b,0} + 2n\omega_{\text{rf}}, \quad (6.26a)$$

$$\epsilon''_{c,n} = \epsilon''_{c,0} + 2n\omega_{\text{rf}}, \quad (6.26b)$$

where $\epsilon''_{b,0}$ and $\epsilon''_{c,0}$ are the zeroth harmonic quasienergies. The repeated structure of the quasienergy spectrum, given by Equation (6.26), is shown in Figure 6.3(a), where the dark red lines represent the excited state manifold and the light blue are the ground state manifold.

To approximate the quasienergy, we, first, consider the off-diagonal block Toeplitz matrices [149] of Equation (6.25), \mathbf{V} , in which the elements on the same diagonal are identical. The size of the elements of the matrix of the n -th diagonal away from the main diagonal ($n = 0$), $\Omega_c J_n/2$, couple the Floquet states $|b', m\rangle$ with $|c', n + m\rangle$. Moreover, this Toeplitz matrix is symmetric (neglecting the plus and minus signs). Supposing that the argument of the Bessel function is small, i.e., $\Sigma/2\omega_{\text{rf}} \ll 1$, the value of the Bessel function decreases when its order increases; and thus \mathbf{V} is approximately a diagonal matrix whose diagonal elements are $\Omega_c J_0/2$. With this approximation, the quasienergies of the zeroth harmonic are,

$$\epsilon_{b,0}''^{(1)} = \frac{1}{2}(\Sigma - \Delta_c) - \frac{1}{2}\sqrt{(\Sigma - \Delta_c)^2 + \Omega_c^2 J_0^2}, \quad (6.27a)$$

$$\epsilon_{c,0}''^{(1)} = \frac{1}{2}(\Sigma - \Delta_c) + \frac{1}{2}\sqrt{(\Sigma - \Delta_c)^2 + \Omega_c^2 J_0^2}. \quad (6.27b)$$

The superscript 1 means the first iteration of the quasienergy. This interaction lifts up the degeneracy between $|b', n\rangle$ and $|c', n\rangle$ and causes the avoided-crossing at $\Delta_c = \Sigma$ as shown in Figure 6.3(a). It is clear that if there is no rf field, i.e., $\Sigma = 0$, then Equation (6.27) is identical to Equation (6.15) and the effect of Stark shift disappears.

The sets of quasienergies built from Equation (6.27) produce the level-crossings on both sides of the zeroth order avoided-crossing. The degeneracy of these level-crossings is lifted by the interaction $\Omega_c J_{\pm 1}$, which couples $|b', n\rangle$ with $|c', n \pm 1\rangle$. The improved quasienergies, obtained by calculating the shift in energy due to the interaction of $\Omega_c J_{\pm 1}$ at the level-crossings, are

$$\epsilon_{b,n}''^{(2)} = \frac{1}{2}(\epsilon_{b,0}''^{(1)} + \epsilon_{c,0}''^{(1)} - 2\omega_{\text{rf}}) + \frac{1}{2}\sqrt{(\epsilon_{b,0}''^{(1)} - \epsilon_{c,0}''^{(1)} + 2\omega_{\text{rf}})^2 + \Omega_c^2 J_1^2} + 2n\omega_{\text{rf}}, \quad (6.28a)$$

$$\epsilon_{c,n}''^{(2)} = \frac{1}{2}(\epsilon_{b,0}''^{(1)} + \epsilon_{c,0}''^{(1)} - 2\omega_{\text{rf}}) - \frac{1}{2}\sqrt{(\epsilon_{b,0}''^{(1)} - \epsilon_{c,0}''^{(1)} + 2\omega_{\text{rf}})^2 + \Omega_c^2 J_1^2} + 2(n+1)\omega_{\text{rf}}. \quad (6.28b)$$

This is the second iteration of the quasienergy (as labelled by superscript 2). If one wants to include $(n - 1)$ -th interaction, one has to iterate the

quasienergy n times. We refer to this method as the iteration method. The principle of this method is based on the periodic structure of the quasienergy spectrum and the Toeplitz structure of the matrix, \mathbf{V} . The quasienergy calculated from Equation (6.28a) (shown as the crossed line) for $\Omega_c = \Sigma = \omega_{\text{rf}} = 2\pi \times 10$ MHz is plotted in Figure 6.3(a), whereas the actual quasienergy calculated by numerically diagonalising \mathbf{H}'_{2F} is shown in Figure 6.3(b).

We could also use perturbation theory to calculate the quasienergy of the system. For an interval of Δ_c around the $(m - n)$ -th resonance where $|b', n\rangle$ is nearly degenerate with $|c', m\rangle$, the interaction around the avoided crossing is given by a 2×2 matrix

$$\begin{pmatrix} -2n\omega_{\text{rf}} - \zeta_{m-n} & \Omega_c J_{m-n}/2 \\ \Omega_c J_{m-n}/2 & \Sigma - \Delta_c - 2m\omega_{\text{rf}} + \zeta_{m-n} \end{pmatrix}, \quad (6.29)$$

where ζ_{m-n} is the correction due to the interaction between $|b', n\rangle$ (and $|c', m\rangle$) and the other states through $\Omega_c J_k/2$, except for the interaction between $|b', n\rangle$ and $|c', m\rangle$ themselves, i.e., $k \neq m - n$. ζ_{m-n} is calculated using perturbation theory with the result

$$\zeta_{m-n} = \sum_{k \neq m-n} \frac{(\Omega_c J_k/2)^2}{\Sigma - \Delta_c - 2k\omega_{\text{rf}}}. \quad (6.30)$$

Thus the quasienergies are the eigenvalues of Equation (6.29) and they are given by

$$\begin{aligned} \epsilon''_{b,n} = & \frac{1}{2}(\Sigma - \Delta_c - 2(n+m)\omega_{\text{rf}}) + \frac{1}{2}\{[\Sigma - \Delta_c - 2(n+m)\omega_{\text{rf}}]^2 + \Omega_c^2 J_{m-n}^2 \\ & + 4(2n\omega_{\text{rf}} + \zeta_{m-n})(\Sigma - \Delta_c - 2m\omega_{\text{rf}} + \zeta_{m-n})\}^{1/2}, \end{aligned} \quad (6.31a)$$

$$\begin{aligned} \epsilon''_{c,m} = & \frac{1}{2}(\Sigma - \Delta_c - 2(n+m)\omega_{\text{rf}}) - \frac{1}{2}\{[\Sigma - \Delta_c - 2(n+m)\omega_{\text{rf}}]^2 + \Omega_c^2 J_{m-n}^2 \\ & + 4(2n\omega_{\text{rf}} + \zeta_{m-n})(\Sigma - \Delta_c - 2m\omega_{\text{rf}} + \zeta_{m-n})\}^{1/2}. \end{aligned} \quad (6.31b)$$

The disadvantage of the perturbation method is that it is only correct around the avoided-crossing between $|b', n\rangle$ and $|c', m\rangle$, while it fails at all the other

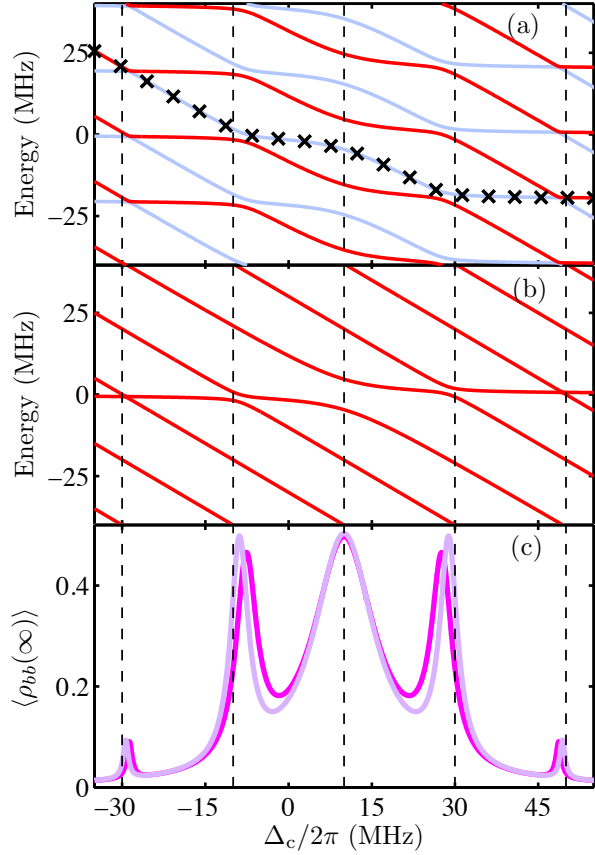


Figure 6.3: The quasienergy spectrum of H'_{2F} and $\langle \rho_{bb}(\infty) \rangle$ are shown in (a) and (c) (dark pink line), respectively, whereas the similar plots in (b) and (c) (light purple) are calculated from H_{2N} . We have taken N upto 4. The parameters used in this figure are $\Omega_c = \Sigma = \omega_{\text{rf}} = 2\pi \times 10$ MHz and $\Gamma_c = 2\pi \times 1$ MHz. In plot (a), the eigenspectrum shows the repeated structure with the period of $2\omega_{\text{rf}}$. The crossed line represents the quasienergy calculated from Equation (6.28). The Stark shift of the zeroth order resonance and the higher order sidebands are clearly shown in (c). The positions of the n -th avoided-crossings calculated from H_{2N} are half of those calculated from H'_{2F} . This is clearly illustrated in (c). This half-reduction of the shift comes from the symmetry breaking the H_{2N} . Since $|\Omega_c J_0 / 2\omega_{\text{rf}}| \approx 0.5$, which is relatively large, the agreement between the two lineshapes is not perfect.

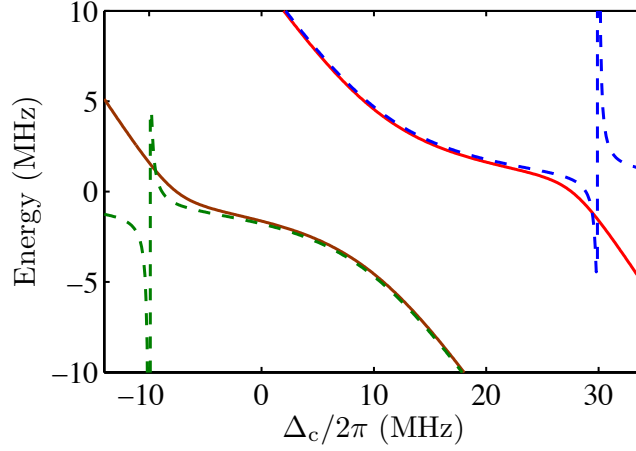


Figure 6.4: (solid lines) The quasienergy calculated using the iteration method. (dashed lines) The quasienergy calculated using the perturbation method in which the interaction around the zeroth avoided-crossing is of interest. The parameters used in this figure are the same as those used in Figure 6.3. The quasienergies calculated from the perturbation method are in good agreement with those calculated using the iteration method for Δ_c around the zeroth avoided crossing. The poles of ζ_0 result in the glitches in the quasienergies around $n = \pm 1$, shown in the figure.

avoided-crossings due to the poles $\Sigma - 2k\omega_{\text{rf}}$ in Equation (6.30). On the other hand, the iteration method is valid for both degenerate and non-degenerate cases as there are no poles presented in Equation (6.27) and (6.28).

Figure 6.4 shows the quasienergies calculated from Equation (6.28) (solid lines) around the zeroth avoided-crossing and those calculated from Equation (6.31) (dashed lines). The parameters used in the figure are the same as those used in Figure 6.3. The results from both methods are clearly in good agreement only when Δ_c is around zeroth order avoided-crossing. The glitches of the quasienergies at $n = \pm 1$, illustrated in the figure, are caused by the poles of ζ_0 .

According to Figure 6.3(a), the position of the first order avoided-crossings are not exactly at $\Delta_c = \pm 2\omega_{\text{rf}}$, which is the energy separation between the

adjacent Floquet states. But they are slightly shifted towards the zeroth order avoided-crossing due to the effect of the finite Rabi coupling Ω_c . Thus the Floquet formalism predicts a slight shift in frequency which has not been discussed in previous works [43, 46–51, 53]. The position of the first order avoided-crossings can be determined by searching for the level-crossings of the quasienergies given by Equation (6.27), and this gives

$$\Delta_c^{\pm 1} = \Sigma \mp \sqrt{4\omega_{\text{rf}}^2 - \Omega_c^2 J_0^2}. \quad (6.32)$$

Note that Equation (6.32) can be obtained by setting the terms in the bracket under the square root of Equation (6.28) to zero, as, at this detuning, the quasienergy changes its curvature, which corresponds to an avoided-crossing [45]. Using Equation (6.32), the first order approximation of the first avoided-crossing is $\Delta_c^{\pm 1} \approx \Sigma \mp 2\omega_{\text{rf}} \pm \delta$, where $\delta = \Omega_c J_0^2 / 4\omega_{\text{rf}}$.

One could obtain the the first order resonance position using perturbation theory by considering the interaction between $|b', 0\rangle$ and $|c', -1\rangle$. The 2×2 matrix which represents this interaction is

$$\begin{pmatrix} -\zeta_{-1} & \Omega_c J_{-1}/2 \\ \Omega_c J_{-1}/2 & \Sigma - \Delta_c + 2\omega_{\text{rf}} + \zeta_{-1} \end{pmatrix}, \quad (6.33)$$

with

$$\zeta_{-1} = \sum_{k \neq -1} \frac{(\Omega_c J_k/2)^2}{\Sigma - \Delta_c - 2k\omega_{\text{rf}}}. \quad (6.34)$$

The resonance occurs when the elements on the diagonal are degenerate, i.e., $\Sigma - \Delta_c + 2\omega_{\text{rf}} + \zeta_{-1} = -\zeta_{-1}$. Assuming that the first resonance occurs at

$\Delta_c = \Sigma + 2\omega_{\text{rf}} - \delta$, then we have

$$\begin{aligned}
 \delta &= -2\zeta_{-1} \\
 &= \sum_{k \neq -1} \frac{2(\Omega_c J_k/2)^2}{2k\omega_{\text{rf}} + 2\omega_{\text{rf}} - \delta} \\
 &= \sum_{k \neq -1} \frac{2(\Omega_c J_k/2)^2}{2(k+1)\omega_{\text{rf}}} \left(1 - \frac{\delta}{2\omega_{\text{rf}}(k+1)}\right)^{-1} \\
 &= \sum_{k \neq -1} \frac{2(\Omega_c J_k/2)^2}{2(k+1)\omega_{\text{rf}}} \left[1 + \mathcal{O}\left(\frac{\delta}{2\omega_{\text{rf}}(k+1)}\right)\right] \\
 &\approx \sum_{k \neq -1} \frac{(\Omega_c J_k/2)^2}{(k+1)\omega_{\text{rf}}}, \tag{6.35}
 \end{aligned}$$

in which the leading term of the expansion yields the same result as that obtained using the iteration method.

Consider the zeroth order avoided-crossing ($\Delta_c^0 = \Sigma$), the energy gap between the n -th dressed Floquet states, i.e., $|b'', n\rangle$ and $|c'', n\rangle$, is given by $\Omega_c J_0$ from Equation (6.27). Thus, for small Ω_c compared to ω_{rf} , the energy separation between the adjacent pairs of the dressed Floquet states is larger than the energy gap of the dressed Floquet state. The mathematical equivalent of this statement is

$$\left| \frac{\Omega_c J_0}{2\omega_{\text{rf}}} \right| \ll 1. \tag{6.36}$$

This means that each pair of the dressed Floquet states can approximately be treated independently from one another. In addition, $|c'', n-1\rangle$ and $|b'', n+1\rangle$ asymptotically approach $|c', n-1\rangle$ and $|c', n+1\rangle$ respectively. The system is, now, similar to the case in which the ground state $|b', 0\rangle$ interacts with the manifold of excited state with the coupling $\Omega_c J_n$, i.e., the N -level approximation. When $|\Omega_c J_0| \geq 2\omega_{\text{rf}}$, the pair of the dressed Floquet states overlap with the next and causes the failures of the iteration method, as well as of the N -level approximation. This will be discussed in Subsection 6.2.3. We can obtain Equation (6.36) by noting that the argument of the square root of Equation (6.32) must be positive in order to make the square root meaningful, i.e., a real number.

The condition $\Sigma/2\omega_{\text{rf}} \ll 1$, imposed previously, is now no longer required as long as Equation (6.36) is satisfied. This is because $\Sigma/2\omega_{\text{rf}}$ is included as the argument of the Bessel function in Equation (6.36). Figure 6.6(b) shows the lineshape calculated for $\Sigma/2\omega_{\text{rf}} = 2$. The lineshape shows the strong evidence of the sideband resonances even though $\Sigma/2\omega_{\text{rf}} > 1$. Note that for a large value of $\Sigma/2\omega_{\text{rf}}$, the avoided-crossings (as well as the sideband resonances) disappear because the Bessel function vanishes for large argument.

6.2.3 N -level approximation

If we are in the regime where Equation (6.36) is satisfied, the N -level picture is a good approximation for the rf-dressed system. The diagram shown in Figure 6.1(b) describes the N -level picture. It is composed of a ground state, $|b', 0\rangle$, the manifold of the excited state, $|c', n\rangle$ and the Rabi coupling between $|b', 0\rangle$ and $|c', n\rangle$, given by $\Omega_c J_n$ from \mathbf{H}'_{2F} ; thus, the matrix form of the Hamiltonian of N -level system, \mathbf{H}_{2N} , is

$$\mathbf{H}_{2N} = \begin{pmatrix} 0 & \cdots & \Omega_c J_{-1}/2 & \Omega_c J_0/2 & \Omega_c J_{+1}/2 & \cdots \\ \vdots & \ddots & \vdots & \vdots & \vdots & \cdots \\ \Omega_c J_{-1}/2 & \cdots & \Sigma - \Delta_c + 2\omega_{\text{rf}} & 0 & 0 & \cdots \\ \Omega_c J_0/2 & \cdots & 0 & \Sigma - \Delta_c & 0 & \cdots \\ \Omega_c J_{+1}/2 & \cdots & 0 & 0 & \Sigma - \Delta_c - 2\omega_{\text{rf}} & \cdots \\ \vdots & \vdots & \vdots & \vdots & \vdots & \ddots \end{pmatrix}. \quad (6.37)$$

This N -level picture has been confirmed as a good approximation of the rf-dressed system (under the condition given by Equation (6.36)) in many experiments [25, 43, 47]. The locations of the n -th order avoided-crossings were reported to occur at $\Sigma \pm 2n\omega_{\text{rf}}$, without frequency shift. However, this is only true when $|\Omega_c J_0|$ is much smaller than $2\omega_{\text{rf}}$. As we shall see later, the leading term of the frequency shift is minute and can be neglected. For a comparatively large value of Ω_c , but subject to the Equation (6.36), the n -th

order avoided-crossings are not exactly located at $\Sigma \pm 2n\omega_{\text{rf}}$. In fact they are slightly shifted towards the zeroth order avoided-crossing due to the effect of the Rabi coupling. Using perturbation theory³, the interaction at the n -th avoided-crossing is approximated by the 2×2 matrix

$$\begin{pmatrix} -\zeta_n & \Omega_c J_n/2 \\ \Omega_c J_n/2 & \Sigma - \Delta_c - 2n\omega_{\text{rf}} \end{pmatrix}, \quad (6.38)$$

where ζ_n is defined in Equation (6.34) and the shift of the n -th avoided-crossing, δ_n , is approximately given by

$$\delta_n \approx \sum_{k \neq n} \frac{(\Omega_c J_k/2)^2}{2\omega_{\text{rf}}(n-k)}, \quad (6.39)$$

(δ_n is defined by the equation $\Delta_c^n = \Sigma - 2n\omega_{\text{rf}} + \delta_n$). Note that for $n = 0$, Equation (6.39) gives zero shift in frequency, i.e., the resonance of the zeroth order resonance is equal to the Stark shift. It turns out that the shift calculated from Equation (6.39) is always half of that calculated using the full Floquet Hamiltonian. For example, the shift of the first sideband is given by $\Omega_c^2 J_0^2 / 8\omega_{\text{rf}}$ calculated from \mathbf{H}_{2N} (Equation (6.39)), which is half of that calculated from \mathbf{H}'_{2F} (Equation (6.32)). The reason is that \mathbf{H}'_{2F} takes into account the shift of both the ground state and the excited state manifolds whereas \mathbf{H}_{2N} only takes into account the shift of the excited state manifold. The effect of this half-reduction of the frequency shift is illustrated in Figure 6.3(a) and (b), in which the position of the avoided-crossing calculated from \mathbf{H}_{2N} is at half the distance of that calculated from \mathbf{H}'_{2F} . (This effect will be observed clearly in the resonances of the population lineshape in Figure 6.3(c).)

Thus, rather than having $\Sigma - \Delta_c - 2n\omega_{\text{rf}}$ along the diagonal of Equation (6.37), we need to compensate the half-reduction shift to the energy level. After the frequency shift compensation, the elements of Equation (6.37) along the

³The iteration method is not effective in this case. The better approach is to use perturbation theory.

diagonal are

$$[\mathbf{H}_{2N}]_{nn} \approx \Sigma - \Delta_c - 2m\omega_{\text{rf}} + \sum_{k \neq n} \frac{(\Omega_c J_k / 2)^2}{2\omega_{\text{rf}}(n - k)}. \quad (6.40)$$

Until now we have only discussed the eigenspectrum of the full Floquet Hamiltonian and the N -level Hamiltonian, without concern for the relaxation process, which is, in fact, important in the real atomic system. We will see in the next subsection that the relaxation process, as well as the condition given by Equation (6.36), will control the visibility of the resonance structure in the actual system.

6.3 Dressed state dynamics of rf-dressed two-level subsystems

The system evolution and the resonance structure of the transferred population lineshape can be understood in the framework of the dressed (Floquet) states. Also the effect of the relaxation process will be discussed in this subsection.

6.3.1 Dynamics of Floquet Hamiltonian

The solution of the population dynamics, without the relaxation process, can be obtained by searching for the eigenvalues and eigenvectors of \mathbf{H}'_{2F} (or \mathbf{H}_{2F}) and the general solution is given by Equation (6.8). Generally, the values of the Fourier coefficients, a_n and b_n , for large n , are minute and can be neglected. Thus the solutions have an oscillatory form with frequency mode composed of the characteristic frequency, $\tilde{\Omega}$, and the harmonics of the rf frequency in the form of $\tilde{\Omega} \pm 2n\omega_{\text{rf}}$. From Equation (6.27), the characteristic frequency is approximately $\sqrt{(\Sigma - \Delta_c)^2 + \Omega_c^2 J_0^2} / 2$.

Numerically solving Equation (6.7), the population transferred, defined by

Equation (6.5), against the detuning, $\Delta_c/2\pi$, is shown in Figure 6.3(c) (dark pink curve). The positions of the resonances correspond to that of the avoided-crossings since the system is most interactive at the avoided-crossings.

The physics around the avoided-crossings is very interesting and important because, in this region, the bare states strongly interact with one another to form the dressed states, containing both bare states. For example, consider Equation (6.16) when $\Delta_c = 0$, the dressed states contain exactly an equal amount of $|b, n\rangle$ and $|c, n\rangle$. Hence, the ground state, $|b, n\rangle$ is also a superposition of the dressed states with equal probability. And this causes the population to widely oscillate in time between the ground and excited states as $|b, n\rangle$ is no longer an eigenstate of the system. This corresponds to a large population transferred in the lineshape, i.e., a resonance. For large Δ_c , the dressed states asymptotically approach the bare states. Thus if the system is prepared in the ground state, there would be no population oscillation.

This argument based on dressed states can also be applied to the eigenspectrum of the Floquet Hamiltonian. In the regime where Equation (6.36) is applied, at the zeroth avoided-crossing, the dressed Floquet states of the n -th two-level system in the manifold are formed from $|b', n\rangle$ and $|c', n\rangle$, with little amount from other harmonic Floquet states. Because the energy separation between the pair of these dressed states to the next is larger than the energy gap, we can assume that there is no interaction between the n -th two-level system and the others. Furthermore, the distance between the zeroth avoided-crossing to the first avoided-crossing on the right (and left) is so large ($\sim 2\omega_{\text{rf}}$) that the dressed Floquet states, $|b'', n+1\rangle$ and $|c'', n\rangle$ (and $|b'', n\rangle$ and $|c'', n-1\rangle$) are approximately equal to $|c', n+1\rangle$ and $|b', n\rangle$ (and $|b', n\rangle$ and $|c', n-1\rangle$), respectively. These two dressed states interact with each other at the first avoided-crossing with the interaction strength of $|\Omega_c J_{+1}|$. It is now clear that the interaction at each avoided-crossing can

be approximated as a two-level like interaction. Thus the height of the n -th resonance, h_n , can be approximate by the two-level model and it is given by [68, 76]

$$h_n = \frac{\Omega_c^2 J_n^2 / 2}{\gamma_\perp \Gamma_c + \Omega_c^2 J_n^2}, \quad (6.41)$$

where $\gamma_\perp = \Gamma_c/2 + \gamma_c$. According to Equation (6.41), the height of the resonance is scaled by the Bessel function. For large n , the Bessel function tends to zero and the higher order resonances disappear. For the parameters given in Figure 6.3, the height of the zeroth, first and second resonances, calculated from Equation (6.41), are 0.50, 0.46 and 0.08, respectively. These values are in agreement with the numerical result calculated from Equation (6.7) as shown in Figure 6.3(c).

The sideband resonances are evidence that the excited state is turned into a manifold and the resonances occur when each Floquet state within the manifold is on-resonance with the ground state. The system is, now, well-described by the N -level approximation. As mentioned in Subsection 6.2.2, increasing Ω_c results in the break down of the N -level picture as the n -th two-level system starts interacting with the others in the manifold via the rf field. In addition, the resonance sidebands become closer to the zeroth resonance, and eventually, overlap and disappear inside the zeroth resonance. In this case, the dressed Floquet states are formed from $|b', n\rangle$, $|c', n\rangle$, $|b', n+1\rangle$ and $|c', n-1\rangle$ and the interaction at the avoided-crossing is no longer a two-level like interaction.

Not only is Equation (6.36) related to the formation of the dressed Floquet states, it is also related to the time scale in which the system evolves. When $|\Omega_c J_0| \ll 2\omega_{\text{rf}}$ (the time scale (or period) of the rf field is much shorter than that of the Rabi oscillation), the interaction due to the rf field is much faster than the interaction due to the laser field. This causes the formation of the Floquet states. In other words, the laser field interacts with the atomic system as if the excited state of the atoms were a manifold of Floquet

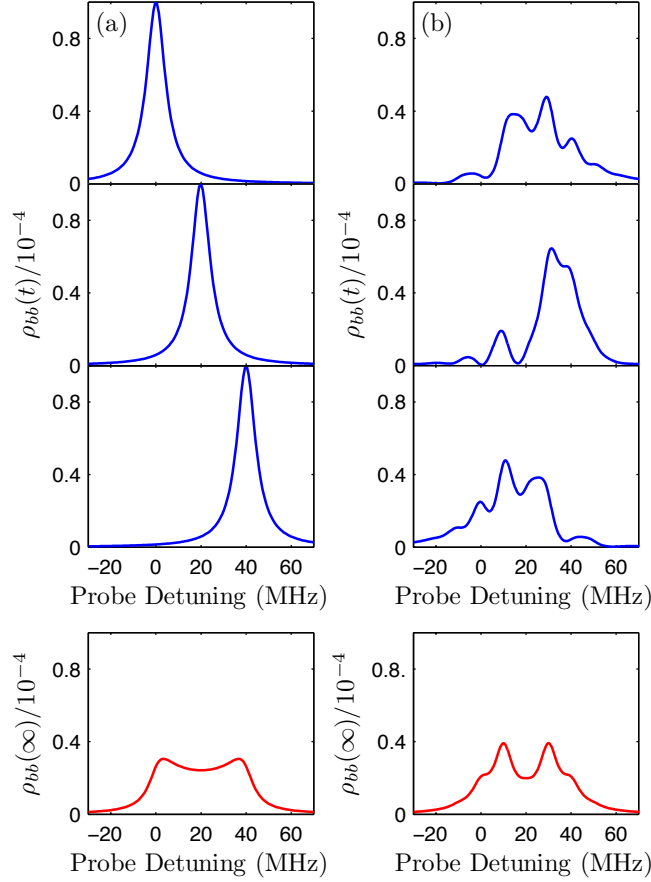


Figure 6.5: The plots in the first three rows show the instantaneous lineshape of ρ_{bb} , evolving in time, whereas the plots in the last row show the time-averaged lineshape over one period. For column (a) $\omega_{\text{rf}}/2\pi = 0.01$ MHz and for column (b) $\omega_{\text{rf}}/2\pi = 5$ MHz. The values of $\Omega_c/2\pi$, $\Sigma/2\pi$ and $\Gamma_c/2\pi$ are 0.1 MHz, 20 MHz and 10 MHz, respectively. In column (a), the time scale of the rf field is much longer than the Rabi oscillation of the system. Thus the system experiences constant rf field at any instantaneous of time, resulting in a slow oscillation of the lineshape with a separation in frequency of Σ . The opposite case is shown in column (b), where the time scale of the rf field is much shorter than the Rabi oscillation of the system. This causes the excited state to exhibit a manifold structure due to the rf interaction, which is clearly seen as a wiggly instantaneous lineshape. The laser interaction then couples the ground state to the manifold. Note that ω_{rf} is half of Γ_c in this case which is why the resonances are just resolved.

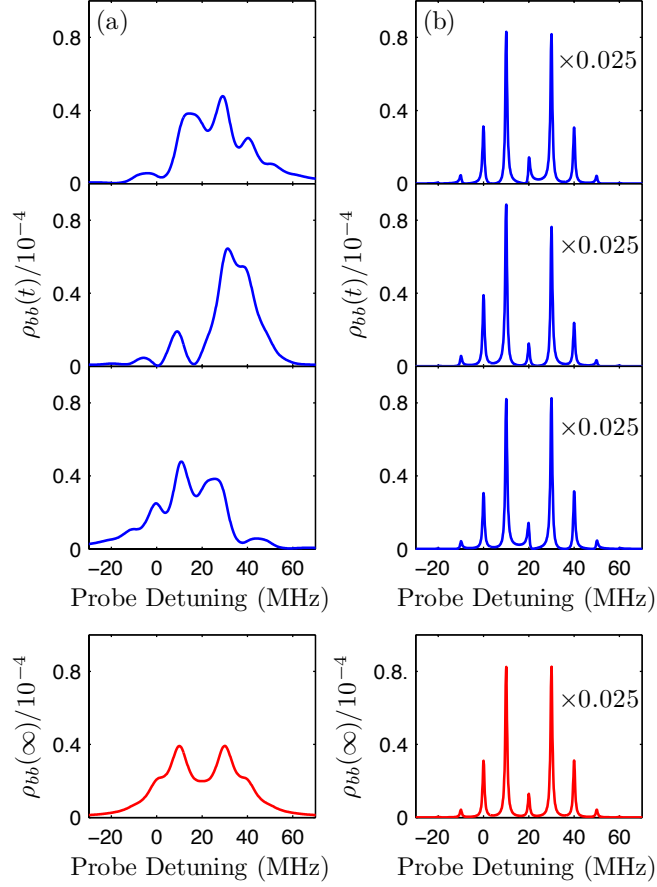


Figure 6.6: The plots in the first three rows show the instantaneous lineshape of ρ_{bb} , evolving in time, whereas the plots in the last row show the time-averaged lineshape over one period. For column (a) $\Gamma_c/2\pi = 10$ MHz and for column (b) $\Gamma_c/2\pi = 1$ MHz. The values of $\Omega_c/2\pi$, $\Sigma/2\pi$ and $\omega_{\text{rf}}/2\pi$ are 0.1 MHz, 20 MHz and 5 MHz, respectively. Column (a) is the same as in Figure 6.5(b). In column (b), Γ_c is much less than $2\omega_{\text{rf}}$, which implies that the coherent time of the system (determined by Γ_c) is much longer than the time scale of the rf interaction, i.e., the system has some time to interact with the rf field before its coherence is destroyed. This results in non-overlapping resonances. The instantaneous lineshapes show strong evidence of the excited state manifold.

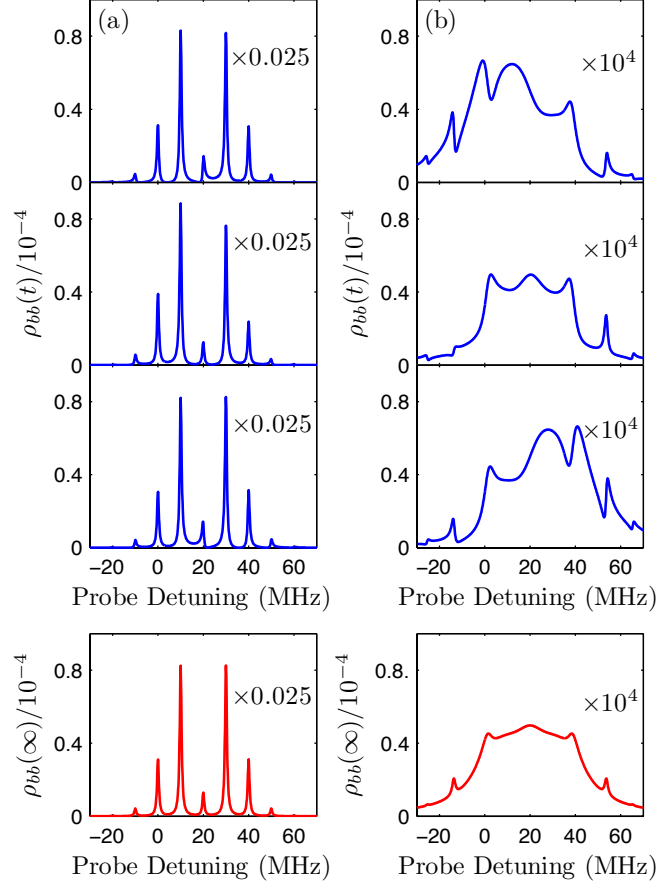


Figure 6.7: The plots in the first three rows show the instantaneous lineshape of ρ_{bb} , evolving in time, whereas the plots in the last row show the time-averaged lineshape over one period. For column (a) $\Omega_c/2\pi = 0.1$ MHz and for column (b) $\Omega_c/2\pi = 20$ MHz. The values of $\Gamma_c/2\pi$, $\Sigma/2\pi$ and $\omega_{\text{rf}}/2\pi$ are 1 MHz, 20 MHz and 5 MHz, respectively. Column (a) is the same as in Figure 6.6(b). In column (b), the Rabi frequency is twice as large as $2\omega_{\text{rf}}$; however, the condition $\Omega_c J_0/2\omega_{\text{rf}} \ll 1$ still loosely holds. This results in tiny sideband resonances. Note that the first sidebands are no longer visible as they are destroyed by power broadening of the zeroth resonance; thus, the N -level picture is no longer a good description of this system.

states. In the opposite situation, where the time scale of the rf field is much longer than that of the Rabi oscillation, the rf field changes adiabatically and the atom feels the constant rf field at any instantaneous time step. In this case the excited state does not become a manifold, and the detuning, Δ_c , undergoes an adiabatic oscillation at frequency of $2\omega_{\text{rf}}$. The population transferred lineshape oscillates back and forth in time, with the separation in frequency space determined by the Stark shift Σ . This situation is illustrated in column (a) of Figure 6.5.

It turns out that the time scale of the relaxation is another important factor which governs the sideband structure of the population transferred lineshape. If the time over which the system decays, Γ_c^{-1} , is shorter than the interaction time of the rf field, the coherence of the system is destroyed before the manifold develops. Thus in order to observe the sideband, it is required that

$$\Gamma_c \ll 2\omega_{\text{rf}}. \quad (6.42)$$

In the language of spectral linewidth, it is required that the linewidth Γ_c of the resonance is less than the distance between the adjacent resonances ($\sim 2\omega_{\text{rf}}$) so there is no overlap feature between the resonances. Figure 6.6 column (a) shows the case where the decay width just equals to $2\omega_{\text{rf}}$. The system exhibits a sideband structure for the instantaneous lineshapes in the first three row of column (a). Whereas the sidebands of the time-averaged lineshape in the fourth row are not clearly observed as they just become resolved. In column (b), we fix ω_{rf} at $2\pi \times 5$ MHz as in (a), but reduce Γ_c to $2\pi \times 1$ MHz to prevent the overlap between the sidebands. In this situation, the rf interaction is much faster than the system evolution and the decay; thus the sidebands are clearly observed in both the instantaneous and the time-averaged lineshapes. Note that, for the parameters in column (b), $\Sigma/2\omega_{\text{rf}}$ is larger than 1. However, the resonance and the manifold structure are clearly observed from the lineshape as Equation (6.36) is satisfied.

In column (b) of Figure 6.7, we have $\Omega_c = 2\pi \times 20$ MHz while $\Omega_{\text{rf}} = 2\pi \times 5$

MHz. In this case the Rabi frequency is twice as large as that of $2\omega_{\text{rf}}$; however, the condition $\Omega_c J_0/2\omega_{\text{rf}} \ll 1$ is still loosely hold. This results in tiny sideband resonances. Note that the first sidebands are no longer visible as they are destroyed by power broadening of the zeroth resonance; thus, the Floquet picture is no longer a good description of this system.

6.3.2 Dynamics in the N -level approximation

The dressed state dynamics in the N -level approximation is much simpler than that of the full Floquet Hamiltonian because the ground state contains only one eigenstate $|b', 0\rangle$. The main interaction, caused by $\Omega_c J_0$, leads to the zeroth avoided-crossing in the middle. The dressed states, $|\pm\rangle$, are formed from $|b', 0\rangle$ and $|c', 0\rangle$. Then the first order avoided-crossing on the right (left) is caused by the interaction between $|+\rangle$ and $|c', 1\rangle$ ($|-\rangle$ and $|c', -1\rangle$) where the interaction strength is $|\Omega_c J_{+1}|$. Suppose that Ω_c is so small that the dressed states, $|\pm\rangle$, asymptotically equal $|b', 0\rangle$. The interactions at the first avoided-crossings, now, are that between $|b', 0\rangle$ and $|c', 1\rangle$ ($|c', -1\rangle$). It is clear from the view point of the dressed state that the N -level picture is a good approximation of the rf-dressed system.

To obtain the population transferred lineshape, we look for the time-dependent solution of \mathbf{H}_{2N} . The equations of motion for this Hamiltonian are

$$\dot{\rho}_{bb} = \sum_{k=-N}^N \Gamma_c \rho_{kk} - \frac{i\Omega_c}{2} \sum_{k=-N}^N J_k (\rho_{kb} - \rho_{bk}), \quad (6.43a)$$

$$\begin{aligned} \dot{\rho}_{bk} = - \left[\frac{\Gamma_c}{2} + \gamma_c - i(\Sigma - \Delta_c - 2k\omega_{\text{rf}}) \right] \rho_{bk} \\ - \frac{i\Omega_c J_k}{2} (\rho_{kk} - \rho_{bb}) - \frac{i\Omega_c}{2} \sum_{\substack{m=-N \\ m \neq k}}^N J_m \rho_{mk}, \end{aligned} \quad (6.43b)$$

$$\dot{\rho}_{jk} = - [\Gamma_c - 2i(j-k)\omega_{\text{rf}}] \rho_{jk} + \frac{i\Omega_c J_k}{2} \rho_{jb} - \frac{i\Omega_c J_j}{2} \rho_{ak}, \quad (6.43c)$$

where b is $|b', 0\rangle$ and the numbers $j(k)$ represent the states $|c', j(k)\rangle$. The

steady state solutions of Equation (6.43) are constant as there is no driving terms present in the Hamiltonian; thus $\langle \rho_{bb}(\infty) \rangle = \rho_{bb}(\infty)$.

Figure 6.3(c) shows the population transferred lineshape (plotted in light purple) calculated using the N -level model. The figure clearly shows the effect of the half-reduction of the frequency shift as discussed in Subsection 6.2.3. In the figure, the ratio of Ω_c and $2\omega_{\text{rf}}$ is about 0.5, which is relatively large. This results in the deviation between the two lineshapes. However, the agreement can be improved if one calibrates the frequency shift using Equation (6.40).

In the next section, the full three-level system will be studied by the use of the two-level subsystem which has been discussed until now. We also consider the absorption lineshape for the case of thermal vapour at the end of the three-level system discussion.

6.4 RF-dressed three-level systems

With the rf field, as known from the two-level rf-dressed system, we expect the system to exhibit a manifold structure; thus an infinite number of dressed states are formed, resulting in a rich pattern of EIT structure. Furthermore, the coupling gives rise to infinitely many dark states which are formed between the ground state and the manifold of the excited state. These are the topics which will be discussed in the subsequent sections.

6.4.1 Floquet formalism

The manifold structure of the rf-dressed system is described in the Floquet formalism, using the procedure given in Subsection 6.2.1. The Floquet Hamil-

tonian, H_{3F} , of Equation (6.3), is

$$H_{3F} = \begin{pmatrix} A & \Omega_p & 0 \\ \Omega_p^\dagger & B & \Omega_c \\ 0 & \Omega_c^\dagger & C \end{pmatrix}, \quad (6.44)$$

where,

$$A = \text{diag}(\dots, 2\omega_{\text{rf}}, 0, -2\omega_{\text{rf}}, \dots),$$

$$B = \text{diag}(\dots, -\Delta_p + 2\omega_{\text{rf}}, -\Delta_p, -\Delta_p - 2\omega_{\text{rf}}, \dots),$$

$$\Omega_p = \text{diag}(\dots, \frac{\Omega_p}{2}, \frac{\Omega_p}{2}, \frac{\Omega_p}{2}, \dots),$$

$$\Omega_c = \text{diag}(\dots, \frac{\Omega_c}{2}, \frac{\Omega_c}{2}, \frac{\Omega_c}{2}, \dots),$$

and

$$C = \begin{pmatrix} \ddots & & & & & \\ & \Sigma - \Delta_R + 2\omega_{\text{rf}} & -\Sigma/2 & 0 & & \\ \dots & -\Sigma/2 & \Sigma - \Delta_R & -\Sigma/2 & \dots & \\ & 0 & -\Sigma/2 & \Sigma - \Delta_R - 2\omega_{\text{rf}} & & \\ & & & & & \ddots \end{pmatrix}.$$

The notation $\text{diag}(\dots, i, j, k, \dots)$ represents the infinite dimensional, diagonal matrix whose diagonal components are \dots, i, j, k, \dots .

From the structure of the matrix H_{3F} , the manifolds of the intermediate and excited states, which have governed by the block matrix containing B , C and Ω_c (and their hermitian conjugates), is similar to that of two-level rf-dressed system. Note that the detuning between $|b, n\rangle$ and $|c, n\rangle$ is kept constant at $\Sigma - \Delta_c$ in this situation. The complication of three-level system arises because the n -th harmonic Floquet state from the intermediate state manifold couples to the n -th harmonic Floquet state of the ground state manifold via the coupling Ω_p . This effectively means that $|a, n\rangle$ can couple to any Floquet states of the excited state manifold via $|b, n\rangle$; for example, $|a, 0\rangle$ couples with $|c, 2\rangle$ by making four transitions; namely, the two-photon transition ($|a, 0\rangle \rightarrow |b, 0\rangle \rightarrow |c, 0\rangle$) from the laser fields and the two-photon

transition ($|c, 0\rangle \rightarrow |c, 2\rangle$) from the rf field. For zero rf-field, the system reduces to an infinite number of three-level systems, which are independent of one another. Thus, in the zero-field limit, we obtain an infinite set of identical solutions from an infinite set of three-level systems. This means that the solution can be obtained by solving just one of these infinite systems.

In the basis where \mathbf{C} is diagonalized, \mathbf{C} and $\mathbf{\Omega}_c$, change to,

$$\mathbf{C}' = \begin{pmatrix} \ddots & & & & & & \\ & \Sigma - \Delta_{\text{R}} + 2\omega_{\text{rf}} & 0 & & 0 & & \\ \cdots & 0 & \Sigma - \Delta_{\text{R}} & & 0 & \cdots & \\ & 0 & 0 & \Sigma - \Delta_{\text{R}} - 2\omega_{\text{rf}} & & & \\ & & & & \ddots & & \\ & & & & & & \ddots \end{pmatrix}, \quad (6.45a)$$

$$\mathbf{\Omega}'_c = \begin{pmatrix} \ddots & & & & & & \\ & \Omega_c J_0/2 & \Omega_c J_{-1}/2 & \Omega_c J_{-2}/2 & & & \\ \cdots & \Omega_c J_{+1}/2 & \Omega_c J_0/2 & \Omega_c J_{-1}/2 & \cdots & & \\ & \Omega_c J_{+2}/2 & \Omega_c J_{+1}/2 & \Omega_c J_0/2 & & & \\ & & & & \ddots & & \\ & & & & & & \ddots \end{pmatrix}, \quad (6.45b)$$

where the structure of the new Floquet Hamiltonian, \mathbf{H}'_{3F} , is the same as \mathbf{H}_{3F} , given by Equation (6.44). We denote the Floquet states and quasienergies associated with \mathbf{H}'_{3F} as $|i', n\rangle$ and $\epsilon'_{i,n}$, respectively. Thus we could solve this system as if $|a', 0\rangle$ interacts with $|b', 0\rangle$ via the coupling Ω_p , and $|b', 0\rangle$ interacts with $|c', n\rangle$ via the coupling $\Omega_c J_n$. This is the N -level approximation of the system; it will be discussed in Subsection 6.4.2.

The eigenvalue (quasienergy) spectrum of \mathbf{H}_{3F} (or \mathbf{H}'_{3F}) is typically complicated, and has no general expression. However, we can try to understand the structure of the eigenvalue from the view point of perturbation theory and the property of the Floquet Hamiltonian. The first feature of the quasienergy is the repetition in frequency space due to the periodic Hamiltonian. There are three quasienergy combs associated with the three atomic states of the system. Let $\epsilon''_{a,n}$, $\epsilon''_{b,n}$ and $\epsilon''_{c,n}$ be the quasienergies of the n -th harmonic dressed

Floquet states $|a'', n\rangle$, $|b'', n\rangle$ and $|c'', n\rangle$. (The double prime means that the Floquet states and quasienergies are the eigenvectors and eigenvalues of \mathbf{H}_{3F} or \mathbf{H}'_{3F} once their matrices have been diagonalised.) If the quasienergies of the zeroth harmonic components are known, then

$$\epsilon''_{a,n} = \epsilon''_{a,0} + 2n\omega_{\text{rf}}, \quad (6.46a)$$

$$\epsilon''_{b,n} = \epsilon''_{b,0} + 2n\omega_{\text{rf}}, \quad (6.46b)$$

$$\epsilon''_{c,n} = \epsilon''_{c,0} + 2n\omega_{\text{rf}}. \quad (6.46c)$$

This is shown in Figure 6.8(a), which is a plot of the eigenspectrum of \mathbf{H}_{3F} (or \mathbf{H}'_{3F}) against probe detuning, $\Delta_p/2\pi$. The ground state manifold is shown as horizontal lines at the level of $2n\omega_{\text{rf}}$. The intermediate state manifold is the group formed by the crossed line and its harmonics, while those of the excited state manifold are labelled by circled lines. For small Ω_p and the system satisfies Equation (6.36) and (6.42), the intermediate and excited states manifolds are approximately an isolated system; and hence, using perturbation theory, the quasienergies of $|b'', 0\rangle$ and $|c'', 0\rangle$ are

$$\epsilon''_{b,0} = - \sum_{n=-\infty}^{\infty} \frac{(\Omega_c J_n/2)^2}{(\Sigma - \Delta_c - 2n\omega_{\text{rf}})}, \quad (6.47a)$$

$$\epsilon''_{c,0} = \Sigma - \Delta_c + \sum_{n=-\infty}^{\infty} \frac{(\Omega_c J_n/2)^2}{(\Sigma - \Delta_c - 2n\omega_{\text{rf}})}. \quad (6.47b)$$

Note that Equation (6.47) is only valid when $|\Sigma - \Delta_c \pm 2n\omega_{\text{rf}}| \gg |\Omega_c J_n|$, i.e., no degeneracy occurs between these two manifolds. For the degenerate case, we can obtain $\epsilon''_{b,0}$ and $\epsilon''_{c,0}$ from Equation (6.27) and (6.28). The quasienergies of $|b'', n\rangle$ and $|c'', n\rangle$ are

$$\epsilon''_{b,n} = -\Delta_p + \epsilon''_{b,0} + 2n\omega_{\text{rf}}, \quad (6.48a)$$

$$\epsilon''_{c,n} = -\Delta_p + \epsilon''_{c,0} + 2n\omega_{\text{rf}}. \quad (6.48b)$$

The quasienergy of $|b'', 0\rangle$, calculated from Equation (6.48), is shown as the crossed line in Figure 6.8(a), while those of $|c'', 0\rangle$ and $|c'', \pm 1\rangle$ are shown as the circled lines in the same figure. The positions of the resonances occur

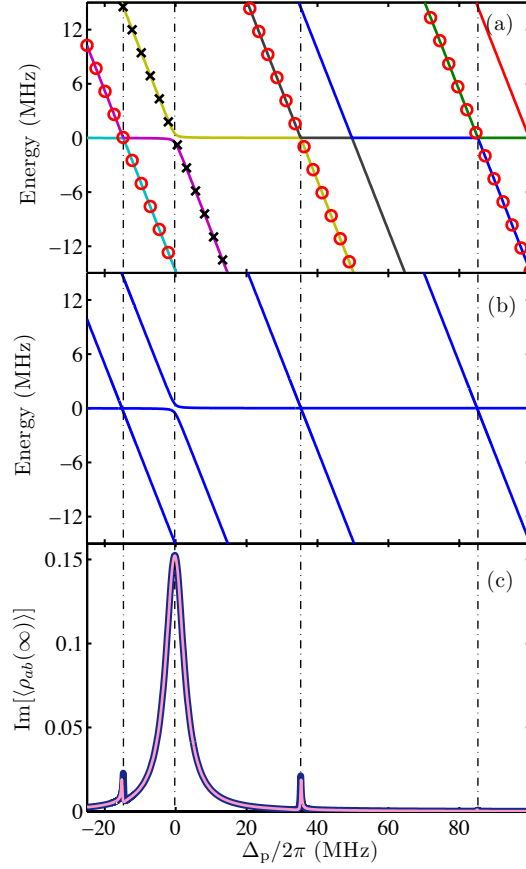


Figure 6.8: The quasienergy spectrum and the $\text{Im}[\langle \rho_{ab}(\infty) \rangle]$ lineshape calculated from \mathbf{H}'_{3F} are shown in (a) and (c) (thick blue line), while the corresponding results calculated from \mathbf{H}_{3N} are shown in (b) and (c) (thin pink line), where the sideband is taken upto $N = 4$. The parameters used in this figure are $\Omega_p = 2\pi \times 1$ MHz, $\Omega_c = 2\pi \times 8$ MHz, $\Sigma = 2\pi \times 35$ MHz, $\Delta_c = 0$ MHz, $\omega_{\text{rf}} = 2\pi \times 25$ MHz, $\Gamma_b = 2\pi \times 6$ MHz, $\Gamma_c = 2\pi \times 0.01$ MHz and $\gamma_p = \gamma_c = 2\pi \times 0.1$ MHz. The crossed and circled lines in (a), calculated from Equation (6.48), shows the quasienergies of $|b'', 0\rangle$, $|c'', 0\rangle$ and $|c'', \pm 1\rangle$, respectively. The eigenspectrum of the N -level approximation is shown in plot (b). The locations of the resonances (or avoided crossings) in (b) are different from (a) due to the symmetry breaking of the intermediate manifold. The vertical dot-dashed lines show the position of the resonances calculated from Equation (6.47).

where these lines from the intermediate and excited states manifolds cross the quasienergy of the ground state level. This is shown as the avoided-crossing in Figure 6.8(a). These avoided-crossings are at

$$\Delta_p(b'', n) = \epsilon''_{b,0} + 2n\omega_{\text{rf}}, \quad (6.49a)$$

$$\Delta_p(c'', n) = \epsilon''_{c,0} + 2n\omega_{\text{rf}}. \quad (6.49b)$$

Figure 6.8(c) shows the resonance structure of the average of $\text{Im}[\rho_{ab}]$ (proportional to the absorption coefficient) against probe detuning, $\Delta_p/2\pi$. Though a quantitative description of these resonances would be excessively difficult, we can understand the formation of these resonances qualitatively. When the ground state manifold is far off-resonance with the intermediate and excited state manifolds, the dressed states of the ground state manifold are asymptotically equal to $|a', n\rangle$, while the dressed states of the intermediate and excited state manifolds are approximately superposition of $|b', n\rangle$ and $|c', n\rangle$. The mixing angle of these dressed states are determined by Ω_c and $\Sigma - \Delta_c$. Let us consider the mixing between $|a', 0\rangle$, $|b', 0\rangle$, $|c', 0\rangle$ and $|c', \pm 1\rangle$ as these states are shown in Figure 6.8(a). Since $|b', 0\rangle$, $|c', 0\rangle$ and $|c', \pm 1\rangle$ are far-detuned from one another, the dressed states are asymptotically equal to their own bare states, i.e., $|i'', n\rangle \rightarrow |i', n\rangle$, with a little amount of the other bare states mixed in. When Δ_p is tuned such that one of these dressed states approaches $|a'', 0\rangle$, they start coupling to each other in the same way like two-level interaction with the effective Rabi coupling [71, 72]. Since $|b'', 0\rangle$ contains a large percentage of $|b', 0\rangle$, this results in the widest resonance ($\sim \Gamma_b$) close to the zero detuning. While the resonance of $|c'', 0\rangle$ with $|a'', 0\rangle$ is smaller in height and narrower in its width ($\sim \Gamma_c$). The generation of the next sidebands are due to the interaction between $|c'', \pm 1\rangle$ and $|a'', 0\rangle$, where the physics is the same. However, the heights of these sidebands can be very small compared to those of $|b'', 0\rangle$ and $|c'', 0\rangle$. This is because Ω_c is scaled by the first order Bessel function, whose value is less than 1. In addition to Ω_c , the detuning between $|b', 0\rangle$ and $|c', n\rangle$ has a significant effect to

the effective Rabi coupling as it inversely proportional to the detuning. Both $\Omega_c J_{+1}$ and large detuning cause the dramatic suppression of $|c'', 1\rangle$ resonance. The dashed-dotted vertical lines shows the resonance position predicted from Equation (6.49).

In Figure 6.8(a), there is a line crossing the ground state level at $\Delta_p \approx 50$ MHz. This line represents the Floquet state from the intermediate state manifold, $|b'', 1\rangle$. However no resonance is observed at this position in Figure 6.8(c). This is because the Floquet sidebands from the intermediate state are so weak that they do not exhibit the resonance structure. The existence of these sidebands will become important when Ω_c is large such that the sideband of the intermediate state is induced by the sideband of the excited state. This will be discussed in Subsection 6.4.2.

From the results shown in this subsection, it is clear that if the system satisfies the same conditions as imposed in the rf-dressed two-level system, we would be able to reduce this infinite system with the N -level approximation, where we only concern the manifold of the excited state.

6.4.2 N -level approximation

If Inequalities (6.36) and (6.42) are fulfilled, the Floquet states in the excited state manifold do not overlap with one another, i.e., the Floquet states are well-defined in frequency space; and hence the N -level approximation is a good description of the rf-dressed three-level system. Results for this N -level system are shown in Figure 6.8(b), where Ω_p couples $|a', 0\rangle$ with $|b', 0\rangle$, and

$\Omega_c J_n$ couples $|b', 0\rangle$ to $|c', n\rangle$. The Hamiltonian of the system is

$$\mathbf{H}_{3N} = \begin{pmatrix} 0 & \Omega_p/2 & \cdots & 0 & 0 & 0 & \cdots \\ \Omega_p/2 & -\Delta_p & \cdots & \Omega_c J_{-1}/2 & \Omega_c J_0/2 & \Omega_c J_{+1}/2 & \cdots \\ 0 & \vdots & \ddots & \vdots & \vdots & \vdots & \cdots \\ 0 & \Omega_c J_{-1}/2 & \cdots & \Sigma - \Delta_R + 2\omega_{\text{rf}} & 0 & 0 & \cdots \\ 0 & \Omega_c J_0/2 & \cdots & 0 & \Sigma - \Delta_R & 0 & \cdots \\ 0 & \Omega_c J_{+1}/2 & \cdots & 0 & 0 & \Sigma - \Delta_R - 2\omega_{\text{rf}} & \cdots \\ \vdots & \vdots & \vdots & \vdots & \vdots & \vdots & \ddots \end{pmatrix}. \quad (6.50)$$

Having determined the Hamiltonian, the equations of motion for this N -level system are

$$\dot{\rho}_{aa} = \Gamma_b \rho_{bb} + \frac{i\Omega_p}{2}(\rho_{ab} - \rho_{ba}), \quad (6.51a)$$

$$\begin{aligned} \dot{\rho}_{bb} = & -\Gamma_b \rho_{bb} + \sum_{k=-N}^N \Gamma_c \rho_{kk} - \frac{i\Omega_p}{2}(\rho_{ab} - \rho_{ba}) \\ & + \frac{i\Omega_c}{2} \sum_{k=-N}^N J_k(\rho_{bk} - \rho_{kb}), \end{aligned} \quad (6.51b)$$

$$\dot{\rho}_{ab} = -\left(\frac{\Gamma_b}{2} + \gamma_b + i\Delta_p\right) \rho_{ab} + \frac{i\Omega_p}{2}(\rho_{aa} - \rho_{bb}) + \frac{i\Omega_c}{2} \sum_{k=-N}^N J_k \rho_{ak}, \quad (6.51c)$$

$$\begin{aligned} \dot{\rho}_{ak} = & -\left[\frac{\Gamma_c}{2} + \gamma_b + \gamma_c + i(\Delta_p + \Delta_c - \Sigma + 2k\omega_{\text{rf}})\right] \rho_{ak} \\ & - \frac{i\Omega_p}{2} \rho_{bk} + \frac{i\Omega_c J_k}{2} \rho_{ab}, \end{aligned} \quad (6.51d)$$

$$\begin{aligned} \dot{\rho}_{bk} = & -\left[\frac{\Gamma_b + \Gamma_c}{2} + \gamma_c + i(\Delta_c - \Sigma + 2k\omega_{\text{rf}})\right] \rho_{bk} + \frac{i\Omega_c J_k}{2}(\rho_{bb} - \rho_{kk}) \\ & - \frac{i\Omega_c}{2} \sum_{\substack{j=-N \\ j \neq k}}^N J_j \rho_{jk} - \frac{i\Omega_p}{2} \rho_{ak}, \end{aligned} \quad (6.51e)$$

$$\dot{\rho}_{jk} = -(\Gamma_c - 2i(j-k)\omega_{\text{rf}})\rho_{jk} - \frac{i\Omega_c J_j}{2} \rho_{bk} + \frac{i\Omega_c J_k}{2} \rho_{jb}, \quad (6.51f)$$

where $a \equiv |a', 0\rangle$, $b \equiv |b', 0\rangle$, and $j(k) \equiv |c', j(k)\rangle$. The lineshape of $\text{Im}[\rho_{ab}(\infty)]$ is obtained when the system reaches the steady state solution.

Figure 6.8(c) shows the absorption lineshape (thin pink line) obtained using the N -level model, and the eigenspectrum is plotted in Figure 6.8(b). The similar structure of both lineshape and eigenspectrum with the correct results suggests that the N -level model is a good approximation. However, the resonance positions are slightly different due to the absence of the intermediate sideband. In this N -level system, the resonant peaks are at,

$$\Delta_p^N(b'', 0) = - \sum_{n=-\infty}^{\infty} \frac{(\Omega_c J_n/2)^2}{(\Sigma - \Delta_c - 2n\omega_{\text{rf}})}, \quad (6.52a)$$

$$\Delta_c^N(c'', n) = \Sigma - \Delta_c - 2n\omega_{\text{rf}} + \frac{(\Omega_c J_n/2)^2}{(\Sigma - \Delta_c - 2n\omega_{\text{rf}})}. \quad (6.52b)$$

These equations are valid for small Ω_p and no degeneracy is found in the system. It is clear that the main resonance of $|b'', 0\rangle$, obtained from Equation (6.52a), occurs at the same position as that of the actual result. However, the N -level approximation does not correctly predict the resonance positions of the sidebands of the excited state manifold as the contribution from the intermediate state manifold is neglected. To correct this we need to compensate the difference of the quasienergies of $|c', n\rangle$, i.e., the diagonal elements of the excited state manifold of \mathbf{H}_{3N} as described in Subsection 6.2.3. After frequency compensation, the diagonal elements of the Rydberg manifold are

$$[\mathbf{H}_{3N}]_{mn} \approx \Sigma - \Delta_R - 2n\omega_{\text{rf}} + \sum_{k \neq n} \frac{(\Omega_c J_k/2)^2}{\Sigma - \Delta_c - 2k\omega_{\text{rf}}}. \quad (6.53)$$

The dressed state dynamics of this system can be understood as follows. The dressed state $|b'', 0\rangle$, formed by $|a', 0\rangle$, $|b', 0\rangle$ and $|c', n\rangle$, approximately equal to $|b', 0\rangle$ when $|b', 0\rangle$ is far-off resonance with $|a', 0\rangle$ and $|c', n\rangle$. Using similar argument, $|a'', 0\rangle$ is approximately by $|a', 0\rangle$ and $|c'', n\rangle$ is approximately by $|c', n\rangle$. However when any two of these dressed states become close to each other, the effective Rabi coupling couples them and forms a two-level like interaction. This leads to the resonances observed in the lineshape, shown in Figure 6.8(c). It should be noted that the heights of the sideband resonances

produced from the N -level approximation are slightly different from those of the actual result. This effect is, however, insignificant when we work in the real atomic system as the dephasing decay is typically $2\pi \times (1 - 2)$ MHz [25]. At this values of the dephasing decay, the sideband resonances are suppressed and the deviation between the N -level model and the actual result becomes negligible. However, it is very interesting to study the origin of this deviation and it turns out that the origin of this difference in height comes from the fact that the Floquet states of the intermediate manifold are not taken into account. This is one of the important features for the presence of the intermediate state manifold. Thus, to some extent, the intermediate manifold is important to the system and cannot be neglected. This presence of the sidebands of intermediate state will be discussed in the next subsection.

6.4.3 Strong coupling field

Until now, we have discussed the properties of the rf-dressed three-level system in the regime where Equation (6.36) and (6.42) are satisfied. Recall that these conditions physically mean that the time scale on which the system evolves must be longer than that of the rf field and the Floquet states do not overlap due to the natural linewidths of the system. However, Ω_c , which we have used in the condition throughout the discussion so far, does not actually represent the time scale of the system evolution. This means that there should be another criterion for the rf-dressed three-level system to exhibit the manifold feature.

Suppose that we increase Ω_c so that it becomes larger than $2\omega_{\text{rf}}$, i.e., the condition of Equation (6.36) breaks down, it turns out that we still be able to observe a manifold structure until a certain value has been reached. This value is associated with the effective Rabi oscillation, i.e., the actual time scale over which the system evolves. The approximate effective Rabi fre-

quency is given by $\Omega_p\Omega_c/2\Sigma$ [71, 72]; and hence the criterion is

$$\frac{\Omega_p\Omega_c}{2\Sigma} \ll 2\omega_{\text{rf}}. \quad (6.54)$$

When the condition given by Equation (6.54) fails, the system exhibits no manifold structure and becomes a usual three-level system, whose excited state oscillates adiabatically due to the rf field. In term of the lineshape of $\text{Im}[\langle\rho_{ab}(\infty)\rangle]$, we observe the oscillation of the sharp resonance from $|c\rangle$. Thus, when we are in the regime which lies within the conditions set by Equation (6.36) and (6.54), the N -level approximation, described in the previous subsection, is invalid. This is because the sidebands in the excited state manifold overlap with one another, i.e., the sidebands are hidden inside the zeroth resonance. The break down of N -level approximation is illustrated in Figure 6.9, where $\Omega_c = 2\pi \times 30$ MHz in (a) and $\Omega_c = 2\pi \times 60$ MHz in (b). It is clear that, when Ω_c approaches $2\omega_{\text{rf}}$, the deviation between the results from N -level approximation (pink solid line) and the actual results from Equation (6.4) (green solid line) becomes significant and the lineshape structure changes in both the positions and the heights of the resonances. In (a), since Ω_c is still less than $2\omega_{\text{rf}}$, the resonance patterns from both results are not much different. The main resonances due to the interaction with intermediate state from both results are approximately the same. However, when Ω_c goes beyond $2\omega_{\text{rf}}$, in (b), the actual result becomes more complicated and the pattern of the actual result is completely different from that of the N -level approximation.

Not only does the N -level fail to predict the positions of the resonances, it also fails to predict the existence of the resonances due to the intermediate manifold. In the actual lineshape, the sidebands due to the intermediate manifold are visible, as shown in Figure 6.9(a) and (b). In (a), one of the sideband from intermediate manifold is shown as a small resonance (labelled by 1), just next to the right of the sideband of the Rydberg state (labelled by 2). The separation between the sidebands from the intermediate manifold

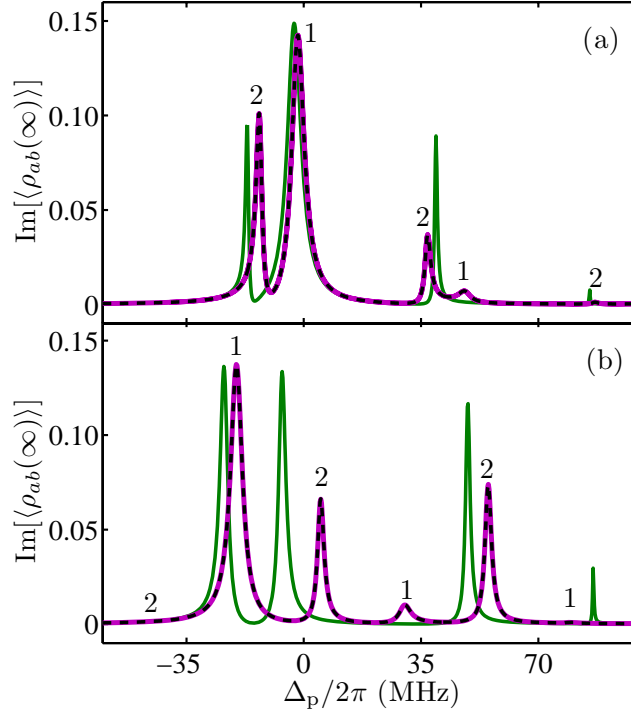


Figure 6.9: Comparison of three resonance lineshapes - the correct result calculated from Equation (6.4) (pink solid line), the N -level approximation (green solid line), and the $(N + N)$ -level approximation result (black dashed line), in which the sidebands from the intermediate level are taken into account. The set of parameters used in the plot are the same as those used in Figure 6.8, except that $\Omega_c = 2\pi \times 30$ MHz in (a) and $\Omega_c = 2\pi \times 60$ MHz in (b). For large Ω_c , compared to $2\omega_{\text{rf}}$, the N -level approximation clearly breaks down as shown in the figure. The N -level approximation fails to predict both positions and heights of the resonances. To recover the N -level approximation, the sidebands from the intermediate level need to be included; thus we refer to the new model as the $(N + N)$ -level approximation. The sideband resonances from the intermediate level are clearly observed in the results (labelled by 1 in the figure), as well as the sideband resonances from the excited (Rydberg) state (labelled by 2).

is exactly $2\omega_{\text{rf}} = 2\pi \times 50$ MHz as expected from Floquet theory. In (b), the sideband of the intermediate manifold (labelled by 1) is clearly observed since it does not overlap with the sideband from the Rydberg manifold (labelled by 2) as observed in the case shown in (a). The resonance structure of the system, now, becomes more profound due to the manifold from the intermediate state. Again the frequency separation between the adjacent resonances in the same manifold is exactly $2\omega_{\text{rf}}$ as in (a).

The appearance of the resonances due to the intermediate manifold suggests that, in order to recover the validity of the N -level approximation, we need to include the sidebands from the intermediate state into the model. Since this effect happens when Ω_c is larger than $2\omega_{\text{rf}}$, and it appears as if the intermediate state forms the manifold structure due to the excited state manifold, we refer to this effect as the induced sidebands effect. Note that this effect is not due to the intermediate state's interaction with the rf field to form the manifold, as the Stark shift of the intermediate state cannot be observed. When the intermediate sidebands are taken into account, we refer to the resulting model as the $(N+N)$ -level approximation. The results of this new approximation are shown in Figure 6.9 as black dashed line. Since the manifold of the intermediate state is kept in the approximation, the symmetry between the intermediate and Rydberg manifolds are not broken. And the positions of the resonances obtained from this new approximation are exactly the same as those of the actual results. Not only does the $(N+N)$ -level approximation predict the correct resonance positions, the height mismatch feature, encountered in the N -level approximation, also disappears.

In the next section, we will use the N - and $(N+N)$ -level approximations to explain the formation of the Rydberg darks states and compare the results with the actual results.

6.4.4 Electromagnetically induced transparency

Another important feature of the ladder system is the formation of dark states which do not contain the intermediate state of the system and the accompanying occurrence of EIT [3, 71]. In this subsection, we study EIT in both cold atomic ensembles and thermal vapour.

Cold atomic ensembles

In cold atomic ensembles, the atomic velocity is approximately zero, i.e., all atoms are approximately at rest⁴. Thus the resonance lineshape is given by $\text{Im}[\langle \rho_{ij}(\infty) \rangle]$. The typical lineshape for EIT is the absorption lineshape as this lineshape gives the information about the transparency of the ensembles.

For Ω_c small compared to $2\omega_{\text{rf}}$, the system is well described by the N -level approximation. With this approximation the formation of the dark states is understood as follows. The dark states, in this system, are the states that do not contain the intermediate state $|b', 0\rangle$. To form the dark state, any three bare states, i.e., $|a', 0\rangle$, $|b', 0\rangle$ and $|c', n\rangle$, must be nearly on-resonance with one another at the same time as it is a three-level interaction. For the configuration in Figure 6.8(c), we cannot observe the dark state EIT in the resonance lineshape as the intermediate state, $|b', 0\rangle$, is always off resonance with the Floquet states in the Rydberg state manifold, $|c', n\rangle$. In order to create a three-level interaction, we scan the coupling detuning (Δ_c), rather than that of the probe laser, and we tune the probe detuning to zero ($\Delta_p = 0$). With this configuration, the ground state of the system is always on-resonance with the intermediate state. The dark state is formed when Δ_c is scanned such that, the ground, intermediate and one of the Floquet states are on-resonance at the same time. The EIT result of N -level approximation, for $\Omega_c = 2\pi \times 8$ MHz, is shown in Figure 6.10(a) as the red solid line. In the figure, the zeroth order resonances at Σ corresponds to the dark state,

⁴For the discussion on this topic, see Chapter 2.

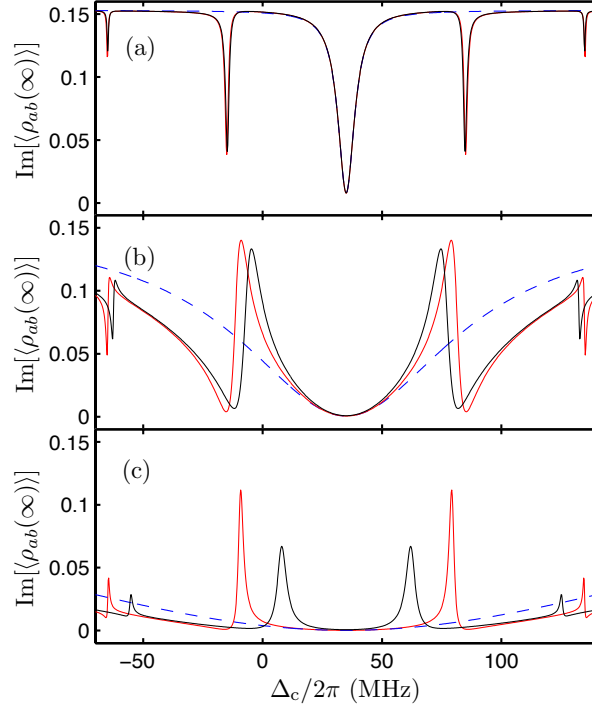


Figure 6.10: $\text{Im}[\langle\rho_{ab}(\infty)\rangle]$ against $\Delta_c/2\pi$ for (a) $\Omega_c/2\pi = 8$ MHz, (b) $\Omega_c/2\pi = 30$ MHz and (c) $\Omega_c/2\pi = 60$ MHz. The set of parameters used in the calculation are the same as in Figure 6.8, except that Δ_c is scanned instead of Δ_p . The probe detuning is set to zero, as to make the ground state on resonance with the intermediate state. In (a), the dark states are observed as EIT features. The detunings at which the resonances occur are slightly shifted from the two-photon Raman condition by δ_n , given by Equation (6.56). In (b), the EIT resonances are broadened due to power broadening and the shifts δ_n increase as Ω_c increases. In (c), the EIT resonances are so broadened that they saturate and the flat background absorption in (a) becomes EIA resonances. The red curves show the results from the N -level approximation, while those in black are the actual results. The dashed blue lines refer to the case where the system contains only three levels, i.e., the ground, the intermediate and the Rydberg state. For large Ω_c , the N -level approximation clearly breaks down.

formed from $|c', 0\rangle$, and the next two resonances are formed from $|c', \pm 1\rangle$ and so on. The actual EIT result calculated from Equation (6.4) is shown as the black solid line in Figure 6.10(a). The blue dashed line is the EIT lineshape calculated from the three-level system, containing $|a', 0\rangle$, $|b', 0\rangle$ and $|c', 0\rangle$.

Note that the positions of the n -th sideband resonances, from the exact results (black solid line), do not occur at $\Delta_c = \Sigma - 2n\omega_{\text{rf}}$ as predicted from the N -level approximation. In fact there is a slight shift in frequency which displaces the sidebands towards the zeroth order resonance. Using perturbation theory, the three-level interaction of the n -th resonance is given by a 3×3 matrix

$$\begin{pmatrix} 0 & \Omega_p/2 & 0 \\ \Omega_p/2 & -\delta_n & \Omega_c J_n/2 \\ 0 & \Omega_c J_n/2 & \Sigma - \Delta_c - 2\omega_{\text{rf}} + \delta_n \end{pmatrix}, \quad (6.55)$$

with

$$\delta_n = \sum_{k \neq n} \frac{(\Omega_c J_k/2)^2}{2\omega_{\text{rf}}(n-k)}. \quad (6.56)$$

The EIT resonance occurs when $\Sigma - \Delta_c - 2\omega_{\text{rf}} + \delta_n = 0$, i.e., $\Delta_c^n = \Sigma - 2n\omega_{\text{rf}} + \delta_n$. However, the N -level approximation gives the resonance positions at $\Delta_c^n = \Sigma - 2n\omega_{\text{rf}}$. This is because there are no perturbation to $|c', n\rangle$ from the sidebands of the intermediate state. Another difference between the actual and N -level approximation results is the depth of the sidebands, which is too large in the N -level approximation. This is because the effect of the sidebands from the intermediate state is not included as discussed in Subsection 6.4.3

It is interesting to note that for a large value of Ω_c , the $\text{Im}[\langle \rho_{ab}(\infty) \rangle]$ lineshape shows the effect of enhanced absorption instead of enhanced transmission. This effect can be explained as follows. Increasing Ω_c results in two components, namely, the power broadening of the dark state resonances and the increase in the shift δ_n , as seen in Figure 6.10(b). If one further increases Ω_c , the dark state resonances are so much broadened that they saturate and become a background of the lineshape. On the other hand,

the flat background in (a) is enhanced and becomes absorption resonances as shown in Figure 6.10(c). These enhanced absorption peaks occur when the ground state interacts with the manifold of the dressed states formed by the intermediate and Rydberg states. This is a two-level like interaction. If there were no rf fields, the zeroth order resonance would be broadened and become the background of the lineshape, without any enhanced absorption feature as shown by the blue dashed line in Figure 6.10(a) to (c).

Thermal atomic ensemble

In thermal vapours, the atomic velocity in the system is distributed according to the Maxwell-Boltzmann distribution, which is given by Maxwell-Boltzmann distribution, namely, Equation (3.8c). Hence each atom in the system sees different values of probe and coupling frequencies due to the Doppler shift effect. The total lineshape is the velocity average of the atomic velocity in the system.

To calculate the total lineshape, we assume that the probe and coupling lasers are set in counter-propagating direction in one dimension. Suppose that an atom moving with the speed v in the direction towards the probe laser, it sees the frequency of the probe laser is upshifted by $k_p v$, where $k_p = 2\pi/\lambda_p$ and λ_p is the wavelength of the probe laser. Thus the probe detuning is also upshifted to $\Delta_p + k_p v$. Similarly, the coupling detuning is downshifted to $\Delta_c - k_c v$, where $k_c = 2\pi/\lambda_c$ and λ_c is the wavelength of the coupling laser. Then the total lineshape is given by solving the equations of motion with the replacement of Δ_p and Δ_c by $\Delta_p + k_p v$ and $\Delta_c - k_c v$, respectively, and then averaging ρ_{ij} over the velocity space [84]. This is,

$$\langle \rho_{ij}(\Delta_p, \Delta_c, \infty) \rangle = \int_{-\infty}^{\infty} f(v) \langle \rho_{ij}(\Delta_p + k_p v, \Delta_c - k_c v, \infty) \rangle dv, \quad (6.57)$$

where $\langle \rho_{ij}(\Delta_p + k_p v, \Delta_c - k_c v, \infty) \rangle$ is defined as in Equation (6.5).

Figure 6.11 shows the EIT lineshapes calculated using the N -level approxi-

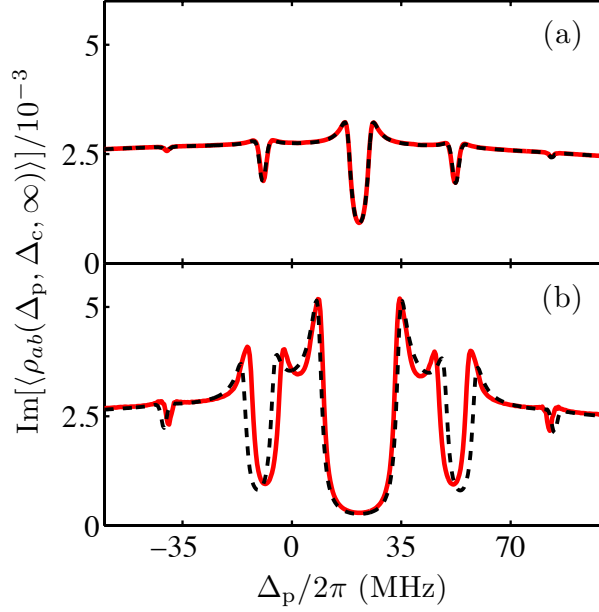


Figure 6.11: Figures (a) and (b) shows the EIT lineshapes calculated using N -level approximation (dotted lines) and the actual lineshape calculated from Equation (6.4) with Doppler averaging (solid lines) for $\Omega_c = 2\pi \times 8$ and $2\pi \times 30$ MHz, respectively. The lineshapes are calculated for ^{85}Rb at the temperature 40°C , and the probe and coupling lasers are in the counter-propagating configuration. The wavelengths of the probe and coupling lasers are 780 and 480 nm, respectively. The other parameters are the same as used in Figure 6.10. In figure (a), both results are in good agreement as the frequency shift is approximately 100 MHz. However, the frequency shift becomes significant for large value of Ω_c . This is illustrated in figure (b).

mation (dotted lines) and the actual lineshape calculated from Equation (6.4) (solid lines) for different Ω_c , while the other parameters are the same as those used in Figure 6.8. We assume that $\lambda_p = 780$ nm and $\lambda_c = 480$ nm. The thermal cell contains atoms of ^{85}Rb at the temperature of 40°C . In figure (a) where $\Omega_c = 2\pi \times 8$ MHz, the N -level approximation is a good approximation for the actual lineshape. Note that the frequency separation between adjacent EIT resonances is not $2\omega_{\text{rf}}$ as the distance is scaled by a factor of k_p/k_c

due to the Doppler averaging. To understand the shifting mechanism of the resonance, we need to use that fact that each EIT resonance corresponds to the velocity class such that $\Delta_p + k_p v = 0$ and $\Delta_c - k_c v - \Sigma + 2n\omega_{\text{rf}} = 0$ at the same time. Thus, for a fixed value of Δ_c , the probe detuning which satisfies these conditions is,

$$\Delta_p^n = \frac{k_p}{k_c}(\Sigma - \Delta_c - 2n\omega_{\text{rf}}). \quad (6.58)$$

From Equation (6.58), it is clear that the separation between any adjacent EIT dips is $2\omega_{\text{rf}}k_p/k_c$. Note that Equation (6.58) is for the results calculated using the N -level approximation. For the actual results calculated from Equation (6.4), the condition for Δ_c changes to $\Delta_c - k_c v - \Sigma + 2n\omega_{\text{rf}} - \delta_n = 0$, where δ_n is given by Equation (6.56). Thus Equation (6.58) changes to

$$\Delta_p^n = \frac{k_p}{k_c}(\Sigma - \Delta_c - 2n\omega_{\text{rf}} + \delta_n). \quad (6.59)$$

However, the change in frequency between Equation (6.58) and (6.59) is small. For the typical parameters used in Figure 6.11(a), the change is approximately 100 kHz. Though the change is tiny, this shifting in frequency can be observed in the differential lineshape, i.e., the difference between the actual and the calculated EIT lineshapes as shown in Figure 5.5 in Chapter 5. For large value of Ω_c , the N -level approximation breaks down as shown in Figure 6.11(b), where $\Omega_c = 2\pi \times 30$ MHz. There is a clear difference in resonance positions between the actual lineshape (solid line) and the N -level approximation lineshape (dashed line). Moreover, the EIT resonances are broadened and have large widths because of the power broadening effect. The validity of N -level approximation can be recovered if we include the sidebands of the intermediate state into the model and the result is in agreement with the actual result (not shown in the figure).

6.5 Conclusions

In this chapter, we have characterised the conditions for which the effect of the rf field is to turn the eigenstate of the atom into a manifold of quasienergy states. It was shown that the manifold structure is well-defined when the rf interaction is much faster than that of the system evolution; this gives the condition in Equation (6.36). In the Floquet states picture, this means that there are no overlaps among these Floquet states; and hence, we observe the well-defined resonance sidebands in the population transferred lineshape of the two-level system. This picture of stationary, well-defined Floquet states has been known from the previous work [25, 47, 51, 53, 142]. We also found the resonance shift, similar to Bloch-Siegart shift [144], which is the result of the interaction between the well-defined sidebands. This effect does not appear to have yet been discussed elsewhere. When the condition (given by Inequality (6.36)) breaks down, the sidebands start overlapping with the zeroth resonance, and the sideband resonances disappear. In addition, the coherence property of the system must be maintained during the rf interaction; this is the requirement set by Equation (6.42). This condition prevents the overlap between the sidebands due to their width being too large.

When the coupling Rabi frequency becomes larger such that Equation (6.36) breaks down, the N -level approximation is no longer a good approximation for the actual system. However, the effect of the manifold structure of the excited state is still observed in the absorption lineshape as shown in Figure 6.9. In the limit where Ω_c is larger than that determined by Equation (6.36) but less than that determined by Equation (6.54), the $N + N$ -level approximation is a good approximation to the actual system. In the $N + N$ -level approximation, we include the manifold of the intermediate state into the model. It appears as if the intermediate state forms the manifold structure due to the excited state manifold when Ω_c is larger than $2\omega_{\text{rf}}$. We refer to this effect as the induced sidebands effect. Not only does the inclusion

of the intermediate sidebands improve the absorption lineshapes, but the heights of the resonances are, also, corrected.

Chapter 7

Microwave dressing of Rydberg dark states

In the previous two chapters, we have shown that Rydberg states can effectively turn into a manifold when they interact with a far-off resonance radio frequency (rf) field. The manifold structure of the Rydberg states can be useful in the context of precision measurement of electric field [25]. In this chapter we study the effect of resonant microwave fields on electromagnetically induced transparency (EIT) involving highly excited Rydberg states. As shall be seen, by adding the microwave into the system, more than one dark resonance can be created. We also show that the number of the dark resonances can be controlled by the interference effect of the microwave couplings. This interference occurs at particular ratios between the microwave Rabi frequencies for the transition between the relevant states. By modelling the experimental data we show that adding a microwave coupling between Rydberg states can switch the group index of the sample by $\pm 10^5$. We also illustrate the appearance of superluminal pulse propagation when the group index of the medium becomes negative.

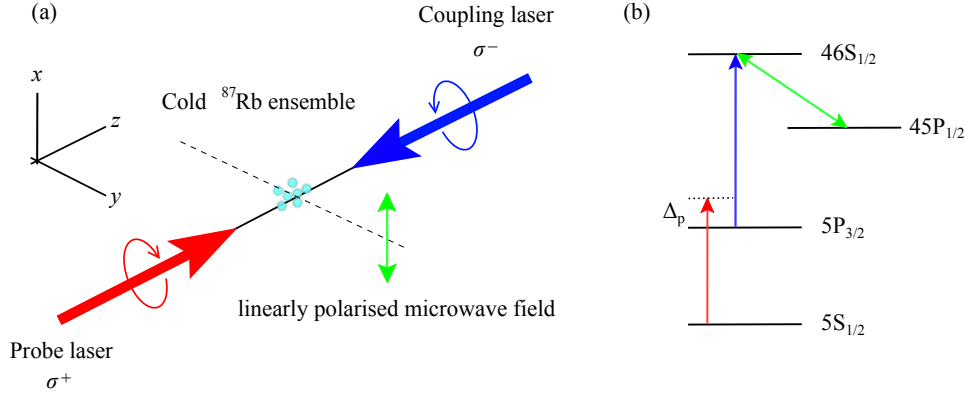


Figure 7.1: (a) Schematic of the experimental setup. The probe beam (driving σ^+ transition) and coupling beams (driving σ^- transition) counter-propagate through a cold ^{87}Rb cloud. Microwaves, whose polarisation are in the x direction, are applied from a perpendicular direction. Since the quantisation axis is pointed in the positive z direction, the microwave field can be decomposed into σ^+ and σ^- transitions, as shown in Figure 7.2. The probe transmission is measured using a single-photon avalanche detector (SPAD). (b) Simplified level scheme showing microwave coupling between the $46\text{S}_{1/2}$ and $45\text{P}_{1/2}$ Rydberg states.

7.1 Experimental set up

Schematics of the experimental set up and of the energy levels scheme are shown in Figure 7.1. Pritchard et al. performed the experiment on a cloud of laser-cooled ^{87}Rb atoms using the experimental setup described in [21, 39]. The atoms are loaded into a magneto-optical trap in 1 s and then prepared in the state $5\text{s } ^2\text{S}_{1/2} |F = 2, m_F = 2\rangle$ by optical pumping. The weak probe beam (with σ^+ polarisation) and the co-axial, counter-propagating beam (with σ^- polarisation) are directed along the $+z$ and $-z$ axes, respectively. The focused probe beam has a $1/e^2$ radius of $12 \mu\text{m}$ at the centre of the MOT. The corresponding value for the coupling beam is $66 \mu\text{m}$. The latter is stabilised to the $5\text{p } ^2\text{P}_{3/2} (F' = 3) \rightarrow 46\text{s } ^2\text{S}_{1/2} (F'')$ transition using an EIT locking

scheme [140]. The two beams are set up as to perform EIT spectroscopy between the $5s\ ^2S_{1/2}(F=2)$ and $46s\ ^2S_{1/2}(F''=2)$ states. Then the additional microwave field is applied orthogonal to the probe laser axis and its polarisation is in the x direction. This microwave field is to drive the transition $46s\ ^2S_{1/2}(F''=2) \rightarrow 45p\ ^2P_{1/2}(F'''=1,2)$ transition. Such configuration of the beams and the microwave field leads to microwave coupling of the multiple-magnetic sublevels, shown as the W-shaped transition in Figure 7.2. The microwave transition frequency between Rydberg states was calculated using quantum defects¹ from Li et al. [104] and is 44.559 GHz for $46S_{1/2} \rightarrow 45P_{1/2}$. The weak probe beam is scanned through the $5s\ ^2S_{1/2}(F=2)$ and $5p\ ^2P_{3/2}(F'=3)$ transition using acousto-optic modulation. The transmission through the MOT is monitored as a function of probe detuning using single photon avalanche photodiode (SPAD). For each dataset, the transmission is repeated over 100 times and the averaged transmission is calculated. The EIT transmission is then recorded for various microwave powers.

Figure 7.3 shows the evolution of the EIT signal with increasing microwave power. As the strength of the microwave coupling is increased the EIT peak undergoes an Autler-Townes splitting due to the dressing of the Rydberg state. To understand the evolution of the spectra with increasing microwave power the data is fitted using the model described in Section 7.2. The fits obtained from the model are also shown in Figure 7.3.

7.2 Theoretical modelling of EIT lineshapes

The experiment is modelled by the ten-level system shown in Figure 7.2 interacting with an EM field given by

$$\mathbf{E}(t) = \frac{1}{\sqrt{2}}E_p\hat{\epsilon}_+e^{-i\omega_p t} + \frac{1}{\sqrt{2}}E_c\hat{\epsilon}_-e^{-i\omega_c t} + \frac{1}{2}E_\mu\hat{\mathbf{x}}e^{-i\omega_\mu t} + \text{c.c.}, \quad (7.1)$$

¹Quantum defect gives the correction to the atomic energy calculated using Rydberg formula [23].

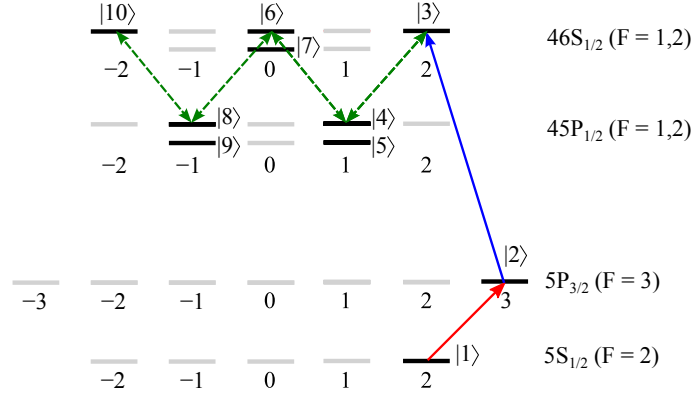


Figure 7.2: Schematic of the level scheme used to model the system. Given the quantisation axis, the microwave field is a superposition of σ^\pm , leading to the W-shaped couplings, shown by the green dashed lines. The probe and coupling lasers have the polarisation of σ^+ and σ^- , respectively. The hyperfine levels of both $46S_{1/2}$ and $45P_{1/2}$ are assumed to be degenerate.

where $\hat{\epsilon}_\pm$ are the polarisation unit vectors representing σ^\pm transitions and $\hat{\mathbf{x}}$ is the polarisation unit vector in the x direction. The first term in Equation (7.1) represents the probe field, whose amplitude and angular frequency are E_p and ω_p , respectively. The second term represents the coupling field with amplitude E_c and angular frequency ω_c . The third term is the microwave field with amplitude E_μ and angular frequency ω_μ and it propagates in the $-y$ direction. Setting the quantization axis along $+z$, the linearly-polarised microwave field is described as the superposition of $\hat{\epsilon}_\pm$, i.e., $\hat{\mathbf{x}} = (\hat{\epsilon}_- - \hat{\epsilon}_+)/\sqrt{2}$, leading to a W-shaped coupling between the Rydberg states (green dotted lines in Figure 7.2). The hyperfine splitting between the $F'' = 1$ and 2 Rydberg states is neglected, i.e., states $|3\rangle, |6\rangle, |7\rangle$ and $|10\rangle$, and, $|4\rangle, |5\rangle, |8\rangle$ and $|9\rangle$, are assumed to be degenerate. This is justified as the typical Rabi frequency of the microwave transition (~ 10 MHz) is significantly larger than the hyperfine splitting of the Rydberg levels (about $400 \times 2\pi$ kHz for $46s^2S_{1/2}$ and even less for $45p^2P_{1/2}$ [104]).

Applying the rotating-wave approximation and the slowly-varying variables

transformation, the Hamiltonian of the system is given by $\mathcal{H} = \mathcal{H}_0 + \mathcal{H}_{\text{EIT}} + \mathcal{H}_\mu$, where

$$\begin{aligned} \mathcal{H}_0 = & -\Delta_1 |2\rangle \langle 2| - \Delta_2 (|3\rangle \langle 3| + |6\rangle \langle 6| + |7\rangle \langle 7| + |10\rangle \langle 10|) \\ & - \Delta_3 (|4\rangle \langle 4| + |5\rangle \langle 5| + |8\rangle \langle 8| + |9\rangle \langle 9|), \end{aligned} \quad (7.2a)$$

$$\mathcal{H}_{\text{EIT}} = \frac{\hbar\Omega_p}{2} |1\rangle \langle 2| + \frac{\hbar\Omega_c}{2} |2\rangle \langle 3| + \text{h.c.}, \quad (7.2b)$$

$$\begin{aligned} \mathcal{H}_\mu = & \sum_{i=\{3,5,7,9\}} \frac{\hbar\Omega_\mu^{(i,i+1)}}{2} |i\rangle \langle i+1| + \sum_{i=3}^8 \frac{\hbar\Omega_\mu^{(i,i+2)}}{2} |i\rangle \langle i+2| \\ & + \sum_{i=\{4,6\}} \frac{\hbar\Omega_\mu^{(i,i+3)}}{2} |i\rangle \langle i+3| + \text{h.c.} \end{aligned} \quad (7.2c)$$

Here $\Delta_1 \equiv \hbar\Delta_p$, $\Delta_2 \equiv \hbar(\Delta_p + \Delta_c)$, $\Delta_3 \equiv \hbar(\Delta_p + \Delta_c - \Delta_\mu)$ and, Δ_p , Δ_c and Δ_μ are the detunings of the probe, coupling and microwave fields, respectively. The Rabi frequencies associated with the probe, coupling and microwave fields, Ω_p , Ω_c and $\Omega_\mu^{(n,m)}$ respectively, are given by

$$\Omega_p = \frac{\sqrt{2}E_p}{\hbar} \langle 2| \mathbf{er} \cdot \hat{\mathbf{e}}_+ |1\rangle, \quad (7.3a)$$

$$\Omega_c = \frac{\sqrt{2}E_c}{\hbar} \langle 3| \mathbf{er} \cdot \hat{\mathbf{e}}_- |2\rangle, \quad (7.3b)$$

$$\Omega_\mu^{(i,j)} = \frac{E_\mu}{\sqrt{2}\hbar} (\langle i| \mathbf{er} \cdot \hat{\mathbf{e}}_- |j\rangle - \langle i| \mathbf{er} \cdot \hat{\mathbf{e}}_+ |j\rangle), \quad (7.3c)$$

where \mathbf{er} is the dipole operator, and, i and j correspond to the magnetic sublevels of $46S_{1/2}$ and $45P_{1/2}$. Using the Wigner-Eckart theorem, the Rabi frequency of the microwave field reduces to

$$\begin{aligned} \Omega_\mu^{(i,j)} = & \Omega_\mu^r \times (-1)^{m_F^i} \sqrt{(2F^i + 1)(2F^j + 1)} \\ & \times \begin{Bmatrix} J^i & J^j & 1 \\ F^j & F^i & 3/2 \end{Bmatrix} \begin{Bmatrix} L^i & L^j & 1 \\ J^j & J^i & 1/2 \end{Bmatrix} \begin{pmatrix} L^j & 1 & L^i \\ 0 & 0 & 0 \end{pmatrix} \\ & \times \left[\begin{pmatrix} F^j & 1 & F^i \\ m_F^j & -1 & -m_F^i \end{pmatrix} - \begin{pmatrix} F^j & 1 & F^i \\ m_F^j & 1 & -m_F^i \end{pmatrix} \right], \end{aligned} \quad (7.4)$$

where $\Omega_\mu^r = \sqrt{6}E_\mu/\hbar \times \langle 46S_{1/2}|er|45P_{1/2}\rangle$ contains the radial integral as defined in Chapter 3. Note that Ω_μ^r is one of the free parameters whose value is determined by the minimum residuals fit.

The equation of motion for the density matrix ρ of the ten-level system is given by

$$\frac{\partial \rho}{\partial t} = -\frac{i}{\hbar}[\mathcal{H}, \rho] + \mathcal{L}(\rho) + \mathcal{L}_d(\rho), \quad (7.5)$$

where $\mathcal{L}(\rho) = \sum_i c_i \rho c_i^\dagger - (c_i^\dagger c_i \rho + \rho c_i^\dagger c_i)/2$ is the Lindblad superoperator [90] describing spontaneous decay and $\mathcal{L}_d(\rho)$ is a dephasing matrix which accounts for the linewidth of the EM fields. The natural decay linewidths of the $46S_{1/2}$ and $45P_{1/2}$ states are approximately 2 kHz and can be neglected, so only the decay from $5P_{3/2}$ to $5S_{1/2}$ at a rate $\Gamma/2\pi = 6$ MHz is included, using the operator $c = \sqrt{\Gamma}|1\rangle\langle 2|$. In addition to spontaneous emission, the dephasing due to the finite linewidth of the probe and coupling fields (giving rise to dephasing rates γ_p and γ_c , respectively) is included, as well as the dephasing of the Rydberg states with respect to the other states (rate γ_{Ry}). The latter is most likely due to fluctuating electric and magnetic stray fields. The linewidth of the microwave source is negligible. For EIT the important linewidth is the relative linewidth γ_{rel} of the two-photon transition between the probe and coupling laser, typically taken equal to $\gamma_p + \gamma_c$ [84]. However, for the EIT locking scheme used to stabilise the coupling laser transition [140], γ_{rel} is actually less than the linewidth of either laser. The resulting dephasing matrix $\mathcal{L}_d(\rho)$ is given by

$$\mathcal{L}_d(\rho) = -\sum_{i,j} \gamma_{ij} \rho_{ij} |i\rangle\langle j|, \quad (7.6)$$

where the laser-induced dephasing rates γ_{ij} are obtained from summing over the linewidth of all fields coupling $|i\rangle$ to $|j\rangle$. Replacing $\gamma_p + \gamma_c$ by γ_{rel} for the reason above, the total dephasing rates are given by the following equation:

The steady state solution of Equation (7.5) is found by setting $\partial\rho/\partial t = 0$. Within the semiclassical theory described in Chapter 2, the susceptibility of the system, $\chi(\Delta_p)$, is proportional to the steady state coherence, ρ_{21}^s , between the intermediate and ground states, i.e.,

$$\chi(\Delta_p) = -\frac{2Nd_{21}^2}{\hbar\epsilon_0\Omega_p}\rho_{21}^s, \quad (7.8)$$

where N is the atomic density, $d_{21} = \langle 2 | \mathbf{er} \cdot \hat{\epsilon}_+ | 1 \rangle = 1/\sqrt{3} \times 5.177 ea_0$ [110] is the dipole matrix element for the probe transition and the superscript s denotes the steady state solution. The transmission through the medium, T , is then given by the Beer-Lambert law

$$T = \exp\left(\frac{2NLd_{21}^2k_p}{\hbar\epsilon_0\Omega_p}\text{Im}[\rho_{21}^s]\right), \quad (7.9)$$

where L is the length of the atomic cloud and $k_p = 2\pi/\lambda_p$ is the wavenumber of probe laser. At the relatively low probe powers considered in this work, ρ_{21}^s is independent of γ_c ; instead it is only through γ_{rel} that the linewidth of the coupling laser enters. Setting the column density, $CD \equiv NL$ and assuming the weak probe limit, the transmission becomes a function of eight parameters, i.e., $\Omega_c, \Omega_\mu^r, \Delta_c, \Delta_\mu, \gamma_p, \gamma_{\text{rel}}, \gamma_{\text{Ry}}$, and CD which can be determined from fitting experimental data.

We begin by fitting Equation (7.9) to data using the probe laser only, reducing the system to two-levels to obtain CD and $\gamma_p/2\pi$ ($1.5 \times 10^{13} \text{ m}^{-2}$ and 0.33 MHz, respectively). Subsequently, we fit the three-level EIT transmission, which determines the quantities $\Omega_c/2\pi$, $\Delta_c/2\pi$ and $\gamma_{\text{rel}}/2\pi$ (5.5 MHz, -1.9 MHz and 0.14 MHz, respectively). Finally the remaining three variables, related to the microwave dressing, Ω_μ^r , Δ_μ and γ_{Ry} are determined using the ten-level model. Ω_μ^r scales proportional to the applied microwave field as expected, $\Delta_\mu/2\pi$ fluctuates between -0.2 and 0 MHz and $\gamma_{\text{Ry}}/2\pi$ is 0.3 MHz.

Using this method we obtain excellent agreement between the theoretical prediction (red solid curve) and the experimental data (black solid curve)

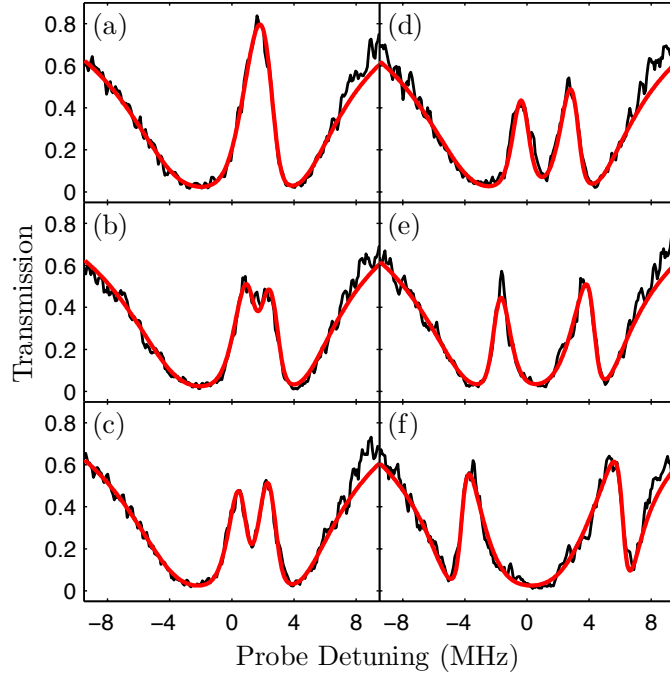


Figure 7.3: EIT spectra with increasing microwave coupling. The microwave Rabi frequencies, Ω_{μ}^r from the fit parameters, are (a) 0, (b) 2.2, (c) 3.6, (d) 6.8 (e) 12.2, and (f) $21.0 \times 2\pi$ MHz; these values match the scaling of the microwave power in the experiment, although the microwave electric field cannot be measured. Adding microwave fields into the system causes the dark resonance (EIT resonance) to split to two, similar to the Autler-Townes splitting [43], and the separation of the EIT resonances increase with the strength of the microwave coupling.

for each microwave power, as shown in Figure 7.3. The calculated lineshape is sensitive to the number of levels included in the model. Removing the states of $5s \ ^2S_{1/2} \ F'' = 1$ and $5p \ ^2P_{1/2} \ F''' = 1$ breaks down the symmetry of the microwave couplings, leading to anomalous resonances, i.e., a single EIT resonance in the three-level system splits into five EIT resonances, which are not observed in the experiment. In fact, for the ten-level system, one would expect the ground state, $|1\rangle$, to interact with the nine dressed states, which are formed from $|2\rangle, |3\rangle, \dots, |8\rangle$ and $|9\rangle$; and hence, eight EIT resonances (or

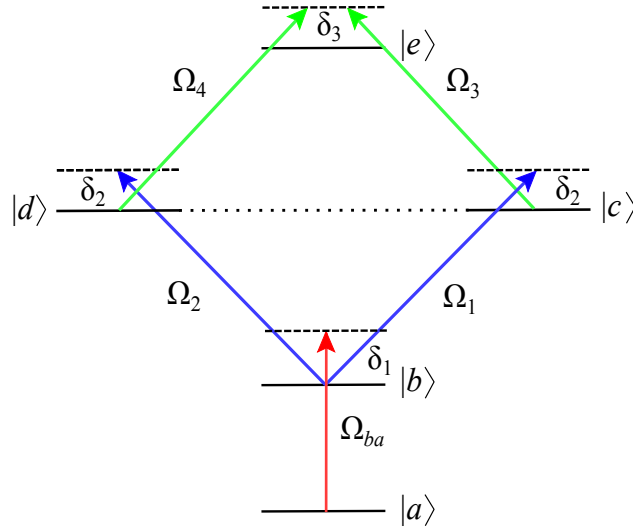


Figure 7.4: Schematic of the level scheme used in the five-level toy-model systems. The ground state, $|a\rangle$, couples to the intermediate state, $|b\rangle$, via the weak coupling Ω_{ba} . There are two pathways with which $|b\rangle$ can couple to $|e\rangle$: either via $|c\rangle$ or $|d\rangle$, in which the energies of $|c\rangle$ and $|d\rangle$ are degenerate. The Rabi frequencies for the coupling between $|b\rangle$, $|c\rangle$, $|d\rangle$ and $|e\rangle$ are Ω_j , where $j = 1, 2, 3, 4$ and their orders are shown in the diagram. The detunings δ_1 , δ_2 and δ_3 are also defined as shown in the diagram. The natural linewidths of $|b\rangle$, $|c\rangle$ ($|d\rangle$), and $|e\rangle$ are Γ_1 , Γ_2 , and Γ_3 , respectively.

nine absorption resonances) are expected to be observed. However, due to the destructive interference of the microwave couplings, only two EIT resonances are predicted from the theory and this is consistent with the experimental data. This destructive interference is the main subject of the next section.

7.3 Destructive interference of the microwave couplings

As mentioned in the previous section, due to the destructive interference between the microwave couplings, we observe only two EIT resonances in the experiment, not eight as expected using the dressed state formalism. The suppression of the EIT resonances is caused by the interference between different microwave coupling paths. For example, in the ten-level model $|3\rangle$ couples to $|6\rangle$ via either $|4\rangle$ or $|5\rangle$. To understand this phenomenon, we consider the simpler five-level system shown in Figure 7.4. The ground state, $|a\rangle$, couples to the intermediate state, $|b\rangle$, via the Rabi frequency Ω_{ba} . The energy levels of $|b\rangle$, $|c\rangle$, $|d\rangle$ and $|e\rangle$ form a diamond-shaped configuration, and $|c\rangle$ and $|d\rangle$ are degenerate in energy. From the intermediate state, $|b\rangle$, there exist two paths in which $|b\rangle$ can couple to $|e\rangle$: $|b\rangle \xrightarrow{\Omega_1} |c\rangle \xrightarrow{\Omega_3} |e\rangle$ and $|b\rangle \xrightarrow{\Omega_2} |d\rangle \xrightarrow{\Omega_4} |e\rangle$. The Rabi frequencies, Ω_j ($j = 1, 2, 3, 4$), represents the strength of the coupling between the corresponding states. The Hamiltonian of this system is given by $\mathcal{H}_{5L} = \mathcal{H}_0 + \mathcal{H}_{\text{int}}$, where

$$\mathcal{H}_0 = -\hbar\delta_1 |b\rangle \langle b| - \hbar(\delta_1 + \delta_2) (|c\rangle \langle c| + |d\rangle \langle d|) - \hbar(\delta_1 + \delta_2 + \delta_3) |e\rangle \langle e|, \quad (7.10a)$$

$$\mathcal{H}_{\text{int}} = \frac{\hbar\Omega_{ba}}{2} |a\rangle \langle b| + \frac{\hbar\Omega_1}{2} |b\rangle \langle c| + \frac{\hbar\Omega_2}{2} |b\rangle \langle d| + \frac{\hbar\Omega_3}{2} |c\rangle \langle e| + \frac{\hbar\Omega_4}{2} |d\rangle \langle e| + \text{h.c.} \quad (7.10b)$$

δ_1 , δ_2 and δ_3 are the detunings defined as shown in Figure 7.4. For simplicity, assuming that $\Gamma_2 = \Gamma_3 = 0$ MHz and all dephasing decays are zero, the equations of motion for the system is obtained by applying Equation (7.5) to the Hamiltonian \mathcal{H}_{5L} with $c = \sqrt{\Gamma_1} |a\rangle \langle b|$, representing the natural decay from $|b\rangle$. In the weak probe limit, the steady state of ρ_{ab} , ρ_{ac} , ρ_{ad} , and ρ_{ae}

Table 7.1: The expressions for the dressed states and their associated eigenenergies when $\Omega_2^*\Omega_3 = \Omega_1^*\Omega_4$. The parameter, β , is defined as $\beta = \sqrt{|\Omega_1|^2 + |\Omega_2|^2 + |\Omega_3|^2 + |\Omega_4|^2}$.

Dressed state	Eigenvalue	Non-normalised Eigenvector
$ D_1\rangle$	$-\delta_1$	$(0, \Omega_4^*, -\Omega_3^*, 0)$
$ D_2\rangle$	$-\delta_1$	$(\Omega_3, 0, 0, -\Omega_1^*)$
$ D_3\rangle$	$-\beta/2 - \delta_1$	$(\Omega_1 ^2 + \Omega_2 ^2, -\beta\Omega_1^*, -\beta\Omega_2^*, \Omega_1^*\Omega_3^* + \Omega_2^*\Omega_4^*)$
$ D_4\rangle$	$\beta/2 - \delta_1$	$(\Omega_1 ^2 + \Omega_2 ^2, \beta\Omega_1^*, \beta\Omega_2^*, \Omega_1^*\Omega_3^* + \Omega_2^*\Omega_4^*)$

are determined from the set of equations given by

$$\left(\frac{\Gamma_1}{2} + i\delta_1\right) \rho_{ab}^s = \frac{i\Omega_1^*}{2} \rho_{ac}^s + \frac{i\Omega_2^*}{2} \rho_{ad}^s + \frac{i\Omega_{ba}}{2}, \quad (7.11a)$$

$$i(\delta_1 + \delta_2) \rho_{ac}^s = \frac{i\Omega_1}{2} \rho_{ab}^s + \frac{i\Omega_3^*}{2} \rho_{ae}^s, \quad (7.11b)$$

$$i(\delta_1 + \delta_2) \rho_{ad}^s = \frac{i\Omega_2}{2} \rho_{ab}^s + \frac{i\Omega_4^*}{2} \rho_{ae}^s, \quad (7.11c)$$

$$i(\delta_1 + \delta_2 + \delta_3) \rho_{ae}^s = \frac{i\Omega_3}{2} \rho_{ac}^s + \frac{i\Omega_4}{2} \rho_{ad}^s. \quad (7.11d)$$

In this approximation, we assume that $\rho_{aa}^s \approx 1$ and the other density matrix elements are approximately zero in their steady state. To further simplify the problem, we assume that $\delta_2 = \delta_3 = 0$; thus, ρ_{ab}^s is given by

$$\rho_{ab}^s = \frac{-2\Omega_{ba}\delta_1 (|\Omega_3|^2 + |\Omega_4|^2 - 4\delta_1^2) \times 1}{(\Omega_2^*\Omega_3 - \Omega_1^*\Omega_4)^2 - 4\delta_1^2 (|\Omega_1|^2 + |\Omega_2|^2) + 2i\delta_1 (\Gamma + 2i\delta_1) (|\Omega_3|^2 + |\Omega_4|^2 - 4\delta_1^2)}. \quad (7.12)$$

The first term in the denominator, $(\Omega_2^*\Omega_3 - \Omega_1^*\Omega_4)^2$ represents the interference between the microwave couplings in the diamond configuration. According to Equation (7.12), we can categorise the symmetry of the system into three cases.

Case 1: No symmetry, i.e., $\Omega_2^*\Omega_3 \neq \Omega_1^*\Omega_4$

In this case, the absorption lineshape of the system contains four resonances

(corresponding to three EIT resonances) since ρ_{ab}^s has four poles as a function of δ_1 . The corresponding dressed state picture is that $|b\rangle$, $|c\rangle$, $|d\rangle$ and $|e\rangle$ form dressed states $|D_n\rangle$ due to the interactions represented by the Rabi frequencies Ω_j 's. All of these dressed states contain $|b\rangle$ so that the overlap integral between each of these dressed states and the ground state, $\langle a|e\rangle\langle D_n|$, does not vanish. The absorption resonances occur when δ_1 is tuned such that one of these dressed states is on resonance with the ground state; in this vicinity the dressed state couples strongly to the ground state with the interaction strength given by $k_b\Omega_{ba}$, where $|k_b|^2$ is the probability of finding $|b\rangle$ in the dressed state.

Case 2: $\Omega_2^*\Omega_3 = \Omega_1^*\Omega_4$

In this situation, Equation (7.12) reduces to

$$\rho_{ab}^s = \frac{\Omega_{ba}(|\Omega_3|^2 + |\Omega_4|^2 - 4\delta_1^2)}{2\delta_1(|\Omega_1|^2 + |\Omega_2|^2) - i(\Gamma + 2i\delta_1)(|\Omega_3|^2 + |\Omega_4|^2 - 4\delta_1^2)}, \quad (7.13)$$

in which the denominator contains three poles in δ_1 . This indicates that the symmetry of the coupling frequencies destroy one resonance from the absorption lineshape (as well as the EIT resonance). According to the dressed state formalism, the three resonances correspond to the interactions between the ground state with the three dressed states which contain $|b\rangle$ in their superpositions, i.e., $|D_2\rangle$, $|D_3\rangle$ and $|D_4\rangle$ as shown in Table 7.1. (The explicit expressions for the dressed states and their associated energies are shown in Table 7.1.) The resonances occur where their eigenvalues collapse to zero, i.e., $\delta_1 = 0$ or $\pm\beta/2$.

Case 3 The hidden symmetry, i.e., $\Omega_2 = \mp\Omega_1$ and $\Omega_4 = \pm\Omega_3$

In this situation, Equation (7.12) reduces to

$$\rho_{ab}^s = -\frac{\Omega_{ba}\delta_1}{\Omega_1^2 + i\delta_1(\Gamma + 2i\delta_1)}, \quad (7.14)$$

in which the denominator contains only two poles in δ_1 , corresponding to the two absorption resonances (and hence one EIT resonance). Though the system has no obvious symmetry of $\Omega_2^*\Omega_3 = \Omega_1^*\Omega_4$, the system behaves as

Table 7.2: The expressions for the dressed states and their associated eigenenergies when $\Omega_2 = \mp\Omega_1$ and $\Omega_4 = \pm\Omega_3$.

Dressed state	Eigenvalue	Normalised Eigenvector
$ D_1\rangle$	$-\Omega_1/\sqrt{2} - \delta_1$	$(\pm\sqrt{2}, \mp 1, 1, 0)/2$
$ D_2\rangle$	$\Omega_1/\sqrt{2} - \delta_1$	$(\mp\sqrt{2}, \pm 1, 1, 0)/2$
$ D_3\rangle$	$-\Omega_3/\sqrt{2} - \delta_1$	$(0, -1, \mp 1, \sqrt{2})/2$
$ D_4\rangle$	$\Omega_3/\sqrt{2} - \delta_1$	$(0, 1, \pm 1, \sqrt{2})/2$

if it were four-level system containing $|a\rangle$, $|b\rangle$, $|c\rangle$ and $|d\rangle$ (since $|D_1\rangle$ and $|D_2\rangle$ contain both $|c\rangle$ and $|d\rangle$) when the conditions $\Omega_2 = -\Omega_1$ and $\Omega_4 = \Omega_3$ or $\Omega_2 = \Omega_1$ and $\Omega_4 = -\Omega_3$ are fulfilled. Thus we refer to this symmetry as hidden symmetry. This is illustrated in Figure 7.5(c). From the perspective of the dressed state picture, the two absorption resonances correspond to the interaction between the ground state and $|D_1\rangle$ and $|D_2\rangle$ (whose components are shown in Table 7.2) and the positions of the resonances are at $\pm\Omega_1/2$.

The effect of the interference of the absorption lineshapes (proportional to $\text{Im}[\rho_{ba}^s]$) are illustrated in Figure 7.5, where (a) corresponds to Case 1 with $\Omega_1 = -\Omega_3 = 2 \times 2\pi$ MHz and $\Omega_2 = \Omega_4 = 3 \times 2\pi$ MHz, (b) corresponds to Case 2 with $\Omega_1 = \Omega_3 = 2 \times 2\pi$ MHz and $\Omega_2 = \Omega_4 = 3 \times 2\pi$ MHz, and (c) corresponds to Case 3 with $\Omega_1 = -\Omega_2 = 2 \times 2\pi$ MHz and $\Omega_3 = \Omega_4 = 3 \times 2\pi$ MHz. The weak probe Rabi frequency (Ω_{ba}) and the linewidth of $|b\rangle$ are $0.01 \times 2\pi$ and $6 \times 2\pi$ MHz, respectively. By adjusting the values of the Rabi couplings, Ω_j , one can switch from an opaque medium to a transparent medium, as well as, increasing (or decreasing) the numbers of dark resonances. Switching from Case 1 to Case 2, we destroy the dark resonance and the photon is blocked by the medium at $\delta_1 = 0$, this effect is referred to as photon inhibition [150–152]. Note that not only can we adjust the magnitude of the Rabi frequencies in order to switch among the three cases, but we are also able to control their phases for the same purpose if

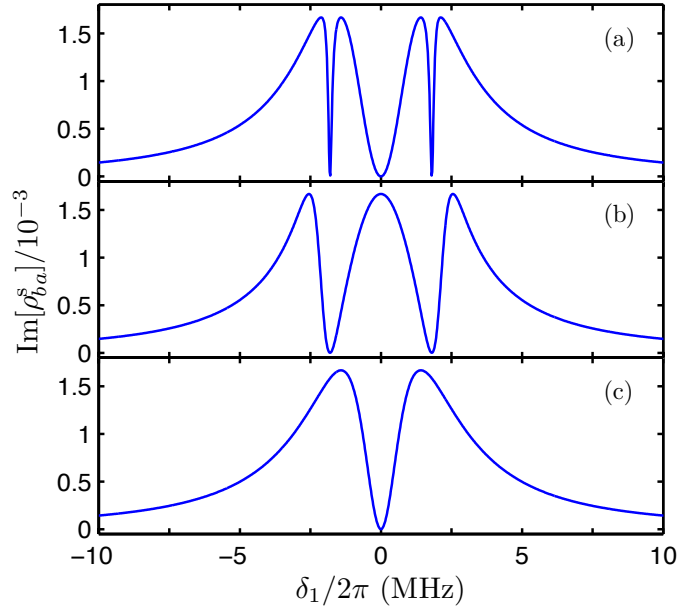


Figure 7.5: $\text{Im}[\rho_{ba}^s]$ are plotted against probe detuning, δ_1 , for various set of parameters corresponding to three cases: (a) $\Omega_1 = -\Omega_3 = 2 \times 2\pi$ MHz and $\Omega_2 = \Omega_4 = 3 \times 2\pi$ MHz (Case 1), (b) $\Omega_1 = \Omega_3 = 2 \times 2\pi$ MHz and $\Omega_2 = \Omega_4 = 3 \times 2\pi$ MHz (Case 2), and (c) $\Omega_1 = -\Omega_2 = 2 \times 2\pi$ MHz and $\Omega_3 = \Omega_4 = 3 \times 2\pi$ MHz (Case 3). The weak probe Rabi frequency (Ω_{ba}) and the linewidth of $|b\rangle$ are $0.01 \times 2\pi$ and $6 \times 2\pi$ MHz. The illustration begins with the case in which there is no symmetry in the system (figure (a)), where we obtain two narrow feature of EIT resonances. When the condition $\Omega_2^* \Omega_3 = \Omega_1^* \Omega_4$ is realised, the two narrow EIT resonances disappear, while the central broadened EIT splits into two EIT resonances (figure (b)). This process is referred to as photon inhibition, in which the medium switches from being transparent to being absorptive at $\delta_1 = 0$. Finally when the hidden symmetry condition is fulfilled, the system reduces to an effective three-level system as shown in (c).

we have an independent control of each field. For example, if the phase of one of the Rabi frequencies changes from the value it must have for having $\Omega_2^* \Omega_3 = \Omega_1^* \Omega_4$, the condition is no longer valid and we recover the three EIT

resonances.

From the perspective of path interference, the destructive interference of the resonances in Case 2 and 3 is the result from the quantum interference between different pathways for the $|a\rangle \rightarrow |b\rangle$ transition. To explicitly show the pathways coupling $|a\rangle$ and $|b\rangle$, we extend Equation (7.12) to the case where neither δ_2 and δ_3 are assumed to vanish and Γ_2 and Γ_3 are not neglected. This gives

$$\rho_{ab}^s = \frac{i\Omega_{ba}}{2G_1} \left\{ 1 - \frac{\Omega_1^2}{4G_1G_2 + \Omega_1^2} - \frac{4G_1G_2\Omega_2^2}{(4G_1G_2 + \Omega_1^2)(4G_1G_2 + \Omega_1^2 + \Omega_2^2)} + \frac{4G_1G_2(\Omega_1\Omega_3 + \Omega_2\Omega_4)^2 / (4G_1G_2 + \Omega_1^2 + \Omega_2^2)}{(\Omega_2\Omega_3 - \Omega_1\Omega_4)^2 + 4G_2G_3(\Omega_1^2 + \Omega_2^2) + 4G_1G_2(4G_2G_3 + \Omega_3^2 + \Omega_4^2)} \right\}, \quad (7.15)$$

with

$$G_1 = \frac{\Gamma_1}{2} + i\delta_1, \quad (7.16a)$$

$$G_2 = \frac{\Gamma_2}{2} + i(\delta_1 + \delta_2), \quad (7.16b)$$

$$G_3 = \frac{\Gamma_3}{2} + i(\delta_1 + \delta_2 + \delta_3). \quad (7.16c)$$

Here, Γ_2 and Γ_3 are the natural linewidths of $|c\rangle$ ($|d\rangle$) and $|e\rangle$, respectively. They are included in order to prevent singularity in Equation (7.15) when $\delta_1 = \delta_2 = \delta_3 = 0$. We also assume that all Rabi frequencies are real for simplicity. The first term in Equation (7.15) represents the effect of the two-level absorption ($|a\rangle \rightarrow |b\rangle$). The correction to the absorption lineshape due to the perturbation from Ω_1 is given in the second term in which $|a\rangle$, $|b\rangle$ and $|c\rangle$ form a cascade three-level system [84]. The coupling Ω_2 plays a role via the third term in the equation which represents the correction to the lineshape in a Y-system. The signature of the interference between the couplings, Ω_j , is given in the fourth term, in which $(\Omega_2\Omega_3 - \Omega_1\Omega_4)^2$ is explicitly shown in the denominator. Expanding the fourth term of Equation (7.15) (considering only the terms involving $(\Omega_2\Omega_3 - \Omega_1\Omega_4)^2$) and setting $\delta_1 = \delta_2 = \delta_3 = 0$, the

leading terms of the expansion are

$$\begin{aligned}
& - \frac{i\Omega_{ba}}{2\Gamma_1^2\Gamma_2^4\Gamma_3^2} (\Omega_1^2\Omega_2^2\Omega_3^4 - 2\Omega_1^3\Omega_2\Omega_3^3\Omega_4 + 2\Omega_1\Omega_2^3\Omega_3^3\Omega_4 + \Omega_1^4\Omega_3^2\Omega_4^2 - 4\Omega_1^2\Omega_2^2\Omega_3^2\Omega_4^2 \\
& \quad + \Omega_2^4\Omega_3^2\Omega_4^2 + 2\Omega_1^3\Omega_2\Omega_3\Omega_4^3 - \Omega_1\Omega_2^3\Omega_3\Omega_4^3 + \Omega_1^2\Omega_2^2\Omega_4^4) \\
& + \frac{i\Omega_{ba}}{2\Gamma_1^3\Gamma_2^5\Gamma_3^2} (\Omega_1^4\Omega_2^2\Omega_3^4 + \Omega_1^2\Omega_2^4\Omega_3^4 - 2\Omega_1^5\Omega_2\Omega_3^3\Omega_4 + 2\Omega_1\Omega_2^5\Omega_3^3\Omega_4 + \Omega_1^6\Omega_3^2\Omega_4^2 \\
& \quad - 3\Omega_1^4\Omega_2^2\Omega_3^2\Omega_4^2 - 3\Omega_1^2\Omega_2^4\Omega_3^2\Omega_4^2 + \Omega_2^6\Omega_3^2\Omega_4^2 + 2\Omega_1^5\Omega_2\Omega_3\Omega_4^3 \\
& \quad - 2\Omega_1\Omega_2^5\Omega_3\Omega_4^3 + \Omega_1^4\Omega_2^2\Omega_4^4 + \Omega_1^2\Omega_2^4\Omega_4^4). \quad (7.17)
\end{aligned}$$

According to Equation (7.17), the interference between the couplings comes from nine- and eleven-photon transition. Following the argument given in [153], each term in the bracket represents a transition pathway from $|a\rangle$ to $|b\rangle$. For example, $i\Omega_{ba}\Omega_1^2\Omega_2^2\Omega_3^4/2\Gamma_1^2\Gamma_2^4\Gamma_3^2$ represents the transition $|a\rangle \rightarrow |b\rangle \rightarrow |c\rangle \rightarrow |e\rangle \rightarrow |c\rangle \rightarrow |e\rangle \rightarrow |c\rangle \rightarrow |b\rangle \rightarrow |d\rangle \rightarrow |b\rangle$. Under the condition given by Case 2, the nine pathways of the nine-photon transitions (first bracket) interfere with one another, while twelve pathways in the eleven-photon transition (second bracket) also destructively interferes with one another. In the hidden symmetry case, the destructive interference of the pathways in the nine-photon transition and the pathways in the eleven-photon transition is at their maximum, i.e., the sum in each bracket are exactly zero. Note that the second and third terms of Equation (7.15) always tend to reduce the absorption due to the minus sign while the sign of the last term is not positive definite, but it depends on the condition of the couplings. For example, when $\Omega_2\Omega_3 = \Omega_1\Omega_4$ the last term is positive and it helps increasing the absorption (Figure 7.5(b)). On the other hand the last term vanishes when the system is subject to the condition given by the hidden symmetry, thus the absorption decreases as a result of the second and third terms (Figure 7.5(c)).

In the ten-level model, the system is subject to the condition described in Case 2. For example, the Rabi couplings of $|4\rangle$, $|5\rangle$, $|6\rangle$ and $|7\rangle$ form a diamond-shaped configuration: $|4\rangle \xrightarrow{-\Omega_\mu^r/\sqrt{12}} |6\rangle \xrightarrow{-\Omega_\mu^r/\sqrt{6}} |5\rangle$ and $|4\rangle \xrightarrow{\Omega_\mu^r/\sqrt{12}}$

$|7\rangle \xrightarrow{\Omega_\mu/\sqrt{6}} |5\rangle$. Thus the condition $\Omega_2\Omega_3 = \Omega_1\Omega_4$ is fulfilled and the EIT lineshape shows two EIT resonances, c.f. Figure 7.5(b).

7.4 Group index, dispersion and pulse propagation

One attractive aspect of EIT is the possibility of obtaining a very high group index resulting in slow light [11]. By varying the group index one can change the mixing angle between the light and matter components of dark state polaritons [14] and thereby implement photon storage [15, 16]. The large group index arises from the rapid variation of the refractive index with probe frequency due to the presence of the coupling laser. An interesting feature of microwave dressing is the ability to modify the dispersion and hence the dynamics of the Rydberg dark state polaritons [154]. Furthermore, microwave dressing can switch the group index to negative sign, giving rise to “superluminal” propagation or fast light [20, 155].

We begin this section with a discussion of how microwave dressing changes the group index of the system. Then the propagation of a Gaussian pulse through the system is theoretically investigated.

7.4.1 Switching signs of group index

The group index of the system, n_{gr} , is given by [93]

$$n_{\text{gr}} = n_{\text{ph}} + \omega_{\text{p}} \frac{\partial n_{\text{ph}}}{\partial \omega_{\text{p}}}, \quad (7.18)$$

where ω_{p} is the frequency of the probe laser and $n_{\text{ph}} = 1 + \text{Re}[\chi]/2$ is the refractive index. According to Equation (7.18), the group index depends on how the refractive index varies as a function of frequency, i.e. $\partial n_{\text{ph}}/\partial \omega_{\text{p}}$. In three-level systems, the dark resonance causes a sudden variation in the

refractive index of the medium, resulting in a large (positive) $\partial n_{\text{ph}}/\partial\omega_{\text{p}}$; and hence, a large group index. Hau *et al.* [11] has shown that the group velocity of a pulse can reduce to 17 m/s in the medium. On the other hand, if the dispersion of the medium is large and anomalous, i.e., $\partial n_{\text{ph}}/\partial\omega_{\text{p}} < 0$, the group index and group velocity become negative, leading to “superluminal” propagation or fast light. This means that the maximum of the outgoing pulse may be generated out of the medium before the maximum of the incident pulse has arrived at the medium. Note that this phenomenon does not violate the principle of relativity as the group velocity is not the velocity at which the information travels [155–157].

In our system, the group index can be switched between positive and negative values by turning on and off the microwave field. To illustrate the potential of microwave dressing to modify the dispersion we extract the real part of the susceptibility from the ten-level model and use this to calculate the group index which is plotted in Figure 7.6. We see that on resonance, the microwave field allows independent control of the group index and absorption which could be useful in controlling the interaction between dark state polaritons. At a probe detuning of $\Delta_{\text{p}}/2\pi = 1$ MHz without and with the microwave field the group index is switched from approximately $+5 \times 10^4$ (Figure 7.6(e)) to -10^5 (Figure 7.6(f)) within the transparency window. The negative group index corresponds to “superluminal” or backwards propagation [158], albeit with increased dissipation. The term backwards propagation comes from the fact that the pulse travels backwards within the medium with negative group index. However, in contrast to the simple probe-only case (Figure 7.6(a)), with microwave dressing one can vary both the microwave and coupling laser powers to trade-off between pulse speed, bandwidth and transparency.

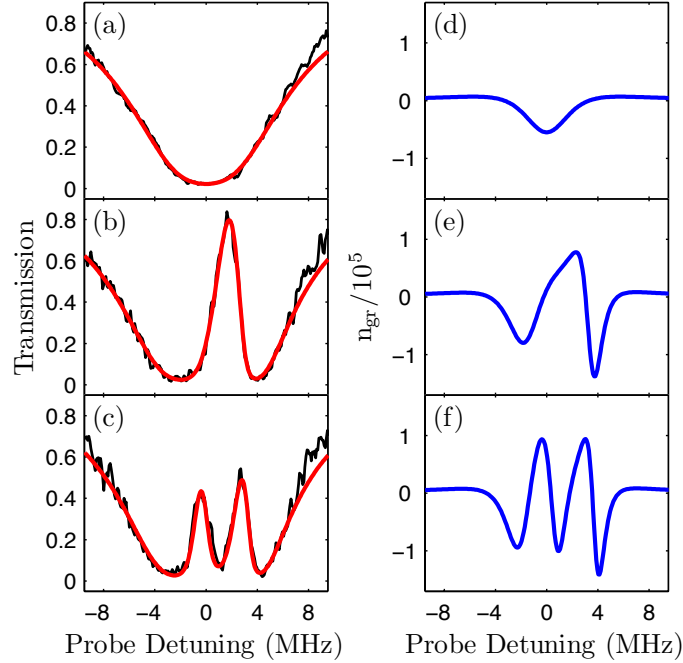


Figure 7.6: Transmission and calculated group index, n_{gr} , for two-level absorption (a,d), EIT (b,e) and EIT with microwave dressing (c,f). This illustrates how the coupling and microwave fields can be used to control the transparency and pulse propagation speed of the medium. At a probe detuning of $\Delta_p/2\pi = 1$ MHz without and with the microwave field the group index is switched from approximately $+5 \times 10^4$ (Figure 7.6(e)) to -10^5 (Figure 7.6(f)) within the transparency window.

7.4.2 Gaussian pulse propagation

Consider a Gaussian pulse at $z = 0$ whose temporal form is given by

$$\mathcal{E}(0, t) = e^{-t^2/(2\tau^2)} e^{-i\bar{\omega}t}, \quad (7.19)$$

where $\bar{\omega}/2\pi$ is the carrier frequency and the full width at half maximum (FWHM) of the electric field² is $\Delta t = \tau\sqrt{8\ln 2}$. To describe the propagation of the Gaussian pulse through the medium, we consider the one-dimensional

²The FWHM of the intensity profile is given by $\Delta t_I = 2\tau\sqrt{\ln 2}$.

wave equation in the medium: [93, 159–161]

$$\left(\frac{\partial^2}{\partial z^2} - \frac{1}{c^2} \frac{\partial^2}{\partial t^2} \right) \mathcal{E}(z, t) = \mu_0 \frac{\partial^2}{\partial t^2} \mathcal{P}(z, t), \quad (7.20)$$

where $c = 1/\sqrt{\epsilon_0\mu_0}$, ϵ_0 is the permittivity of free space, μ_0 is the permeability of free space and $\mathcal{P}(z, t)$ is the polarisation of the medium. Taking the Fourier transform of Equation (7.20), the wave equation, in the frequency space, becomes,

$$\left(\frac{\partial^2}{\partial z^2} + \frac{\omega^2}{c^2} \right) \tilde{\mathcal{E}}(z, \omega) = -\mu_0 \omega^2 \tilde{\mathcal{P}}(z, \omega), \quad (7.21)$$

where $\tilde{\mathcal{E}}(z, \omega)$ and $\tilde{\mathcal{P}}(z, \omega)$ are the Fourier transform of the electric field and the polarisation, respectively. They are defined as [91, 93, 159]

$$\tilde{\mathcal{E}}(z, \omega) = \frac{1}{\sqrt{2\pi}} \int_{-\infty}^{\infty} \mathcal{E}(z, t) e^{i\omega t} dt, \quad (7.22a)$$

$$\tilde{\mathcal{P}}(z, \omega) = \epsilon_0 \chi(\omega) \tilde{\mathcal{E}}(z, \omega), \quad (7.22b)$$

with

$$\chi(\omega) = \int_{-\infty}^{\infty} \chi(t') e^{i\omega t'} dt'. \quad (7.23)$$

Substituting Equation (7.22b) into Equation (7.21) and rearranging, the wave equation becomes

$$\left[\frac{\partial^2}{\partial z^2} + \frac{\omega^2}{c^2} n^2(\omega) \right] \tilde{\mathcal{E}}(z, \omega) = 0, \quad (7.24)$$

where $n(\omega)$ is the complex refractive index,

$$n^2(\omega) = 1 + \chi(\omega). \quad (7.25)$$

The solution of Equation (7.24) for an electric field propagating in the $+z$ direction is given by

$$\tilde{\mathcal{E}}(z, \omega) = \tilde{\mathcal{E}}(0, \omega) e^{i\omega n z / c}. \quad (7.26)$$

Then the temporal variation of the electric field at z is given by the inverse Fourier transform of Equation (7.26), i.e.,

$$\mathcal{E}(z, t) = \frac{1}{\sqrt{2\pi}} \int_{-\infty}^{\infty} \tilde{\mathcal{E}}(0, \omega) e^{i[\omega n(\omega)z/c - \omega t]} d\omega, \quad (7.27)$$

with

$$\tilde{\mathcal{E}}(0, \omega) = \tau e^{-\tau^2(\omega - \bar{\omega})^2/2}. \quad (7.28)$$

This equation is the starting point for the investigation of pulse propagation. It implies that if one knows the initial temporal variation of the pulse, then the temporal variation of the pulse at any point in space is the sum of the plane wave components whose phases accumulate the additional phase through the distance travelled, z , given by $\exp(i\omega n z/c)$. This is known as the re-phasing mechanism [162, 163]. In the case of superluminal pulse propagation, the phases of the Fourier components of the input pulse are altered by the re-phasing term, $\exp(i\omega n z/c)$, such that the Fourier components at the front of the medium (in the case of negative group index) constructively interfere with one another to create the output pulse before the input pulse arrives at the medium [162, 164]. Note that the effect of absorption is implicitly included in the complex refractive index as $\text{Im}[n]$ is proportional to $\text{Im}[\chi]$, and hence, to the absorption coefficient.

Figure 7.7 and 7.8 illustrate the propagation of a pulse through a medium of length approximately 0.5 mm for two pulse widths of 0.5 and 0.05 μs , respectively. The corresponding FWHMs in frequency of the pulses are 0.75 and 7.5 MHz, respectively. The carrier frequency is centred at approximately $\Delta_p/2\pi = 1 \text{ MHz}^3$, corresponding to a group velocity around $-4 \times 10^3 \text{ m/s}$ or a group index of -7.5×10^4 (see Figure 7.6). For the pulse in Figure 7.7, the dispersion of the medium is approximately linear; and hence, the pulse propagation shows no effect of pulse broadening and pulse distortion due to the contributions of second and higher order in ω to the dispersion. Nevertheless, the pulse suffers from the loss of energy due to absorption as shown by the red solid line in Figure 7.7. The time delay of the pulse is given by

$$t_d = \frac{L}{v_{\text{gr}}}. \quad (7.29)$$

³The carrier frequency is given in term of probe detuning and their relationship is $\Delta_p = \bar{\omega} - \omega_0$, where ω_0 is the transition frequency between $5S_{1/2}$ (F=2) and $5P_{3/2}$ (F=3).

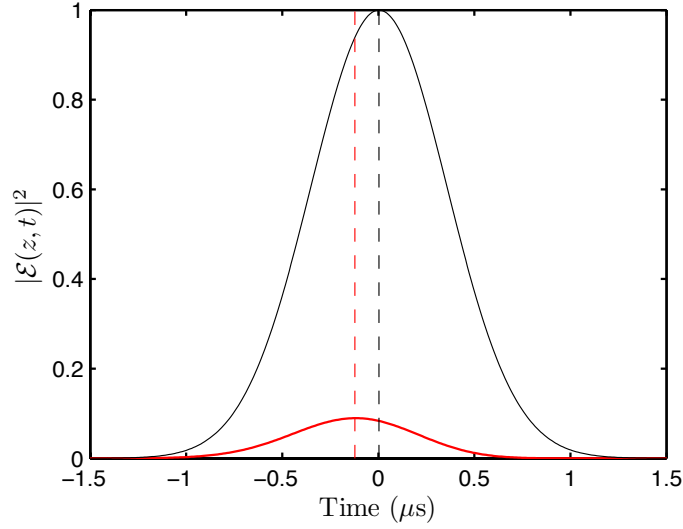


Figure 7.7: A pulse whose width is $0.5 \mu\text{s}$ is propagated through the medium of width 0.5 mm . The carrier frequency of the pulse is approximately at $\Delta_p/2\pi = 1 \text{ MHz}$. The advancement of the output pulse from the medium (red solid line) is clearly illustrated in the figure when compared to the output pulse which is propagated in the free space with the same distance (black solid line). The time delay of the output pulse is $-0.1 \mu\text{s}$, which corresponds to the group velocity of $-4 \times 10^3 \text{ m/s}$ as expected from Figure 7.6. Note that the output pulse does not suffer from distortion as the linear approximation of the dispersion is a good approximation for the range of the frequency covered by the input pulse.

The time delay of the pulse shown in Figure 7.7 is $t_d = 0.5 \times 10^{-3}/(-4 \times 10^3) = -0.1 \mu\text{s}$. The negative value in the time delay means that the pulse arrives early. This value is consistent with the numerical result. When the frequency of the pulse covers the region where the dispersion relation is not linear in frequency space, not only does the output pulse suffer from the loss in energy due to absorption, the effect of pulse distortion is also clearly observed, i.e., the input pulse splits into many pulses (shown as red solid line in Figure 7.8). This distortion effect is entirely caused by the third and higher order terms in ω in the dispersion relation and is not due to the absorption as

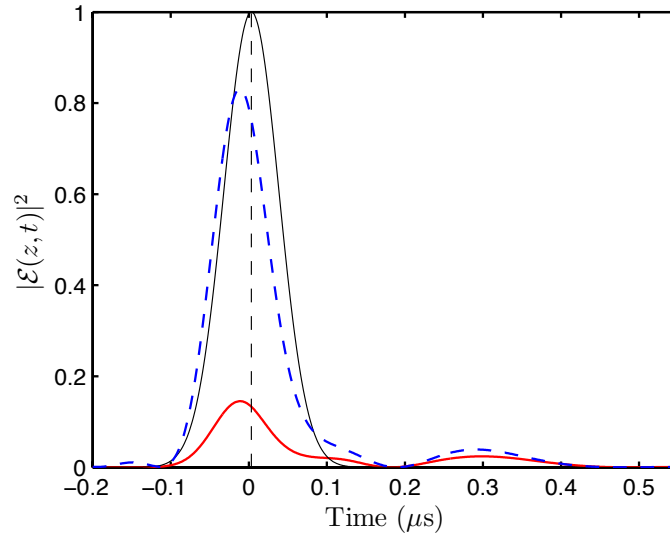


Figure 7.8: A pulse whose width is $0.05 \mu\text{s}$ is propagated through the medium of width 0.5 mm . The carrier frequency of the pulse is approximately at $\Delta_p/2\pi = 1 \text{ MHz}$. Since the FWHM of the input pulse is large, the linear expansion of the dispersion is now not valid, i.e., the higher order terms in the expansion must be included. This causes the output pulse (red solid line) to suffer from distortion, namely, the input pulse splits into many output pulses as shown in the figure. Even in a lossless medium, the pulse distortion is still observable for the output pulse (dashed blue line). The black solid line is the output pulse which propagates in free space over the same distance. Note that the main output pulse (with the largest area) clearly shows the effect of superluminal propagation.

discussed in [163]. The blue dashed line in Figure 7.8 shows the output pulse in the situation in which the medium is lossless⁴. There is no absorption, but yet this output pulse still suffers from distortion. Note that the main output pulse (with the largest area) still exhibits superluminal propagation. In particular, the blue dashed signal is higher than the black signal around $-0.15 \mu\text{s}$ due to the different interference between Fourier components in the

⁴The absorption coefficient vanishes in the lossless medium, i.e., $\alpha = 0$.

two cases.

7.5 Conclusions and Outlook

In conclusion, we demonstrated microwave dressing of electromagnetically induced transparency involving highly excited Rydberg states. The microwave field splits the EIT peak allowing us to tune the probe laser to such that the absorption is relatively small while the slope of the dispersion remains steep and negative. This results in the superluminal propagation. One can switch from transparent medium to an opaque medium by turning on and off the microwave field. Consequently a microwave field could be used to control the interaction time between Rydberg polaritons. Switching the group index to a negative value, we showed that the output pulse can lead the reference by about $0.1 \mu\text{s}$, which is relatively large compared to the work by Wang *et al.* [165]. We also discussed the interference of the microwave couplings in the simpler case of a five-level system. Based on the symmetry of the microwave couplings, one can reduce the five-level system to four- and three-level systems for particular combination of Rabi frequencies. In our ten-level model, the system is such that only two EIT resonances are observed.

An interesting application of microwave dressing is the enhancement of the long-range dipole-dipole interactions due to an effective increase in the blockade radius. As demonstrated in [21], the long-range dipole-dipole interaction shifts the energy between Rydberg states. Such microwave tuning of the non-linear optical response of the blockaded ensemble could be useful in the realisation of single photon phase gates [40]. It is also interesting to extend this system to the case of thermal atoms.

Chapter 8

Conclusions

In this thesis, we have investigated how Rydberg dark states interact with external applied fields and studied some of the applications of their interactions. The thesis began with a discussion of the general problem of a three-level system interacting with two electromagnetic fields. The use of the dressed state formalism makes it possible to thoroughly understand the physics of the three-level system, in particular in regards to, e.g., electromagnetically induced transparency, coherent population trapping and stimulated Raman adiabatic passage. We also discussed the weak probe condition ($\Omega_p^2 \ll \Gamma_3(\Gamma_3 + \Gamma_2)$) under which the steady state solution of the optical Bloch equation can be found analytically.

We then developed a theoretical model of Rydberg EIT systems with Doppler broadening using the theory presented in Chapter 2. This theoretical model was fitted against EIT data measured by Bason et al. in ^{85}Rb [92] and a good agreement between the model and the experimental data was demonstrated. We also showed the effect of the wavevector mismatch which scales the frequency distance between the EIT resonances by a factor of $(k_p - k_c)/k_p$. This effect arises from the fact that the wavevector of the two lasers do not exactly cancel each other. We further demonstrated that the reduced dipole matrix elements for the transition between the $5\text{P}_{3/2}$ state and $n\text{S}_{1/2}$ Rydberg states

can be obtained by fitting the theoretical model to the experimental data. A rather similar method has recently been used by Piotrowicz et al., who developed a sophisticated model to tackle the problem of inhomogeneity of the coupling field and to fit the EIT signal in order to obtain the reduced matrix element between the $5P_{3/2}$ state and nD_J Rydberg states [101].

A problem with using a two-photon transition as in Chapter 3 is the presence of screening charges [25, 32], produced by the photoionisation of Rb atoms deposited on the inside of the vapour cell [114]. This is because the wavelength of the blue laser (~ 480 nm) is less than the threshold wavelength of Rb metal (~ 550 nm) [115]. To avoid this problem, in Chapter 4 the 480 nm laser was replaced by two lasers whose wavelengths are 776 nm and 1290 nm. We showed that an effect of the third laser is to cause Autler-Townes splitting of the EIT resonance in cold atoms. In addition to the case of cold atoms, we further investigated the absorption profiles of thermal atoms. We demonstrated that for the case of parallel configuration in which the probe laser counter-propagates with respect to the two coupling lasers (c_1 and c_2), the transmission lineshape of the thermal atom exhibits an extra EIT resonance at zero probe detuning when the ratio of Rabi frequencies $\Omega_{c_2}/\Omega_{c_1}$ is small. This extra EIT resonance is not observed in the transmission lineshape for cold atoms. For a large value of $\Omega_{c_2}/\Omega_{c_1}$, the EIT resonance at zero probe detuning also disappears and the absorption coefficient of the system significantly increases. It turns out that the existence of the middle EIT resonance is due to the incomplete destruction of the EIT resonance, which manifests when averaging the absorption coefficient over all velocity classes. For the Doppler-free configuration, one needs to work at a very high Ω_{c_1} as, in the step of the first two-photon transition, a positive residual wavevector suppresses the EIT resonance. An EIA resonance can be created when the detunings Δ_{c_1} and Δ_{c_2} are both zero; this physically corresponds to an enhanced three-photon transition when the three lasers are simultaneously on resonance [117]. If one detunes the first coupling laser by a finite amount, the

system is now effectively a three-level system. This results in a displacement of one of the transmission dip to either side of the lineshape, depending on the sign of Δ_{c_1} , and in EIT at the centre of the dip. The next step of this work on three-photon transitions would be to apply the theory to an actual atomic system where the hyperfine structure is taken into account.

Following this discussion of Rydberg EIT, we developed a theory of EIT in the presence of an external radio frequency (rf) field. The frequency of this rf field is far off-resonance from any atomic transition. In this limit, we demonstrated the formation of Floquet dark states induced by the application of an ac field to a ladder system involving a highly-polarised Rydberg state. By fitting the theoretical model to the experimental data of Bason et al. [25], we obtained the value of the dc electric field applied across the vapour cell in the experiment. We showed that the information on the strength of the dc field is encoded into the relative frequency distance between sidebands and their relative heights; and hence, it is independent of the laser frequency. We have shown that charge imbalances in an enclosed vapour cell can cancel the spatial inhomogeneities of the field. Therefore for local field measurements the interaction region may need to be limited to a small volume. This would be the case, for instance, in the three-photon Doppler-free excitation scheme considered in Chapter 4, in which the two pump and the probe laser beams intersect at appropriate angles within a restricted volume.

In Chapter 6, we extended the theory of the Rydberg dark state dressed by an rf field to cover the case when the Floquet sideband breaks down. The conditions for which the effect of the rf field yields stable Floquet states were investigated. We showed that the latter have a well-defined manifold structure when the rf modulation is faster than the rf-free dynamics of the system. In the Floquet states picture, this means that there are no overlaps among these Floquet states; and hence, we observe well-defined resonance sidebands in the variation with probe frequency of the population transferred

to the upper state. This picture of stationary, well-defined Floquet states obtained in this thesis is similar to that discussed in previous works [25, 47, 51, 53, 142]. Furthermore, we demonstrated a resonance shift, similar to a Bloch-Siegert shift, due to the interaction between well-defined sidebands. We are not aware that this effect had been discussed previously in an atomic physics context of rf dressing; however, it has been reported in condensed matter physics [66]. In addition, the coherence property of the system must be maintained during the rf interaction. In terms of the spectral lineshape, this condition means that the linewidth of the resonance must be smaller than the frequency distance between two adjacent resonances so that EIT sidebands are resolved. When the system exhibits well-defined sidebands, we showed that an N -level model, consisting of a ground state and a manifold of N excited states, is a good approximation of the rf-dressed system. In the case of a three-level system, the N -level model breaks down when Ω_c is larger than $2\omega_{\text{rf}}$. We found that in order to reconcile the model with the actual rf-dressed system, the manifold of intermediate state sidebands must be included into the model. We called this effect the formation of induced sidebands and the new model the $N + N$ -level approximation. The focus of future work could be the investigation of the system when a three-photon transition is introduced in order to alleviate the problem of space charges as mentioned above, or/and when a dc field is added to the system.

In Chapter 7, Rydberg EIT in a cold atoms ensemble was dressed by a microwave field which resonantly couples two Rydberg states. In this case the transmission lineshape of the probe beam shows a splitting of the EIT peak, with the distance between the components being proportional to the strength of the microwave field. This allows us to control the absorptive and dispersive properties of the medium by adjusting the strength of the microwave field. For example, one can also switch from a transparent medium to an opaque medium by turning on and off the microwave field. Switching the group index to a negative value, we showed that, for parameters typical to

experiments done in Durham [21], the output pulse of width $0.5 \mu\text{s}$ can precede the reference pulse by about $0.13 \mu\text{s}$, which is relatively large compared to the shift found by Wang et al. [165]. We also discussed the interference of the microwave couplings in the simpler case of a five-level system. Based on the symmetry of the microwave couplings, one can reduce the five-level system to four- and three-level systems for particular combination of Rabi frequencies. In our full ten-level model, the system is such that only two EIT resonances are observed. It would be interesting to extend this system to the case of thermal atoms.

Appendix A

Factorising the dipole matrix element

We have seen that the dipole matrix element is one of the key quantities discussed throughout the thesis. Suppose that a laser couples a lower state $|a\rangle$ and a higher state $|b\rangle$. The dipole matrix element is given by $\langle b|er_q|a\rangle$, where r_q is the component of the position operator written in the spherical basis [74]. For a real atomic system in which the states $|a\rangle$ and $|b\rangle$ are represented by the hyperfine states $|F, m_F\rangle$ and $|F', m'_F\rangle$, respectively, the dipole matrix element is then $\langle F', m'_F|er_q|F, m_F\rangle$. One can separate the geometrical component out from the dipole matrix element using the Wigner-Eckart theorem [108, 109], that is

$$\langle F', m'_F|er_q|F, m_F\rangle = \langle F' ||er||F \rangle (-1)^{F-1+m'_F} \begin{pmatrix} F & 1 & F' \\ m_F & q & -m'_F \end{pmatrix} \sqrt{2F'+1}, \quad (\text{A.1})$$

where the bracket containing six elements is known as a 3j symbol and $\langle F' ||er||F \rangle$ is the reduced matrix element [108, 109]. The reduced matrix element only depends on the states F and F' , but not on m_F , m'_F and q , i.e., it is free from the choices of the orientation of the reference frame [109].

It is unusual to write the reduced matrix element in terms of F and F' states as the radial wavefunction of the atomic system depends on the principal quantum number n and the orbital angular momentum quantum number L . To express the reduced matrix element in terms of L and L' , we use [108]

$$\langle F' \| \mathbf{er} \| F \rangle = \langle J' \| er \| J \rangle (-1)^{I+J'+F+1} \sqrt{(2F+1)(2J'+1)} \left\{ \begin{array}{ccc} J' & J & 1 \\ F & F' & I \end{array} \right\}, \quad (\text{A.2})$$

and

$$\langle J' \| \mathbf{er} \| J \rangle = \langle L' \| er \| L \rangle (-1)^{J+L'+S+1} \sqrt{(2J+1)(2L'+1)} \left\{ \begin{array}{ccc} L' & L & 1 \\ J & J' & S \end{array} \right\}, \quad (\text{A.3})$$

to re-write $\langle F' \| er \| F \rangle$. Thus the dipole matrix element is given by

$$\begin{aligned} \langle F', m'_F | er_q | F, m_F \rangle &= \sqrt{(2F'+1)(2F+1)(2J'+1)(2J+1)(2L'+1)} \\ &\times \begin{pmatrix} F & 1 & F' \\ m_F & q & -m'_F \end{pmatrix} \left\{ \begin{array}{ccc} J' & J & 1 \\ F & F' & I \end{array} \right\} \left\{ \begin{array}{ccc} L' & L & 1 \\ J & J' & S \end{array} \right\} \\ &\times (-1)^{I+L'+S+m'_F+1} \langle L' \| er \| L \rangle. \end{aligned} \quad (\text{A.4})$$

Here I is the nuclear spin of the atom, S is the spin of the electron and the curly bracket containing six elements is known as a 6j symbol.

Appendix B

Diagonalising the matrix H_c

We follow the method given in [66]. The eigenvalue equation of the tridiagonal matrix H_c can be obtained by using the Floquet-Fourier transformation of the ODE, given by

$$h(t)\phi(t) = i\frac{\partial}{\partial t}\phi(t), \quad (\text{B.1})$$

with

$$h(t) = b + 2a \cos(2\omega t), \quad (\text{B.2})$$

where a and b are constant. Since $h(t)$ is time-periodic, the solution of this type of equation can be written using Floquet-Fourier theorem as

$$\phi(t) = \exp(-i\lambda t)\psi(t), \quad (\text{B.3})$$

where λ is the quasi-eigenvalue of the ODE and the function $\psi(t)$ is periodic in time with the angular frequency of 2ω , i.e., the same as that of $h(t)$. Substituting (B.3) into (B.1), the differential equation (B.1) becomes,

$$\left[h(t) - i\frac{\partial}{\partial t} \right] \psi(t) = \lambda\psi(t). \quad (\text{B.4})$$

It is now clear that Equation (B.1) takes the form of an eigenvalue equation with the eigenvalue λ and the eigenvector $\psi(t)$. Since $\psi(t)$ is periodic, it can be expanded using Fourier series:

$$\psi(t) = \sum_{k=-\infty}^{\infty} \alpha_k \exp(-2i\omega kt), \quad (\text{B.5})$$

where α_k is the coefficient of expansion. Substituting Equation (B.5) into (B.4), Equation (B.4) becomes the infinite sum of the algebraic recurrence equation,

$$\sum (b\alpha_k + a\alpha_{k+1} + a\alpha_{k-1} - 2\omega k\alpha_k) \exp -2i\omega kt = \sum \lambda\alpha_k \exp -2i\omega kt. \quad (\text{B.6})$$

This recurrence relation can be transformed into coupled equations, namely

$$(b - 2k\omega)\alpha_k + a\alpha_{k+1} + a\alpha_{k-1} = \lambda\alpha_k, \quad (\text{B.7})$$

which, in turn, can be re-written in the matrix eigenvalue equation as

$$\begin{pmatrix} \ddots & \vdots & \vdots & \vdots & \\ \cdots & b + 2\omega & a & 0 & \cdots \\ \cdots & a & b & a & \cdots \\ \cdots & 0 & a & b - 2\omega & \cdots \\ & \vdots & \vdots & \vdots & \ddots \end{pmatrix} \begin{pmatrix} \vdots \\ \alpha_{-1} \\ \alpha_0 \\ \alpha_{+1} \\ \vdots \end{pmatrix} = \lambda \begin{pmatrix} \vdots \\ \alpha_{-1} \\ \alpha_0 \\ \alpha_{+1} \\ \vdots \end{pmatrix}. \quad (\text{B.8})$$

Note that the form of the matrix in Equation (B.8) is actually the same as that of H_c ; thus if one can solve Equation (B.4) for $\psi(t)$, then the eigenvalue problem of H_c is simultaneously solved.

It turns out that a trivial solution of Equation (B.4) is

$$\psi(t) = \exp \left[-i \frac{a}{\omega} \sin(2\omega t) \right], \quad (\text{B.9})$$

with the associated eigenvalue of b . This can be confirmed by substituting the ansatz into (B.4):

$$\begin{aligned} \left[h(t) - i \frac{\partial}{\partial t} \right] \psi(t) &= [b + 2a \cos(2\omega t)] \exp \left[-i \frac{a}{\omega} \sin(2\omega t) \right] \\ &\quad - i \frac{\partial}{\partial t} \exp \left[-i \frac{a}{\omega} \sin(2\omega t) \right] \\ &= [b + 2a \cos(2\omega t)] \exp \left[-i \frac{a}{\omega} \sin(2\omega t) \right] \\ &\quad - 2a \cos(2\omega t) \exp \left[-i \frac{a}{\omega} \sin(2\omega t) \right] \\ &= b \exp \left[-i \frac{a}{\omega} \sin(2\omega t) \right] \\ &= \lambda \exp \left[-i \frac{a}{\omega} \sin(2\omega t) \right]. \end{aligned} \quad (\text{B.10})$$

Thus Equation (B.9) is indeed the eigen-solution of Equation (B.4). Using the Jacobi-Anger expansion [139], Equation (B.9) then becomes,

$$\psi(t) = \sum_{k=-\infty}^{\infty} J_{-k} \left(-\frac{a}{\omega} \right) \exp(-2ik\omega t). \quad (\text{B.11})$$

According to the Floquet-Fourier theorem, we expect a manifold of quasi-eigenenergies whose energy separation is 2ω . Thus the whole set of the quasi-eigenenergy is

$$\lambda_n = b - 2n\omega, \quad (\text{B.12})$$

where n is the set of integers. For the quasi-eigenvalue λ_n , the associated eigenvector is given by the product of $\exp(-2in\omega t)$ with $\psi(t)$ ¹:

$$\begin{aligned} \psi_n(t) &= \exp(-2in\omega t) \exp \left[-i\frac{a}{\omega} \sin(2\omega t) \right] \\ &= \exp(-2in\omega t) \sum_{k=-\infty}^{\infty} J_{-k} \left(-\frac{a}{\omega} \right) \exp(-2ik\omega t) \\ &= \sum_{k=-\infty}^{\infty} J_{n-k} \left(-\frac{a}{\omega} \right) \exp(-2ik\omega t). \end{aligned} \quad (\text{B.13})$$

In our case, $a = -\Sigma/2$ and $b = \Sigma - \Delta_c$; thus the eigenvector of \mathbf{H}_c is given by

$$|c', n\rangle = \sum_{k=-\infty}^{\infty} J_{n-k} \left(\frac{\Sigma}{2\omega_{\text{rf}}} \right) |c, k\rangle. \quad (\text{B.14})$$

¹c.f. Bloch's theorem [148].

Bibliography

- [1] S. E. Harris, *Phys. Today* **50**, 36 (1995).
- [2] J. P. Marangos, *J. Mod. Opt.* **45**, 471 (1998).
- [3] M. Fleischhauer, A. Imamoglu, and J. P. Marangos, *Rev. Mod. Phys.* **77**, 633 (2005).
- [4] P. R. Hemmer and M. G. Prentiss, *J. Opt. Soc. Am. B* **5**, 1613 (1988).
- [5] C. L. Garrido Alzar, M. A. G. Martinez, and P. Nussenzveig, *Am. J. Phys.* **70**, 37 (2002).
- [6] K.-J. Boller, A. Imamoglu, and S. E. Harris, *Phys. Rev. Lett.* **66**, 2593 (1991).
- [7] A. Kasapi, M. Jain, G. Y. Yin, and S. E. Harris, *Phys. Rev. Lett.* **74**, 2447 (1995).
- [8] M. Xiao, Y.-Q. Li, S.-Z. Jin, and J. Gea-Banacloche, *Phys. Rev. Lett.* **74**, 666 (1995).
- [9] S. E. Harris, J. E. Field, and A. Kasapi, *Phys. Rev. A* **46**, R29 (1992).
- [10] M. O. Scully, *Phys. Rev. Lett.* **67**, 1855 (1991).
- [11] L. V. Hau, S. E. Harris, Z. Dutton, and C. H. Behroozi, *Nature* **397**, 594 (1999).

-
- [12] D. Budker, D. F. Kimball, S. M. Rochester, and V. V. Yashchuk, Phys. Rev. Lett. **83**, 1767 (1999).
- [13] M. O. Scully and M. Fleischhauer, Phys. Rev. Lett. **69**, 1360 (1992).
- [14] M. Fleischhauer and M. D. Lukin, Phys. Rev. Lett. **84**, 5094 (2000).
- [15] T. Chanelière et al., Nature **438**, 833 (2005).
- [16] M. D. Eisaman et al., Nature **438**, 837 (2005).
- [17] D. F. Phillips, A. Fleischhauer, A. Mair, R. L. Walsworth, and M. D. Lukin, Phys. Rev. Lett. **86**, 783 (2001).
- [18] U. Schnorrberger et al., Phys. Rev. Lett. **103**, 033003 (2009).
- [19] C. Liu, Z. Dutton, C. H. Behroozi, and L. V. Hau, Nature **406**, 490 (2001).
- [20] A. M. Akulshin and R. J. McLean, J. Opt. **12**, 104001 (2010).
- [21] M. Tanasittikosol et al., J. Phys. B: At. Mol. Opt. Phys. **44**, 184020 (2011).
- [22] H. Kang, G. Hernandez, and Y. Zhu, Phys. Rev. A **70**, 011801 (2004).
- [23] T. F. Gallagher, *Rydberg Atoms*, Cambridge: Cambridge University Press, 1994.
- [24] M. Saffman, T. G. Walker, and K. Mølmer, Rev. Mod. Phys. **82**, 2313 (2010).
- [25] M. G. Bason et al., New J. Phys. **12**, 065015 (2010).
- [26] D. Jaksch et al., Phys. Rev. Lett. **85**, 2208 (2000).
- [27] M. D. Lukin et al., Phys. Rev. Lett. **87**, 037901 (2001).
- [28] T. A. Johnson et al., Phys. Rev. Lett. **100**, 113003 (2008).

-
- [29] D. Møller, L. B. Madsen, and K. Mølmer, *Phys. Rev. Lett.* **100**, 170504 (2008).
- [30] I. I. Beterov et al., arXiv:1102.5223v4 (2011).
- [31] A. Osterwalder and F. Merkt, *Phys. Rev. Lett.* **82**, 1831 (1999).
- [32] A. K. Mohapatra, T. R. Jackson, and C. S. Adams, *Phys. Rev. Lett.* **98**, 113003 (2007).
- [33] S. Mauger, J. Millen, and M. P. A. Jones, *J. Phys. B: At. Mol. Opt. Phys.* **40**, F319 (2007).
- [34] K. J. Weatherill et al., *J. Phys. B: At. Mol. Opt. Phys.* **41**, 201002 (2008).
- [35] H. Kübler, J. P. Shaffer, T. Baluksian, R. Löw, and T. Pfau, *Nat. Photon.* **4**, 112 (2010).
- [36] P. Schwindt et al., *Appl. Phys. Lett.* **85**, 6409 (2004).
- [37] A. K. Mohapatra, M. G. Bason, B. Butscher, K. J. Weatherill, and C. S. Adams, *Nat. Phys.* **8**, 890 (2008).
- [38] U. Raitzsch et al., *New J. Phys.* **11**, 055014 (2009).
- [39] J. D. Pritchard et al., *Phys. Rev. Lett.* **105**, 193603 (2010).
- [40] I. Friedler, D. Petrosyan, M. Fleischhauer, and G. Kurizki, *Phys. Rev. A* **72**, 043803 (2005).
- [41] M. Müller, I. Lesanovsky, H. Weimer, H. P. Büchler, and P. Zoller, *Phys. Rev. Lett.* **102**, 170502 (2009).
- [42] F. Bariani, Y. O. Dudin, T. A. B. Kennedy, and A. Kuzmich, arXiv:1107.3202v1 (2011).
- [43] S. H. Autler and C. H. Townes, *Phys. Rev.* **100**, 703 (1955).

-
- [44] C. H. Townes and A. L. Schawlow, *Microwave Spectroscopy*, London: McGrawHill, 1955.
- [45] J. H. Shirley, Phys. Rev. **138**, B979 (1965).
- [46] C. H. Townes and F. R. Merritt, Phys. Rev. **72**, 1266 (1947).
- [47] J. E. Bayfield, L. D. Gardner, Y. Z. Gulkok, and S. D. Sharma, Phys. Rev. A **24**, 138 (1981).
- [48] M. Ciocca, C. E. Burkhardt, J. J. Leventhal, and T. Bergeman, Phys. Rev. A **45**, 4720 (1992).
- [49] N. Spellmeyer et al., Phys. Rev. Lett. **79**, 1650 (1997).
- [50] H. B. van Linden van den Heuvell, R. Kachru, N. H. Tran, and T. F. Gallagher, Phys. Rev. Lett. **53**, 1901 (1984).
- [51] C. S. E. van Ditzhuijzen, A. Tauschinsky, and H. B. van Linden van den Heuvell, Phys. Rev. A **80**, 063407 (2009).
- [52] A. Tauschinsky, C. S. E. van Ditzhuijzen, L. D. Noordam, and H. B. van Linden van den Heuvell, Phys. Rev. A **78**, 063409 (2008).
- [53] Y. Zhang, M. Ciocca, L.-W. He, C. E. Burkhardt, and J. J. Leventhal, Phys. Rev. A **50**, 1101 (1994).
- [54] T. Shirahama, X.-M. Tong, K.-i. Hino, and N. Toshima, Phys. Rev. A **80**, 043414 (2009).
- [55] V. Bouchiat, D. Vion, P. Joyez, D. Esteve, and M. H. Devoret, Phys. Scr. **1998**, 165 (1998).
- [56] Y. Nakamura, Y. A. Pashkin, and J. S. Tsai, Science **398**, 786 (1999).
- [57] Y. Makhlin, G. Schön, and A. Shnirman, Rev. Mod. Phys. **73**, 357 (2001).

-
- [58] D. Vion et al., *Science* **296**, 886 (2002).
- [59] E. Collin et al., *Phys. Rev. Lett.* **93**, 157005 (2004).
- [60] A. Shnirman, G. Schön, and Z. Hermon, *Phys. Rev. Lett.* **79**, 2371 (1997).
- [61] D. V. Averin, *Solid State Commun.* **105**, 659 (1998).
- [62] Y. Makhlin, G. Schön, and A. Shnirman, *Nature* **398**, 305 (1999).
- [63] J. E. Mooij et al., *Science* **285**, 1036 (1999).
- [64] C. H. van der Wal et al., *Science* **290**, 773 (2000).
- [65] I. Chiorescu, Y. Nakamura, C. J. P. M. Harmans, and J. E. Mooij, *Science* **299**, 1869 (2003).
- [66] S.-K. Son, S. Han, and S.-I. Chu, *Phys. Rev. A* **79**, 032301 (2009).
- [67] T. P. Orlando et al., *Phys. Rev. B* **60**, 15398 (1999).
- [68] D. Suter, *The Physics of Laser-Atom Interactions*, Cambridge: Cambridge University Press, 1997.
- [69] G. Grynberg, A. Aspect, and C. Fabre, *Introduction to Quantum Optics: From the Semi-classical Approach to Quantized Light*, Cambridge: Cambridge University Press, 2010.
- [70] E. Brion, L. H. Pedersen, and K. Mølmer, *J. Phys. A: Math. Theor.* **40**, 1033 (2007).
- [71] P. M. Radmore and P. L. Knight, *J. Phys. B: At. Mol. Phys.* **15**, 561 (1982).
- [72] A. F. Linskens, I. Holleman, N. Dam, and J. Reuss, *Phys. Rev. A* **54**, 4854 (1996).

-
- [73] F. H. Read, *Electromagnetic Radiation*, Bristol: John Wiley & Sons, 1980.
- [74] B. H. Bransden and C. J. Joachain, *Physics of Atoms and Molecules*, London: Prentice Hall, 2003.
- [75] A. Corney, *Atomic and Laser Spectroscopy*, Oxford: Oxford University Press, 2006.
- [76] R. Loudon, *The Quantum Theory of Light*, Oxford: Oxford University Press, 1997.
- [77] C. J. Foot, *Atomic Physics*, Oxford: Oxford University Press, 2004.
- [78] R. J. Cook, Phys. Rev. A **20**, 224 (1979).
- [79] F. W. Byron and R. W. Fuller, *Mathematics of classical and Quantum Physics*, New York: Dover Publications, 1992.
- [80] A. Messiah, *Quantum Mechanics*, New York: Dover Publications, 2003.
- [81] S. R. de Echaniz et al., Phys. Rev. A **64**, 013812 (2001).
- [82] K. Bergmann, H. Theuer, and B. W. Shore, Rev. Mod. Phys. **70**, 1003 (1998).
- [83] I. Lizuain, E. Hernández-Concepción, and J. G. Muga, Phys. Rev. A **79**, 065602 (2009).
- [84] J. Gea-Banacloche, Y. Li, S. Jin, and M. Xiao, Phys. Rev. A **51**, 576 (1995).
- [85] B. W. Shore et al., Phys. Rev. A **45**, 5297 (1992).
- [86] T. Cubel et al., Phys. Rev. A **72**, 023405 (2005).

-
- [87] P. M. Anisimov, J. P. Dowling, and B. C. Sanders, arXiv:1102.0546v2 (2011).
- [88] T. Y. Abi-Salloum, Phys. Rev. A **81**, 053836 (2010).
- [89] I. Lizuain, J. Echanobe, A. Ruschhaupt, J. G. Muga, and D. A. Steck, Phys. Rev. A **82**, 065602 (2010).
- [90] G. Lindblad, Commun. Math. Phys. **48**, 119 (1976).
- [91] M. Weissbluth, *Photon-Atom Interactions*, London: Academic Press, 1989.
- [92] M. G. Bason, *Coherent atom-light interactions in multi-level systems*, PhD thesis, Durham University, 2009.
- [93] J. Jackson, *Classical Electrodynamics*, New York: Wiley, 1975.
- [94] U. D. Rapol and V. Natarajan, Eur. Phys. J. D **28**, 317 (2004).
- [95] P. Anisimov and O. Kocharovskaya, J. Mod. Opt. **55**, 3159 (2008).
- [96] W. Rindler, *Introduction to Special Relativity*, Oxford: Oxford University Press, 1991.
- [97] C. Kittel and H. Kroemer, *Thermal Physics*, US: W. H. Freeman, 1980.
- [98] H. E. Fettis, J. C. Caslin, and K. R. Cramer, Math. Comput. **27**, 401 (1973).
- [99] G. P. M. Poppe and C. M. J. Wijers, ACM T. Math. SOFTWARE **16**, 38 (1990).
- [100] J. Deiglmayr et al., Opt. Commun. **264**, 293 (2006).
- [101] M. J. Piotrowicz et al., arXiv:1103.0109v2 (2011).

-
- [102] D. A. Steck, Rubidium 85 D Line Data, 2010.
- [103] J. E. Sansonetti, J. Phys. Chem. Ref. Data **37**, 1183 (2008).
- [104] W. Li, I. Mourachko, M. W. Noel, and T. F. Gallagher, Phys. Rev. A **67**, 052502 (2003).
- [105] J. Qi, Phys. Scr. **81**, 015402 (2010).
- [106] S. Blundell and K. Blundell, *Concepts in Thermal Physics*, Oxford: Oxford University Press, 2006.
- [107] C. B. Alcock, V. P. Itkin, and M. K. Horrigan, Can. Metall. Q. **23**, 309 (1984).
- [108] R. N. Zare, *Angular momentum: Understanding Spatial Aspects in Chemistry and Physics*, Wiley Inter-Science.
- [109] A. R. Edmonds, *Angular Momentum in Quantum Mechanics*, Princeton University Press.
- [110] P. Siddons, C. S. Adams, C. Ge, and I. G. Hughes, J. Phys. B: At. Mol. Opt. Phys. **41**, 155004 (2008).
- [111] I. G. Hughes and T. P. A. Hase, *Measurements and their uncertainties: A practical guide to modern error analysis*, Oxford: Oxford University Press, 2010.
- [112] A. Sargsyan, D. Sarkisyan, U. Krohn, J. Keaveney, and C. Adams, Phys. Rev. A **82**, 045806 (2010).
- [113] A. Sargsyan, M. Bason, D. Sarkisyan, A. Mohapatra, and C. Adams, Opt. Spectroscopy (USSR) **109**, 529 (2010).
- [114] J. H. Xu, A. Gozzini, F. Mango, G. Alzetta, and R. A. Bernheim, Phys. Rev. A **54**, 3146 (1996).

-
- [115] H. B. Michaelson, *J. Appl. Phys.* **48**, 4729 (1977).
- [116] F. Luna, G. Cavalcanti, L. Coutinho, and A. Trigueiros, *J. Quant. Spectrosc. Radiat. Transfer* **75**, 559 (2002).
- [117] C. Y. Ye, A. S. Zibrov, Y. V. Rostovtsev, A. B. Matsko, and M. O. Scully, *J. Mod. Opt.* **49**, 2485 (2002).
- [118] C. Goren, A. D. Wilson-Gordon, M. Rosenbluh, and H. Friedmann, *Phys. Rev. A* **69**, 053818 (2004).
- [119] T. Hong, C. Cramer, W. Nagourney, and E. N. Fortson, *Phys. Rev. Lett.* **94**, 050801 (2005).
- [120] A. S. Zibrov, C. Y. Ye, Y. V. Rostovtsev, A. B. Matsko, and M. O. Scully, *Phys. Rev. A* **65**, 043817 (2002).
- [121] Wei, Xiao-Gang et al., *Europhys. Lett.* **78**, 44002 (2007).
- [122] L. Kong, X. Tu, J. Wang, Y. Zhu, and M. Zhan, *Opt. Commun.* **269**, 362 (2007).
- [123] Y. Bai, W. Yang, and X. Yu, *Opt. Commun.* **283**, 5062 (2010).
- [124] J. Kou et al., *J. Opt. Soc. Am. B* **27**, 2035 (2010).
- [125] X. Yan, L. Wang, B. Yin, and J. Song, *Optik* **122**, 986 (2011).
- [126] Z. Kis and F. Renzoni, *Phys. Rev. A* **65**, 032318 (2002).
- [127] E. Paspalakis and P. L. Knight, *J. Opt. B: Quantum Semiclass. Opt.* **4**, S372 (2002).
- [128] M. G. Bason, A. K. Mohapatra, K. J. Weatherill, and C. S. Adams, *J. Phys. B: At. Mol. Opt. Phys.* **42**, 075503 (2009).
- [129] B. J. Dalton, *J. Phys. A: Math. Gen.* **15**, 2157 (1982).

-
- [130] R. R. Moseley, S. Shepherd, D. J. Fulton, B. D. Sinclair, and M. H. Dunn, *Opt. Commun.* **119**, 61 (1995).
- [131] O. S. Heavens, *J. Opt. Soc. Am.* **51**, 1058 (1961).
- [132] S. Barnett and P. Radmore, *Methods in Theoretical Quantum Optics*, Oxford: Oxford University Press.
- [133] M. Abramowitz and I. A. Stegun, *Handbook of Mathematical Functions with Formulas, Graphs, and Mathematical Tables*, New York: Dover Publications.
- [134] A. M. Akulshin, S. Barreiro, and A. Lezama, *Phys. Rev. A* **57**, 2996 (1998).
- [135] A. V. Taichenachev, A. M. Tumaikin, and V. I. Yudin, *Phys. Rev. A* **61**, 011802 (1999).
- [136] E. Tilchin, A. D. Wilson-Gordon, and O. Firstenberg, *Phys. Rev. A* **83**, 053812 (2011).
- [137] M. S. O'Sullivan and B. P. Stoicheff, *Phys. Rev. A* **31**, 2718 (1985).
- [138] M. Pont, R. M. Potvliege, R. Shakeshaft, and Z.-J. Teng, *Phys. Rev. A* **45**, 8235 (1992).
- [139] G. Dattoli, L. Giannessi, L. Mezi, and A. Torre, *II Nuovo Cimento B (1971-1996)* **105**, 327 (1990).
- [140] R. P. Abel et al., *Appl. Phys. Lett.* **94**, 071107 (2009).
- [141] A. Bondeson, T. Rylander, and P. Ingelström, *Computational Electromagnetics*, New York: Springer.
- [142] Y. Zhang, M. Ciocca, L.-W. He, C. E. Burkhardt, and J. J. Leventhal, *Phys. Rev. A* **50**, 4608 (1994).

-
- [143] M. Yan, E. G. Rickey, and Y. Zhu, *J. Opt. Soc. Am. B* **18**, 1057 (2001).
- [144] D. Budker, D. F. Kimball, and D. DeMille, *Atomic Physics : an exploration through problems and solutions*, Oxford: Oxford University Press.
- [145] N. B. Delone and V. P. Krainov, *Sov. Phys. Usp.* **42**, 669 (1999).
- [146] S. R. Barone, M. A. Narcowich, and F. J. Narcowich, *Phys. Rev. A* **15**, 1109 (1977).
- [147] G. Floquet, *Ann. École Norm. Sup.* **12**, 47 (1883).
- [148] N. W. Ashcroft and N. D. Mermin, *Solid State Physics*, Tokyo: CBS Publishing, 1981.
- [149] W. Press, S. Teukolsky, W. Vetterling, and B. Flannery, *Numerical Recipes: The Art of Scientific Computing*, Cambridge University Press, Cambridge, England, 2007.
- [150] D. McGloin, D. J. Fulton, and M. H. Dunn, *Opt. Commun.* **190**, 221 (2001).
- [151] J.-Y. Gao et al., *Phys. Rev. A* **61**, 023401 (2000).
- [152] G. S. Agarwal and W. Harshawardhan, *Phys. Rev. Lett.* **77**, 1039 (1996).
- [153] S. Wielandy and A. L. Gaeta, *Phys. Rev. A* **58**, 2500 (1998).
- [154] M. G. Bason, A. K. Mohapatra, K. J. Weatherill, and C. S. Adams, *Phys. Rev. A* **77**, 032305 (2008).
- [155] L. Brillouin, *Wave Propagation and Group Velocity*, New York: Academic, 1960.
- [156] P. W. Milonni, *Fast Light, Slow Light, and Left-Handed Light*, Bristol: Institute of Physics Publishing, 2005.

-
- [157] G. Diener, Phys. Lett. A **223**, 327 (1996).
- [158] G. M. Gehring, A. Schweinsberg, C. Barsi, N. Kostinski, and R. W. Boyd, Science **312**, 895 (2006).
- [159] G. P. Agarwal, *Nonlinear Fiber Optics*, Academic Press, San Diego, CA, 1995.
- [160] C. G. B. Garrett and D. E. McCumber, Phys. Rev. A **1**, 305 (1970).
- [161] M. D. Crisp, Phys. Rev. A **1**, 1604 (1970).
- [162] A. Dogariu, A. Kuzmich, H. Cao, and L. Wang, Opt. Express **8**, 344 (2001).
- [163] R. W. Boyd and D. J. Gauthier, Chapter 6 “slow” and “fast” light, volume 43 of *Progress in Optics*, pages 497 – 530, Amsterdam: Elsevier, 2002.
- [164] K. T. McDonald, Am. J. Phys. **69**, 607 (2001).
- [165] L. J. Wang, A. Kuzmich, and A. Dogariu, Nature **406**, 277 (2000).